Multi-solitonic states in a Bose-Einstein Condensate mixture

Guillaume Brochier

THÈSE DE DOCTORAT DE SORBONNE UNIVERSITÉ

préparée par

GUILLAUME BROCHIER

sous la direction de

JÉRÔME BEUGNON ET JEAN DALIBARD

Multi-solitonic states in a Bose-Einstein Condensate mixture

Soutenue le 13 mars 2026 devant le jury composé de :

M. Stefan KUHR ..... Rapporteur
M. Pascal SZRIFTGISER ..... Rapporteur
Mme. Claire MICHEL ..... Examinatrice
Mme. Laurence PRUVOST ..... Présidente du jury
M. Jérôme BEUGNON ..... Directeur de thèse

Travail réalisé au Laboratoire Kastler Brossel, au sein du Collège de France.

ABSTRACT

Once its phase-space density is high enough, an interacting dilute Bose gas can be described by a macroscopic wave function obeying nonlinear dynamics. Ultracold Bose gases thus form coherent quantum fluids whose behavior becomes particularly rich in one dimension, where interactions and integrability tightly guide the evolution. In this thesis, we study a two-component weakly interacting 1D Bose gas that maps onto the attractive nonlinear Schrödinger equation (NLSE) in a certain limit, and more generally onto the Landau–Lifshitz equation (LLE), governing spin-chains. This correspondence enables the controlled preparation and exploration of multi-soliton solutions of both models.
We first realize NLSE multi-solitons and characterize their dynamics, including their distinctive breathing behavior. Using the full LLE mapping, we then extend this implementation to multi-solitons with arbitrary depletion, thereby accessing a broader family of solitons and revealing features intrinsic to the underlying spin-chain description.
Finally, we investigate weak integrability breaking and show that it drives the decomposition of multi-solitons into their constituents, rendering their encoded scattering data experimentally accessible. This provides a controlled pathway to probe integrable structures, opening prospects for studying soliton gases, interacting nonlinear waves, and the emergence of complex dynamics from nearly integrable systems.

RÉSUMÉ

Pour une densité de l'espace de phase suffisamment élevée, un gaz de Bose dilué en interaction peut être décrit par une fonction d'onde macroscopique obéissant à une dynamique non linéaire. Les gaz de Bose ultrafroids forment ainsi des fluides quantiques cohérents dont le comportement devient particulièrement riche à une dimension, où les interactions et l'intégrabilité guident fortement l'évolution. Dans cette thèse, nous étudions un gaz de Bose 1D à deux composantes en interaction faible, qui se décrit par l'équation de Schrödinger non linéaire attractive (NLSE) dans un certain régime, et plus généralement par l'équation de Landau-Lifshitz (LLE), régissant la dynamique de chaînes de spin. Cette correspondance permet la préparation et l'exploration contrôlées de solutions multi-solitons des deux modèles.
Nous réalisons d'abord des solitons multiples NLSE et caractérisons leur dynamique, notamment leur comportement respirant distinctif. En utilisant une description complète via LLE, nous étendons ensuite cette mise en œuvre à des solitons multiples avec une déplétion arbitraire, accédant ainsi à une famille plus large de solitons et révélant des caractéristiques intrinsèques à la description sous-jacente de la chaîne de spin.
Enfin, nous étudions la brisure de l'intégrabilité et montrons qu'elle entraîne la décomposition des multi-solitons en leurs constituants, rendant ainsi leurs données de diffusion accessibles expérimentalement. Cela fournit une voie contrôlée pour sonder les structures intégrables, ouvrant des perspectives pour l'étude des gaz de solitons, des ondes non linéaires en interaction et de l'émergence de dynamiques complexes à partir de systèmes presque intégrables.

REMERCIEMENTS

Je souhaiterais dédier les quelques lignes qui suivent à toutes les personnes qui ont permis l'accomplissement de ce long travail.

En premier lieu, je voudrais remercier tous les membres du jury, Stefan Kuhr, Pascal Szriftgiser, Claire Michel, Laurence Pruvost, d'avoir accepté de lire ma thèse et d'assister à ma soutenance.

Jérôme, bien que faisant également partie du jury, occupe une place plus importante encore en tant que directeur de thèse. Je lui suis particulièrement reconnaissant de m'avoir accepté dans l'équipe Condensat de Bose-Einstein, plus précisement sur la manip Rb, il y a maintenant quatre ans. Sa présence au quotidien, ses conseils (scientifiques ou non) ont toujours été précieux. Ton implication, ainsi que mes nombreuses visites matinales (intempestives ?) pour discuter des différents projets m'ont sans aucun doute beaucoup apporté. Je continue aussi de m'entraîner pour te dépasser un jour en course à pied !

L'équipe Rb compte deux autres membres permanents, Jean et Sylvain, dont les contributions ont toujours été cruciales. En plus de dispenser des cours d'une qualité inégalée, Jean reste invariablement ouvert à la discussion, et ce avec une bonne humeur constante. Ses notes pour éclaircir un nouveau projet se sont toujours révélées précieuses. De manière similaire, les discussions avec Sylvain sont très enrichissantes, notamment de par son intuition physique impressionnante.

Durant ces années au Collège de France, j'ai également eu la chance de travailler avec de nombreux autres doctorants. Brice et Chloé m'ont d'abord accueilli dans leur bureau, et le récent retour de Brice au Collège de France nous a également permis de nombreux échanges. Mon travail de thèse a débuté avec Guillaume (alias GC) et Franco, sur la construction d'une nouvelle manip. Vous m'avez tous les deux impressionné dès mes premiers jours à la fois par votre compréhension, et votre grande capacité de travail. J'aurais aimé davantage collaborer avec GC, qui a rapidement été transféré sur Rb3 avant de rédiger sa thèse. Nous avons cependant eu l'occasion de partager de nombreux moments conviviaux, que ce soit autour d'un tup, une baguette, ou durant nos footings. Merci encore de nous avoir accueillis à Chartres et à Vallandry, et je t'attends sur les sentiers savoyards dès cet été ! Franco a toujours été le couteau suisse du labo : il sait à peu près tout faire, avec une capacité incroyable de s'approprier un nouveau sujet et prendre le temps de le maîtriser. Sa persévérance a permis de mener à bien les différents projets où il était impliqué. Le hasard a également fait que nous nous retrouverons prochainement à Munich, où je serai ravi de tester les Biergarten avec toi !

De nouveaux doctorants ont ensuite pris le relais, et en premier lieu Sarah, qui a courageusement repris la manip Rb4 pendant que je poursuivais avec Rb3. Malgré des premiers mois à mener un projet difficile, tu as ensuite pris à cœur la reconstruction complète de la manip, en t'appropriant tous ses éléments. Je sais qu'une thèse peut être stressante et délicate par moment, mais je suis sûr que tu vas réussir avec brio. L'équipe s'est encore agrandie en recrutant Yifan en postdoc, qui a pu nous aider alternativement sur les deux manip et nous faire partager son expérience. Plus récemment, c'est au

tour de deux doctorants allemands, Sarah puis Jonathan, de nous rejoindre, et je leur souhaite d'apprécier au moins autant que moi leur passage au Collège. J'ai eu la chance de côtoyer une équipe très chaleureuse, qui savait alterner les moments de travail avec les soirées plus détendues, toujours très appréciables dans les moments plus difficiles.

L'équipe BEC ne se résume pas à la (aux) manip Rb, et j'aimerais également remercier toutes les autres personnes que j'ai pu fréquenter. Pour commencer, Raphaël, avec qui j'ai partagé le labo durant ma première année. Les nombreux autres (post-)doctorants ont également été essentiels à la vie de l'équipe : Rémy, Tanish, Aurélien, Qi, JB, Quentin, Nehal, Evgenii, Tristan, Mathis, Maxime, Alexandre, Julie, Ethan, Nils. On compte notamment de nombreux coureurs, avec qui j'ai eu le plaisir d'explorer les nombreux quais de Paris (voir le tour complet!), ainsi que des experts de billard ou même de bière, toujours prêts à partager un moment convivial.

Notre équipe est hébergée au Collège de France, dont je remercie tout le personnel pour son soutien dans nos problèmes du quotidien. Un mot en particulier pour Carmen, qui a toujours su régler admirablement toutes les difficultés administratives. Le Collège compte de nombreuses autres équipes, de physique ou non. Les membres du rez-de-chaussée, en particulier Andres, Gauthier et Baptiste, m'ont beaucoup apporté par leurs discussions et le partage de leur sujet de recherche. Il faut également souligner l'implication des Chadoc pour permettre aux différents doctorants du Collège de se rencontrer et d'échanger, à travers de nombreux événements chaleureux.

Le LKB s'étend au-delà du Collège, notamment à l'ENS et à Jussieu. Je souhaiterais tout d'abord remercier Stéphanie Dubois ainsi que toute l'équipe administrative pour leur aide durant ces quatre années. Les séminaires et journées du labo ont également été l'occasion de découvrir de fascinantes thématiques de recherche à travers de nombreuses discussions. J'adresse plus particulièrement mes remerciements à l'équipe d'optique quantique, avec qui il a toujours été agréable d'échanger depuis mon stage de master.

Enfin, tout ce travail n'aurait pas non plus été possible sans le soutien de mes proches, notamment le long de ces (longues) études. Je remercie particulièrement Émilien qui m'a toujours accompagné pour un tour de vélo dans le Chablais malgré mon sous-entraînement notoire, le groupe HX1, Martin, Coco, Théo, Lucie, Olivier, Victor, (rejoint maintenant par Ella et Floriane), dont une partie a pu se regrouper à Paris, les membres de l'AS de l'ENS de Lyon et en particulier l'équipe de basket, Maxime, Thomas, Zoé (et maintenant la petite Charlie), le groupe de parisien·ne·s toujours partant pour une crêpe-party, Léa, Lisa, Evan, Camille, Pauline, Johanna, Coline, ainsi que tout le club du Raid orientation Paris, qui m'a permis de nombreuses escapades dans les forêts parisiennes pour décompresser le samedi matin, et des week-ends (boueux ?) de courses. Je n'oublie pas Victoire, qui m'accompagne au quotidien, m'a toujours soutenu, et a maintenant décidé de continuer l'aventure avec moi à Munich : merci de me faire sourire tous les matins et tous les soirs, je t'aime.

Je conclus ces remerciements avec ma famille, j'ai une pensée pour mon grand-père qui nous a quittés l'année dernière, ma grand-mère, mes oncles. Merci aussi à Camille, qui a grandi avec moi et avec qui je partage de plus en plus de passions (notamment sportives, j'attends de voir ton nouveau gravel en action). Ces derniers mots vont à mes parents, que je ne remercierai jamais assez de m'avoir rendu aussi curieux, de m'avoir aidé à découvrir tant de choses (même les duomo), qui m'ont toujours soutenu dans tous mes projets, et continueront sans aucun doute de m'accompagner.

Merci à tous·tes !

Acronyms

AKNS Ablowitz-Kaup-Newell-Segur. 62, 63

AOM Acousto-Optic Modulator. 12, 14

BEC Bose-Einstein Condensate. 3, 4, 8, 10, 11, 13, 14, 18, 20, 21, 30, 33, 35, 43, 45, 69, 70, 84, 114, 125

BECn Bose-Einstein Condensation. 1, 8, 11, 22, 24, 25, 26

BKT Berezinskii-Kosterlitz-Thouless. 24, 25, 26

BO Bloch Oscillation. 92, 94, 95, 96, 107

CCD Charge-Coupled Device. 12

DMD Digital Micro-mirror Device. 9, 12, 13, 14, 15, 29, 70, 73, 74, 75, 76, 115, 119, 120, 125

EOM Electro-Optic Modulator. 8, 14

FPUT Fermi-Pasta-Ulam-Tsingou. 2

FT Fourier Transform. 2, 40, 46, 51, 55, 125

GPE Gross-Pitaevskii Equation. 1, 4, 20, 22, 23, 24, 25, 28, 29, 31, 32, 33, 34, 35, 36, 41, 43, 69, 70, 75, 79, 82, 83, 89, 90, 91, 115, 116, 118, 125

IST Inverse Scattering Transform. 2, 4, 40, 41, 45, 46, 47, 49, 51, 52, 54, 55, 57, 58, 60, 62, 63, 64, 65, 66, 68, 75, 77, 79, 80, 83, 84, 92, 95, 97, 103, 110, 111, 112, 113, 115, 120, 122, 125, 126

KdV Korteweg-de Vries. 1, 2, 40, 41, 42, 46, 47, 62, 110

LDA Local Density Approximation. 24, 119

LLE Landau-Lifshitz Equation. 3, 4, 88, 89, 91, 92, 94, 95, 97, 98, 99, 100, 101, 102, 103, 104, 106, 107, 110, 118, 120, 122, 123, 126, 127, 137, 139, 140

LRO Long-Range Order. 24, 25

MDDI Magnetic Dipole-Dipole Interactions. 69, 133

MOT Magneto-Optical trap. 10

MW MicroWave. 14, 16, 17, 18, 71, 73, 120, 121

NLSE Nonlinear Schrödinger Equation. 1, 2, 4, 20, 36, 40, 41, 42, 43, 44, 45, 46, 55, 58, 60, 61, 62, 63, 64, 65, 66, 68, 72, 75, 77, 78, 80, 81, 83, 84, 88, 97, 98, 99, 100, 101, 102, 103, 104, 106, 107, 110, 112, 113, 115, 116, 117, 118, 120, 121, 122, 123, 125, 126, 127, 137, 139, 140

OD Optical Density. 17, 71, 96, 120

PDE Partial Differential Equation. 41, 46, 66

RMS Root Mean Square. 77, 82

ROI Region Of Interest. 15

Physical Constants

Speed of Light	$c = 299\,792\,458\,\mathrm{m\,s^{-1}}$ (exact)
Planck constant	$h = 6.626\,070\,15 \times 10^{-34}\,\mathrm{J\,s}$ (exact)
Reduced Planck constant	$\hbar = \frac{h}{2\pi} = 1.054\,571\,817 \times 10^{-34}\,\mathrm{J\,s}$
Boltzmann constant	$k_B = 1.380\,649 \times 10^{-23}\,\mathrm{J\,K^{-1}}$ (exact)
Vacuum permittivity	$\epsilon_0 = 8.854\,187\,818\,8(14) \times 10^{-12}\,\mathrm{F\,m^{-1}}$
Vacuum permeability	$\mu_0 = 1.256\,637\,061\,27(20) \times 10^{-6}\,\mathrm{H\,m^{-1}}$
Elementary charge	$e = 1.602\,176\,634 \times 10^{-19}\,\mathrm{C}$ (exact)
Electron mass	$m_e = 9.109\,383\,713\,9(28) \times 10^{-31}\,\mathrm{kg}$
Bohr radius	$a_B = \frac{4\pi\epsilon_0\hbar^2}{2m_e} = 5.291\,772\,105\,44(82) \times 10^{-11}\,\mathrm{m}$
Bohr magneton	$\mu_B = \frac{e\hbar}{2m_e} = 9.274\,010\,065\,7(29) \times 10^{-24}\,\mathrm{J\,T^{-1}}$
Atomic mass of ^{87}Rb	$m = 1.443\,160\,895\,00(50) \times 10^{-25}\,\mathrm{kg}$

Contents

INTRODUCTION

At the turn of the 20th century, Planck introduced his now-famous constant to explain blackbody radiation [1], a phenomenon that had resisted classical interpretation. Following this initial breakthrough, quantum physics rapidly developed into a general and robust theoretical framework describing the behavior of matter, particularly at atomic scales. Quantum mechanics challenges our classical intuition while simultaneously providing some of the most precise and far-reaching predictions in science. Its interpretation has remained a subject of debate [2], epitomized by the Einstein–Podolsky–Rosen "paradox" [3], which awaited experimental resolution for nearly half a century [4].

Among its major successes is the statistical description of many-body systems, where particle indistinguishability leads to two fundamental quantum statistics: those of bosons and fermions. In particular, Bose and Einstein showed that non-interacting bosons can macroscopically occupy a single quantum state [5, 6], when cooled at a sufficiently low temperature. This phase transition, now known as Bose-Einstein Condensation, endows the system with a collective wavefunction shared by all particles, allowing it to be described as a coherent field. This peculiar state of matter was first realized experimentally in dilute atomic gases in 1995 [7–9]. Its field-like nature was soon made manifest through landmark interference experiments, where distinct parts of the condensate were allowed to overlap, revealing high-contrast fringes that directly demonstrated long-range phase coherence [10, 11].

Taking interactions into account is a major challenge, as they generate correlations that require exploring a Hilbert space whose dimension grows exponentially with the system size. A paradigmatic example is the physics of high-temperature superconductors, which continues to stimulate intense research efforts [12]. In contrast, weakly interacting systems allow significant simplifications. For dilute Bose gases with contact interactions, the dynamics can be accurately captured by a mean-field description, the Gross-Pitaevskii Equation (GPE) [13, 14], also called the Nonlinear Schrödinger Equation (NLSE). The resulting nonlinearity is the price paid for this reduction of complexity: although the full many-body wavefunction evolves according to the linear Schrödinger equation, its effective description as a coherent field obeys intrinsically nonlinear dynamics. This equation has proved extraordinarily fruitful: it accounts for the collective excitation modes of Bose–Einstein condensates [15], supports topological defects such as quantized vortices [16], and provides a theoretical framework for understanding superfluid flows [17].

Equations sharing the same nonlinear-wave character arise in many areas of physics, including optics and fluid mechanics, underscoring the broad relevance of nonlinear wave dynamics. In hydrodynamics, prominent examples include the Navier–Stokes equation [18, 19] and the Korteweg-de Vries (KdV) equation [20], though the diversity of fluid behaviors naturally leads to a variety of effective models [21]. In particular, under a deep-water approximation, the envelope of surface waves is governed by the

attractive NLSE [22]. Nonlinearities play an equally central role in optics, where the intensity dependence of a medium's refractive index leads to Kerr effects [23], self-phase modulation, and the reshaping of optical pulses [24]. In this context, the NLSE emerges as the fundamental equation governing the propagation of slowly varying envelopes of electromagnetic fields in optical fibers [25]. These parallels between hydrodynamics, optics, and quantum gases highlight the universality of nonlinear wave equations and the broad range of physical phenomena they capture.

Nonlinearities are often associated with chaos: setting arbitrarily close initial conditions on a chaotic system will ultimately cause their phase-space trajectories to diverge, a behavior formally characterized by a positive Lyapunov exponent [26]. Such systems are very rich and can exhibit striking structures, such as Lorenz attractors [27]. In fluid flows, this sensitivity to initial conditions manifests as turbulence [28], a high-dimensional form of chaos in which energy injected at large scales is redistributed through the Kolmogorov cascade down to progressively smaller eddies [29]. This phenomenon was recently observed in a cold-atom platform [30], where energy was pumped into the largest length-scale and the following transfer was characterized. Nonlinear equations are also central to the study of rogue waves [31–35], which aim to model and understand the emergence of these rare and extreme events.

Despite these complex behaviors, nonlinear media were also found to host peculiar "solitary waves", first reported by Russell in a shallow-water canal [36]. These localized wavepackets propagate while retaining their shape, a remarkable property in a dispersive medium, where linear physics would normally cause any wavepacket to spread. In 1965, Zabusky and Kruskal performed a pioneering numerical experiment showing that these waves even preserve their form after colliding with one another [37], prompting them to coin the term *soliton* to describe these structures. Solitons were subsequently observed across a wide range of physical systems, including optical fibers [38], ferromagnetic materials, and even polymer chains [39].

A breakthrough in the study of nonlinear systems was realized with the analysis of the Fermi-Pasta-Ulam-Tsingou (FPUT) problem [40], which was also the motivation of the work of [37]. First formulated in the 1950s, it explores the dynamics of a chain of coupled oscillators with weak nonlinear interactions. Originally designed to investigate thermalization in a simple model of a crystal lattice, the FPUT experiment revealed an unexpected recurrence phenomenon: instead of distributing energy evenly among the normal modes, the system exhibited quasi-periodic returns to its initial state. This surprising behavior challenged early assumptions about energy equipartition in nonlinear systems. It was recently studied in optical fibers [41, 42], evidencing periodic resurgences of given wavepackets.

Eventually, the common origin of these peculiar structures in nonlinear equations was elucidated from a mathematical standpoint through the introduction of the Inverse Scattering Transform (IST). This method was first applied to the KdV equation [43], and later extended to the NLSE [44] and other classes of integrable equations [45], following a reformulation proposed by Lax [46]. Conceptually, the IST can be seen as a nonlinear extension of the Fourier Transform, in which the time evolution of the system is represented in a transformed space where the relevant data, representing a scattering problem, evolve trivially. This formalism extends the notion of integrability [47], which in classical dynamical systems refers to the existence of a set of conserved quantities whose number matches the degrees of freedom of the system. In addition to formally solving the corresponding nonlinear equation, the IST provides profound physical insight. It reveals the central role of solitons in the system's dynamics, explaining their remarkable stability, and particle-like interactions, through the conservation of their associated scattering data.

The development of ultracold-atom experiments has opened a new arena for studying nonlinear wave dynamics. These systems offer unprecedented tunability, allowing many nonlinear equations to be realized in clean and controllable conditions. Beyond their relevance for nonlinear dynamics, ultracold atomic gases have emerged as extraordinarily versatile quantum platforms [48]. A key advantage of these systems is the precise and independent control over both internal and external degrees of freedom. Spinor gases, for instance, exploit the internal hyperfine structure to realize multicomponent quantum fluids with tunable spin interactions and rich magnetic phases [49]. Interparticle interactions can be finely adjusted using Feshbach resonances [50, 51], enabling access to regimes from weak to strongly correlated. Simultaneously, external trapping potentials can be engineered with remarkable flexibility: optical lattices allow the clean realization of lattice Hamiltonians [52], while spatial light modulators provide arbitrary, dynamically reconfigurable landscapes [53]. These capabilities underpin landmark achievements. We can mention the observation of the superfluid–Mott insulator transition [54]. For fermionic gases, interaction tuning has allowed the exploration of the BEC–BCS crossover [55], providing a unified picture of pairing across interaction regimes. Atomic precision metrology has likewise benefited from these systems, with optical lattice clocks reaching unprecedented accuracy [56]. In the context of quantum information, Rydberg-atom arrays now constitute a powerful platform for programmable quantum computation and quantum simulation [57]. Finally, quantum gas microscopes have revolutionized the study of strongly correlated matter, enabling single-atom, single-site resolution in Bose and Fermi Hubbard systems [58–61]. Altogether, these developments illustrate the exceptional tunability and breadth of phenomena accessible in cold-atom experiments, making them uniquely suited for probing complex quantum many-body physics.

Ultracold atomic gases provide a natural platform to study nonlinear excitations, and solitons in particular. Interactions can be finely tuned, and the system remains highly coherent. Bright solitons were first realized in attractive Bose-Einstein Condensates (BECs), as demonstrated by [62], while repulsive interactions enabled the observation of dark solitons [63]. Advances in experimental control have allowed the creation and manipulation of soliton trains and collisions in quasi-one-dimensional geometries [64], demonstrating the robustness of these objects. The range of accessible nonlinear dynamics is broad, including solitons in optical lattices [65–68] and higher-dimensional solutions such as the Townes soliton [69, 70]. In multi-component condensates, dark-bright solitons, where a density dip in one component traps a localized peak in another, require precise control over the internal spin states to engineer and stabilize the wavepacket [71, 72]. These experiments provide a highly controllable environment to study fundamental aspects of nonlinear physics, revealing soliton interactions, stability, and the underlying integrable structure of the system.

Studying multi-soliton states, that is wavepackets containing several solitons, is particularly important, as the interactions between solitons reflect the rich structure of integrable dynamics and provide a direct window into the conservation laws and scattering properties that govern these nonlinear systems. In particular, the Satsuma–Yajima wavepacket [73], composed of multiple solitons moving at the same velocity, illustrates how a complex wavepacket can retain and manifest its underlying solitonic structure throughout its evolution. Such states have been investigated in optical fibers [74] and, more recently, in attractive BEC experiments [75].

In our platform, we exploit the internal structure of Rubidium atoms to engineer such states, creating effective attractive interactions. Moreover, the spinor nature of the system allows a direct mapping onto ferromagnetic spin chains, described by the Landau-Lifshitz Equation (LLE) [76], which provide a rich physical playground [77].

Owing to the integrability of these spin chains, multi-soliton states exist [78] and can be mapped to NLSE solitons [79–81], greatly facilitating their theoretical and experimental study. While the dynamics of these multi-soliton states are fully determined by the integrable structure of the underlying equations, small perturbations away from integrability can lead to rich and experimentally accessible phenomena [82]. Tuning these perturbations may even provide an inner view of the solitonic content of a wavepacket, demonstrating experimentally the IST.

This thesis brings together the experimental tools available in our setup and the theoretical framework of integrable nonlinear dynamics to investigate multi-soliton physics in a quasi-one-dimensional two-component Bose gas. The work presented here aims to connect the capabilities of our platform with the predictions of the underlying models, and to explore how controlled deviations from ideal conditions influence the observed dynamics. The manuscript is organized as follows:

- Chapter 1 describes the experimental platform and the essential tools used throughout this thesis. We detail the preparation of a quasi-two-dimensional BEC of ^{87}Rb atoms, along with the manipulation of both their external and internal degrees of freedom.
- Chapter 2 provides a theoretical framework for our system, justifying the mean-field treatment and the use of the GPE. We give insight into the superfluid properties of the gas in situations with broken translational invariance, and introduce the key quantities characterizing spin mixtures, emphasizing the regime where the system maps onto the attractive one-component NLSE.
- Chapter 3 introduces the IST and examines in detail its application to the attractive NLSE. We explain how the method yields an exact solution of the nonlinear dynamics, clarify the physical connection between scattering data and solitons, and discuss several relevant multi-soliton states.
- Chapter 4 presents our experimental generation of multi-soliton wavepackets governed by the NLSE, enabled by the deterministic imprinting of tailored wavefunctions in a two-component spin mixture.
- Chapter 5 offers an alternative description of our system based on its mapping to ferromagnetic spin chains described by the LLE. We detail the formal correspondence between the NLSE and the LLE, which allows us to realize and characterize multi-soliton states of the latter equation.
- Chapter 6 introduces perturbation theory within the IST framework and shows how controlled departures from integrability provide direct access to the scattering data of a given wavepacket.

I Production, manipulation and characterization of ultracold samples

1 Realization of ultracold Bose gases

Outline of the current chapter

Introduction

This chapter presents the experimental apparatus used to realize and probe ultracold atomic gases in our laboratory. Our setup is designed to produce a quantum-degenerate gas of ^{87}Rb atoms and to provide a high level of control over their external and internal degrees of freedom. Since its construction was finished when I joined the team, we refer the reader to previous PhD theses for additional details [83–86]. After obtaining a Bose-Einstein Condensate (BEC) (Sec. 1.1), we can confine the atoms in tailored optical potentials and shape their dimensionality, allowing the realization of quasi-two-dimensional systems (Sec. 1.2).

A central aspect of the experiment is the precise manipulation of the atomic spin states, which enables the preparation of spin mixtures and the implementation of coherent coupling schemes (Sec. 1.3). Finally, we discuss the imaging methods used to measure the atomic density and spin populations with high accuracy (Sec. 1.4).

1.1 Preparation of a 3D Bose-Einstein Condensate

Rubidium-87 atoms were the first to be Bose–Einstein condensed [7], followed shortly after by sodium atoms [8]. These alkali species each possess a single valence electron, resulting in a relatively simple electronic structure. In the case of ^{87}Rb, the nonzero nuclear spin gives rise to a hyperfine structure, leading to rich spin-dependent physics [see for instance 87–89]. Moreover, the main optical transitions of rubidium correspond to wavelengths accessible with commercially available lasers. For these reasons, ^{87}Rb remains one of the most widely used and versatile platforms in cold atom research.

1.1.1 The Rubidium atom

We use ^{87}Rb atoms, a bosonic isotope with the electronic configuration $[\mathrm{Kr}]5s^1$. Consequently, the atomic structure is primarily determined by the single valence electron. Fig. 1.1 illustrates the energy levels of ^{87}Rb relevant to this work. The fine structure arises from the coupling between the electron's orbital angular momentum $\mathbf{L}$ and its spin $\mathbf{S}$, giving the total electronic angular momentum $\mathbf{J} = \mathbf{L} + \mathbf{S}$ [see, e.g., 90]. The hyperfine structure, in turn, results from the coupling between $\mathbf{J}$ and the nuclear spin $\mathbf{I}$, leading to the total angular momentum quantum number $\mathbf{F} = \mathbf{J} + \mathbf{I}$.

We use the D_2 line of ^{87}Rb for all stages of laser cooling and for absorption imaging. This line includes a closed cycling transition $F = 2 \rightarrow F' = 3$, enabling efficient cooling of atoms with a single optical frequency. However, atoms can occasionally decay or be transferred to the $F = 1$ ground state, for instance through inelastic collisions or off-resonant scattering. To repump these atoms, an Electro-Optic Modulator (EOM) is used to generate frequency sidebands on the laser light. The modulation frequency, approximately 6.8 GHz, brings one sideband into resonance with the $F = 1 \rightarrow F' = 2$ transition, thereby optically pumping the atoms back into the $F = 2$ manifold.

1.1.2 Experimental control

A precise control of many devices is required to reach the Bose-Einstein Condensation (BECn) phase transition. Besides, the imaging process is destructive, and one must repeat continuously the experimental cycle.

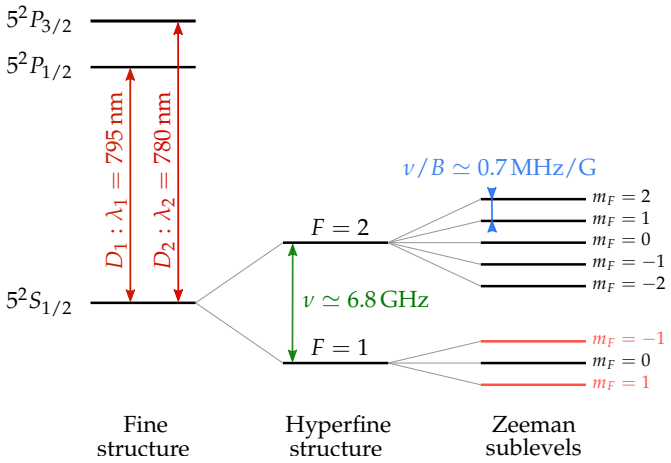

Figure 1.1: Scheme of the electronic structure of ^{87}Rb, showing the ground state and the first two excited states. The ground state has orbital angular momentum $L = 0$ and electronic spin $S = 1/2$, corresponding to the spectroscopic term symbol $^{2S+1}L_J \rightarrow {}^2S_{1/2}$. All three states exhibit hyperfine structure; however, for clarity, the hyperfine splitting of the excited states is not shown. In the presence of an external magnetic field, the degeneracy of the hyperfine levels is further lifted due to the Zeeman effect. Only the linear Zeeman shift is considered in this work, as the resulting splitting remains small compared to the ground-state hyperfine splitting of 6.8 GHz. We highlight in orange the hyperfine levels used in the experimental work of Chap. 4–6. For a comprehensive review of the properties of ^{87}Rb, see [91]. This schematic is not to scale.

Computer control

Most devices are operated during the experimental sequence using National Instruments analog and digital interface cards. The analog outputs span a voltage range of $-10\,\mathrm{V}$ to $10\,\mathrm{V}$, with a resolution of approximately $5\,\mathrm{mV}$. Synchronization across all cards is ensured by a shared clock signal provided by a field-programmable gate array. The timing and parameters of each experimental sequence are defined using the Cicero-Word Generator software [92]. Other instruments, such as waveform generators, piezo controllers, and Digital Micro-mirror Devices (DMDs), are driven via dedicated Python scripts. These scripts can also integrate instructions from Cicero-Word through RS232 communication, allowing unified control of the entire setup.

Magnetic fields

Magnetic fields and magnetic-field gradients are essential tools for manipulating atomic samples. For instance, defining a quantization axis suppresses spin-mixing processes [93], while a magnetic-field gradient can exert a controllable force on the atoms. Several sets of coils are used to generate and tune these fields:

- Three orthogonal coil pairs generate uniform magnetic fields at the position of the atoms (red coils in Fig. 1.2b, closest to the glass cell). Their low inductance enables rapid field adjustments throughout the experimental sequence. These coils are not arranged in a Helmholtz configuration (see Chap. 4 for a discussion of the resulting effects on the atoms).

- Four larger coils are positioned further from the atoms (red coils in Fig. 1.2a). The coil along z provides a feedforward signal to compensate for parasitic magnetic fields, primarily originating from the nearby subway. The coil along y produces the quantization field used in the experiments described in Chap. 4–6.

- Two sets of quadrupole coils (orange coils oriented along x and z in Fig. 1.2b) are used to produce magnetic-field gradients. One set is used during the Magneto-Optical trap (MOT) phase, while the other forms the magnetic trap used in the initial stage of evaporative cooling (see Sec. 1.1.3).
- An additional single coil (orange, oriented along y in Fig. 1.2b) provides control over the magnetic-field gradient along this direction.

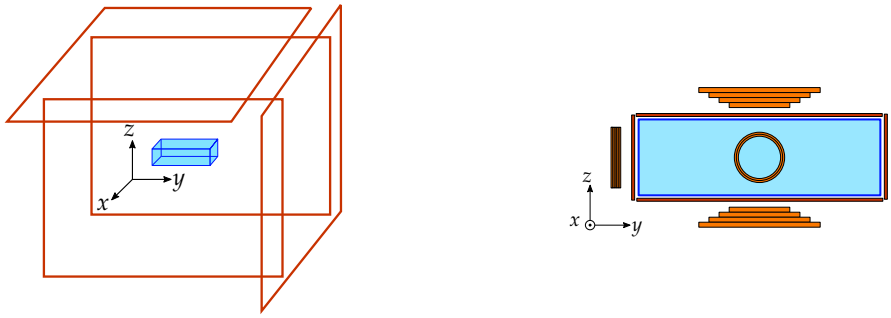

(a) **(b)**

Figure 1.2: (a, b) Schematics of the coil assemblies surrounding the glass cell where the ^{87}Rb atoms are trapped. Its dimensions are 25 mm × 25 mm × 105 mm. The largest coils, which are around 1 m in size, surround the optical table. Red coils are used to generate uniform magnetic fields, while orange coils produce magnetic-field gradients. See main text for details. **(b)** Zoomed view of the coils located closest to the glass cell, not shown in **(a)**. The atomic source is positioned along the y direction, towards $y \to \infty$.

1.1.3 Bose-Einstein condensation

We describe in this section the main stages leading to the formation of a 3D BEC:

- A piece of ^{87}Rb is heated in an oven, and part of the resulting vapor is captured in a 2D MOT. A resonant push beam then directs the atoms toward the main glass cell.
- The atoms are subsequently loaded into a 3D MOT for 7 s. This is followed by an optical molasses stage, during which the quadrupole magnetic field is turned off and the atoms are optically pumped into the $F = 1$ hyperfine state.
- The quadrupole coils along z (see Fig. 1.2b) then ramp the magnetic-field gradient up to 240 G/cm. Low-field-seeking atoms in the $|F = 1, m_F = -1\rangle$ state are magnetically trapped. A radio-frequency evaporation sequence lasting 12 s is applied, yielding approximately 2×10^7 atoms at a temperature of 20 µK.
- Before Majorana losses become significant, the atoms are transferred into a pair of crossed optical dipole traps operating at $\lambda = 1064$ nm. These traps generate a potential [94]:

$$V(\mathbf{r}) = -\frac{1}{2\epsilon_0 c}\mathcal{R}(\alpha_\lambda) I(\mathbf{r}) \,, \tag{1.1}$$

where α_λ is the ground-state polarizability at wavelength λ, and $I(\mathbf{r})$ is the local intensity of the trapping beam. Since $\mathcal{R}(\alpha_{1064}) > 0$, the atoms are confined at the intensity maxima. The laser power is gradually reduced over 4 s for a second stage of evaporative cooling, resulting in a 3D BEC of approximately 4×10^5 atoms at a temperature below 100 nK.

1.2 Lowering the dimensions

The final stage of the experimental sequence employs repulsive optical traps generated by a laser at $\lambda = 532\,\mathrm{nm}$. This configuration produces a quasi–two-dimensional sheet of atoms confined in a flat-bottom potential. According to the Hohenberg–Mermin–Wagner theorem [95, 96], a true BECn cannot occur at the thermodynamic limit in systems of reduced dimensionality at finite temperature. Nevertheless, owing to the finite size of our system, quasi-long-range phase coherence can emerge [see, e.g., 97]. Thus, we obtain a 2D BEC. This aspect is further discussed in Sec. 2.1.4.

1.2.1 Optical accordion

After reaching the BECn, the atoms are loaded into a single node of an optical lattice formed by two beams of repulsive light at $\lambda = 532\,\mathrm{nm}$, with an initial fringe spacing of 13 µm. The objective is to confine the atomic cloud along the vertical direction in a potential characterized by a frequency $\hbar\omega_z$ that greatly exceeds all other relevant energy scales in the system, namely the thermal and interaction energies. Rather than increasing the laser power to enhance confinement, an alternative approach, originally proposed in [98], consists in dynamically tuning the lattice period, thereby realizing an accordion lattice. The implementation of this technique in our setup is described in [85, 99]. We illustrate this process in Fig. 1.3. A mirror is placed on a translation stage which is tuned during the experimental sequence, hence effectively changing the lattice spacing.

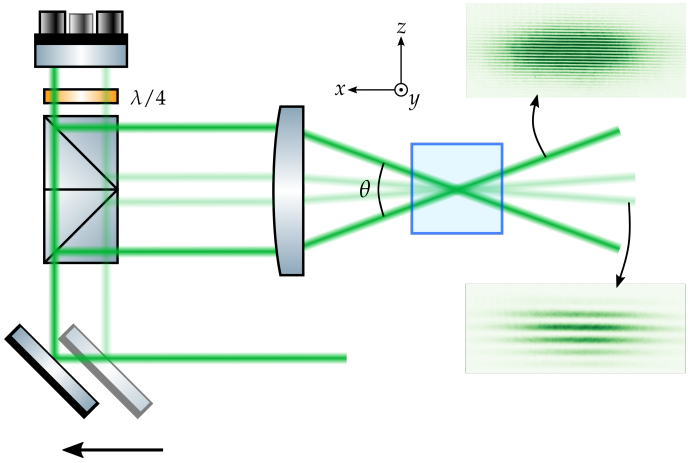

Figure 1.3: Schematic of the accordion setup. Two polarizing beam splitters divide the lattice light into parallel beams, and a quarter waveplate ensures that all light is reflected. An aspheric lens then deflects the beams such that they interfere at the position of the atoms, and the interfringe is given by $i = \lambda/[2\sin(\theta/2)]$. Translating the bottom mirror leads to a change of the lattice period. We illustrate the initial (bottom) and final (top) states with images taken on an auxiliary camera. The position of the central fringe is adjusted at the beginning of each sequence thanks to a piezoelectric stack glued below the top mirror.

The final lattice spacing is set to 3 µm. The trapping frequency is measured through parametric heating [100], we reach $\omega_z \simeq 2\pi \times 4\,\mathrm{kHz}$. Thus, the extent of the cloud along z is approximately $l_z = \sqrt{\hbar/(m\omega_z)} \simeq 170\,\mathrm{nm}$.

1.2.2 Digital Micro-mirror devices

Since the atoms are trapped at a dark fringe of the accordion lattice, additional in-plane confinement is required to prevent them from spilling out of the trap. This confinement is provided by the DMDs [see, e.g., 101, for details on the working principles of DMDs], whose light is projected onto the atoms through a microscope objective. A schematic of the optical setup is shown in Fig. 1.4. A DMD consists of a matrix of mirrors, which can be tuned independently and with a fast refresh rate (approximately 10 kHz). In practice, three DMDs are used to manipulate the atomic cloud, each consisting of 1024×768 mirrors. DMD1 and DMD2 operate with light at 532 nm, and shape repulsive potentials in the atomic plane. Although derived from the same laser as the accordion lattice, undesired interferences between these beams are suppressed using Acousto-Optic Modulators (AOMs), which slightly shift the frequency of each beam. The role of the DMD3 is discussed in Sec. 1.3.2.

All three DMDs are conjugated to the atomic plane, such that the image displayed on the matrix of mirrors is imprinted on the atoms. It is possible to use DMDs to shape the phase of the beam [102] by positioning them in a Fourier plane with respect to the atoms. However, this option presents several drawbacks (additional calibrations, most of the laser light is lost) and was not chosen in our setup.

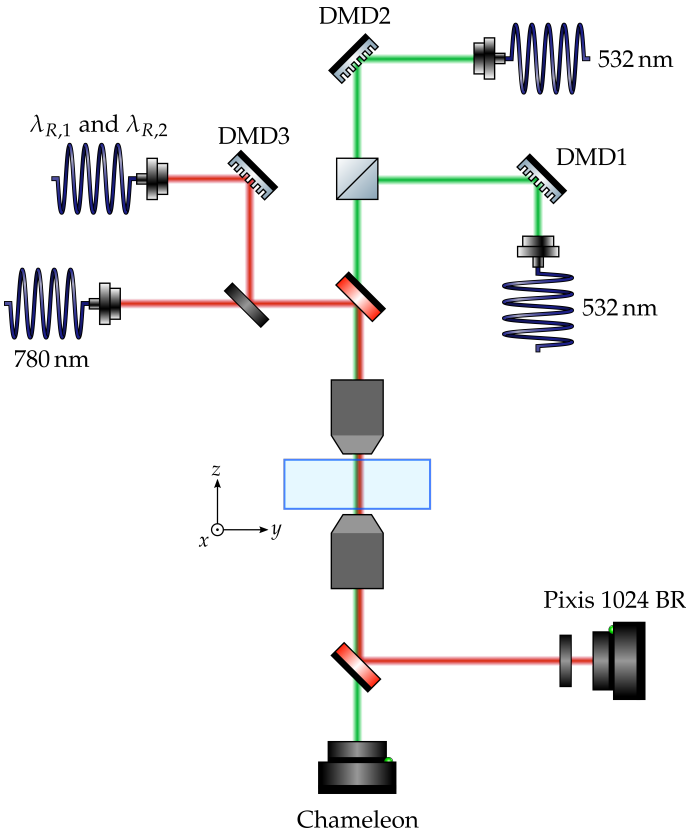

Figure 1.4: Simplified optical setup involving the DMDs. The beams are combined with a dichroic mirror before being focused onto the atoms through a microscope objective with a numerical aperture of approximately 0.4, corresponding to a resolution of about 1 µm at 780 nm. A Charge-Coupled Device (CCD) camera (Chameleon) monitors the green potential. An additional resonant beam at $\lambda = 780$ nm is combined with the Raman beams ($\lambda_{R,1}$ and $\lambda_{R,2}$, see Sec. 1.3.2) using an interference filter and serves for absorption imaging; its signal is collected on a second CCD camera (Pixis 1024 BR), preceded by another interference filter.

In practice, the atoms are initially confined using DMD1 alone. A final stage of evaporative cooling follows, during which the powers of the accordion lattice and DMD1 are gradually reduced. This process yields a 2D BEC containing approximately 1×10^5 atoms at a temperature below 20 nK. We illustrate in Fig. 1.5 the resulting atomic densities, using either a circle on DMD1, or after displaying a sequence of images to form a ring (see Chap. 4 for details).

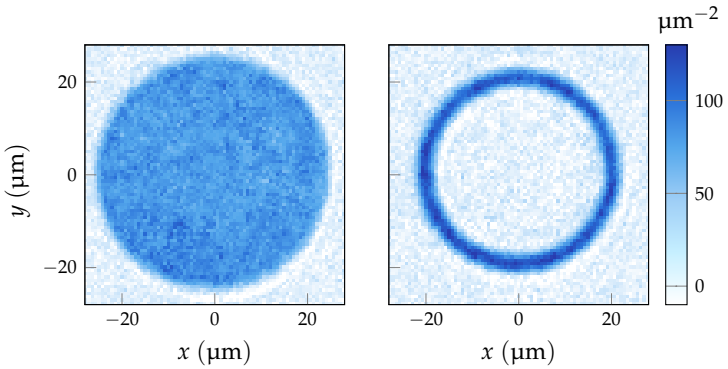

Figure 1.5: Absorption images of the 2D BEC. The atoms are confined in a flat-bottom box generated solely by DMD1. Left: Circle of radius 25 μm. Right: Ring of radius 20 μm and width 3 μm. The colorbar is common to both pictures. The vertical confinement is brought by the accordion lattice. The images are averages of 40 realizations.

Dithering

The DMDs 1 and 2 are imaged onto the atomic plane with a demagnification factor of approximately 70. Each micro-mirror, of size 13.7 μm, therefore corresponds to about 0.20 μm in the atomic plane. This scale is well below the resolution limit of our microscope objective (around 1 μm), which thus acts as a low-pass spatial filter. This property allows us to overcome one of the main drawbacks of DMDs: they can only display binary images. In some contexts, the fast refresh rate of the DMD is used to modulate light intensity over time, effectively creating smoother average profiles. However, such temporal modulation could lead to heating of the atomic sample, since the trapping frequencies lie in the kHz range, and we therefore discard this approach. Instead, we employ the Floyd–Steinberg dithering algorithm [103] to approximate grayscale images. Fig. 1.6 illustrates this procedure in the case of a triangular lattice potential (see Sec. 2.2.3 for a detailed description of the corresponding experiment).

Gray-level loop

The versatility of the potential landscape given by the DMDs can be further enhanced through a feedback loop acting on the atomic signal [105]. Imperfections in the optical beam and aberrations arising during propagation to the atomic plane can distort the intended potential profile. This issue is mitigated by iteratively adjusting the image displayed on the DMD based on the measured atomic response. Such a method was employed, for example, in [70] to achieve a target atomic density distribution. In the experiments presented in this manuscript, it was used to produce a flat-top beam in the atomic plane. The desired potential was subsequently superimposed onto this calibrated correction [see 106, Sec. 5.1.3 for details].

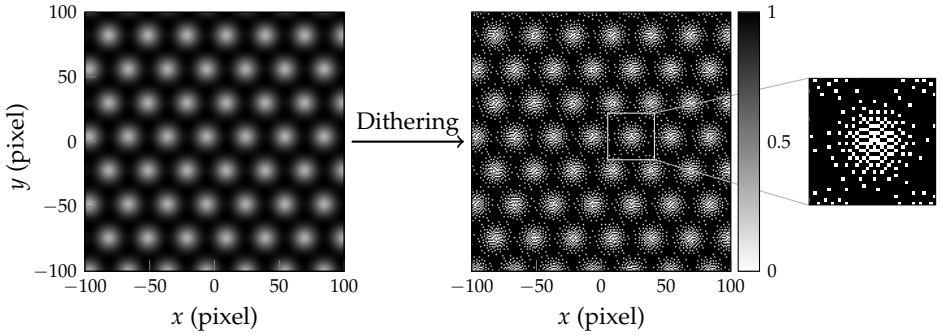

Figure 1.6: Left: Example of a grayscale image. To obtain an intensity profile $I(x,y) = I_0\, s(x,y)$ in the atomic plane, we use an input amplitude profile $\sqrt{A + B\, s(x,y)}$, with A and B chosen such that the square root remains between 0.1 and 1. Indeed, the DMD acts as an amplitude modulator [104], and the lower bound of 0.1 ensures smooth dithering results. Right: Corresponding binary pattern obtained after applying the Floyd–Steinberg algorithm, ready to be projected onto the DMD. The zoom-in highlights the binary nature of the resulting image.

1.3 The spin degree of freedom

In our setup, the BEC is prepared in the $|F = 1, m_F = -1\rangle$ hyperfine state. Precise control over the Zeeman state of the sample is essential for realizing, among other applications, mixtures of different spin components. Such control can be implemented either globally or locally, depending on the desired configuration.

1.3.1 Global control with microwaves

When a quantization magnetic field is applied to the atomic sample, the degeneracy of all hyperfine sublevels is lifted. Each transition can then be selectively addressed using a MicroWave (MW) field of the appropriate frequency. The system effectively reduces to a two-level configuration, which can be coherently driven. In this regime, Rabi oscillations [107] enable controlled population transfer between the states. In practice, two antennas are positioned around the glass cell, each driven by a Rohde & Schwarz SMB100AV synthesizer. Typical Rabi frequencies are $\Omega_R \simeq 2\pi \times 10\,\mathrm{kHz}$ for all polarizations. Given the transition frequency $\nu \simeq 6.8\,\mathrm{GHz}$, the wavelength of the MW field is on the order of several centimeters, giving a homogeneous intensity across the entire atomic cloud.

1.3.2 Local control with Raman beams

In order to locally manipulate the hyperfine state of the atoms, we address a two-photon transition using Raman beams. This method was first demonstrated with caesium atoms in [108] and is extensively described for our setup in [85]. We employ a laser of wavelength $\lambda_L \simeq 790\,\mathrm{nm}$, close to the tune-out wavelength between the D_1 and D_2 lines, so that no dipole potential acts on the atoms. The light is divided into two paths: one passes through an EOM ($\omega_{\mathrm{EOM}} = 2\pi \times 6.8\,\mathrm{GHz}$) and an AOM ($\omega_{\mathrm{AOM},1} = 2\pi \times 115\,\mathrm{MHz}$), while the second goes through another AOM operating at a slightly different frequency ($\omega_{\mathrm{AOM},2} \simeq 2\pi \times 80\,\mathrm{MHz}$). The two paths are then recombined into the same optical fiber and spatially modulated with the DMD3 before being projected onto the atomic cloud (see Fig. 1.4). Because of the sidebands generated by the EOM, four optical frequencies effectively interact with the atoms. Owing to the difference between the two AOM frequencies, only one pair of beams fulfills the resonance condition for the

two-photon transition, as illustrated in Fig. 1.7a. More precisely:

$$\omega_L + \omega_{\mathrm{EOM}} + \omega_{\mathrm{AOM},1} - (\omega_L + \omega_{\mathrm{AOM},2}) \simeq 2\pi \times 6.835\,\mathrm{GHz}\,, \tag{1.2}$$

and $\omega_{\mathrm{AOM},2}$ is finely adjusted to address the desired transition. For the experiments described in Chap. 4–6, the Raman coupling drives the transition $|F = 1, m_F = -1\rangle \rightarrow |F = 2, m_F = 0\rangle$, which requires one π-polarized and one σ_+-polarized photon. Since the beams propagate along the vertical z direction, the quantization axis must lie in the x–y plane in order to have π-polarized photons. The two Raman beams have crossed linear polarizations; assuming one is aligned with the quantization axis, the other can be decomposed as $\sigma_+ + \sigma_-$. This configuration enables the desired transition. An example of the resulting Rabi oscillations is shown in Fig. 1.7b, with a measured Rabi frequency of approximately 30 kHz.

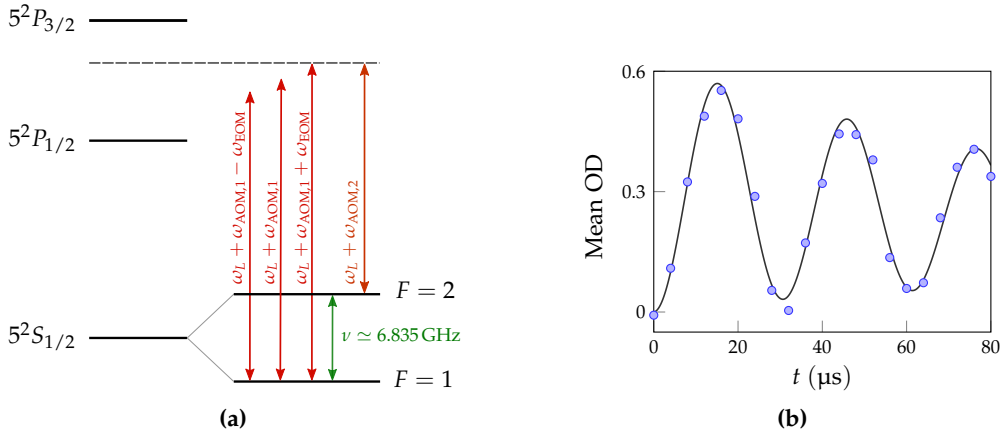

Figure 1.7: **(a)** Scheme of the four optical frequencies of the Raman beams, and the two-photon transition that can be addressed. The dashed gray line highlights that the resonance condition is obtained for one pair of beams only. **(b)** Example of Rabi oscillations driven by the Raman beams. We project a white image on the DMD3, and restrict the Region Of Interest (ROI) to an area comparable to the size of the desired soliton (see Chap. 4). The damping is attributed to the finite linewidth of the two-photon excitation.

1.4 Imaging the atoms

At the end of each experimental sequence, the atomic cloud is imaged using absorption imaging. Several cameras are installed in the setup; however, all the data presented in this manuscript were acquired along the z axis, corresponding to images of the x–y atomic plane (see Fig. 1.4). We use a Pixis 1024 BR camera, which features a pixel size of 13 µm. With an overall magnification of approximately 18, this corresponds to an effective pixel size of 0.71 µm in the atomic plane. The magnification was calibrated using Bragg diffraction of atoms on an optical lattice generated by DMD2 [see 84, Chap. 7 for details about this procedure].

A distinctive feature of this camera is its frame-transfer capability, which allows the illuminated pixels to be rapidly shifted into a storage region of the sensor. This enables a rapid sequence of imaging pulses, thereby minimizing possible fluctuations of the imaging beam intensity. The accumulated frames are then read out in a single operation after all exposures are completed.

1.4.1 Absorption imaging

Partial-transfer

We rely on absorption imaging to measure the atomic density distribution. This technique is widely used in cold-atom experiments, although it is typically preceded by a time-of-flight expansion so that the cloud becomes dilute. In contrast, in in-situ imaging, nontrivial effects may arise [109–111], for instance due to multiple scattering events. It is therefore crucial to maintain a low atomic density during the measurement. We use a MW partial transfer to fulfill this criteria. Since the probe beam is resonant with the $|F = 2\rangle \rightarrow |F' = 3\rangle$ transition, only atoms in the $|F = 2\rangle$ hyperfine state interact with it. To control the detected fraction of atoms, we apply MW pulses that transfer a chosen population from $|F = 1\rangle$ to $|F = 2\rangle$. In this way, only a small portion of the atoms are probed, while most remain in the dark $|F = 1\rangle$ state. The total atom number n is inferred from the calibrated π-pulse duration t_π of the MW transition:

$$n(x, y) = \frac{n_{|F=2\rangle}(x, y)}{\sin^2\left(\frac{\pi}{2}\frac{t}{t_\pi}\right)}, \tag{1.3}$$

where t is the MW pulse duration, and $n_{|F=2\rangle}$ is the atomic density detected with absorption imaging.

Mean-field absorption imaging

Since the cloud is sufficiently dilute, one can apply Beer-Lambert's law to describe the evolution of the intensity $I(\mathbf{r})$ of a beam through the atomic sample:

$$\frac{\mathrm{d}I}{\mathrm{d}z} = -n(\mathbf{r})\,\sigma\,\frac{I(\mathbf{r})}{1 + I/I_{\mathrm{sat}}}, \tag{1.4}$$

where $n(\mathbf{r})$ is the local atomic density, and I_{sat} takes into account the saturation effect of the atomic transition [91]. The effective scattering cross section σ is defined as follows:

$$\sigma = \frac{1}{\mathcal{F}}\frac{7}{15}\frac{3\lambda^2}{2\pi}. \tag{1.5}$$

$\mathcal{F}$ is a correction factor, typically close to unity, that accounts for non-ideal experimental conditions (see Sec. 1.4.3 for its calibration). The factor $7/15$ reflects the fact that the probe beam is supposed to couple all Zeeman sublevels of the $F = 2 \rightarrow F' = 3$ transition with a π-polarization.

Integrating the above expression yields:

$$\sigma n_{2\mathrm{D}}(x, y) = \ln\left(\frac{I_i}{I_f}\right) + \frac{I_i - I_f}{I_{\mathrm{sat}}}, \tag{1.6}$$

where I_i and I_f are the incident and transmitted intensities, and $n_{2\mathrm{D}}(x, y)$ is the column density. We obtain I_f and I_i by taking two subsequent images of the atomic plane, with and without atoms respectively. In the case $I_{i,f} \ll I_{\mathrm{sat}}$, we recover:

$$n_{2\mathrm{D}}(x, y) = \frac{1}{\sigma}\ln\left(\frac{I_i}{I_f}\right) = \frac{1}{\sigma}\mathrm{OD}(x, y), \tag{1.7}$$

where we introduced the Optical Density (OD). We assumed throughout this calculation that the atomic density was time independent. This hypothesis is verified when the imaging pulse is sufficiently short to neglect the displacement of atoms [112].

1.4.2 Saturated correction

To obtain reliable absorption images, two conditions must be satisfied: the probe intensity should remain low, and the pulse duration short. As a direct consequence, only a small number of photons are collected on the camera, and the signal-to-noise ratio is limited by photon shot noise. One way to circumvent this limitation is to relax one of these constraints and operate with higher probe intensities. This approach has been successfully implemented in, e.g., [112, 113]. Starting from Eq. (1.6), we note that the light intensity in the atomic plane is not directly measurable. It is therefore convenient to express the equation in terms of the camera counts:

$$\sigma n_{2\mathrm{D}}(x_j, y_k) = \ln\left(\frac{C_i}{C_f}\right) + \frac{C_i - C_f}{C_{\mathrm{sat}}}\,, \tag{1.8}$$

where (x_j, y_k) denote the discrete pixel coordinates, and C_α is proportional to the corresponding light intensity I_α. Calibrating this proportionality factor amounts to determining the parameter C_{sat}. In our system, the procedure is as follows:

- Apply a flat-bottom potential to the atoms, so that the column density $n_{2\mathrm{D}}(x_j, y_k)$ can be assumed uniform.
- Acquire a series of images while varying the probe-beam intensity.
- Plot $d_{\mathrm{diff}} = C_i - C_f$ as a function of $d_{\log} = \ln\left(\frac{C_i}{C_f}\right)$. The resulting data should lie on a straight line with slope $-C_{\mathrm{sat}}$.

We show in Fig. 1.8 the outcome of this calibration procedure. As illustrated in the inset, the extracted value of C_{sat} scales linearly with the imaging pulse duration t_{img}, as expected.

Then, Eq. (1.8) allows us to measure the column density. This calibration is used throughout this manuscript when performing absorption imaging.

1.4.3 Atom number calibration

Eventually, the last step to determine precisely the atom number in our experiment is the calibration of the correction factor $\mathcal{F}$ in the scattering cross section. Several methods can be employed, such as measuring the breathing frequency of a triangular atomic pattern [85], or the speed of sound of the homogeneous Bose gas [106].

In the experimental work of Chap. 4-6, we implement a method introduced in [114]. It relies on measuring the frequency shift $\Delta\nu$ of a MW transition, due to mean-field effects. This shift is given by [see e.g. 115]:

$$\Delta\nu = \frac{\hbar}{m}\frac{\Delta a}{\sqrt{2\pi}l_z} n_{2\mathrm{D}}\,, \tag{1.9}$$

where Δa is the difference in scattering lengths between the two hyperfine states. In practice, we use the clock transition, for which $\Delta a = 6.0\,a_B$ [116]. By comparing with $n_{2\mathrm{D}}$ obtained through absorption imaging, we eventually measure $\mathcal{F} = 0.87(6)$, and this value is used in Chap. 4-6. This calibration is performed regularly, due to the small long-term variations of $\mathcal{F}$.

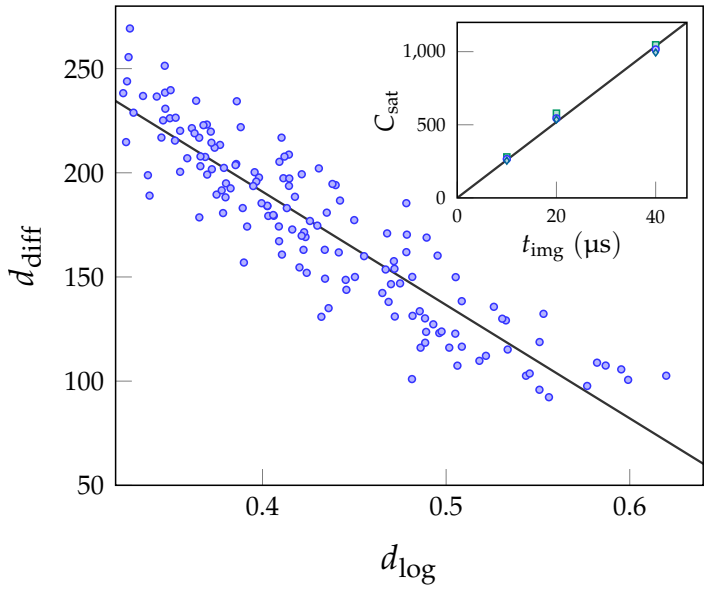

Figure 1.8: Calibration of the saturation coefficient C_{sat}. To reduce shot noise, 20 repetitions of the experiment are averaged for each probe-beam intensity, and the quantities d_{diff} and d_{log} are computed over 9×9 pixel regions. The inset confirms that C_{sat} increases linearly with the imaging duration t_{img}. Moreover, this calibration is verified to be independent of the atomic density: three datasets corresponding to different MW partial-repump durations of 5, 7, and 9 µs (with a π-pulse duration of 43 µs) are displayed as squares, circles, and diamonds, respectively. A linear fit yields $C_{\text{sat}} = 26(1)\,\mu\text{s}^{-1}\, t_{\text{img}}$. The main panel shows the dataset for $t_{\text{img}} = 20\,\mu\text{s}$ and $t_{\text{MW}} = 7\,\mu\text{s}$, for which the counts C_i were varied approximately between 200 and 1,000.

Conclusion

In this chapter, we have described the experimental apparatus used in this work. We first detailed the production of a BEC of ^{87}Rb, then introduced the instruments that enable us to reduce the dimensionality of the atomic cloud and to shape its potential landscape. We also presented the techniques employed to manipulate the spin degree of freedom of the ^{87}Rb ground state. Both the MW pulses and the Raman beams introduced here will play a central role in the experiments discussed in the following chapters.
In Chap. 2, we turn to the study of the two-dimensional Bose gas, focusing on its superfluid properties and on the behavior of spin mixtures.

2 Mean-field description of weakly-interacting Bose gases in low dimensions

Outline of the current chapter

Introduction

In this chapter, we develop a mean-field description of the system introduced in Chap. 1, within the framework of the Gross-Pitaevskii Equation (GPE), which provides an accurate description of weakly-interacting Bose gases at low temperatures (Sec. 2.1). This formalism captures both the static properties of the condensate and its collective excitations, thereby linking the microscopic wavefunction to the macroscopic manifestations of superfluidity. In particular, we discuss how superfluidity emerges from the phase coherence associated with superfluid flow, and how it can be quantitatively characterized through the superfluid fraction (Sec. 2.2). Finally, we extend our description to spin mixtures of BECs (Sec. 2.3), and show how, in a suitable limit, our system can be mapped onto an attractive single component Nonlinear Schrödinger Equation (NLSE).

2.1 Description at T=0

In this section, we establish a theoretical description of the Bose gas realized in our experimental platform. We consider a system of N weakly interacting bosons of mass m, in the dilute regime where only pairwise interactions are relevant [117]. The Hamiltonian of the system can be written in the second-quantized form:

$$\begin{aligned}\hat{H} = \int \frac{\hbar^2}{2m}\left[\nabla\hat{\Psi}^\dagger(\mathbf{r})\nabla\hat{\Psi}(\mathbf{r})\right] + V(\mathbf{r})\hat{\Psi}^\dagger(\mathbf{r})\hat{\Psi}(\mathbf{r})\,\mathrm{d}^3r \\ + \frac{1}{2}\int \hat{\Psi}^\dagger(\mathbf{r}')\hat{\Psi}^\dagger(\mathbf{r})U(\mathbf{r}'-\mathbf{r})\hat{\Psi}(\mathbf{r}')\hat{\Psi}(\mathbf{r})\,\mathrm{d}^3r'\,\mathrm{d}^3r\ ,\end{aligned} \tag{2.1}$$

where $\hat{\Psi}(\mathbf{r})$ and $\hat{\Psi}^\dagger(\mathbf{r})$ are the field operators annihilating and creating a particle at position $\mathbf{r}$ respectively. The term $V(\mathbf{r})$ denotes the trapping potential, and $U(\mathbf{r})$ is the two-body potential, describing the interactions of pairs of particles. Our goal is to determine the ground state of this Hamiltonian, corresponding to the zero-temperature limit of the system. This is, in general, a challenging problem, as the Hilbert space grows exponentially with the particle number N.

2.1.1 Collisions and dimensionality

A first step toward finding an expression for the ground state of $\hat{H}$ consists in simplifying the two-body interaction potential $U(\mathbf{r})$. At low collision energies, bosonic interactions are dominated by s-wave scattering. In this regime, the details of the microscopic potential become irrelevant, and the interaction can be fully characterized by a single parameter: the scattering length a [117, 118]. In the case of ^{87}Rb atoms in the ground state, $a \simeq 100\,a_B$. The true potential $U(\mathbf{r})$ can then be replaced by a pseudo-potential acting on a function f as follows [119]:

$$\tilde{U}[f(\mathbf{r})] = \underbrace{\frac{4\pi\hbar^2 a}{m}}_{g}\delta(\mathbf{r})\frac{\partial}{\partial r}\left(rf(\mathbf{r})\right)\ , \tag{2.2}$$

where δ denotes the Dirac distribution, and g is the effective interaction constant. The presence of the derivative and the prefactor r ensures a proper regularization of wavefunctions exhibiting a $1/r$ divergence, as encountered in three-dimensional scattering

theory [118]. In cold atom platforms, the scattering length a can be tuned through Fano-Feshbach resonances [see 51, for a review]. For ^{87}Rb however, these resonances are relatively narrow and occur only at high magnetic fields [120]. Therefore, we did not make use of them in the experiments described in this work.

This simplification of the potential, however, does not straightforwardly extend to the two-dimensional case. Indeed, in two dimensions the inverse of the scattering amplitude diverges logarithmically as the collision energy approaches zero [97, 121], leading to the interaction constant [117]:

$$g_{2D} = \frac{4\pi\hbar^2}{m} \frac{1}{\ln\left(1/na_{2D}^2\right)}, \tag{2.3}$$

where n is the atomic density, and a_{2D} the two-dimensional scattering length. In practice, our system is not strictly two-dimensional: it is confined along one spatial direction with a finite width $l_z = \sqrt{\hbar/(m\omega_z)}$. This quasi-2D geometry, discussed in [122, 123], allows one to relate a_{2D} to the 3D scattering length a and the confinement length l_z as [123, 124]:

$$a_{2D} = l_z \underbrace{\left(2e^{-\gamma}\sqrt{\frac{\pi}{B}}\right)}_{\kappa} \exp\left(-\sqrt{\frac{\pi}{2}}\frac{l_z}{a}\right), \tag{2.4}$$

where $B \simeq 0.915$, and $\gamma \simeq 0.577$ is the Euler constant. Substituting this expression into the logarithmic form of g_{2D} yields:

$$g_{2D} = \frac{4\pi\hbar^2}{m} \frac{1}{\sqrt{2\pi}l_z/a + \ln(1/n\kappa^2 l_z^2)} \simeq \frac{\sqrt{8\pi}\hbar^2}{m}\frac{a}{l_z}, \tag{2.5}$$

where, in the last step, we neglected the logarithmic term, leading to a density-independent interaction parameter. This approximation is well justified for our system, since $l_z \gg a$. This means that the interactions keep their three-dimensional character, resulting in an effective coupling constant that mirrors the 3D expression. It corresponds to the weakly-interacting regime, $\tilde{g} = g_{2D}m/\hbar^2 \ll 1$. In our setup, we measure $\tilde{g} \simeq 0.16$. The fact that $\tilde{g}$ is dimensionless brings interesting features, such as scale invariance [70, 125].

2.1.2 The Gross-Pitaevskii equation

We now derive the evolution equation associated with the field operator $\hat{\Psi}$. In the Heisenberg representation, we obtain:

$$i\hbar\frac{\partial}{\partial t}\hat{\Psi}(\mathbf{r},t) = [\hat{\Psi}(\mathbf{r},t), \hat{H}] = \left[-\frac{\hbar^2}{2m}\nabla^2 + V(\mathbf{r},t) + g\hat{\Psi}^\dagger(\mathbf{r})\hat{\Psi}(\mathbf{r})\right]\hat{\Psi}(\mathbf{r},t), \tag{2.6}$$

where we used the standard bosonic commutation relations, and the pseudo-potential $\tilde{U}$. For a BEC, the atoms share the same single-particle wavefunction, described by the order parameter $\psi(\mathbf{r})$. We can then write:

$$\begin{cases} \hat{\Psi}(\mathbf{r}) = \psi(\mathbf{r})\hat{a} \quad \rightarrow \quad \Psi(\mathbf{r}) = \psi(\mathbf{r})\sqrt{N} \\ \hat{\Psi}^\dagger(\mathbf{r}) = \psi^*(\mathbf{r})\hat{a}^\dagger \rightarrow \Psi^*(\mathbf{r}) = \psi^*(\mathbf{r})\sqrt{N}, \end{cases} \tag{2.7}$$

where the arrow denotes the Bogoliubov approximation, in which the field operators $\hat{a}, \hat{a}^\dagger$ are replaced by the number $\sqrt{N}$. This amounts to neglecting their commutator,

$[\hat{a}, \hat{a}^\dagger] = 1$, compared to the macroscopic particle number N. We also neglect the non-condensed component [117]. The system can then be described by a classical field Ψ. Inserting this expression into Eq. (2.6) yields the GPE, first derived independently by [13] and [14]:

$$i\hbar \frac{\partial}{\partial t}\Psi(\mathbf{r},t) = \left[-\frac{\hbar^2}{2m}\nabla^2 + V(\mathbf{r},t) + g|\Psi(\mathbf{r},t)|^2 \right] \Psi(\mathbf{r},t)\,, \tag{2.8}$$

subject to the normalization condition:

$$\int |\Psi(\mathbf{r},t)|^2 \, \mathrm{d}^3 r = N\,. \tag{2.9}$$

Thus, we retrieve the atomic density $n(\mathbf{r}) = |\Psi(\mathbf{r})|^2$. This approach remains valid for a two-dimensional gas in the limit $T = 0$. Indeed, BECn can also occur in such systems [124]. The GPE (2.8) stays unchanged, except for the substitution $g \to g_{2D}$. We note that the dimension of Ψ is also modified.

The physics described by the GPE is referred to as mean-field, in the sense that quantum correlations between particles are neglected. Indeed, assigning a common wavefunction to all atoms amounts to performing a Hartree–Fock approximation of the many-body wavefunction Φ:

$$\Phi(\mathbf{r}_1, \dots \mathbf{r}_N) = \left(\tfrac{1}{\sqrt{N}}\Psi(\mathbf{r}_1)\right) \dots \left(\tfrac{1}{\sqrt{N}}\Psi(\mathbf{r}_N)\right)\,. \tag{2.10}$$

Corrections beyond the mean-field approximation may arise due to quantum effects. We can mention for instance the Lee–Huang–Yang correction [126, 127]. These phenomenon, however, lie beyond the scope of this manuscript.

Gross-Pitaevskii energy

Another method to derive the GPE relies on a variational approach, using the energy functional of the system:

$$E[\Psi] = \int \left[\frac{\hbar^2}{2m}|\nabla\Psi(\mathbf{r})|^2 + V(\mathbf{r})|\Psi(\mathbf{r})|^2 + \frac{g}{2}|\Psi(\mathbf{r})|^4 \right] \mathrm{d}^3 r\,, \tag{2.11}$$

which we obtained under the Bogoliubov approximation. This approach provides an alternative derivation of g_{2D}: we write $\Psi(\mathbf{r}) = \phi(z)\,\psi(x,y)$, where $\phi(z)$ is the ground state of the harmonic oscillator with frequency ω_z. Substituting this form into Eq. (2.11) yields the 2D GPE for ψ, with a renormalized coupling constant g_{2D}. However, it should be noted that this derivation implicitly assumes the condition $l_z \gg a$.

2.1.3 Ground state and Bogoliubov excitations

The GPE is a nonlinear equation, and solving it can, in general, only be done numerically. We can build some intuition about its solutions by developing its equilibrium properties, and the spectrum of excitations of the ground state of the equation. In this section, we restrict ourselves to the description of 2D repulsive Bose gases, meaning $g_{2D} > 0$.

Bogoliubov spectrum

We can determine the elementary excitations above the ground state by adding a small perturbation and linearizing the resulting GPE. Considering a uniform gas ($V = 0$) as a starting point, one obtains the Bogoliubov spectrum of excitations [128]:

$$\hbar\omega_k = \frac{\hbar^2 k}{2m}\sqrt{k^2 + 4\tilde{g}n} = \frac{\hbar^2 k}{2m}\sqrt{k^2 + \frac{2}{\xi^2}}\,, \tag{2.12}$$

where we have introduced the healing length $\xi = 1/\sqrt{2\tilde{g}n}$. It sets the characteristic scale over which the condensate wavefunction recovers its equilibrium value in response to an external perturbation, and quantifies the balance between the kinetic and interaction energy terms in the GPE. This point is illustrated in Fig. 2.1a, where we show the density in a box with hard-wall boundaries for different atom numbers.

The spectrum of Eq. (2.12) presents two distinct regimes:

- For $k \ll 1/\xi$, the dispersion becomes linear, $\omega_k = \sqrt{g_{2D}n/m}\,k = c_s k$. The excitations are then phonons, propagating in the system at the Bogoliubov speed of sound c_s. In our system, we estimate $c_s \simeq 2\,\mathrm{mm\,s^{-1}}$, assuming a density $n = 50\,\mu\mathrm{m}^{-2}$. Sound propagation has been probed experimentally, for example in [129].
- For $k \gg 1/\xi$, the dispersion becomes quadratic, up to a constant, $\omega_k = \hbar k^2/2m + \hbar/2m\xi^2$. Thus, it approaches the free-particle limit.

The Bogoliubov spectrum, together with its asymptotic behaviors, is shown in Fig. 2.1b. We note that there are no excitations at velocities below c_s, a hallmark of superfluidity (see Sec. 2.2 for a more detailed discussion).

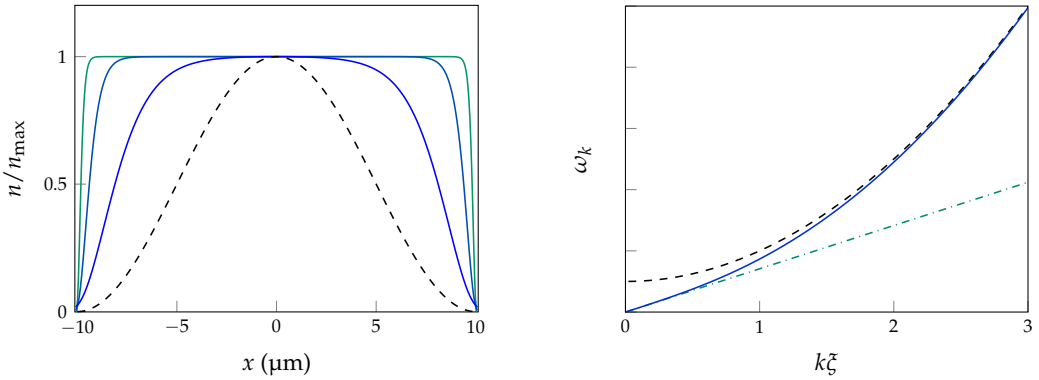

Figure 2.1: **(a)** Cut of the atomic density n in a two-dimensional box with hard-wall boundary conditions. The solid curves, blue to green, show simulations of the GPE with central densities $n_{\max} = 1, 10, 100\,\mu\mathrm{m}^{-2}$. The corresponding healing length ξ decreases with increasing density. The black dashed curve shows the non-interacting Bose gas limit. **(b)** Bogoliubov spectrum (solid blue line). The green dash-dotted curve indicates the phononic regime, while the black dashed curve shows the parabolic free-particle limit, up to an energy offset.

Finally, we note that the Bogoliubov spectrum can be extended to the case of a quasicondensate [130], such as a two-dimensional Bose gas at finite temperature.

Thomas-Fermi regime

Considering stationary solutions of the GPE, the wavefunction evolves according to [see e.g. 117, Sec. 2.2]:

$$\Psi(\mathbf{r},t) = \psi(\mathbf{r}) \exp\left(-\frac{i\mu t}{\hbar}\right) \quad \text{with} \quad \mu = \frac{\partial E}{\partial N}, \tag{2.13}$$

where we have introduced the chemical potential μ. We can then simplify Eq. (2.8), and write the stationary GPE:

$$\mu\psi(\mathbf{r}) = \left[-\frac{\hbar^2}{2m}\nabla^2 + V(\mathbf{r}) + g|\psi(\mathbf{r})|^2\right]\psi(\mathbf{r}). \tag{2.14}$$

The Thomas-Fermi approximation consists in neglecting the kinetic energy term, i.e. the Laplacian term, in Eq. (2.14). It is relevant when the density varies slowly on the scale of the healing length ξ. In this case, the atomic density n can be directly expressed as:

$$n(\mathbf{r}) = |\psi(\mathbf{r})|^2 = \frac{\mu - V(\mathbf{r})}{g}, \tag{2.15}$$

We thus obtain an example of Local Density Approximation (LDA) [see e.g. 117, Sec. 13.6], which allows for a straightforward computation of the atomic density. In particular, for a flat potential $V(\mathbf{r}) = 0$, we have $\mu = g\,n(\mathbf{r})$, and the gas density is uniform.

2.1.4 Zero-temperature hypothesis

We have so far focused on the description of a two-dimensional Bose gas at $T = 0$, where BECn can occur. However, this $T = 0$ assumption is not realistic in experimental systems. Besides, it was demonstrated by [95] and [96] that, for two-dimensional systems with short-range interactions at $T > 0$, no phase transition involving the spontaneous breaking of a continuous symmetry can occur. This result, known as the Mermin–Wagner–Hohenberg theorem, forbids BECn in weakly interacting (infinite) two-dimensional Bose gases. Fortunately, in our case this restriction is circumvented by the Berezinskii-Kosterlitz-Thouless (BKT) topological phase transition [131, 132], which restores a quasi-Long-Range Order (LRO) and allows for BECn in finite-size systems.

The BKT transition

The origin of the BKT phase transition can be quantitatively understood by considering the behavior of quantized vortices [97]. Below a critical temperature T_{BKT}, vortices exist only as bound pairs of opposite circulation, leading to the cancellation of their phase defects at long distances. As a result, quasi-long-range phase coherence is restored at low temperature, and the system exhibits superfluidity. The transition point for a weakly interacting Bose gas can be expressed in terms of a critical phase-space density D_c as:

$$D_c = (n\lambda_{\mathrm{dB}}^2)_c = \log\left(\frac{C}{\tilde{g}}\right) \tag{2.16}$$

where $C = 380(3)$ is obtained from Monte Carlo simulations [133], and $\lambda_{\mathrm{dB}} = h/\sqrt{2\pi m k_B T}$ is the thermal de Broglie wavelength. In our system, we find $T_{\mathrm{BKT}} \simeq 250\,\mathrm{nK}$, well above the gas temperature $T \lesssim 20\,\mathrm{nK}$, placing it deep in the

superfluid regime. The BKT transition has been studied experimentally, first in ^{4}He thin films [134], and more recently in ultracold atomic gases [135].

Quasi-Long-Range Order

The BECn can be associated with the emergence of LRO in the system. This concept is formally expressed by the Penrose–Onsager definition of BECn [136]:

$$\lim_{r\to\infty} g_1(\mathbf{r}) = \Pi_0 > 0 \quad \text{where} \quad g_1(\mathbf{r}) = \left\langle \hat{\Psi}^\dagger(\mathbf{r})\hat{\Psi}(0) \right\rangle . \tag{2.17}$$

We introduced Π_0, the largest eigenvalue of the one-body density function g_1, which corresponds to the condensed fraction. According to the Mermin–Wagner–Hohenberg theorem, $\Pi_0 = 0$ in infinite two-dimensional systems. However, below the BKT transition, the decay of g_1 is algebraic rather than exponential, and thus much slower than in the ideal two-dimensional Bose gas. In this regime, one finds:

$$g_1(\mathbf{r}) = n_s \left(\frac{\xi}{r}\right)^{1/(n_s\lambda_{\mathrm{dB}}^2)} , \tag{2.18}$$

where n_s denotes the superfluid density. This slow algebraic decay gives rise to a so-called quasi-LRO. In finite-size systems, such behavior can effectively lead to the restoration of true BECn. An estimate of the condensed fraction is given by [97]:

$$\Pi_0 \simeq \left(\frac{\pi}{\tilde{g}N}\right)^{1/(2n\lambda_{\mathrm{dB}}^2)} , \tag{2.19}$$

where we have approximated the superfluid density by the total density n. Using typical experimental parameters, $N \simeq 1\times10^5$ in a box of size $L \simeq 40\,\mu\mathrm{m}$, $\tilde{g} \simeq 0.16$, and a temperature $T \lesssim 20\,\mathrm{nK}$, we find a condensed fraction $\Pi_0 \gtrsim 0.96$. We can therefore safely describe our experimental platform within the framework of the GPE.

2.2 Superfluidity of the Bose gas

This section describes a work performed during my thesis, which resulted in two publications [137, 138]. It is extensively described in previous PhD theses [86, 106, 139], and we highlight here only the main results.

Superfluidity is a phenomenon that typically arises in systems of interacting particles, where coherence extends over macroscopic scales. It was first discovered and studied in liquid helium. In 1938, Kapitza [140], and independently Allen and Misener [141], observed that ^{4}He below a certain temperature could flow through extremely narrow capillaries without any measurable viscosity, marking the onset of what is now known as the superfluid phase. More recently, the study of superfluidity has been extended to ultracold atomic quantum gases, with the realization and precise exploration of superfluid phases in dilute Bose and Fermi systems [17, 142, 143], as well as in fluids of light platforms [144, 145]. In particular, two-dimensional weakly interacting Bose gases become superfluid below the BKT phase transition, a behavior that was experimentally demonstrated in [146].

2.2.1 The two-fluid model

Although dramatically reduced, the viscosity of a superfluid can remain nonzero, as first demonstrated for liquid ^{4}He by [147]. A thought experiment that helps to understand superfluidity more formally is the rotating annulus experiment [148, 149]. We consider a cylinder of radius R rotating at an angular velocity ω, small enough to ensure the absence of a persistent current. At a finite temperature T, we study the free energy F of the system. For a classical fluid, we have:

$$F(\omega) = F(0) + \frac{1}{2} N m R^2 \omega^2 \,, \tag{2.20}$$

where N is the number of particles, each of mass m. For a superfluid, the expression becomes [149]:

$$F(\omega) = F(0) + \frac{1}{2} N m R^2 \omega^2 \left(1 - f_s\right) \,, \tag{2.21}$$

where f_s denotes the *superfluid fraction*. It represents the fraction of the fluid that is in the superfluid state and was introduced within the so-called two-fluid model, developed by Tisza [150] and Landau [151]. In this picture, the fluid is conceptually divided into two components: a normal component of density n_n and a superfluid component of density n_s, such that $n_{\text{tot}} = n_n + n_s$. The superfluid fraction is then defined as $f_s = n_s / n_{\text{tot}}$, corresponding to the portion of the fluid that is not dragged by the walls of the container, thus reducing the free energy. This reduction was experimentally observed for liquid helium by [152]. It is important to note that the superfluid fraction should not be confused with the condensed fraction associated with BECn.

This model had many successes, one of which is the prediction of two distinct sound modes, corresponding to the normal and superfluid densities. They were observed for a 2D Bose gas by [153], showing that one of the sound modes disappears at the BKT transition when f_s reaches zero.

2.2.2 The superfluid fraction in quantum gases

The superfluid fraction is a temperature-dependent quantity. It has been notably measured in uniform quantum gases through the observation of two sound modes, both in fermionic systems [154] and in bosonic ones [153, 155]. In this section, we focus instead on systems at $T = 0$. A condition was established by Leggett [156] for a bosonic system to exhibit a unit superfluid fraction: both the Hamiltonian and the ground state must possess translational invariance and time-reversal symmetry [see 106, Sec. 4.2.1 for details, and for the extension to fermionic systems]. For the remainder of this section, we will only consider time-reversal symmetric systems.

As a consequence, one can expect that spatially modulated systems, even at $T = 0$, may display a sub-unity superfluid fraction. A prominent example is the Mott-insulating state [54, 157], in which atoms are pinned to fixed lattice sites and $f_s = 0$. In general, the superfluid fraction is reduced when the gas is confined in optical lattices. This effect has been studied for bosons [158] and for fermions [159, 160] in one-dimensional lattices. A similar reduction also occurs in disordered trapping potentials [161, 162].

We note that this reduction of the superfluid fraction arises whether the modulation of the atomic density is externally imposed or self-generated, as in the case of supersolids [148, 163], where [164] measured the superfluid fraction through the observation of Josephson-like oscillations.

The superfluid fraction tensor

We now generalize the concept of the superfluid fraction beyond the rotating annulus experiment. Let us consider a three-dimensional system of size L_x, L_y, L_z containing N particles. An external potential V_{ext} is applied to the system and moves at a velocity $\mathbf{v}$. In general, the superfluid fraction is a tensor [165], where $f_s^{(i,j)}$ quantifies the response of the system along direction j to a perturbation applied along direction i.

We first consider the case where V_{ext} is translationally invariant along y and z, and the perturbation moves along the x direction, $\mathbf{v} = v_x \mathbf{e}_x$, with $\mathbf{e}_i$ the unit vector along axis i. In the reference frame of the perturbation, the normal component remains at rest while the superfluid component moves at a velocity $-v_x$. For sufficiently small velocities, the corresponding increase in energy is given at lowest order by [149]:

$$E(v_x) \simeq E(0) + \frac{1}{2} N m f_s^{(x,x)} v_x^2 = E(0) + \Delta E \,, \tag{2.22}$$

We emphasize that the choice of reference frame is crucial, since it is only in the co-moving frame that the Hamiltonian becomes time independent, and the ground-state energy becomes a relevant thermodynamic potential [117, 148]. From this expression of the energy, we obtain a general definition of the superfluid fraction:

$$f_s^{(x,x)} = \frac{1}{Nm} \lim_{v_x \to 0} \frac{\partial^2 \Delta E}{\partial v_x^2} \,. \tag{2.23}$$

This reasoning can be extended to account for a general perturbation moving in an arbitrary direction, yielding [165]:

$$f_s^{(i,j)} = \frac{1}{Nm} \lim_{\mathbf{v} \to 0} \frac{\partial^2 \Delta E}{\partial v_i \partial v_j} \,. \tag{2.24}$$

So far, we have assumed periodic boundary conditions for the wavefunction ψ of the system. Additional insights can be gained by using twisted boundary conditions, introduced by [148]. This approach consists in taking a stationary external potential V_{ext}, and setting, for $k \in \{x, y, z\}$:

$$\psi(k + L_k) = \mathrm{e}^{\mathrm{i}\Delta\theta_k} \psi(k) \quad \text{with} \quad \Delta\theta_k \ll 2\pi \,. \tag{2.25}$$

In this hydrodynamic regime, the superflow is generated by the relation between the velocity field and the gradient of the phase θ of the wavefunction [117]:

$$\mathbf{v}_s = \frac{\hbar}{m} \nabla\theta \,, \tag{2.26}$$

where $\mathbf{v}_s$ denotes the superfluid velocity. For a uniform system, the gradient is simply $(\nabla\theta)_i = \Delta\theta_i / L_i$ along each direction, as illustrated in Fig. 2.2a. In this case, $f_s^{(x,x)} = 1$. However, as soon as $V_{\text{ext}} \neq 0$, the phase profile becomes more complex. We provide an illustration of this phenomena in Fig. 2.2b, for which $f_s \simeq 0.58$. The twisted boundary condition precisely probes the phase stiffness of the wavefunction: it enforces a phase twist $\Delta\theta_i$ across the system, thereby mimicking a superflow with velocity $\mathbf{v}_s$. In the case of a sub-unity superfluid fraction, the twist can be relaxed, and creates a lesser energy increase compared to a uniform system for which $f_s^{(x,x)} = 1$, as illustrated in Fig. 2.2. An

alternative expression for the superfluid fraction can thus be derived [165]:

$$f_s^{(i,j)} = \frac{mL_iL_j}{N\hbar^2} \lim_{\substack{\Delta\theta_i\to 0\\ \Delta\theta_j\to 0}} \frac{\partial^2 \Delta E}{\partial\Delta\theta_i \partial\Delta\theta_j} \,. \tag{2.27}$$

Of course, the two definitions of the superfluid fraction are equivalent, as can be shown explicitly by considering the unitary transformation that connects the two boundary conditions [106].

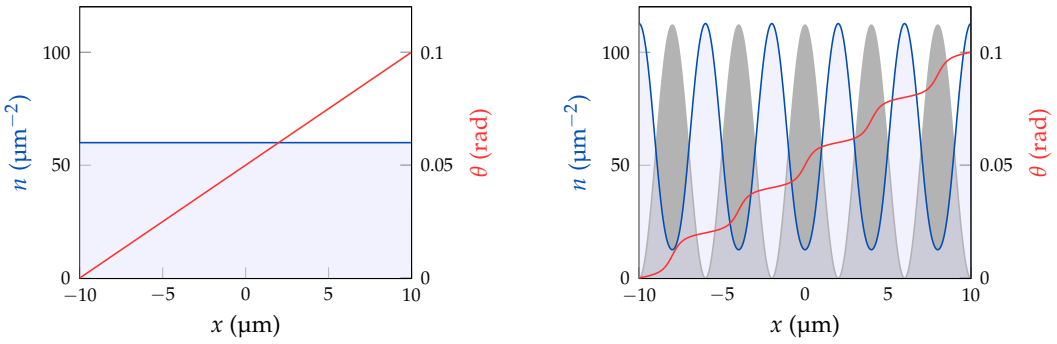

(a) $V_0 = k_B \times 0\,\mathrm{nK}$ **(b)** $V_0 = k_B \times 100\,\mathrm{nK}$

Figure 2.2: (a, b) We perform two-dimensional simulations of the GPE with twisted boundary conditions, setting $\Delta\theta_x = 0.1 \ll 2\pi$. We add an external potential $V_{\mathrm{ext}} = V_0 \cos(2\pi x/\lambda)/2$, with $\lambda = 4\,\mu\mathrm{m}$. We show in blue the resulting densities, and in red the phases θ of the wavefunctions. The grey area indicates the potential, expressed in units of density. In **(a)** the potential is set to 0, whereas we use $V_0 = k_B \times 100\,\mathrm{nK}$ in **(b)**. In addition to the modification of the density profile, it leads to an adjustment of the phase, with higher gradients in the low-density areas. We used the following parameters: $\langle n\rangle = 60\,\mu\mathrm{m}^{-2}$ and $\tilde{g} = 0.16$.

Bounds of the superfluid fraction

The definitions Eq. (2.24) and Eq. (2.27) of the superfluid fraction tensor rely on the knowledge of the energy of the system under the action of a perturbation. However, an analytical formula is in general not accessible. Nevertheless, one can establish some bounds on the superfluid fraction. An upper bound was first proposed by Leggett in [148]. He used a variational approach to estimate the energy, reducing the parameter space of possible wavefunctions by taking a Hartree ansatz, with an additional separability condition on the phase [106], leading to:

$$f_s^{(i,i)} \leq f_+^{(i,i)} = \frac{1}{\langle n\rangle} \left(\left\langle \frac{1}{\langle n\rangle_{j,k}} \right\rangle_i \right)^{-1} , \tag{2.28}$$

where $\langle\cdot\rangle_i = \int \cdot\, \mathrm{d}i\,/L_i$ is the spatial average along a given direction i, and $\langle\cdot\rangle$ is the average over the entire system. The indices j,k denote the directions orthogonal to i. We note that these bounds only apply to the diagonal components of the superfluid fraction tensor, meaning that the axis i should be an eigenaxis of the system.

This upper bound was later refined by Saslow [166, 167], using a more general variational ansatz. Considering twisted boundary conditions as in Eq. (2.25), the wavefunction can be written, at first order in the phase twist, as:

$$\psi = \psi_{\mathrm{eq}}(\mathbf{R}) \exp(\mathrm{i}\phi(\mathbf{R})) \quad \text{with} \quad \mathbf{R} = \mathbf{r}_1, \dots \mathbf{r}_N \,, \tag{2.29}$$

where ψ_{eq} is the equilibrium wavefunction in the absence of a phase twist, which can be chosen to be real. The variational ansatz for the phase then reads:

$$\phi(\mathbf{R}) = \sum_{k=1}^{N} \theta(\mathbf{r}_k)\,. \tag{2.30}$$

Under these assumptions, one obtains [138]:

$$S^{(i,j)} = \lim_{\substack{\Delta\theta_i\to 0\\ \Delta\theta_j\to 0}} \frac{1}{\langle n\rangle \langle \partial_i\theta\rangle} \langle n\,\partial_j\theta\rangle \quad \text{and} \quad \sum_{i,j} f_s^{(i,j)} \frac{\Delta\theta_i\Delta\theta_j}{L_iL_j} \le \sum_{i,j} S^{(i,j)} \frac{\Delta\theta_i\Delta\theta_j}{L_iL_j}\,. \tag{2.31}$$

One can deduce from the second equality that the eigenvalues of S are bounds of the superfluid fraction. Eq. (2.31) can equivalently be expressed in terms of $\tilde\theta = \theta - \sum_i i\,\Delta\theta_i/L_i$, which satisfies periodic boundary conditions. This yields [106]:

$$S^{(i,j)} = \delta^{(i,j)} + \lim_{\substack{\Delta\theta_i\to 0\\ \Delta\theta_j\to 0}} \frac{L_i}{N\,\Delta\theta_i} \langle n\,\partial_j\tilde\theta\rangle\,, \tag{2.32}$$

where $\delta^{(i,j)}$ is the Kronecker delta. Contrary to the bound proposed by Leggett, $S^{(i,j)}$ provides a more general upper bound, which is relevant for any choice of axis. Since the construction of [166] extends the variational space of [148], we have the hierarchy $f_s^{(i,i)} \le S^{(i,i)} \le f_+^{(i,i)}$. Leggett also derived a lower bound for the superfluid fraction [156]. In the more restrictive case of a Hartree–Fock-type wavefunction, as in the GPE, this reads:

$$f_s^{(i,i)} \ge f_-^{(i,i)} = \frac{1}{\langle n\rangle} \left\langle \left\langle \frac{1}{n} \right\rangle_i^{-1} \right\rangle_{j,k}\,. \tag{2.33}$$

It is instructive to identify some cases where these inequalities are saturated:

- The assumption of Eq. (2.30) corresponds to a Hartree–Fock approximation and is thus exactly satisfied for wavefunctions governed by the GPE, giving $f_s^{(i,j)} = S^{(i,j)}$.
- When, in addition, the density is separable, i.e. $n(\mathbf{r}) = \prod_i n_i(i)$ with $n_i > 0$, all bounds coincide [137]: $f_- = f_s = S = f_+$.

These limiting cases provide striking examples in which the superfluid fraction, a dynamical quantity, can be inferred from purely static observables.

2.2.3 Experimental investigation of the superfluid fraction

Having established the theoretical framework for the superfluid fraction tensor and its variational bounds, we now discuss its experimental characterization in our platform for two distinct configurations of broken translational symmetry. In [137], we considered a one-dimensional optical lattice (a similar geometry was also explored independently in [168]), while a triangular lattice potential was later implemented in [138]. In the following, we detail the main results obtained for these two cases.

One-dimensional modulation

The atoms are confined in a uniform square box of size $L = 40\,\mu\mathrm{m}$, generated by DMD1 (see Chap. 1 for details). A second DMD then superimposes a one-dimensional

modulation of the form:

$$V(\mathbf{r}) = \frac{V_0}{2}\cos(kx) + A \quad \text{with} \quad k = \frac{2\pi}{\lambda}, \tag{2.34}$$

where A is a constant offset irrelevant for the physics at play. In practice, we set $\lambda \simeq 4\,\mu\text{m}$. The resulting atomic density is shown in Fig. 2.3: it exhibits a clear modulation along x, while remaining uniform along y. From this symmetry, several consequences follow immediately for the superfluid fraction tensor:

- The x–y basis is the natural one for the problem, and the tensor is diagonal in this basis: a phase twist along x (resp. y) does not induce any current along y (resp. x).
- The density profile is separable, implying that the superfluid fraction equals both the Leggett and Saslow bounds.
- Along the unmodulated direction y, the superfluid fraction is equal to unity. This result can be directly obtained from Eq. (2.33).

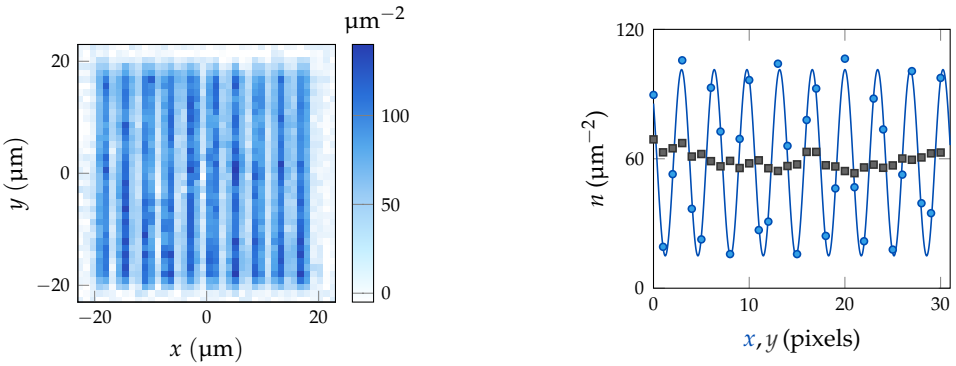

Figure 2.3: **(a)** Absorption image showing the atomic density in the potential of Eq. (2.34), with $V_0 = 108(10)\,\text{nK}$, $\lambda = 3.93(4)\,\mu\text{m}$, and $\langle n \rangle = 60(3)\,\mu\text{m}^{-2}$. It is an average of 40 experimental realizations. **(b)** Averaged density profiles along y (blue circles) and along x (black squares). The solid line is a sinusoidal fit. The pixel size is 1.15 μm.

Hence, in the x–y basis, the superfluid fraction tensor takes the form:

$$f_s = \begin{pmatrix} f_s^{(x,x)} & 0 \\ 0 & 1 \end{pmatrix} = \begin{pmatrix} f_\pm^{(x,x)} & 0 \\ 0 & 1 \end{pmatrix}. \tag{2.35}$$

We employed two complementary approaches to determine $f_s^{(x,x)}$. The first is a static method, based on the Leggett bounds given in Eq. (2.28) and (2.33), and the second is a dynamic method relying on the hydrodynamic relation [117], valid for a BEC at $T = 0$:

$$f_s^{(x,x)} = m\,\kappa\,c_x^2 \quad \text{and} \quad f_s^{(y,y)} = m\,\kappa\,c_y^2 = 1 \Rightarrow f_s^{(x,x)} = \frac{c_x^2}{c_y^2}, \tag{2.36}$$

where c_i is the speed of (second) sound along direction i, and κ is the compressibility. It is a scalar quantity, defined by:

$$\kappa = \frac{1}{\langle n \rangle}\frac{\partial \langle n \rangle}{\partial \mu}. \tag{2.37}$$

For a uniform gas, $\kappa = 1/(g_{2D}n)$ and $f_s^{(i,i)} = 1$, we recover the Bogoliubov speed of sound $c_i = \sqrt{gn/m}$. Following Eq. (2.36), we extract the superfluid fraction from measurements of the sound velocities $c_{x,y}$ along the two principal directions. In practice, we perturbatively excite the cloud and monitor the propagation of phonons through the resulting center-of-mass oscillations. This method, already demonstrated in similar contexts [see, e.g. 129], provides a direct measurement of the lowest collective excitation frequency ν_i, from which the sound velocity follows as $c_i = 2\nu_i L$. The results obtained for various lattice depths V_0 are presented in Fig. 2.4. We compare the values of $f_s^{(x,x)}$ inferred from this dynamic approach with those deduced from the Leggett bound, computed using the measured in-situ density profiles. The two independent methods yield consistent results over the entire range of modulation depths, and both agree quantitatively with the predictions of a GPE simulation.

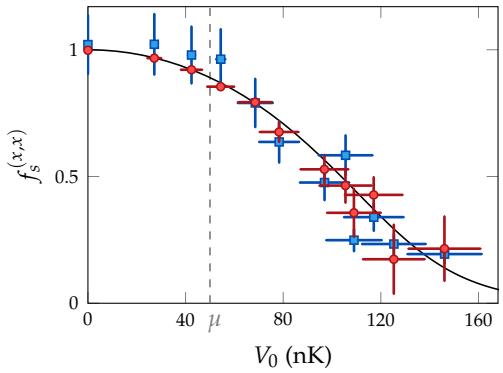

Figure 2.4: Superfluid fraction along the modulated direction of the gas as a function of the lattice depth V_0. Red circles correspond to static estimates from the Leggett bound of Eq. (2.33), while blue squares are obtained dynamically from the measured sound velocities along x and y. The black solid line represents the prediction from GPE simulations. The gray dashed line indicates the chemical potential μ.

Two-dimensional modulation

The one-dimensional optical lattice described above led to considerable simplifications in the estimation of the superfluid fraction, both for static and dynamic measurements. We now turn to a more complex situation, in which the translational symmetry is broken along two directions [138]. We consider a triangular lattice potential, given by:

$$V(\mathbf{r}) = -\frac{2V_0}{9}\sum_{m=0}^{2}\cos(\mathbf{k}_m\cdot(x,y)+\phi_m)+A \quad \text{with} \quad \mathbf{k}_m = \frac{4\pi}{\sqrt{3}\lambda}\begin{pmatrix}\cos(2m\pi/3)\\ \sin(2m\pi/3)\end{pmatrix}, \tag{2.38}$$

where A is a constant offset irrelevant for the physics at play. In practice, we set $\lambda \simeq 6\,\mu$m. The phases ϕ_m are only relevant through their sum, $\Phi = \phi_0 + \phi_1 + \phi_2$. Experimentally, we measure $\Phi = 0.21(1)\,\pi$. The resulting atomic density is shown in Fig. 2.5. The density is clearly non-separable, and therefore the Leggett bounds are not saturated. This can be explicitly shown by noting that (for V_0 not too large) the average density along y is uniform, as shown in Fig. 2.5b. Then, we directly compute that $f_+^{(y,y)} = 1$. A complete discussion of the different Leggett bounds in this geometry can be found in [106, 165].

Due to the threefold rotational symmetry of the potential in Eq. (2.38), the superfluid response is isotropic, and the tensor reduces to a scalar quantity: $f_s = f_s^{(x,x)} = f_s^{(y,y)}$.

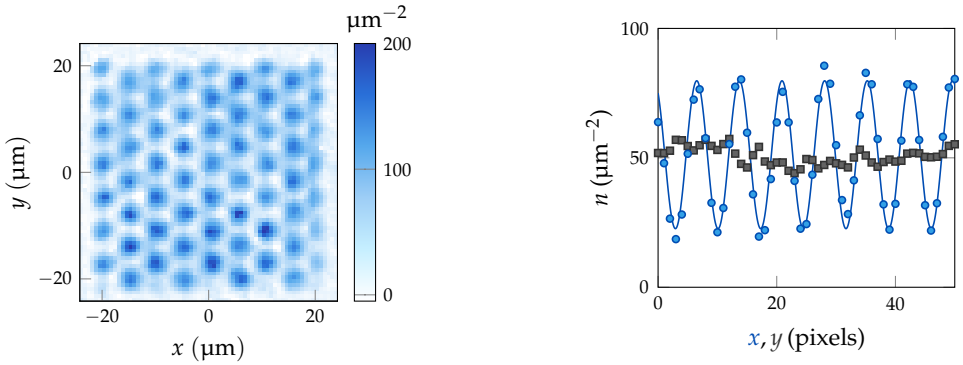

Figure 2.5: **(a)** Absorption image showing the atomic density in the potential of Eq. (2.38), with $V_0 = 193(9)\,\mathrm{nK}$, $\lambda = 6.0(1)\,\mu\mathrm{m}$, $\langle n \rangle = 51(2)\,\mu\mathrm{m}^{-2}$. It is an average of 40 experimental realizations. **(b)** Averaged density profiles along y (blue circles) and along x (black squares). The solid line is a sinusoidal fit. The pixel size is 0.711 μm.

Even though the Leggett bounds no longer yield accurate estimates, the Saslow bound, Eq. (2.31), remains saturated under our experimental conditions. Its determination relies on the measured in-situ density, from which the local phase field $\theta(\mathbf{r})$ is reconstructed [106, 138]. The resulting values are shown in Fig. 2.6. In parallel, we use the hydrodynamic relation of Eq. (2.36), measuring both the compressibility κ and the speed of sound along y. The compressibility is obtained following the protocol of [169], in which a small, uniform external force is applied to the cloud and the resulting center-of-mass displacement is analyzed to extract κ [86, 106]. Together, these measurements provide a consistent evaluation of the superfluid fraction in the triangular lattice geometry, summarized in Fig. 2.6. The small but increasing discrepancy between the experimental data and the GPE predictions may originate from finite-temperature effects, which lie beyond the scope of this work.

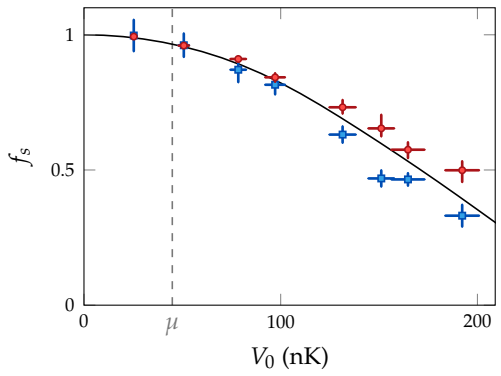

Figure 2.6: Superfluid fraction of the gas, modulated with the potential of Eq. (2.38), as a function of the lattice depth V_0. Red circles correspond to static estimates from the Saslow bound of Eq. (2.31), while blue squares are obtained dynamically from the measured sound velocity and compressibility along y. The black solid line represents the prediction from GPE simulations. The gray dashed line indicates the chemical potential μ.

2.3 Description of a spin mixture

2.3.1 Coupled Gross-Pitaevskii equations

We have so far considered a single BEC described by the GPE. However, using the tools introduced in Sec. 1.3, we can realize spin mixtures, where atoms populate two distinct internal states. Each spin component then forms its own BEC, characterized by a macroscopic wavefunction. In the following, we restrict ourselves to the case of two spin species, with wavefunctions ψ_1 and ψ_2. Their dynamics can still be described within the mean-field approximation, but the interaction term becomes richer than in Eq. (2.8), owing to the multiple possible collision channels. This situation is illustrated in Fig. 2.7: each atom can interact either with another atom in the same spin state or with one belonging to the other component. Consequently, three interaction constants

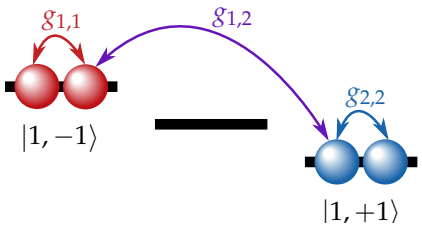

Figure 2.7: Schematic of the possible interaction channels between atoms of two spin states. We introduce intraspecies couplings ($g_{1,1}$ and $g_{2,2}$), and interspecies coupling ($g_{1,2}$). We represent atoms in the states $|F=1, m_F=-1\rangle$ and $|F=1, m_F=+1\rangle$, corresponding to the mixture used in Chap. 4-6.

$g_{i,j}$ (with $g_{i,j} = g_{j,i}$ by symmetry) are needed to describe all possible s-wave collisions between atoms of species i and j. The two wavefunctions are thus linked through the interspecies interaction $g_{1,2}$, leading to the coupled Gross-Pitaevskii Equations [170]:

$$\begin{cases} \mathrm{i}\hbar\dfrac{\partial}{\partial t}\psi_1(\mathbf{r},t) = \left[-\dfrac{\hbar^2}{2m}\nabla^2 + V(\mathbf{r},t) + g_{1,1}|\psi_1(\mathbf{r},t)|^2 + g_{1,2}|\psi_2(\mathbf{r},t)|^2\right]\psi_1(\mathbf{r},t)\,, \\ \mathrm{i}\hbar\dfrac{\partial}{\partial t}\psi_2(\mathbf{r},t) = \left[-\dfrac{\hbar^2}{2m}\nabla^2 + V(\mathbf{r},t) + g_{2,2}|\psi_2(\mathbf{r},t)|^2 + g_{1,2}|\psi_1(\mathbf{r},t)|^2\right]\psi_2(\mathbf{r},t)\,. \end{cases} \tag{2.39}$$

Each equation thus includes both an *intraspecies* mean-field term ($g_{1,1}$ or $g_{2,2}$) and an *interspecies* coupling ($g_{1,2}$), which characterizes the nonlinear coupling between the two condensates. We consider the case of repulsive interactions, $g_{i,j} > 0$, relevant for the ground state of ^{87}Rb.

The interplay between intra and interspecies interactions determines whether the two components spatially overlap or separate. By comparing the interaction energies of mixed and demixed configurations, one can introduce the miscibility parameter [170]:

$$\Delta = \frac{g_{1,2}^2}{g_{1,1}\, g_{2,2}}\,. \tag{2.40}$$

The mixture is miscible when $\Delta < 1$, meaning that the overlap of the two components is energetically favorable. Conversely, for $\Delta > 1$, the interspecies repulsion dominates, and it becomes favorable for the two BECs to demix, forming spatially separated domains. Such phase separation has been observed experimentally in, e.g., [171–173]. This behavior is illustrated in Fig. 2.8: Fig. 2.8a shows an example of time-evolved system with initially overlapping, immiscible components, while Fig. 2.8b displays a corresponding

ground state configuration. We observe that the two spin species interpenetrate each

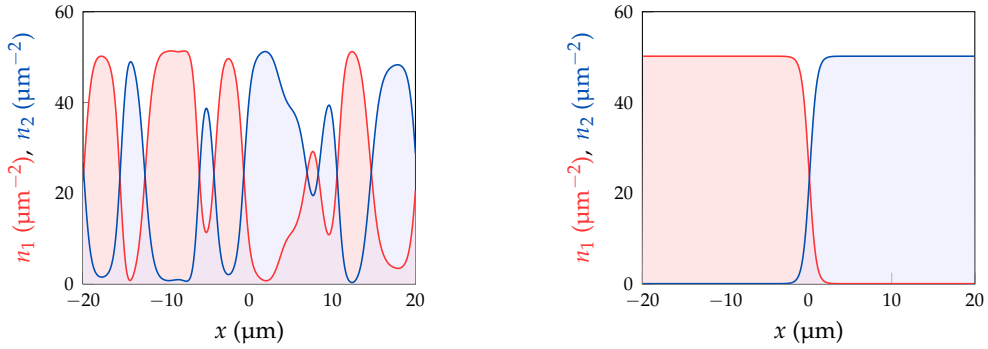

Figure 2.8: (a, b) Illustration of the immiscibility of two spin components in a two-dimensional system, with cuts at constant y. The initial (uniform) densities are set to $n_1 = n_2 = 25\,\mu\text{m}^{-2}$, and the dynamics are obtained from numerical simulations of the coupled GPEs, Eq. (2.39), setting $\Delta = 1.2$ and $g_{1,1} = g_{2,2}$. **(a)** Result of the time evolution of the system (initialized with a small phase noise): the two components dynamically demix, forming domains whose characteristic size agrees with predictions from the Bogoliubov analysis (see main text). **(b)** Ground-state configuration obtained by imaginary-time evolution, showing the spatial separation of the two components with a narrow overlap region around $x = 0$. The left / right symmetry breaking is induced by the initial phase noise inputted in the simulation.

other around $x = 0$, and the region of this overlap has a characteristic length given by ξ_s, the *spin healing length*. Restricting ourselves to the case of the symmetric mixture of Fig. 2.7, for which $g_{1,1} = g_{2,2} = g$, we define [174, 175]:

$$\xi_s = \frac{\xi}{\left(\sqrt{\Delta} - 1\right)^{1/2}} = \frac{\hbar}{\sqrt{2mn\,|\delta g|}} \quad \text{with} \quad \delta g = g_{1,2} - g\,, \tag{2.41}$$

where ξ is the single component healing length, and n the atomic density. For typical experimental parameters (see Chap. 4), $\delta g \ll g$, thus $\xi_s \gg \xi$. In particular, the spin healing length becomes larger than the resolution of our microscope objective, allowing the observation of spin dynamics.

Bogoliubov spectrum

A Bogoliubov analysis can be performed on the coupled Eq. (2.39), in direct analogy with the single-component case discussed in Sec. 2.1.3. We consider an initially uniform configuration, with densities n_i for each spin component i. The excitation spectrum then takes the form [170]:

$$\left(\hbar\omega_k^{\pm}\right)^2 = \left(\hbar c_{\pm} k\right)^2 + \left(\frac{\hbar^2 k^2}{2m}\right)^2 , \tag{2.42}$$

where the sound velocities of the two branches are given by:

$$c_{\pm}^2 = \frac{1}{2}\left(c_1^2 + c_2^2 \pm \sqrt{\left(c_1^2 + c_2^2\right)^2 + 4(\Delta - 1)c_1^2 c_2^2}\right) , \tag{2.43}$$

and $c_i = \sqrt{n_i g_{i,i}/m}$ denotes the speed of sound in each component. The spectrum thus exhibits two excitation branches. When $\Delta > 1$, the lower branch becomes dynamically unstable, since c_- acquires an imaginary part. This leads to exponentially growing modes for $k < k_c = 2m|c_-|/\hbar$, with the maximum growth rate occurring at $k = k_c/\sqrt{2}$. For the case shown in Fig. 2.8a, this corresponds to a characteristic wavelength $\lambda \simeq 7\,\mu$m, in good agreement with the size of the emerging domains. This instability mechanism is analogous to the *modulational instability* of the one-component attractive GPE, discussed in Sec. 3.4.2.

2.3.2 The low-depletion limit

The dynamics induced by the coupled GPE (2.39) are both rich and complex [93, 176, 177]. Yet, in certain limits it is possible to describe the system with an effective single field [178, 179]. We consider here the case of a bath of density $n_1 = |\psi_1|^2$, and a minority component ψ_2 of much smaller density $n_2(x) \ll n_1(x)$. Denoting by n_0 the static density of the bath in the absence of the minority component, we write:

$$\psi_1(\mathbf{r},t) = [\sqrt{n_0} + \delta\psi_1(\mathbf{r},t)]\,\mathrm{e}^{-\mathrm{i}\mu_1 t/\hbar} \quad \text{with} \quad \mu_1 = g_{1,1}n_0\,, \tag{2.44}$$

where $\delta\psi_1$ is a small correction induced by the presence of atoms of component 2. Following the approach of [179], we substitute this expression into Eq. (2.39), obtaining:

$$\begin{aligned} \mathrm{i}\hbar\frac{\partial}{\partial t}\delta\psi_1 + \frac{\hbar^2}{2m}\nabla^2\delta\psi_1 = V(\mathbf{r})\,[\sqrt{n_0} + \delta\psi_1(\mathbf{r},t)] + g_{1,2}(\sqrt{n_0}n_2 + n_2\delta\psi_1) \\ + g_{1,1}n_0\,(\delta\psi_1 + \delta\psi_1^*) + g_{1,1}\sqrt{n_0}\left(\delta\psi_1^2 + 2|\delta\psi_1|^2\right)\,, \end{aligned} \tag{2.45}$$

where terms of order higher than two in $\delta\psi_1$ have been neglected. An important hypothesis consists in neglecting the explicit time evolution of $\delta\psi_1$. This can be viewed as an adiabatic approximation: the bath dynamics, governed by a timescale of order $\hbar/\mu_1$, are much faster than those of the dilute minority component. Consequently, the bath density adapts quasi-instantaneously to the evolution of ψ_2.

Identifying in Eq. (2.45) the terms corresponding to $g_{1,1}|\psi_1|^2$ and expanding $\delta\psi_1/\sqrt{n_0}$ in powers of the depletion n_2/n_0, we can substitute back into the equation for ψ_2 obtaining:

$$\mathrm{i}\hbar\frac{\partial}{\partial t}\psi_2 = -\frac{\hbar^2}{2m}\nabla^2\psi_2 + V_e(\mathbf{r})\psi_2 + g_e|\psi_2|^2\psi_2 + \mathcal{O}\left(\frac{n_2}{n_0}\right) \tag{2.46}$$

where the effective potential and interaction strength are:

$$V_e(\mathbf{r}) = \left(1 - \frac{g_{1,2}}{g_{1,1}}\right)V(\mathbf{r}) \quad \text{and} \quad g_e = g_{2,2} - \frac{g_{1,2}^2}{g_{1,1}}\,. \tag{2.47}$$

To zeroth order in the depletion n_2/n_0, Eq. (2.46) thus reduces to a single-component GPE, with both the potential and interaction terms dressed by the bath. Notably, for immiscible mixtures, one has $g_e < 0$, leading to an effective attractive nonlinearity for the minority component. This effective equation thus provides a powerful framework to engineer and explore attractive nonlinear dynamics, such as solitons, within a repulsively interacting BEC.

Conclusion

In this chapter, we have established a mean-field framework for describing our system, based on the GPE. This approach accurately captures the behavior of weakly interacting Bose gases at low temperatures and provides direct access to their superfluid properties. By analyzing the response of the condensate to phase twists and external perturbations, we defined the superfluid fraction and explored its evolution in the presence of external modulations. We have also shown how this mean-field formalism naturally extends to multi-component condensates, where additional internal degrees of freedom give rise to rich coupled dynamics.
Altogether, this mean-field description provides the theoretical foundation for interpreting the experimental observations presented in the following chapters. In particular, Chap. 3 will address the integrability of the one-dimensional attractive NLSE, to which our system can be mapped.

II The Inverse Scattering Transform and solitonic solutions of the nonlinear Schrödinger equation

3 The Inverse Scattering Transform

Outline of the current chapter

Introduction

The Nonlinear Schrödinger Equation is of fundamental importance in physics, particularly in the context of cold-atom platforms. A central question concerns how such an equation can be solved. The NLSE describes a system with an infinite number of degrees of freedom. In Hamiltonian systems with a finite number n of degrees of freedom, specifying n integrals of motion is sufficient to render the system integrable. However, when dealing with infinitely many integrals of motion, the situation becomes more subtle and requires a more sophisticated framework: the Inverse Scattering Transform (IST). The discovery of solitonic solutions provided the first indication of this hidden integrability.

This chapter aims to describe the IST in the context of the NLSE. We first provide an overview of solitons in various physical systems (Sec. 3.1). We then detail the IST method and its profound connection to solitons (Sec. 3.2). This method can be reformulated to construct explicit many-soliton solutions (Sec. 3.3). Finally, we highlight some variations of the method to illustrate its richness (Sec. 3.4).

3.1 Omnipresence of solitons

3.1.1 Discovery and first observations

The first documented observation of a soliton is attributed to John Scott Russell in his Report on Waves [36], where he describes a "wave of translation": a soliton. Russell lacked the theoretical explanation for this phenomenon, which was provided a few decades later with the rediscovery of the Korteweg-de Vries (KdV) equation [20] (it had already been formulated by Boussinesq in a footnote in [180]). This equation describes the water level in a low-depth, one-dimensional channel and is an approximation of the Navier-Stokes equations [see e.g. 39, Appendix A]. It can be written in dimensionless form:

$$\frac{\partial \phi}{\partial t} + 6\phi \frac{\partial \phi}{\partial x} + \frac{\partial^3 \phi}{\partial x^3} = 0\,, \tag{3.1}$$

where ϕ represents the water height compared to equilibrium, and x, t are space and time coordinates respectively. Eq. (3.1) is expressed in a frame moving at the speed of sound. Of the three terms in this equation, the second is nonlinear. Its effect can be qualitatively understood by removing the last term, which leads to the inviscid Burgers equation. Then, each portion of the wave will move with an approximate velocity 6ϕ, resulting in steeper wave fronts and shock waves. Conversely, considering the case of $\phi \to 0$, thus linearizing the equation, we observe that the dispersion relation for plane waves $\phi \propto \mathrm{e}^{i(kx-\omega t)}$ is $\omega = -k^3$. Hence, the last term creates some dispersion of the initial wavepacket. The balance of these two terms in the KdV equation enables solitons to exist.

Because Eq. (3.1) is nonlinear, it is difficult to find its solutions. In particular, the plane waves are no longer an eigenbasis, rendering the Fourier Transform (FT) useless. One can search for solutions of the form $\phi_v(x,t) = \phi(x - vt)$, corresponding to solutions which propagate without any deformation at a velocity v. This approach matches the "natural" definition of a soliton. After some algebra, one can obtain:

$$\phi_v(x,t) = \frac{v}{2} \operatorname{sech}^2\left[\sqrt{\frac{v}{4}}(x - vt)\right] \quad \text{with} \quad v > 0\,, \tag{3.2}$$

which is the solitonic solution of Eq. (3.1) with velocity v. The condition $v > 0$ does not indicate symmetry breaking because it corresponds to $v > c_s$ in the laboratory frame.

It simply means that KdV solitons are always supersonic. We also have $\phi_v > 0$, which indicates that solitons are bulges of fluid.

However, this procedure overlooks many solutions, due to our ansatz only considering wavepackets that do not deform. In particular, we can mention the two-soliton solution. One example of such a solution is shown in Fig. 3.1. We see that at $|t| \to \infty$ this solution is similar to two independent solitons. Despite the nonlinearity of the KdV equation, we observe that they collide elastically, with no exchange of energy, momentum, or particles. A numerical experiment performed by [37] revealed the remarkable

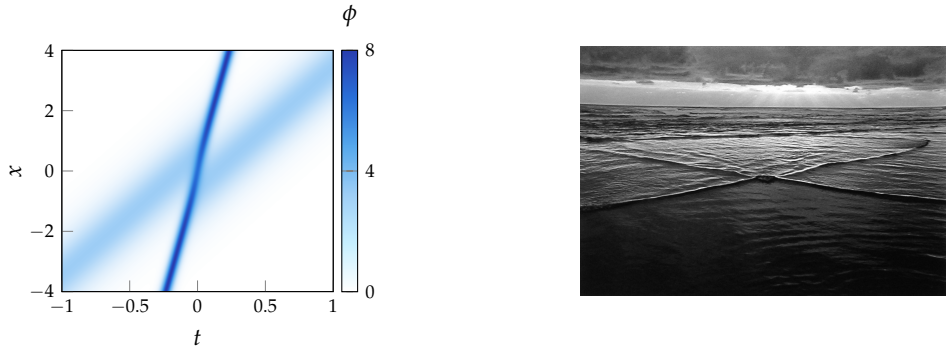

(a) Numerical simulation of KdV solitons. **(b)** Picture from Terry Toedtenieier, 1978.

Figure 3.1: (a) Example of a two-soliton of the KdV equation. When $|t| \to \infty$, we recover two separated solitons well-described by Eq. (3.2). The first has an amplitude of 8, the second an amplitude of 2. The collision results in a shift in position for these two solitons, meaning it is not a linear superposition of two independent wavepackets. **(b)** A qualitative illustration of two solitons colliding. The position shift is clearly visible, while the waveform is conserved.

fact that solitons retain their shape after interacting with each other. The explanation behind this feature of the KdV equation was found closely afterwards by [43], who introduced a new method for solving certain nonlinear Partial Differential Equations (PDEs), now called the IST. This powerful method allows one to construct all solutions of such an equation. In particular, it is applicable to the NLSE, which is the main focus of this chapter.

3.1.2 Solitons of the 1D GPE

Before presenting the general solution to the NLSE, we will briefly review some of the work that has been done on solitons within the context of this equation. We recall that in one dimension, the NLSE (also called GPE for cold atoms) reads:

$$i\hbar\frac{\partial\psi}{\partial t} = -\frac{\hbar^2}{2m}\frac{\partial^2\psi}{\partial x^2} + g|\psi|^2\psi \quad \text{and} \quad \int |\psi(x)|^2\,\mathrm{d}x = N\,, \tag{3.3}$$

where g is the interaction parameter, and ψ is normalized to the atom number. We can rewrite this equation in a dimensionless form by setting:

$$\tilde{t} = \frac{t}{t_0} = t\frac{N^2mg^2}{2\hbar^3} \quad , \quad \tilde{x} = \frac{x}{x_0} = x\frac{Nm|g|}{\hbar^2} \quad \text{and} \quad u(\tilde{x},\tilde{t}) = \sqrt{\frac{x_0}{N}}\psi(x,t)\,. \tag{3.4}$$

The last equality is set by requiring $\int |u|^2 \, \mathrm{d}x = 1$.[1] We obtain the following equation:

$$\mathrm{i}u_t + u_{xx} \pm 2|u|^2 u = 0\,, \tag{3.5}$$

where the $\tilde{\cdot}$ have been omitted, and subscripts indicate a derivative with respect to the variable. The positive or negative sign of the nonlinearity expresses whether we have the *focusing / attractive* or *defocusing / repulsive* NLSE respectively. Eq. (3.5) arises in many different physical contexts, in addition to cold atoms: plasma physics to describe small amplitude Langmuir waves [181], optical fibers [38, 182] (where the roles of the space and time coordinates are swapped), bulk Kerr media [183] (where the propagation happens along a second space axis instead of time), deep-water waves [22], etc.

Eq. (3.5) admits solitonic solutions, the most famous ones being the bright and dark solitons in the case of the attractive and repulsive equation respectively. We can write explicitly these solutions. For the bright soliton:

$$u(x,t) = \frac{\kappa}{\cosh(\kappa x)} \mathrm{e}^{\mathrm{i}\kappa^2 t}\,, \tag{3.6}$$

for a soliton of mass $\int |u|^2 \, \mathrm{d}x = 2\kappa$. The dimensional form can be recovered using Eq. (3.4). It is possible to obtain this solution when searching for solutions that propagate without any deformation, similarly to the KdV case [39]. This wavepacket naturally concentrates all atoms around $x = 0$, due to the attractive interactions. Conversely, atoms with repulsive interactions will tend to spread over the whole space. Hence, the dark soliton of the repulsive NLSE is associated with a density dip, and is given by:

$$u(x,t) = \tanh(x) \mathrm{e}^{-2\mathrm{i}t}\,. \tag{3.7}$$

We note that the dark soliton is an excited state, while the bright soliton is the ground state of the focusing NLSE. Both bright and dark solitons have been extensively studied in cold-atom platforms, using atomic species with either attractive or repulsive interaction parameters: [62, 184–186] and [63, 187, 188] observed bright and dark solitons respectively. We illustrate in Fig. 3.2 a historical example of each.

The NLSE (3.5) is Galilean invariant. This means that one can obtain solutions in a reference frame moving at a uniform velocity v with respect to the initial one thanks to the following transformation:

$$u(x,t) \longrightarrow u(x - vt, t)\, \mathrm{e}^{\mathrm{i}(vx - v^2 t/2)/2}\,. \tag{3.8}$$

This equation can be directly applied to the bright soliton (3.6) in order to obtain solitons moving at a velocity v. However, in the defocusing case, the dark soliton exists on a nonzero background whose phase and current are modified by a Galilean boost, thus breaking the invariance of the solution itself. The Galilean transformation can also be extended to non-inertial reference frames [190], for example to express the solutions in the case of a uniform and constant force.

Similar to the KdV equation, the solitons of the NLSE exhibit remarkable stability properties. In particular, bright solitons maintain their shape and velocity when they collide with one another. Experiments investigating this phenomenon have been conducted in cold-atom systems [64] and in optical fibers [191]. The mathematical reasons behind this feature will become clear in the following sections.

[1] This normalization to unity sets the amplitude of a bright soliton of width $x_0/2$, and atom number N. In the following we will allow the norm of u to vary in order to keep a common x_0 while varying the atom number.

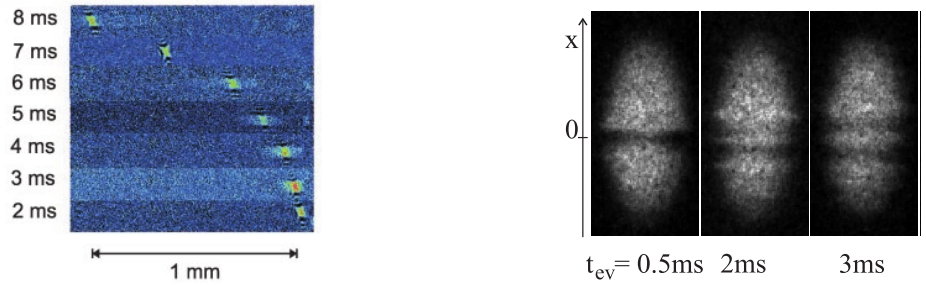

(a) Bright soliton. **(b)** Dark soliton.

Figure 3.2: **(a)** First observation of a bright soliton. The wavepacket was formed by preparing a repulsive BEC, and fine tuning the interactions to the attractive side via a Feshbach resonance. We observe that it retains its width and height over time. Figure adapted from [62]. **(b)** First observation of a dark soliton. It was created using phase imprinting: a constant potential is added to one half of the cloud to generate a phase difference between the two halves. Figure adapted from [63]. We note that due to the imperfect imprinting of the waveform, the authors actually formed a pair of so-called gray soliton. This soliton is not stationary, and the phase jump across it is less than π [see 189, Chap. 3, and references therein for details].

Stability of solitons

Until now, we have considered objects that are solutions of Eq. (3.5). One might wonder about the stability of such solutions in physically realistic systems, such as cold atoms. In particular, atoms are typically confined within cigar-shaped traps. This means that they experience a harmonic confinement along the longitudinal direction. The three-dimensional nature of the atomic cloud should cause it to implode in the case of the focusing NLSE [192]. Besides, the GPE is a mean-field description and neglects some quantum effects. Let us briefly discuss the validity of our assumptions:

- The longitudinal trap a priori breaks the integrability of Eq. (3.5). When the trap is shallow enough, one can show that the solitonic solutions still exist and remain stable [193].
- The atoms are typically confined in harmonic traps of frequency $\omega_\perp$ in the transverse directions. The ground state wavefunction has a typical size in the transverse plane of $a_{\text{ho}} = \sqrt{\hbar/(m\omega_\perp)}$. In order to have a frozen motion in this plane, it is necessary that the quantum of energy of the harmonic oscillator is much greater than the chemical potential μ, meaning $\hbar\omega_\perp \gg |\mu|$. We can rewrite this condition: $a_{\text{ho}}/|a| \gg N$, with a the scattering length between two atoms.
- For attractive interactions, the absolute ground state of the atomic cloud approaches a Dirac peak. However, a local energy minimum corresponding to a soliton exists under the condition that $N|a|/a_{\text{ho}} \lesssim 0.7$ [194].
- The solitonic solution was found within the Hartree ansatz hypothesis, which underlies the GPE. By relaxing this constraint, [195] found the true N-particle ground state of interacting attractive bosons. This solution converges to Eq. (3.6) when $N \gg 1$. Quantum effects were also studied by [196, 197], who discovered the quantum analog of a dark soliton.

Dealing with effects resulting from these considerations lies outside the scope of this manuscript, and we will assume in the following that the NLSE (3.5) is fully valid.

3.1.3 A widespread topic

For the moment, we have only considered two equations that contain solitonic solutions. However, solitons are ubiquitous, even when restricting to cold-atom platforms. We should mention that, although most solitons are held in one-dimensional equations, there are several exceptions. Recently, the Townes soliton has been realized in our team [70] and in [69], and the Jones-Roberts soliton in [198]. They are, respectively, solutions to the attractive and repulsive two-dimensional NLSE.

We will detail below some important solitonic solutions linked with the NLSE, restricting ourselves to one-dimensional systems.

Solitons on a background

In this section, we consider the focusing NLSE. The bright soliton of Eq. (3.6) and the multi-solitonic solutions we mentioned have the particularity that $\lim_{|x|\to\infty} |u(x,t)| = 0$. Another class of solutions exists for which $\lim_{|x|\to\infty} |u(x,t)| = 1$. We can mention the Kuznetsov-Ma soliton [199, 200], the Akhmediev soliton [201], or the Peregrine soliton [202]. One should note that these solutions are not stable with respect to the modulational instability [203]. These structures have been proposed as prototypes of rogue waves [see e.g. 204, for a recent review], due to their localized (either in space or time) growth and decay reminiscent of a rogue wave. The wavefunctions of these solutions are illustrated in Fig. 3.3, and can be written out explicitly:

$$u_{\text{Akhm}}(x,t) = \left[1 + \frac{(2-4a)\cosh(2bt) + \mathrm{i}b\sinh(2bt)}{\sqrt{2a}\cos(kx) - \cosh(2bt)}\right] \mathrm{e}^{2\mathrm{i}t} \text{ with } 0 < a < \tfrac{1}{2}\,, \tag{3.9a}$$

$$u_{\text{Pereg}}(x,t) = \left[1 - \frac{4(1+4\mathrm{i}t)}{1+4x^2+16t^2}\right] \mathrm{e}^{2\mathrm{i}t}\,, \tag{3.9b}$$

$$u_{\text{Kuzn}}(x,t) = \left[1 + \frac{(2-4a)\cos(2bt) - \mathrm{i}b\sin(2bt)}{\sqrt{2a}\cosh(kx) - \cos(2bt)}\right] \mathrm{e}^{2\mathrm{i}t} \text{ with } a > \tfrac{1}{2}\,, \tag{3.9c}$$

with $b = 2\sqrt{2a|1-2a|}$, $k = 2\sqrt{|1-2a|}$. One can also introduce a shift in either space or time in the x,t coordinates. The Akhmediev soliton corresponds to a structure of peaks periodic in space appearing around $t = 0$ while the Kuznetsov-Ma soliton is periodic in time, and the peaks are localized near $x = 0$. The Peregrine soliton is the limit of these solitons, both mathematically by taking $a \to 1/2$, and in the sense that it has only one maxima located at $(x,t) = (0,0)$. These solutions have been observed in optical

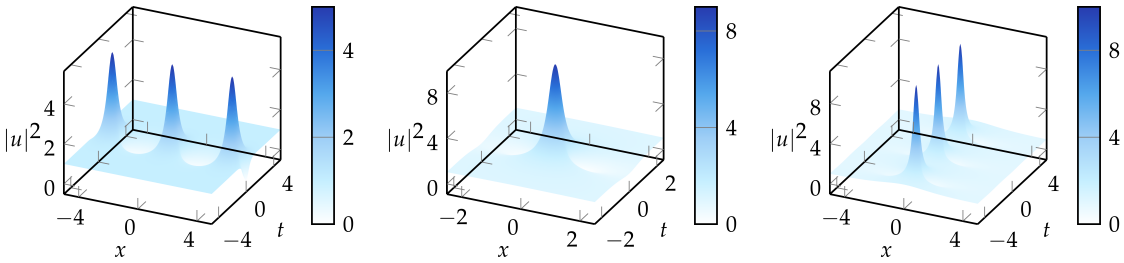

(a) Akhmediev soliton. **(b)** Peregrine soliton. **(c)** Kuznetsov-Ma soliton.

Figure 3.3: (a) Akhmediev soliton with $a = 0.2$. **(b)** Peregrine soliton, which corresponds to $a \to 1/2$ from either the positive or negative side. **(c)** Kuznetsov-Ma soliton with $a = 0.6$. **(a-c)** Note the heights of the peaks for each solution are different, but all wavefunctions approach $|u| \to 1$ at infinity.

fibers [205–207], and more recently in the cold-atom platform where some features of the Peregrine soliton have been observed [208].

We highlight that despite their names, these objects seem to have only a tenuous similarity with the bright soliton. This begs the question: why are they called solitons? They do not follow the criteria of propagating with no deformation. The answer to this question lies once again in the IST, and will be tackled in Sec. 3.4.2.

Vector solitons

A possible extension of the NLSE is to consider coupled equations. In the BEC context, we can consider the case of a spin mixture described by the wavefunctions u, v:

$$\begin{cases} \mathrm{i}u_t + u_{xx} - 2|u|^2u - 2\alpha|v|^2u = 0\,, \\ \mathrm{i}v_t + v_{xx} - 2|v|^2v - 2\alpha|u|^2v = 0\,, \end{cases} \tag{3.10}$$

where we have taken the same (repulsive) intra-species interaction strength for u and v. This corresponds for instance to the case of the spin mixture studied in Chap. 4-6. The constant $\alpha \in \mathbb{R}$ indicates the magnitude of the inter-species interactions, which are by nature symmetric. Eq. (3.10) also admits solitonic solutions.

In the case $\alpha = 1$, we obtain the so-called Manakov system, which was shown to be integrable by [209]. One of the most well-known solution of this system is the dark-bright soliton [210–212], which we illustrate in Fig. 3.4. It was realized with cold atoms by e.g. [71, 72, 177]. Thanks to the SU(2) symmetry of the interaction strengths, it is also possible to write more general solutions [213].

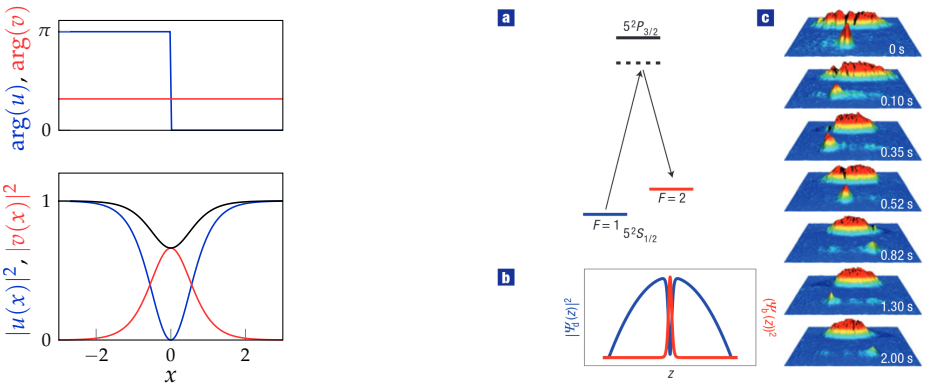

(a) Profile of a dark-bright soliton.

(b) Experimental realization.

Figure 3.4: (a) Numerical profile of a dark-bright soliton: it consists of a bright soliton sitting in the minimum of density of a dark soliton. Top: Phases of the two components. We also have the π phase jump associated to dark solitons. Bottom: Density profiles, the solid black line shows the total density. **(b)** Oscillation of a dark-bright soliton in a harmonic trap. In particular, the subfigure (c) shows the optical densities of each spin component, and we observe that the minority lies in the density hole of the majority component. Figure adapted from [71].

When $\alpha \neq 1$, Eq. (3.10) is no longer integrable. However, keeping $\alpha \simeq 1$, we can map the spin mixture to a one-dimensional ferromagnetic chain of spins [76] (see [77] for a review about spin chains and in particular magnetic solitons, fundamental solutions of such a spin chain). Such a mapping will be the subject of Chap. 5, we postpone discussions until that chapter. We simply mention that magnetic solitons have been demonstrated in cold-atom systems in [214, 215].

3.2 A linear reformulation of the NLSE

The Inverse Scattering Transform was first introduced by [43] in order to solve the KdV equation. While exact soliton solutions can be derived by ansatz in special cases, most solutions of a nonlinear equation cannot be obtained directly. The IST provides a systematic method to compute all solutions by mapping the nonlinear problem into a linear spectral problem.

Their method was reformulated by Lax in [46], which allowed an easier extension to other nonlinear equations. In particular, [44] showed that it was applicable to the NLSE, and [45, 216] further generalized this work. The broad idea of this technique is to reformulate the nonlinear equation in order to successively solve three linear problems instead of a nonlinear one. The principle is quite similar to the FT, and the IST is sometimes called "nonlinear Fourier transform". This analogy is developed in Fig. 3.5.

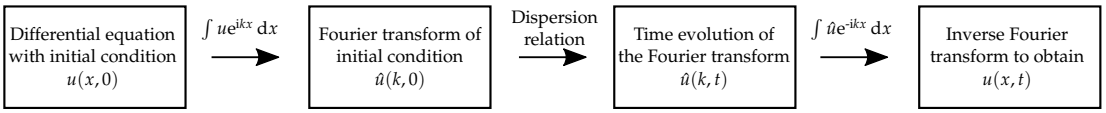

(a) Pathway to solve certain linear PDEs.

(b) Pathway to solve certain nonlinear PDEs.

Figure 3.5: (a) Linear equations that are invariant under spatial translations can be efficiently solved using the FT because plane waves naturally form the basis of their solution space. An example of this is the Helmholtz equation and its paraxial approximation, which describes the propagation of light. The time-evolved solution to such an equation can be easily found by performing a (trivial) time evolution in Fourier space and then inverting the result at the desired time. **(b)** The IST operates on the same principle. The initial condition is mapped to an auxiliary spectral space, or scattering data, where its time evolution is straightforward. The most important aspect of this method is that these three steps are *linear*.

In this section, we will detail the three steps shown in Fig. 3.5b for the focusing NLSE and demonstrate how the IST provides new insights into solitons. We will restrict ourselves to the case of $\lim_{|x|\to\infty} u(x,t) = 0$, which is the focus of the original works of [44, 45]. We will mention extensions of this case in Sec. 3.4.2.

3.2.1 The Lax pair

We consider in this section the focusing NLSE:

$$\mathrm{i}u_t + u_{xx} + 2|u|^2 u = 0\,. \tag{3.11}$$

This equation has a well-defined solution when an initial condition, $u(x,0)$, is given. We consider the problem on the infinite line, meaning $x \in \mathbb{R}$. The method introduced by Lax involves finding two operators $(\hat{L}, \hat{A})$, that depend on u and its spatial derivative, but not its temporal derivative; and $(\hat{L}, \hat{A})$ satisfy:

$$u(x,t) \text{ solution of Eq. (3.11)} \iff \frac{\mathrm{d}\hat{L}}{\mathrm{d}t} = \left[\hat{A}, \hat{L}\right]\,, \tag{3.12}$$

where $[\cdot,\cdot]$ is the commutator between two operators. There is no uniqueness of the $(\hat{L},\hat{A})$ pair, one possible choice is [189]:

$$\hat{L} = \mathrm{i}\begin{pmatrix} \partial_x & u \\ u^* & -\partial_x \end{pmatrix} \quad \text{and} \quad \hat{A} = \mathrm{i}\begin{pmatrix} 2\partial_x^2 + |u|^2 & u_x + 2u\partial_x \\ u^* + 2u^*\partial_x & -2\partial_x^2 - |u|^2 \end{pmatrix}, \tag{3.13}$$

where $\cdot^*$ means complex conjugation. One can immediately verify that this choice satisfies the equivalence Eq. (3.12). There is no straightforward method for forming the operators $(\hat{L},\hat{A})$ for a given equation. As indicated by [46], determining them often relies on educated guesses. In our case, the operators $(\hat{L},\hat{A})$ act on the space of two-component spinors:

$$\Phi(x,t) = \begin{pmatrix} \phi_a(x,t) \\ \phi_b(x,t) \end{pmatrix} \quad \text{with} \quad \phi_{a,b}(x,t) \in \mathbb{C}\,. \tag{3.14}$$

This is not a general feature of the IST: for the KdV equation for instance, $\hat{L}$ is the one-dimensional Schrödinger operator. In the following, the subscripts a,b will denote the components of the spinors. The goal is now to "replace" the nonlinear evolution of u by the evolution of Φ, which is governed by linear operators.

3.2.2 The scattering data

The first step of the IST method consists of solving the so-called Zakharov-Shabat eigenvalue problem:

$$\hat{L}\Phi = \lambda\Phi \quad \text{that is} \quad \begin{cases} \mathrm{i}\partial_x\phi_a + \mathrm{i}u\phi_b &= \lambda\phi_a\,, \\ -\mathrm{i}\partial_x\phi_b + \mathrm{i}u^*\phi_a &= \lambda\phi_b\,. \end{cases} \tag{3.15}$$

We begin solving this system by detailing a few key properties:

- Since $\hat{L}$ is not hermitian, the spectrum λ can be complex. In the following, we will write $\lambda = \xi + \mathrm{i}\eta$, with $\xi,\eta \in \mathbb{R}$.
- The time variable t is a dummy variable in this equation, and will be omitted.
- The function u, although it is complex-valued, now plays the role of a localized potential. Anticipating on what follows, we can already guess that this will lead to both localized and radiative eigenstates, similarly to the linear Schrödinger equation. This analogy is most easily seen by taking $\lambda = 0$, which leads to $\partial_x^2\phi_{a,b} = -|u|^2\phi_{a,b}$.
- An important symmetry of the system of Eq. (3.15) is the following:

$$\left(\Phi = \begin{bmatrix} \phi_a \\ \phi_b \end{bmatrix}, \lambda\right) \text{ solution} \iff \left(\bar{\Phi} = \begin{bmatrix} \phi_b^* \\ -\phi_a^* \end{bmatrix}, \lambda^*\right) \text{ solution}\,. \tag{3.16}$$

  This involution property, noted $\bar{\cdot}$, informs us that the spectrum of λ is symmetric with respect to the real axis.

- If U, V are two solutions of Eq. (3.15), then:

$$\frac{\mathrm{d}}{\mathrm{d}x}\left(U_aV_b - U_bV_a\right) = \frac{\mathrm{d}}{\mathrm{d}x}W(U,V) = 0\,, \tag{3.17}$$

  with W the Wronskian.

- Since $u(x) \to 0$ when $|x| \to \infty$, the system of Eq. (3.15) can be rewritten in this limit:
$$\partial_x \phi_a = -\mathrm{i}\lambda\phi_a \quad \text{and} \quad \partial_x \phi_b = \mathrm{i}\lambda\phi_b\,, \tag{3.18}$$
whose solutions are:
$$\phi_a \propto \mathrm{e}^{-\mathrm{i}\lambda x} \quad \text{and} \quad \phi_b \propto \mathrm{e}^{\mathrm{i}\lambda x}\,. \tag{3.19}$$

Jost functions and analytic properties

We focus first on the case $\lambda = \xi \in \mathbb{R}$, meaning $\eta = 0$. With this restriction, we are guaranteed to avoid any divergence from Eq. (3.19). We define the so-called Jost functions Φ, Ψ [44, 216] which are solutions of Eq. (3.15). We take the following boundary conditions, which are natural given Eq. (3.19):

$$\Phi(x,\xi) \sim \begin{pmatrix}1\\0\end{pmatrix} \mathrm{e}^{-\mathrm{i}\xi x} \quad \text{as} \quad x \to -\infty\,, \tag{3.20a}$$
$$\Psi(x,\xi) \sim \begin{pmatrix}0\\1\end{pmatrix} \mathrm{e}^{+\mathrm{i}\xi x} \quad \text{as} \quad x \to +\infty\,. \tag{3.20b}$$

Following Eq. (3.16), we also define $\bar{\Phi}, \bar{\Psi}$. Thus, $\Phi, \bar{\Phi}, \Psi, \bar{\Psi}$ are all eigenfunctions of Eq. (3.15) for the eigenvalue ξ. Not all of them are linearly independent: only the pairs $(\Phi, \bar{\Phi})$ and $(\Psi, \bar{\Psi})$ are. Hence, there exists coefficients such that:

$$\begin{cases} \Phi(x,\xi) = a(\xi)\bar{\Psi} + b(\xi)\Psi \\ \bar{\Phi}(x,\xi) = \bar{b}(\xi)\bar{\Psi} - \bar{a}(\xi)\Psi \end{cases} \quad \text{i.e.} \quad (\Phi, \bar{\Phi}) = (\bar{\Psi}, \Psi)S\,, \tag{3.21}$$

where we introduced the scattering matrix:

$$S(\xi) = \begin{pmatrix} a & \bar{b} \\ b & -\bar{a} \end{pmatrix}. \tag{3.22}$$

It contains the scattering coefficients $a(\xi), b(\xi)$ which carry the information of the direct scattering process. This relation allows us to connect the limits of $x \to -\infty$ (boundary condition for Φ and $\bar{\Phi}$) and $x \to +\infty$ (boundary condition for Ψ and $\bar{\Psi}$). For instance, we can write:

$$x \to -\infty: \quad \Phi(x,\xi) \sim \begin{pmatrix}1\\0\end{pmatrix} \mathrm{e}^{-\mathrm{i}\xi x}\,, \tag{3.23a}$$
$$x \to +\infty: \quad \Phi(x,\xi) \sim a(\xi)\begin{pmatrix}1\\0\end{pmatrix} \mathrm{e}^{-\mathrm{i}\xi x} + b(\xi)\begin{pmatrix}0\\1\end{pmatrix} \mathrm{e}^{+\mathrm{i}\xi x}\,. \tag{3.23b}$$

The physical interpretation is straightforward: the solution Φ corresponds to a plane wave of amplitude $|a(\xi)|$ coming from $x \to +\infty$. It is partially reflected on the potential $u(x)$ with an amplitude $|b(\xi)|$, and partially transmitted (with a coefficient of transmission normalized to unity). We note that $|a(\xi)|^2 + |b(\xi)|^2 = 1$,[2] following from the facts that $\det(S) = -a\bar{a} - b\bar{b} = -1$ and $\bar{a}(\xi) = a^*(\xi)$, $\bar{b}(\xi) = b^*(\xi)$.

Hence, $\xi \in \mathbb{R}$ is an eigenvalue of Eq. (3.15), and we have constructed a basis of eigenfunctions, Φ and $\bar{\Phi}$. An example of numerical resolution of Eq. (3.15) is presented in

[2] Dividing this equation by $|a|^2$, we obtain $1 = 1/|a|^2 - |b/a|^2$, which differs from the usual expression for reflection and transmission coefficients in Hermitian scattering problems. This difference arises because the Lax operator $\hat{L}$ is non-Hermitian, and the system exhibits different conserved quantities. In the defocusing case, however, $\hat{L}$ becomes hermitian and the sign changes, yielding: $1 = 1/|a|^2 + |b/a|^2$, as expected.

Fig. 3.6, and illustrates the scattering problem. We highlight once more that the complete knowledge of the eigenfunctions is not necessary for the IST method, and only the scattering coefficients $a(\xi), b(\xi)$ are needed.

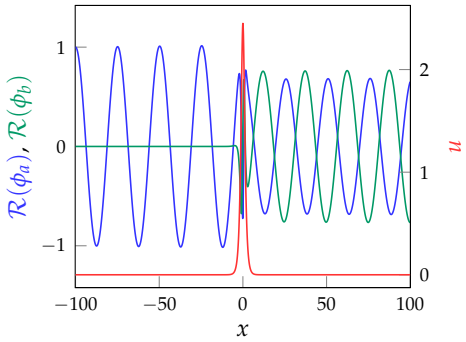

Figure 3.6: Illustration of a numerical resolution of Eq. (3.15), taking $u(x) = 2.45/\cosh x$ and $\xi = -0.25$. We only show the real part of $\Phi = \begin{pmatrix}\phi_a & \phi_b\end{pmatrix}^\mathsf{T}$ for clarity. We recover the limits given in Eq. (3.23a) and (3.23b). The coefficients $|a(\xi)|$ and $|b(\xi)|$ can be directly read off from the amplitudes of the traveling waves when $x \to +\infty$. The behavior of the eigenfunction around $x \simeq 0$ is complex and not relevant for the present discussion.

The next step is to extend the definition of the Jost functions to (parts of) the complex plane, meaning $\eta \neq 0$ (we recall that $\lambda = \xi + i\eta$). One approach to solving this problem is to rewrite Eq. (3.15) in an integral form. More precisely, we can view these equations as a first-order differential equation where the terms in u act as source terms. Then, it is possible to formally integrate them using the method of variation of parameters. Extending the boundary conditions defined in Eq. (3.20), we obtain so-called Volterra integral equations:

$$\Phi = \begin{pmatrix}\phi_a \\ \phi_b\end{pmatrix} = \begin{pmatrix}e^{-i\lambda x} \\ 0\end{pmatrix} + \int_{-\infty}^{x} \begin{pmatrix}-u(y)e^{i\lambda(y-x)}\phi_b \\ u^*(y)e^{i\lambda(x-y)}\phi_a\end{pmatrix} dy \,, \tag{3.24a}$$

$$\Psi = \begin{pmatrix}\psi_a \\ \psi_b\end{pmatrix} = \begin{pmatrix}0 \\ e^{i\lambda x}\end{pmatrix} - \int_{x}^{+\infty} \begin{pmatrix}-u(y)e^{i\lambda(y-x)}\psi_b \\ u^*(y)e^{i\lambda(x-y)}\psi_a\end{pmatrix} dy \,. \tag{3.24b}$$

We introduce the auxiliary functions $\tilde{\phi}_{a,b} = \phi_{a,b}e^{i\lambda x}$ and $\tilde{\psi}_{a,b} = \psi_{a,b}e^{-i\lambda x}$ such that:

$$\tilde{\Phi} = \begin{pmatrix}\tilde{\phi}_a \\ \tilde{\phi}_b\end{pmatrix} = \begin{pmatrix}1 \\ 0\end{pmatrix} + \int_{-\infty}^{x} \begin{pmatrix}-u(y)\tilde{\phi}_b \\ u^*(y)e^{2i\lambda(x-y)}\tilde{\phi}_a\end{pmatrix} dy \,, \tag{3.25a}$$

$$\tilde{\Psi} = \begin{pmatrix}\tilde{\psi}_a \\ \tilde{\psi}_b\end{pmatrix} = \begin{pmatrix}0 \\ 1\end{pmatrix} - \int_{x}^{+\infty} \begin{pmatrix}-u(y)e^{2i\lambda(y-x)}\tilde{\psi}_b \\ u^*(y)\tilde{\psi}_a\end{pmatrix} dy \,. \tag{3.25b}$$

It is clear that for $\lambda \in \mathbb{C}^+$ the integrals on the right-hand-side converge. Indeed, the exponential coefficients are bounded, and u decays sufficiently fast such that $u \in L^1(\mathbb{R})$. In [216] the authors add that the condition $\forall n \in \mathbb{N}, \int_{-\infty}^{\infty} |x|^n |u(x)|\, dx < \infty$ is necessary to extend the analyticity to the real axis. Thus, $\tilde{\Phi}$ and $\tilde{\Psi}$ can be analytically continued to the upper half of the complex plane. A similar reasoning can be followed for $\bar{\Phi}$ and $\bar{\Psi}$, meaning that $\bar{\Phi}e^{-i\lambda x}$ and $\bar{\Psi}e^{i\lambda x}$ are analytic in the lower half of the complex plane. This last property is quite natural given Eq. (3.16).

The scattering coefficient a can be naturally extended to $\lambda \in \mathbb{C}^+$. Indeed, using Eq. (3.21) and the fact that $W(\Psi, \bar{\Psi}) = -1$:

$$a(\lambda) = W(\Phi, \Psi) = \phi_a \psi_b - \psi_a \phi_b = W(\tilde{\Phi}, \tilde{\Psi}) \,. \tag{3.26}$$

Similarly, $\bar{a}(\lambda) = W(\bar{\Phi}, \bar{\Psi})$ is analytic for $\lambda \in \mathbb{C}^-$. However, b and $\bar{b}$ have no general analytic continuation, unless some more stringent constraints are applied to u.

It is important to emphasize that even though for any λ their exists a corresponding Φ to satisfy the Zakharov-Shabat eigenvalue problem Eq. (3.15), we do not have in general $\Phi \in L^2(\mathbb{R})$, due to an exponential blow-up in $x \to +\infty$. The same remark applies to $(\bar{\Phi}, \lambda)$.

Taking a look back at Eq. (3.26), we notice that under the condition $a(\lambda) = 0$, the Wronskian $W(\Phi, \Psi) = 0$. It means that Φ and Ψ are linearly dependent:

$$a(\lambda_k) = 0 \Rightarrow \Phi(x, \lambda_k) = c_k \Psi(x, \lambda_k) \,, \tag{3.27}$$

where we noted λ_k the zeroes of $a(\lambda)$, $k = 1, 2, ...N$. We have $\lambda_k \in \mathbb{C}^+$, since it is the domain of definition of $a(\lambda)$. There is only a finite number of zeroes, and they lie within a bounded region [216]. Following this relation, we obtain the boundary conditions for Φ:

$$x \to -\infty : \quad \Phi(x, \lambda_k) \sim \begin{pmatrix} 1 \\ 0 \end{pmatrix} \mathrm{e}^{-\mathrm{i}\lambda_k x} = \begin{pmatrix} 1 \\ 0 \end{pmatrix} \mathrm{e}^{\eta_k x} \mathrm{e}^{-\mathrm{i}\xi_k x} \,, \tag{3.28a}$$

$$x \to +\infty : \quad \Phi(x, \lambda_k) \sim c_k \begin{pmatrix} 0 \\ 1 \end{pmatrix} \mathrm{e}^{\mathrm{i}\lambda_k x} = c_k \begin{pmatrix} 0 \\ 1 \end{pmatrix} \mathrm{e}^{-\eta_k x} \mathrm{e}^{\mathrm{i}\xi_k x} \,, \tag{3.28b}$$

where we have written $\lambda_k = \xi_k + \mathrm{i}\eta_k$ and $\eta_k > 0$. A numerical example is shown in Fig. 3.7, where we observe that for these eigenvalues $\Phi \in L^2(\mathbb{R})$, due to the boundary conditions of Eq. (3.28). Similar reasoning with $\bar{a}(\lambda)$ in the lower half of the complex plane leads to analogous results concerning $\bar{\Phi}$. The eigenvalues $\bar{\lambda}_k = \lambda_k^*$ owing from the property $\bar{a}(\lambda) = a^*(\lambda^*)$. This symmetry comes from Eq. (3.16).

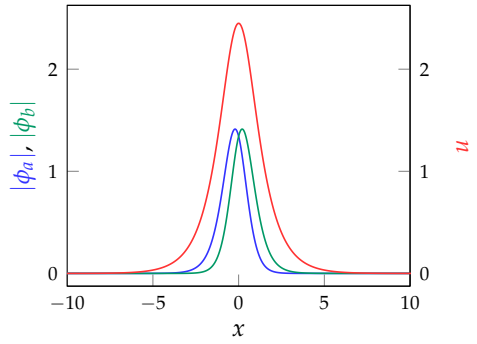

Figure 3.7: Illustration of a numerical resolution of Eq. (3.15), taking $u(x) = 2.45/\cosh x$ and $\lambda_1 = 1.95\mathrm{i}$. We only show the absolute value of $\Phi = \begin{pmatrix} \phi_a & \phi_b \end{pmatrix}^\mathsf{T}$ for clarity. We recover the limits given in Eq. (3.28a) and (3.28b), meaning an exponential decay for both $x \to \pm\infty$: Φ is a localized eigenstate in the potential u. We have $c_1 = 1$, which explains the symmetry between ϕ_a and ϕ_b.

We have now explored all solutions of the Zakharov-Shabat system, Eq. (3.15). In addition to $\lambda \in \mathbb{R}$, this system can also host physically relevant solutions for which $\lambda \in \mathbb{C} \setminus \mathbb{R}$, at the condition that $a(\lambda) = 0$.

Summary of the scattering data

We have distinguished two cases when solving Eq. (3.15):

- $\lambda \in \mathbb{R}$ led to the scattering data $a(\lambda), b(\lambda)$ which represent the transmission and reflection coefficients of a plane wave on the potential u.
- $\lambda_k \in \mathbb{C} \setminus \mathbb{R}$ correspond to localized states in the potential u. The associated scattering data are the coefficients c_k.

One may wonder what information this scattering data conveys. One way to answer this question is to see that the scattering data tends toward the usual FT when the nonlinearity disappears. Indeed, in the limit when $u(x)$ becomes infinitesimally small, $b(\lambda) = \mathcal{FT}(u^*)(2\lambda)$ [see 45, Eq. (4.19a)]. Of course, this picture is valid when no soliton is present in the wavepacket, as will be discussed in Sec. 3.2.5.

3.2.3 Time evolution of the scattering data

Throughout the previous section we have omitted the time dependence of all functions. In order to pursue the IST scheme sketched in Fig. 3.5b, we now reintroduce the time variable and figure out the time evolution of the scattering data. The operators $\hat{L}, \hat{A}$ implicitly depend on time through the function $u(x,t)$. Their time evolution is captured by Eq. (3.12). Before using this relation, we define the evolution operator $\hat{\mathcal{U}}(t)$:

$$\frac{\mathrm{d}\hat{\mathcal{U}}}{\mathrm{d}t} = \hat{A}(t)\hat{\mathcal{U}}(t) \quad \text{and} \quad \frac{\mathrm{d}\hat{\mathcal{U}}^{-1}}{\mathrm{d}t} = -\hat{\mathcal{U}}(t)^{-1}\hat{A}(t)\,, \tag{3.29}$$

where $\hat{\mathcal{U}}(0) = \mathbb{1}$, and the second equation can be deduced from the first one using $\frac{\mathrm{d}}{\mathrm{d}t}\left(\hat{\mathcal{U}}\hat{\mathcal{U}}^{-1}\right) = 0$. We observe that $\hat{\mathcal{U}}^{-1}$ differs from the adjoint of $\hat{\mathcal{U}}$ because $\hat{A}$ is not a Hermitian operator. Multiplying by $\hat{\mathcal{U}}^{-1}$ and $\hat{\mathcal{U}}$ on each side of Eq. (3.12), we derive:

$$\frac{\mathrm{d}}{\mathrm{d}t}\left[\hat{\mathcal{U}}^{-1}(t)\hat{L}(t)\hat{\mathcal{U}}(t)\right] = 0 \quad \text{i.e.} \quad \hat{L}(t)\hat{\mathcal{U}}(t) = \hat{\mathcal{U}}(t)\hat{L}(0)\,. \tag{3.30}$$

Taking an eigenvector $\Theta(0)$ of the operator $\hat{L}(0)$ associated with the eigenvalue $\lambda(0) \in \mathbb{C}^+$, we see that:

$$\hat{L}(t)\underbrace{\left[\hat{\mathcal{U}}(t)\Theta(0)\right]}_{\Theta(t)} = \lambda(0)\underbrace{\left[\hat{\mathcal{U}}(t)\Theta(0)\right]}_{\Theta(t)}\,. \tag{3.31}$$

We deduce that $\lambda(0)$ is still an eigenvalue of the operator $\hat{L}(t)$, with the eigenvector $\Theta(t)$. Using Eq. (3.29), we see its evolution is governed by:

$$\frac{\mathrm{d}\Theta}{\mathrm{d}t} = \hat{A}(t)\Theta(t)\,. \tag{3.32}$$

Once again, only the behavior of the scattering data is of interest to us, and we will solve this equation when $x \to \pm\infty$. In this limit, we can simplify $\hat{A}$:

$$\hat{A} = -2\mathrm{i}\begin{pmatrix}1 & 0\\ 0 & -1\end{pmatrix}\hat{L}^2\,. \tag{3.33}$$

Since $\Theta(t)$ is an eigenvector of $\hat{L}(t)$, Eq. (3.32) becomes:

$$\frac{\mathrm{d}\Theta}{\mathrm{d}t} = -2\mathrm{i}\lambda^2\underbrace{\begin{pmatrix}1 & 0\\ 0 & -1\end{pmatrix}}_{\sigma}\Theta(t) \quad \text{i.e.} \quad \Theta(x\to\pm\infty, t) = \mathrm{e}^{-2\mathrm{i}\lambda^2\sigma t}\,\Theta(x\to\pm\infty, 0)\,. \tag{3.34}$$

However, Θ does not satisfy the boundary conditions defined in Eq. (3.20). It is necessary to add a global phase factor to the eigenvector in order to recover these conditions [see 216, Eq. (1.4.1)]. Hence, we multiply the result of Eq. (3.34) by $e^{2i\lambda^2 t}$ for Φ and by $e^{-2i\lambda^2 t}$ for Ψ. Finally:

$$\Phi(t) = \begin{pmatrix} \phi_a(t) \\ \phi_b(t) \end{pmatrix} = \begin{pmatrix} \phi_a(0) \\ e^{4i\lambda^2 t}\phi_b(0) \end{pmatrix}, \tag{3.35a}$$

$$\Psi(t) = \begin{pmatrix} \psi_a(t) \\ \psi_b(t) \end{pmatrix} = \begin{pmatrix} e^{-4i\lambda^2 t}\psi_a(0) \\ \psi_b(0) \end{pmatrix}. \tag{3.35b}$$

Using these expressions, it is now straightforward to establish the time-dependence of the scattering data. We first recall that $a(\lambda) = W(\Phi, \Psi) = \phi_a\psi_b - \phi_b\psi_a$. It follows that:

$$a(\lambda, t) = a(\lambda, 0) \quad \text{thus} \quad \lambda_k(t) = \lambda_k(0)\,, \tag{3.36}$$

where the second equation is immediately deduced from the fact that the zeros of $a(\lambda)$ do not evolve with time, and confirms Eq. (3.31). Similarly, $b(\xi, t) = -W(\Phi, \bar{\Psi})$ (for $\xi \in \mathbb{R}$) and:

$$b(\xi, t) = b(\xi, 0)e^{4i\xi^2 t} \tag{3.37}$$

Then, using Eq. (3.27):

$$c_k(t) = c_k(0)e^{4i\lambda_k^2 t} \tag{3.38}$$

The set of Eq. (3.36), (3.37), (3.38) gives us the time evolution of the scattering data and completes the second step of the IST scheme.

3.2.4 Solving the equation

Position of the problem

The third step of the IST method consists of retrieving the potential, meaning $u(x)$, from a given set of scattering data $\{a(\xi), b(\xi), \lambda_k, c_k\}$. In this section, the time variable t plays no role and is therefore omitted from the equations. All functions should be understood as having an implicit time dependence.

We impose the condition that $u(x)$ decays faster than any exponential. It leads to $a(\lambda), b(\lambda), \bar{a}(\lambda), \bar{b}(\lambda)$ being analytic in the entire complex plane. This hypothesis leads to an easier derivation of the result, even though the main result holds under less stringent constraints [45, 216]. We begin by writing the eigenfunctions Ψ and $\bar{\Psi}$ in the following way:

$$\Psi(x, \lambda) = \begin{pmatrix} 0 \\ e^{i\lambda x} \end{pmatrix} + \int_x^\infty K(x, s)e^{i\lambda s}\, ds\,, \tag{3.39a}$$

$$\bar{\Psi}(x, \lambda) = \begin{pmatrix} e^{-i\lambda x} \\ 0 \end{pmatrix} + \int_x^\infty \bar{K}(x, s)e^{-i\lambda s}\, ds\,. \tag{3.39b}$$

These equations resemble the Volterra Eq. (3.24), with the major difference that $K, \bar{K}$ *do not* depend on λ. We write $K = \begin{pmatrix} K_1 & K_2 \end{pmatrix}^\mathsf{T}$ and $\bar{K} = \begin{pmatrix} K_2^* & -K_1^* \end{pmatrix}^\mathsf{T}$. The proof that these quantities exist and are unique is given in [45, 216], and will not be detailed here.

The crucial point is the relation between K and the potential u. It can be obtained by performing developments of Eq. (3.39) and (3.24) in the limit of $|\lambda| \to \infty$. Developing

Eq. (3.39), we can write:

$$\psi_a(x,\lambda)\mathrm{e}^{-\mathrm{i}\lambda x} = \int_x^\infty K_1(x,s)\mathrm{e}^{\mathrm{i}\lambda(s-x)}\,\mathrm{d}s \tag{3.40a}$$

$$= \left[\frac{K_1(x,s)}{\mathrm{i}\lambda}\mathrm{e}^{\mathrm{i}\lambda(s-x)}\right]_x^\infty - \int_x^\infty \frac{1}{\mathrm{i}\lambda}\frac{\partial K_1}{\partial s}(x,s)\mathrm{e}^{\mathrm{i}\lambda(s-x)}\,\mathrm{d}s \tag{3.40b}$$

$$= -\frac{1}{\mathrm{i}\lambda}K_1(x,x) + \mathcal{O}\left(\frac{1}{\lambda^2}\right), \tag{3.40c}$$

where we performed successive integration by parts. Doing a similar calculation for Eq. (3.24) yields:

$$\psi_a(x,\lambda)\mathrm{e}^{-\mathrm{i}\lambda x} = -\frac{1}{2\mathrm{i}\lambda}u(x) + \mathcal{O}\left(\frac{1}{\lambda^2}\right). \tag{3.41}$$

We immediately deduce that $u(x) = 2K_1(x,x)$.[3] Thus, our goal in retrieving the potential from the scattering data is to have an equation for solving for K.

Solving for K

We can substitute Eq. (3.39) in Eq. (3.21) (extended to the complex plane) to obtain:

$$\frac{\Phi(x,\lambda)}{a(\lambda)} = \underbrace{\begin{pmatrix}\mathrm{e}^{-\mathrm{i}\lambda x}\\0\end{pmatrix} + \int_x^\infty \bar{K}(x,s)\mathrm{e}^{-\mathrm{i}\lambda s}\,\mathrm{d}s}_{\bar{\Psi}(x,\lambda)} + \frac{b(\lambda)}{a(\lambda)}\Bigg[\underbrace{\begin{pmatrix}0\\\mathrm{e}^{\mathrm{i}\lambda x}\end{pmatrix} + \int_x^\infty K(x,s)\mathrm{e}^{\mathrm{i}\lambda s}\,\mathrm{d}s}_{\Psi(x,\lambda)}\Bigg]. \tag{3.42}$$

Now, we consider a contour C in the complex plane ranging from $-\infty + \mathrm{i}0^+$ to $\infty + \mathrm{i}0^+$, which is above all the zeros of $a(\lambda)$, meaning it is above all λ_k. We perform an integration over this contour, $\frac{1}{2\pi}\int_C \mathrm{e}^{\mathrm{i}\lambda y}\,\mathrm{d}\lambda$ (for $y > x$), on both sides of the equation:

$$0 = \bar{K}(x,y) + \begin{pmatrix}0\\1\end{pmatrix}F(x+y) + \int_x^\infty K(x,s)F(s+y)\,\mathrm{d}s\,, \tag{3.43}$$

where the integral on the left-hand-side vanishes and we have used the Dirac distribution $\delta(x) = \frac{1}{2\pi}\int_C \mathrm{e}^{\mathrm{i}\lambda x}\,\mathrm{d}\lambda$. We have defined:

$$F(x) = \frac{1}{2\pi}\int_C \frac{b(\lambda)}{a(\lambda)}\mathrm{e}^{\mathrm{i}\lambda x}\,\mathrm{d}\lambda \tag{3.44a}$$

$$= \frac{1}{2\pi}\int_{-\infty}^\infty \frac{b(\xi)}{a(\xi)}\mathrm{e}^{\mathrm{i}\xi x}\,\mathrm{d}\xi - \mathrm{i}\sum_{k=1}^N \tilde{c}_k\mathrm{e}^{\mathrm{i}\lambda_k x}\,, \tag{3.44b}$$

where the second line corresponds to the case where the zeros of $a(\lambda)$ are simple and we have performed a sum on the residues, with $\tilde{c}_k = c_k/a'(\lambda_k)$. We have used $a'(\lambda_k)$, the derivative of $a(\lambda)$, evaluated at λ_k. Eq. (3.43) is called the Gelfand-Levitan-Marchenko integral equation, and although solving it may be difficult, it remains *linear*.

In the particular case of $b(\xi) = 0$, meaning a potential u containing only solitons, as discussed below, we can explicitly write a formula for $a(\lambda)$ [44]:

$$a(\lambda) = \prod_{i=1}^N \frac{\lambda - \lambda_i}{\lambda - \lambda_i^*}\,. \tag{3.45}$$

[3] Note the absence of a minus sign compared to e.g. [216]. This comes from our difference in the choice of $\hat{L}$. One can recover the conventions from [216] by substituting $u \to -u$ in all equations above.

It is obtained by noting that $|a(\lambda)| \to 1$ over the whole boundary of $\mathbb{C}^+$. This equation allows in particular the direct computation of $a'(\lambda_k)$.

The Eq. (3.43) completes the IST procedure:

- The scattering data is obtained by looking at the behavior at $|x| \to \infty$ of the eigenfunctions of the Lax operator $\hat{L}$.
- The time evolution of the scattering data is trivial, and in particular $\partial_t \lambda_k = 0$.
- Inverting the scattering data to recover $u(x,t)$ involves solving the Gelfand-Levitan-Marchenko Eq. (3.43).

3.2.5 Solitons as building blocks of any wavefunction

One of the interests of the IST procedure is the insights provided by the scattering data. In particular, we observe that for certain potentials u the reflection coefficient $b(\xi)$ vanishes identically [73]. This case in fact corresponds to a wavefunction only containing solitons. We can look at the example of the bright soliton in order to build a better intuition [see 189, for additional details on the phase and position of a soliton]. A soliton of amplitude κ and velocity $v = 2k$ is given by:

$$u(x,t) = \frac{\kappa e^{ikx}}{\cosh[\kappa(x-2kt)]} e^{i(\kappa^2-k^2)t}. \tag{3.46}$$

The scattering data of such an object is fairly simple: $b(\xi) = 0$, $\lambda_1 = -\frac{k}{2} + \frac{i\kappa}{2}$, $c_1(0) = 1$. We can immediately infer several properties:

- The real part of the eigenvalue λ_k corresponds to the velocity of the associated wavepacket.
- The imaginary part of the eigenvalue λ_k corresponds to the amplitude of the associated wavepacket.
- Since $\partial_t \lambda_k = 0$, the velocity and amplitude of the wavepacket are conserved through time.

We thus call *soliton* the wavepacket connected to a given λ_k, and one can view solitons as a "nonlinear basis" of wavefunctions. The invariance of λ_k immediately explains the conservation properties of solitons, in particular the elastic collisions: they should emerge from a collision with the same velocity and amplitude with which they entered. This point is illustrated in Fig. 3.8 with a numerical example of two solitons colliding. The IST also allows for the calculation of the phase and position shifts of solitons after a collision (which can be seen in Fig. 3.8a) [44].

One may then ask about the physical meaning of $b(\xi) \neq 0$. For example, if a spectrum has one λ_k, then the initial wavefunction is not precisely described by Eq. (3.46), but rather contains additional atoms that distort it. However, these atoms will spread over time, because each has a velocity given by ξ. At $t \to \infty$ we obtain a wavepacket which is now well described by Eq. (3.46), and radiated atoms that spread over the entire x axis. Another way to phrase this is to say that forming a soliton is the only way to have a localized macroscopic number of atoms moving at the same velocity. This explains why solitons are relatively easy to create: it is not necessary to be very precise when imprinting the wavefunction because it will evolve towards to the desired solution by radiating "unwanted" atoms.

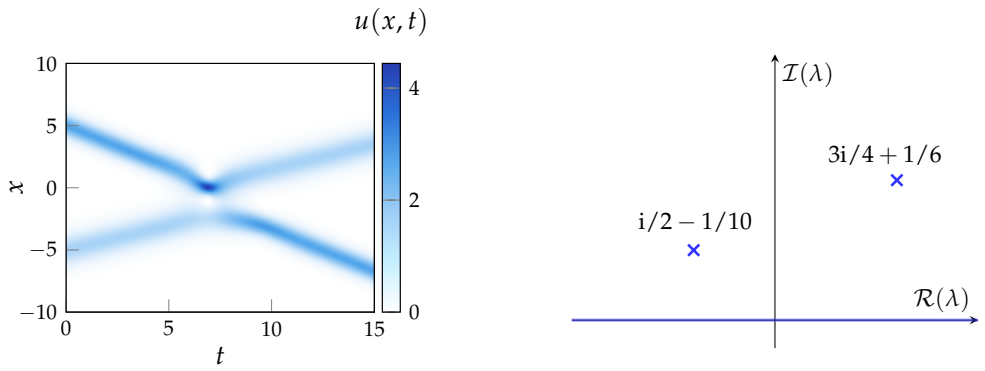

(a) Numerical simulation **(b)** Scattering data

Figure 3.8: (a) We perform a numerical integration of NLSE with the initial wavefunction $u(x,0) = \frac{1}{\cosh(x+5)} e^{ix/5} + \frac{1.5}{\cosh(1.5(x-5))} e^{-ix/3}$. Since the two solitons are far apart at $t = 0$, this is a good approximation of the exact two-soliton wavefunction. They collide at $t \simeq 7$, and emerge from the collision with identical velocities and amplitudes. **(b)** Eigenvalues of the wavefunction $u(x,t)$. These values are constant in time. We have highlighted the real axis to remind that $\lambda \in \mathbb{R}$ is always a solution of the eigenvalue problem. However, since $b(\lambda) = 0$ here, it carries no weight. $\mathcal{R}$ and $\mathcal{I}$ indicate the real and imaginary parts respectively.

3.2.6 Numerical implementation of the IST

In some rare cases, it is possible to solve the eigenvalue problem Eq. (3.15) exactly. We can mention the potential $u(x) = A/\cosh(x)$ explored by [73], or the "box" case of $u(x) = A$ for $x \in [0,1]$ and $u(x) = 0$ elsewhere [see e.g. 217, section 2.4.1]. However, most cases can only be treated numerically. We will detail in this section some numerical methods in order to perform the IST [see 218, 219, for recent reviews].

Collocation method

A natural way to solve Eq. (3.15) would be to discretize all functions on a given spatial grid of length L by replacing ∂_x with a central finite-difference between adjacent grid points. The eigenvalues are then obtained by diagonalizing a matrix of size $2N$, with N the number of points of the grid. However, this method converges slowly, and can be improved by formulating the problem in Fourier space [217, Sec. 2.4.3]. The idea is to take the FT of the Zakharov-Shabat system, Eq. (3.15), then expand the different functions in Fourier series:

$$u(x,0) = \sum_{n=-N}^{N} u_n e^{ink_0 x} \quad \text{where} \quad k_0 = \frac{2\pi}{L}. \tag{3.47}$$

Writing similarly $\varphi_{a,n}$ and $\varphi_{b,n}$ the Fourier coefficients of ϕ_a and ϕ_b respectively, we obtain [217, Eq. (2.180)]:

$$\mathrm{i}\begin{pmatrix} \mathrm{i}k_0 \begin{bmatrix} -N & 0 & \dots \\ 0 & -N+1 & \\ \vdots & & \ddots \end{bmatrix} & \begin{bmatrix} u_0 & u_{-1} & u_{-2} & \dots \\ u_1 & u_0 & u_{-1} & \dots \\ \vdots & & \ddots & \end{bmatrix} \\ {\scriptstyle\dagger} \begin{bmatrix} u_0 & u_{-1} & u_{-2} & \dots \\ u_1 & u_0 & u_{-1} & \dots \\ \vdots & & \ddots & \end{bmatrix} & -\mathrm{i}k_0 \begin{bmatrix} -N & 0 & \dots \\ 0 & -N+1 & \\ \vdots & & \ddots \end{bmatrix} \end{pmatrix} \begin{pmatrix} \varphi_{a,-N} \\ \vdots \\ \varphi_{a,N} \\ \varphi_{b,-N} \\ \vdots \\ \varphi_{b,N} \end{pmatrix} = \lambda \begin{pmatrix} \varphi_{a,-N} \\ \vdots \\ \varphi_{a,N} \\ \varphi_{b,-N} \\ \vdots \\ \varphi_{b,N} \end{pmatrix} \tag{3.48}$$

where $\cdot^\dagger$ means Hermitian conjugation. The left-hand-side matrix has a size $2(2N+1)$, and its blocks naturally correspond to the differentiation, in Fourier space, and to the convolution by $u(x)$. One can then find its eigenvalues and eigenvectors to solve Eq. (3.15). However, this method does not yield the norming constants $\tilde{c}_k$ of solitons and is inefficient to compute the scattering data for $\lambda \in \mathbb{R}$ [219].

Transfer method

Another method introduced by [220] allows the complete retrieval of the scattering data. We first rewrite Eq. (3.15) as a first-order differential equation for a given λ:

$$\partial_x \Phi = \underbrace{\begin{pmatrix} -\mathrm{i}\lambda & -u(x) \\ u(x)^* & \mathrm{i}\lambda \end{pmatrix}}_{Q(u(x),\lambda)} \Phi \tag{3.49}$$

Then, discretizing this equation on a spatial grid for $x \in [-L, L]$ with $2N+1$ intervals of width δx, we have with a direct integration:

$$\Phi(x_n + \delta x) = \underbrace{\exp[\delta x Q(u_n, \lambda)]}_{V(u_n)} \Phi(x_n)\,. \tag{3.50}$$

Then, the authors of [220] write a more general scattering matrix S taking into account both Φ and $\partial_\lambda \Phi$:

$$\begin{pmatrix} \Phi(L) \\ \partial_\lambda \Phi(L) \end{pmatrix} = \underbrace{\begin{pmatrix} \Sigma(\lambda) & 0 \\ \partial_\lambda \Sigma(\lambda) & \Sigma(\lambda) \end{pmatrix}}_{S(\lambda)} \begin{pmatrix} \Phi(-L) \\ \partial_\lambda \Phi(-L) \end{pmatrix} \quad \text{with} \quad \Sigma(\lambda) = \prod_{j=N-1}^{-N} V(u_j)\,. \tag{3.51}$$

We recognize the previously introduced scattering matrix of Eq. (3.21) as $\Sigma(\lambda)$. Using the known boundary condition:

$$\Phi(-L) = \begin{pmatrix} \mathrm{e}^{\mathrm{i}\lambda L} \\ 0 \end{pmatrix} \quad \text{and} \quad \Phi(L) = a(\lambda) \begin{pmatrix} \mathrm{e}^{-\mathrm{i}\lambda L} \\ 0 \end{pmatrix} + b(\lambda) \begin{pmatrix} 0 \\ \mathrm{e}^{\mathrm{i}\lambda L} \end{pmatrix}, \tag{3.52}$$

we recover all the scattering data. One drawback of this method is that it only evaluates the scattering data for the user-chosen value of λ. Hence, finding the roots of $a(\lambda)$, meaning the λ_k, relies on a minimization algorithm such as the Newton–Raphson method [219]. It is possible to verify whether all λ_k have been found by checking a generalized Parseval relation:

$$\int_{-\infty}^{\infty} |u(x)|^2 \,\mathrm{d}x = -\frac{1}{\pi} \int_{-\infty}^{\infty} \ln\left(|a(\xi)|^2\right) \mathrm{d}\xi + 2\mathrm{i} \sum_{k=1}^{N} (\lambda_k^* - \lambda_k)\,. \tag{3.53}$$

Fig. 3.9 shows an example of the results of the above-described procedure, using: $u(x) = 1.4\,\mathrm{e}^{\mathrm{i}x}/\cosh(x)$. We notice that compared to the general equation for a bright soliton, Eq. (3.46), we used a slightly larger amplitude. This leads to $b(\xi) \neq 0$, as illustrated in Fig. 3.9a.

Inverting the scattering data

The time evolution of the scattering data is straightforward and can be incorporated into the definition of the function F of Eq. (3.44b). We then need to solve Eq. (3.43). We

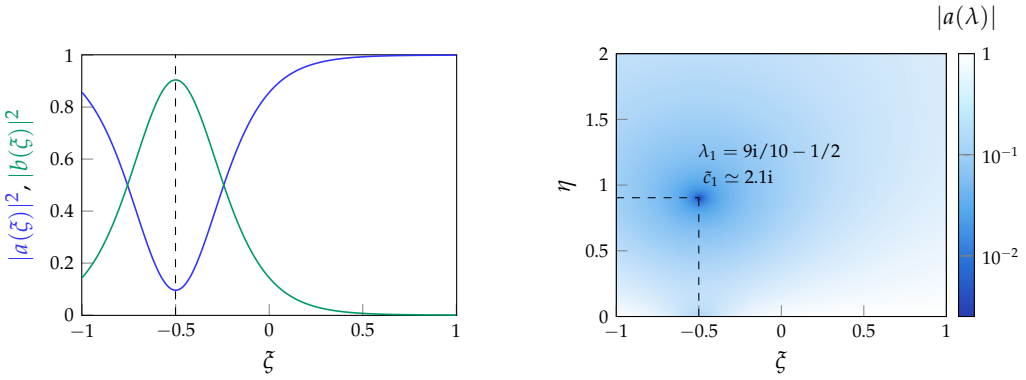

(a) Scattering data for $\lambda \in \mathbb{R}$.

(b) Scattering data for $\lambda \in \mathbb{C}^+$.

Figure 3.9: **(a, b)** Illustration of the scattering data of the potential $u(x) = 1.4\,\mathrm{e}^{\mathrm{i}x}/\cosh(x)$, determined using the procedure given in [220]. We write $\lambda = \xi + \mathrm{i}\eta$. **(a)** Norm squared of the reflection and transmission coefficient b, a, on the real axis. Since $b(\xi) \neq 0$ we have a surplus of atoms compared to a pure soliton. The dashed line indicates $\mathcal{R}(\lambda_1)$. The relation $|a(\xi)|^2 + |b(\xi)|^2 = 1$ is well-verified. **(b)** Norm of the reflection coefficient a in the upper-half of the complex plane. We identify a single zero λ_1 of $a(\lambda)$, and calculate the corresponding coefficient $\tilde{c}_1$. We verify with Eq. (3.53) that we did not miss any λ_k.

can rewrite this equation with the change of variable $s \to s + x$ in the integrals:

$$\begin{cases} -K_1(x,y) + \displaystyle\int_0^\infty K_2^*(x, x+s)F^*(s+x+y)\,\mathrm{d}s = -F^*(x+y) \\ K_2^*(x,y) + \displaystyle\int_0^\infty K_1(x, x+s)F(s+x+y)\,\mathrm{d}s \quad = 0 \end{cases} \tag{3.54}$$

We can, for a given $x = x_k$, discretize this equation on a grid. We take an interval $[0, L]$, with L large enough, and write $s = [s_1 = 0, s_2 = \delta s, ..., s_N = L]$ on this interval. Since $y \geq x$, discretizing y on the same grid leads to $y_n = x_k + s_n$. This last equality allows us to have the same arguments for the functions $K_{1,2}$ in Eq. (3.54). Thus, it is possible to rewrite this problem as a matrix inversion problem:

$$\begin{pmatrix} -\mathbb{1}_N & H^*(x_k)D \\ H(x_k)D & \mathbb{1}_N \end{pmatrix} \begin{pmatrix} k_1(x_k) \\ k_2^*(x_k) \end{pmatrix} = \begin{pmatrix} -f^*(x_k) \\ 0 \end{pmatrix}, \tag{3.55}$$

where we have used the following matrices:

$$(k_{1,2}(x_k))_n = K_{1,2}(x_k, x_k + s_n),\ (f(x_k))_n = F(2x_k + s_n),\ (H(x_k))_{j,n} = F(2x_k + s_n + s_j)\,, \tag{3.56}$$

and $D = \frac{\delta s}{3}\mathrm{diag}(1, 2, 4, 2, ..., 4, 1)$ is used to perform Simpson's rule on the integrals. Eventually, we obtain $u(x_k, t) = 2(k_1(x_k))_0$ after performing the matrix inversion. We can repeat this operation for all the points x_k necessary to fully reconstruct $u(x, t)$, completing the inversion process.

3.3 The IST as a Riemann-Hilbert problem

We have presented in the previous section a historic approach of the IST. Another framework consists of formulating the IST problem as a Riemann-Hilbert problem [217, 221]. Even though it carries the same physical information, it leads to additional insights, and an explicit formula for the n-soliton solutions.

We will formulate a matrix Riemann-Hilbert problem. In the previous section, we have seen that the real axis plays a peculiar role in the IST of the NLSE. Thus, we will define a function P on $\mathbb{C} \setminus \mathbb{R}$ and find the jump condition across the real axis. More generally, a Riemann-Hilbert problem can be set with a contour Σ and a matrix P defined on the complementary of Σ. Our goal is to have a function G defined on Σ such that $P^+(\xi)P^-(\xi) = G(\xi)$, where P^+ and P^- are the limits of P above and below the contour. A usual boundary condition is that $\lim_{\lambda\to\infty} P(\lambda) = \mathbb{1}_2$.

3.3.1 Formulation of the problem

We begin by reformulating the Lax pair $(\hat{L}, \hat{A})$, and now consider the following equations [45, 217]:

$$\partial_x \Phi = \begin{pmatrix} -\mathrm{i}\lambda & -u \\ u^* & \mathrm{i}\lambda \end{pmatrix} \Phi \qquad = \hat{U}\Phi\,, \tag{3.57a}$$

$$\partial_t \Phi = \begin{pmatrix} -2\mathrm{i}\lambda^2 + \mathrm{i}|u|^2 & -\mathrm{i}u_x - 2\lambda u \\ -\mathrm{i}u_x^* + 2\lambda u^* & 2\mathrm{i}\lambda^2 - \mathrm{i}|u|^2 \end{pmatrix} \Phi = \hat{V}\Phi\,, \tag{3.57b}$$

where the first one is simply a rewriting of Eq. (3.15), and the second one can be deduced from the development of $\hat{A}$ in powers of $\hat{L}$ [189]. The equivalence between this set of equations and the NLSE is found by imposing the compatibility condition $\partial_t(\partial_x\Phi) = \partial_x(\partial_t\Phi)$, and λ is now a free parameter, independent of time. The set of matrices $(\hat{U}, \hat{V})$ is also called a Lax pair.

The Jost solutions Φ, Ψ of Eq. (3.57a) can be defined in the same way as in Eq. (3.20), and we have the scattering matrix S defined by Eq. (3.21): $(\Phi, \bar{\Phi}) = (\bar{\Psi}, \Psi)S$. We can then construct the matrix:

$$P^+(x,\lambda) = (\Phi(x,\lambda), \Psi(x,\lambda))\mathrm{e}^{\mathrm{i}\lambda\sigma x} \quad \text{with} \quad \lambda \in \mathbb{C}^+ \quad \text{and} \quad \sigma = \begin{pmatrix} 1 & 0 \\ 0 & -1 \end{pmatrix}. \tag{3.58}$$

From the properties of the Volterra Eq. (3.24), P^+ is analytic in the upper-half of the complex plane. Besides, we have the limit:

$$P^+(x,\lambda) \to \mathbb{1}_2 \quad \text{when} \quad \lambda \in \mathbb{C}^+ \to \infty\,. \tag{3.59}$$

This can be demonstrated by developing Eq. (3.24) in terms of $1/\lambda$. In general, finding P^- requires to look at the adjoint of the scattering problem, Eq. (3.57a) [see for instance 217, Eq. (2.30-34)]. However, due to the involution properties, Eq. (3.16), this is not required here. We can express P^- as [see 217, Eq. (2.57)]:

$$P^-(x,\lambda) = (P^+)^\dagger(x,\lambda^*) = \mathrm{e}^{-\mathrm{i}\lambda^*\sigma x}\begin{pmatrix} \Phi^*(x,\lambda^*) \\ \Psi^*(x,\lambda^*) \end{pmatrix}. \tag{3.60}$$

This leads, for $\xi \in \mathbb{R}$, to:

$$P^-(x,\xi)P^+(x,\xi) = G(x,\xi) \quad \text{with} \quad G(x,\xi) = \mathrm{e}^{-\mathrm{i}\xi\sigma x}\begin{pmatrix} 1 & b^*(\xi) \\ b(\xi) & 1 \end{pmatrix}\mathrm{e}^{\mathrm{i}\xi\sigma x} \tag{3.61}$$

where we have used the fact that $b(\xi) = \phi_a\psi_a^* + \phi_b\psi_b^*$. Thus, we obtain the desired Riemann-Hilbert problem. The goal is to solve for $P^\pm$, knowing the scattering data, meaning G. As previously, we will recover $u(x)$ from the asymptotic behavior of $P^\pm$.

Writing for instance:

$$P^+(x,\lambda) = \mathbb{1}_2 + \frac{1}{\lambda}P_1^+(x) + \mathcal{O}\left(\frac{1}{\lambda^2}\right) \quad \text{when} \quad \lambda \to \infty\,, \tag{3.62}$$

we can express:

$$P_1^+(x) = \frac{1}{2\mathrm{i}}\begin{pmatrix} \int_{-\infty}^{x} |u(s)|^2\,\mathrm{d}s & -u(x) \\ -u^*(x) & \int_{x}^{-\infty} |u(s)|^2\,\mathrm{d}s \end{pmatrix}. \tag{3.63}$$

We have directly: $u(x) = -2\mathrm{i}(P_1^+(x))_{1,2}$.

3.3.2 Resolution of the equation

In general, an explicit solution cannot be found for Eq. (3.61). Here, we will only present a few noteworthy limiting cases and refer interested readers to [217, Sec. 2.1.2] for a more complete discussion.

Solution to the regular Riemann-Hilbert problem

When $\det(P^+(\lambda)) \neq 0$, meaning $a(\lambda) \neq 0$, in the upper half of the complex plane, the Riemann-Hilbert problem is said to be regular. We recall that this corresponds to the case when no soliton is present in the wavepacket. We can rewrite the problem as:

$$(P^+)^{-1}(\xi) - P^-(\xi) = (\mathbb{1}_2 - G)(P^+)^{-1}(\xi)\,. \tag{3.64}$$

Under this form, we can use the Sokhotski–Plemelj theorem, and the boundary conditions, to obtain the solution [217]:

$$(P^+)^{-1}(\lambda) = \mathbb{1}_2 + \frac{1}{2\pi\mathrm{i}}\int_{-\infty}^{\infty} \frac{(\mathbb{1}_2 - G)(P^+)^{-1}(\xi)}{\xi - \lambda}\,\mathrm{d}\xi \quad \text{with} \quad \lambda \in \mathbb{C}^+\,. \tag{3.65}$$

As expected, we do not obtain a closed-form expression.

The solitonic solutions

Since solitons appear at the points where $a(\lambda_k) = 0$, it is necessary to adapt the solution above in order to incorporate them. We suppose that we have N simple zeros, and introduce the vectors v_k that constitute the kernels of $P^+(\lambda_k)$. It was shown by [222] that it is possible to reduce this nonregular Riemann-Hilbert to a regular one. More precisely, defining:

$$P^+(\lambda) = \tilde{P}^+(\lambda)\Gamma(\lambda)\,, \tag{3.66a}$$

$$P^-(\lambda) = \Gamma^{-1}(\lambda)\tilde{P}^-(\lambda)\,, \tag{3.66b}$$

leads to the *regular* Riemann-Hilbert problem:

$$\tilde{P}^-(\xi)\tilde{P}^+(\xi) = \Gamma(\xi)G(\xi)\Gamma^{-1}(\xi)\,, \tag{3.67}$$

and we have used:

$$\Gamma(\lambda) = \mathbb{1}_2 + \sum_{j,k=1}^{N} \frac{v_j \left(M^{-1}\right)_{j,k} v_k^\dagger}{\lambda - \lambda_k^*} \quad \text{with} \quad (M)_{j,k} = \frac{v_j^\dagger v_k}{\lambda_j^* - \lambda_k}\,. \tag{3.68}$$

Considering now pure solitonic solutions, meaning $b(\xi) = 0$, yields great simplifications. We obtain $G(\xi) = \mathbb{1}_2$, thus, using Eq. (3.65), $\tilde{P}^+(\lambda) = \mathbb{1}_2$, leading to $P^+(\lambda) = \Gamma(\lambda)$. Developing this expression in powers of $1/\lambda$ results in:

$$u(x,t) = -2\mathrm{i}\left(\sum_{j,k=1}^{N} v_j \left(M^{-1}\right)_{j,k} v_k^\dagger\right)_{1,2}, \tag{3.69}$$

where the (x,t) dependence is hidden inside the vectors v_k. We derive it using the fact that $P^+\mathrm{e}^{-\mathrm{i}\lambda\sigma x - 2\mathrm{i}\lambda^2\sigma t}$ is a solution of Eq. (3.57a) and (3.57b), and $P^+ v_k = 0$. We determine:

$$v_k(x,t) = v_k(0,0)\mathrm{e}^{-\mathrm{i}\lambda_k\sigma x - 2\mathrm{i}\lambda_k^2\sigma t} = \begin{pmatrix} c_k \\ 1 \end{pmatrix}\mathrm{e}^{\theta_k}, \tag{3.70}$$

where we have taken without loss of generality $v_k(0,0) = \begin{pmatrix} c_k & 1 \end{pmatrix}^\intercal$. The numbers $c_k \in \mathbb{C}$ will determine the initial positions and phases of each soliton. We eventually obtain:

$$u(x,t) = -2\mathrm{i}\sum_{j,k=1}^{N} c_j \mathrm{e}^{\theta_j - \theta_k^*}\left(M^{-1}\right)_{j,k} \quad \text{with} \quad (M)_{j,k} = \frac{1}{\lambda_j^* - \lambda_k}\left[\mathrm{e}^{-(\theta_k + \theta_j^*)} + c_j^* c_k \mathrm{e}^{\theta_k + \theta_j^*}\right]. \tag{3.71}$$

This explicit solution allows us to write multi-soliton wavefunctions. In particular, one can check that inputting $\lambda_1 = \mathrm{i}\kappa/2 - k/2$ and $c_1 = -1$, we retrieve the bright soliton of Eq. (3.46).

3.3.3 The n-soliton solution

Using the formula from Eq. (3.71), one can express multi-soliton solutions of the NLSE. Furthermore, if all the λ_k^2 values are commensurate and the λ_k purely imaginary, the solution will be periodic in time, since the time variable only appears as a phase factor. From this class of solitons, [73] have shown that taking $\lambda_k = \mathrm{i}\left(k - \frac{1}{2}\right), k \in \{1, 2, ..., n\}$ leads to the initial wavefunction $u(x,0) = n/\cosh(x)$ (for well-chosen c_k). We illustrate these wavefunctions and their periodicity in Fig. 3.10. From an experimental point of view, this means that imprinting the same waveform as that of a bright soliton will result in different behaviors when the amplitude is increased sufficiently, i.e., when the number of atoms is increased.

These multi-solitons were realized in optical fibers by [38, 74], who observed the autocorrelation of optical pulses. They identified multi-solitons from $n = 1$ to $n = 4$ by progressively increasing the power of the optical pulses. In a cold-atom platform, [75] have used ^{6}Li atoms to create multi-solitons thanks to a Feshbach resonance. Quenching the interaction strength by the correct amount has the same effect as increasing the number of atoms via the parametrization of Eq. (3.4). We will discuss in greater details the realization of multi-solitons in our platform in Chap. 4.

We note that the application of the general multi-soliton formula given by Eq. (3.71) extends beyond the solutions established by [73]: one can adapt the amplitudes of c_k in order to adjust the initial positions of the solitons, use complex-valued λ_k with a real part to impart a given velocity to solitons, etc. This point is illustrated in Fig. 3.11, where we show a multi-soliton solutions with 3 solitons, one of them having a non-zero velocity.

3.3.4 n-soliton: superposition or bound state?

We have seen that n-soliton solutions are characterized by n eigenvalues of the IST. As such, they constitute a nonlinear superposition of n individual solitons. We consider

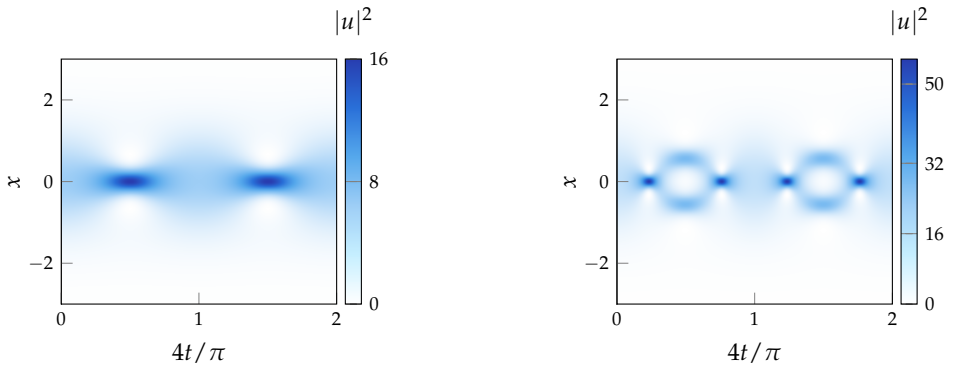

(a) $n = 2$: $u(x,0) = \frac{2}{\cosh(x)}$ **(b)** n=3: $u(x,0) = \frac{3}{\cosh(x)}$

Figure 3.10: (a, b) We use the formula of Eq. (3.71) to numerically show the evolution of multi-solitons for which $\lambda_k = \mathrm{i}\left(k - \frac{1}{2}\right)$. The commensurate angular frequency is $\omega = 4\left(\lambda_2^2 - \lambda_1^2\right) = 4\left(\frac{9}{4} - \frac{1}{4}\right) = 8$, which leads to a period of $\pi/4$. Thus, we show here two periods. **(a)** We have two eigenvalues: $\mathrm{i}/2$ and $3\mathrm{i}/2$. Choosing $c_1 = 1$ and $c_2 = -1$ leads to the solution explored by [73]. **(b)** We have three eigenvalues: $\mathrm{i}/2$, $3\mathrm{i}/2$ and $5\mathrm{i}/2$. We have taken $c_1 = 1$, $c_2 = -1$ and $c_3 = 1$.

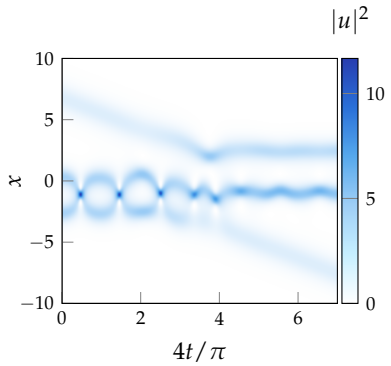

Figure 3.11: Multi-soliton of the NLSE, computed using Eq. (3.71) with the eigenvalues: $\lambda_1 = \mathrm{i}$, $\lambda_2 = \mathrm{i}/\sqrt{2}$, $\lambda_3 = \mathrm{i}/2 + 0.1$. The breathing between the two solitons at zero velocity depends on their initial positions. In particular, the differential position shift induced by the collision with the third soliton alters the breathing pattern, though the periodicity remains.

in this section, for clarity, the case explored by [73], and take $\lambda_j = \mathrm{i}(2j-1)/2$. These eigenvalues correspond to the wavefunctions:

$$u(x,0) = \frac{n}{\cosh(x)} \quad \text{and} \quad u_j(x,0) = \frac{2j-1}{\cosh((2j-1)x)}\,, \tag{3.72}$$

where u, u_j are the wavefunctions of the n-soliton and its constituents respectively. We can verify that the atom number of the n-soliton is equal to the sum of the atom number of its component solitons:

$$\begin{aligned}\int |u(x)|^2\,\mathrm{d}x &= 2n^2 \\ &= \sum_{j=1}^{n} 2\underbrace{(2j-1)}_{\kappa_j} = \sum_{j=1}^{n}\int \left|u_j(x)\right|^2\mathrm{d}x\,.\end{aligned} \tag{3.73}$$

Similarly, we can compute the energy of the n-soliton:

$$\begin{aligned}\int |\partial_x u|^2 - |u|^4\,\mathrm{d}x &= -\frac{2}{3}n^2(2n^2-1) \\ &= -\sum_{j=1}^{n}\frac{2}{3}\underbrace{(2j-1)}_{\kappa_j}{}^3 = \sum_{j=1}^{n}\int \left|\partial_x u_j\right|^2 - \left|u_j\right|^4\mathrm{d}x\,.\end{aligned} \tag{3.74}$$

Therefore, the n-soliton is not a bound state of several solitons. This is consistent with the point of view given by the IST: solitons are the basis from which other wavefunctions are formed. We will explain in Chap. 6 how to reveal this basis experimentally, through controlled integrability breaking.

3.4 More advanced IST topics

For now, we have only discussed about the IST only in the settings of the NLSE, and restricted ourselves to the case of $\lim_{|x|\to\infty} u(x) = 0$. However, this method applies to a wide range of equations. This section will briefly cover some possible extensions.

3.4.1 AKNS hierarchy and more complex solitons

A first notable broadening was given by [45]. They considered a more general Lax pair, namely:

$$\hat{U} = \begin{pmatrix} -\mathrm{i}\lambda & q \\ r & \mathrm{i}\lambda \end{pmatrix} \quad \text{and} \quad \hat{V} = \begin{pmatrix} A & B \\ C & D \end{pmatrix}. \tag{3.75}$$

The coefficients A, B, C, D are chosen such that the compatibility condition is satisfied. There are infinitely many solutions, and one can retrieve several well-known equations such as the KdV equation, the modified KdV equation, or the NLSE. These solutions are said to belong to the Ablowitz-Kaup-Newell-Segur (AKNS) hierarchy. In this equation, q and r are two independent fields, and we recover the matrix $\hat{U}$ we used in Eq. (3.57a) by setting $q = -u$ and $r = u^*$.
Leaving these fields as two independent variables, we can arrive at the coupled NLSE:

$$\begin{cases} \mathrm{i}q_t + q_{xx} - 2q^2 r = 0\,, \\ \mathrm{i}r_t - r_{xx} + 2r^2 q = 0\,. \end{cases} \tag{3.76}$$

Note that this equation is different from Eq. (3.10), which describes a spin mixture. Most importantly, the involution property of Eq. (3.16) is not verified anymore. This leads to $\bar{\lambda}_k$ not being equal to λ_k^*. When this property breaks down, the behavior of solitons can become less intuitive. For instance, we can have single solitons for which the amplitude is not constant [217]. Taking e.g. $\mathcal{R}(\lambda_1) \neq \mathcal{R}(\bar{\lambda}_1)$ and $\mathcal{I}(\lambda_1) = -\mathcal{I}(\bar{\lambda}_1)$ produces an exponentially increasing / decaying soliton amplitude, as is illustrated in Fig. 3.12.

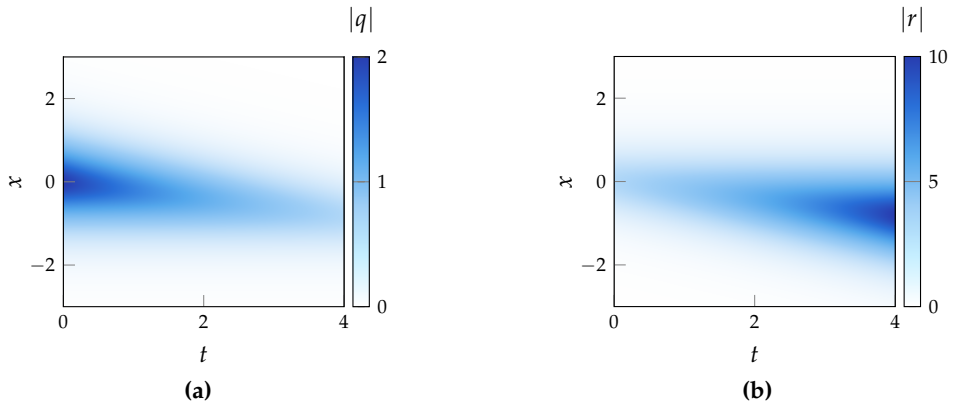

Figure 3.12: **(a, b)** Single soliton of the coupled system of Eq. (3.76), with $\lambda_1 = \mathrm{i}$ and $\bar{\lambda}_1 = 0.1 - \mathrm{i}$. **(a)** Norm of the component q, its amplitude is exponentially decreasing. **(b)** Norm of the component r, its amplitude is exponentially increasing. The conserved quantities of Eq. (3.76) are functions that involve products of r and q, which justifies the existence of such solutions.

Manakov systems

There exists other classes of integrable equations, which are not described by the AKNS hierarchy. A notable example is the Manakov system, shown to be integrable by [209]. Its Lax pair consists of three-by-three matrices. As mentioned earlier, the defocusing Manakov system, Eq. (3.10) with $\alpha = 1$, exhibits dark-bright solitons. The focusing case also admits solitonic solutions, that resemble the standard bright soliton of NLSE, except they have an additional parameter called polarization, which controls the relative weight of the two components. This polarization does not remain constant during soliton collisions [223], which leads to power redistribution between the two solitons within each component.

3.4.2 Solitons on a background

The IST can also be extended to systems for which the condition $\lim_{|x|\to\infty} u(x) = 0$ is not verified anymore. New solutions can then be found. A first notable example is the case of the defocusing NLSE: no soliton exists if $\lim_{|x|\to\infty} u(x) = 0$, but the system holds dark solitons when $\lim_{|x|\to\infty} |u(x)| = A \neq 0$. The IST of this system was performed by [224]. We will mention in this section a couple of boundary conditions, restricting ourselves to the focusing NLSE.

Modulational instability

Before diving into the IST, we recall the concept of modulational instability, which is a central topic of the focusing NLSE. The wavefunction $u(x,t) = A\mathrm{e}^{2\mathrm{i}|A|^2 t}$, $A \in \mathbb{C}$ is a solution of the focusing NLSE. One interesting question is how stable such a wavefunction

is. We can perform a Bogoliubov analysis by looking at the dispersion relation of this initial solution perturbed by plane waves:

$$u(x,t) = A\left[1+\epsilon\left(U\mathrm{e}^{\mathrm{i}(kx-wt)} + V^*\mathrm{e}^{-\mathrm{i}(kx-w^*t)}\right)\right]\mathrm{e}^{2\mathrm{i}|A|^2t}, \tag{3.77}$$

with $U, V \in \mathbb{C}$ and $\epsilon \ll 1$. Plugging this expression in the NLSE, we have at first order in ϵ the system:

$$\begin{pmatrix} w-k^2+2|A|^2 & 2|A|^2 \\ 2|A|^2 & -w-k^2+2|A|^2 \end{pmatrix}\begin{pmatrix} U \\ V \end{pmatrix} = 0\,. \tag{3.78}$$

We have non-zero solutions for (U,V) if and only if the determinant of the matrix cancels. We deduce the dispersion relation:

$$w^2 = k^4 - 4k^2|A|^2\,. \tag{3.79}$$

When $k \in [0, 2|A|]$, the frequency ω becomes imaginary. This results in an exponential growth of perturbations at these wavenumbers, a phenomenon called modulational instability. It was observed with cold atoms in e.g. [225–227]. Two different boundary conditions can be set in order to treat this system with the IST.

Non-zero boundary conditions

Perhaps the most natural boundary condition is to write $\lim_{|x|\to\infty} u(x,t) = A\mathrm{e}^{2\mathrm{i}|A|^2t}$ [200]. This is similar to the settings taken by [224] in the defocusing NLSE. The Lax pair $(\hat{L}, \hat{A})$, Eq. (3.13), still describes our system. The main difference lies in the boundary conditions of the Jost functions, due to the modifications of Eq. (3.19). Looking for instance at the limit $x \to \infty$, the Jost basis is:

$$\Psi(\lambda) \sim \mathrm{e}^{\mathrm{i}px}\begin{pmatrix} \frac{\mathrm{i}}{A}(\lambda-p)\mathrm{e}^{2\mathrm{i}|A|^2} \\ 1 \end{pmatrix} \quad \text{and} \quad \bar{\Psi}(\lambda) \sim \mathrm{e}^{-\mathrm{i}px}\begin{pmatrix} 1 \\ \frac{\mathrm{i}}{A}(\lambda-p)\mathrm{e}^{-2\mathrm{i}|A|^2} \end{pmatrix}, \tag{3.80}$$

where we introduced an additional parameter $p(\lambda) = (\lambda^2 + |A|^2)^{1/2}$. We recover Eq. (3.20) when $|A| \to 0$. However, the good space to evaluate p is not the complex plane, but a two-sheet Riemann surface, due to the square root. It has branch points at $-\mathrm{i}|A|$ and $\mathrm{i}|A|$, and we can take a branch cut along the imaginary axis between these two points. The consequences are straightforward: all scattering quantities must be defined by taking into account the sheet index, and the contour integrals need to be evaluated around the branch cut. The calculations are then similar to the ones performed in this chapter, and we refer interested readers to [200]. This method allows one to obtain the Kuznetsov-Ma soliton (Fig. 3.3c), which corresponds to the scattering data: $b(\xi) = 0, \lambda_1 = \mathrm{i}\alpha, p(\lambda_1) = \mathrm{i}\beta = \mathrm{i}\sqrt{\alpha^2 - |A|^2}$, with $\alpha, \beta > 0$. From the condition on β we see that $\alpha > |A|$: λ_1 cannot be located on the branch cut. Adding a real part to λ_1 will lead to induce a velocity in the soliton. One should remember that these solutions are still subject to the modulational instability.

Periodic boundary conditions

Taking periodic boundary conditions is more suited to tackle the modulational instability [228]. Indeed, the idea is that $u(x,0)$ described by Eq. (3.77) has a spatial period $L = 2\pi/k$. Thus, the IST would allow us to evaluate the growth of such instabilities beyond the simple Bogoliubov analysis shown above. This was the goal from [201],

which led to the discovery of the Akhmediev soliton (Fig. 3.3a). This approach allows the construction of a broad class of solutions of the NLSE [229–231].

The determination of the scattering data still relies on the Lax pair $(\hat{L}, \hat{A})$. The operator $\hat{L}$ is now L-periodic, due to $u(x+L,0) = u(x,0)$. The Jost functions no longer offer a good basis. We simply pick a point x_0 at which we set the solutions:

$$\Phi_{x_0}(x_0,\lambda) = \begin{pmatrix} 1 \\ 0 \end{pmatrix} \quad \text{and} \quad \bar{\Phi}_{x_0}(x_0,\lambda) = \begin{pmatrix} 0 \\ 1 \end{pmatrix}, \tag{3.81}$$

and the matrix $M_{x_0}(x,\lambda) = (\Phi_{x_0}(x,\lambda), \bar{\Phi}_{x_0}(x,\lambda))$ satisfies Eq. (3.15). On the other hand, we can write solutions Ψ of Eq. (3.15) using Bloch theory:

$$\Psi(x+L,\lambda) = \mathrm{e}^{\mathrm{i}p(\lambda)}\Psi(x,\lambda) = m(\lambda)\Psi(x,\lambda), \tag{3.82}$$

where $p(\lambda)$ is the quasi-momentum. By definition of our basis there exists A, B such that $\Psi = A\Phi_{x_0} + B\bar{\Phi}_{x_0}$. We define $\tilde{M}(x_0,\lambda) = M(x_0+L, x_0, \lambda)$. The trace and determinant of $\tilde{M}$ do not depend of the choice of x_0. Evaluating Eq. (3.82) at $x = x_0$, we arrive at:

$$\tilde{M}(x_0,\lambda)\begin{pmatrix} A \\ B \end{pmatrix} = m(\lambda)\begin{pmatrix} A \\ B \end{pmatrix}. \tag{3.83}$$

Solving this eigenproblem directly leads to the reconstruction of the Bloch eigenfunctions and their quasi-momentum. Writing $\mathrm{Tr}(\tilde{M}) = \Delta(\lambda)$, we can express the eigenvalues:

$$m^{\pm}(\lambda) = \frac{\Delta(\lambda) \pm \sqrt{\Delta^2(\lambda) - 4}}{2}, \tag{3.84}$$

where we used the fact that $\det(\tilde{M}) = 1$. Thus, the behavior of the Bloch eigenfunctions relies on the value of the complex function $\Delta(\lambda)$. We can define bands of stability, for which $\Delta^2(\lambda) < 4$, and areas of instability, for which $\Delta^2(\lambda) > 4$ (or $\mathcal{I}(\Delta(\lambda)) \neq 0$). The main spectrum consists of the points λ_k for which $\Delta(\lambda_k) = \pm 2$ [see e.g. the Appendix of 228, for a complete discussion]. For instance, Stokes waves correspond to bands crossing the real axis, which are stable [232]. On the other hand, bands in the upper-half of the complex plane can lead to Rogue wave events [233].

An important feature is that $\Delta(\lambda)$ is invariant with the time evolution of u. Similarly to the IST method for fast-decaying functions, the knowledge of this spectrum already provides substantial information about u. The reconstruction of the wavefunctions $u(x,t)$ then relies on squared eigenfunctions and Riemann theta functions, and is beyond the scope of this manuscript.

Conclusion

The Inverse Scattering Transform is a widespread and powerful method to solve nonlinear Partial Differential Equations. We described in this chapter this formalism in the case of the Nonlinear Schrödinger Equation. It allowed us to formulate a definition of solitons which encapsulates at the same time bright solitons, dark solitons, Kuznetsov-Ma solitons, etc. They correspond to the poles of the transmission coefficient $a(\lambda)$ of the associated scattering problem, each zero being associated with a soliton. Besides, the properties of the IST gave us an immediate explanation for the extraordinary conservation properties exhibited by solitons.
We should mention that there exist several other methods to solve integrable PDEs. Examples include Bäcklung transformations [234], the Hirota bilinear method [235, 236], the Darboux dressing method [237]. However, they are less general and mainly used to obtain explicit many-soliton solutions.
We will explore in Chap. 4 an experimental realization of multi-solitons of the NLSE. Finally, one might wonder about the robustness of this approach if the original equation is perturbed. Although in most cases it breaks the integrability, the IST formalism remains useful. This point will be discussed in Chap. 6.

4 Realization of multi-solitons

Outline of the current chapter

Introduction

In the previous chapter, we explored the Inverse Scattering Transform and its prediction of single and multi-soliton solutions of the NLSE. In this chapter, we translate these theoretical insights into experiment, realizing both single and higher-order bright solitons. These multi-soliton states, corresponding to multiple discrete eigenvalues in the IST spectrum, exhibit characteristic periodic breathing dynamics. We present in Sec. 4.1 the relevant experimental tools. They are used to prepare a bright soliton of NLSE (Sec. 4.2), as well as multi-soliton solutions (Sec. 4.3).

4.1 Experimental protocol

We describe in this section the experimental conditions that allow us to have a system described by the NLSE. Several key ingredients are required:

- A slightly immiscible mixture, such that we can apply the approximation described in Sec. 2.3.2 corresponding to a low-depletion mixture.
- A one-dimensional system, at least in terms of the spin dynamics.
- The absence of additional force applied on the atoms.

4.1.1 An immiscible mixture

The electronic ground state of ^{87}Rb counts 8 magnetic sublevels, distributed over the hyperfine levels $F = 1$ and $F = 2$. We choose a mixture that is long-lived. Indeed, because the spin dynamics are governed by $\tau_s = \hbar/(\delta g\, n) \gg \tau = \hbar/(g\, n)$, with $\delta g = g_{1,2} - g$ (see Chap. 2), we expect phenomena to occur on timescales longer than the density dynamics. In practice, we record the evolution of the wavefunction for several hundred milliseconds. This criterion excludes the $F = 2$ states, which experience spin-relaxation [115, 238]. Consequently, we select the mixture $|1\rangle = |F = 1, m_F = -1\rangle$ and $|2\rangle = |F = 1, m_F = +1\rangle$. This mixture has already been employed in previous experiments [173, 215]. We use a quantization magnetic field of approximately 1.2 G along y (see Chap. 1 for definitions of the coordinates). It leads to a Zeeman shift lifting the degeneracy of the different m_F states. Besides, the quadratic Zeeman shift prevents collisions $|m_F = +1, m_F = -1\rangle \to |m_F = 0, m_F = 0\rangle$ [93], and we verify experimentally that no atom is present in $|F = 0, m_F = 0\rangle$ at the end of the time evolution.

The scattering lengths for this mixture are evaluated using the values reported in [239, 240]. We take $a_0 = 101.78\, a_B$ and $a_2 = 100.40\, a_B$, with a_F being the scattering length of atoms colliding in a channel of total spin F. It leads to:

$$a_{1,1} = a_2 = 100.40\, a_B\,, \tag{4.1a}$$

$$a_{2,2} = a_2 = 100.40\, a_B\,, \tag{4.1b}$$

$$a_{1,2} = \frac{2}{3}a_0 + \frac{1}{3}a_2 = 101.32\, a_B\,. \tag{4.1c}$$

These values yield $\delta g/g = (a_{1,2} - a_{1,1})/a_{1,1} \simeq 9 \times 10^{-3} > 0$, indicating that we have a slightly immiscible mixture ($\delta g/g = \sqrt{\Delta} - 1$).

Magnetic dipole-dipole interactions

Due to the reduced dimensionality of our cloud, Magnetic Dipole-Dipole Interactions (MDDI) must be taken into account [241]. Indeed, ^{87}Rb atoms possess a magnetic moment of 1.0 μ_B [242], and an additional term must thus be added to the contact interaction potential between atoms A and B:

$$\hat{V}_{\text{mag}} = \frac{\mu_0 \mu_B^2}{\pi r^3} \left[\hat{\mathbf{s}}_A \cdot \hat{\mathbf{s}}_B - 3(\hat{\mathbf{s}}_A \cdot \mathbf{u})(\hat{\mathbf{s}}_B \cdot \mathbf{u}) \right] , \tag{4.2}$$

where $\hat{\mathbf{s}}_{A,B}$ denotes the spin of the outer electron of atom A, B respectively, r is the distance between the atoms, and $\mathbf{u}$ the unit vector linking A and B. Although its effect averages out for a uniform 3D cloud, this potential leads to a shift in scattering lengths when different geometries are used (see Appendix B for details). In the case discussed in this manuscript, we obtain corrections equal to a fraction of the Bohr radius for each scattering length of Eq. (4.1):

$$a_{1,1} = 100.40\, a_B - 0.18\, a_B , \tag{4.3a}$$
$$a_{2,2} = 100.40\, a_B - 0.18\, a_B , \tag{4.3b}$$
$$a_{1,2} = 101.32\, a_B + 0.18\, a_B . \tag{4.3c}$$

The immiscibility of our mixture is enhanced: $\delta g / g \simeq 1.3 \times 10^{-2}$. Thus, the MDDI allow us to slightly decrease the time scale τ_s.

4.1.2 Reducing the dimensions

Our initial BEC is intrinsically 3D and described within the mean-field regime by the energy functional of Eq. (2.11). However, similarly to the 2D case discussed in Chap. 2, we can approximate the wavefunction $\phi(\mathbf{r})$ in the case of a strong confinement along certain directions. We write $\phi(\mathbf{r}) = \psi(x)\theta(y)\chi(z)$, with $\theta(y), \chi(z)$ being given by the ground state of harmonic oscillators with angular frequency ω_y, ω_z respectively. Their wavefunctions can be taken of the form:

$$\theta(y) = \frac{1}{(\pi l_y^2)^{1/4}} \exp\left(-\frac{y^2}{2 l_y^2} \right) \quad \text{and} \quad \chi(z) = \frac{1}{(\pi l_z^2)^{1/4}} \exp\left(-\frac{z^2}{2 l_z^2} \right) , \tag{4.4}$$

where $l_{y,z} = \sqrt{\hbar / (m \omega_{y,z})}$. Since θ^2 and χ^2 are normalized to unity, it follows that $\int |\psi|^2 \, \mathrm{d}x = N$. This parametrization is valid, provided that $\hbar \omega_{y,z} \gg k_B T, |\mu|$, where T is the temperature of the cloud and μ the chemical potential. Inserting these expressions in Eq. (2.11) yields:

$$E[\psi] = \int \left[\frac{\hbar^2}{2m} |\nabla \psi(x)|^2 + V(x) |\psi(x)|^2 + \frac{g}{4\pi l_y l_z} |\psi(x)|^4 \right] \mathrm{d}x + \frac{\hbar^2 N}{2m} \left(\frac{1}{l_y^2} + \frac{1}{l_z^2} \right) . \tag{4.5}$$

The last term corresponds to a constant energy offset and can be discarded. Defining $g_{1\text{D}} = 2\hbar a \sqrt{\omega_y \omega_z}$, we obtain the 1D GPE:

$$\mathrm{i}\hbar \frac{\partial \psi}{\partial t} = -\frac{\hbar^2}{2m} \frac{\partial^2 \psi}{\partial x^2} + V(x)\psi(x) + g_{1\text{D}} |\psi|^2 \psi(x) . \tag{4.6}$$

This simple derivation remains valid as long as the interactions maintain their 3D character: $l_{y,z} \gg a$ [122]. The validity of the mean-field treatment is usually determined by

the Lieb-Liniger parameter $\gamma = \frac{g_{1D}m}{n\hbar^2}$, where n is the 1D density of the cloud [243]. This dimensionless parameter compares the interaction energy and the kinetic energy terms of Eq. (4.6). For the experiments described in this manuscript, we calculate $\gamma \sim 10^{-4}$, which justifies our approach.

Experimental parameters

The confinement along the vertical direction is provided by the so-called accordion lattice (see Chap. 1). We determine its frequency using parametric heating, and obtain $w_z = 2\pi \times 4.3(1)$ kHz. The in-plane confinement is produced by a DMD, referred to as DMD1 in Chap. 1. In practice, the DMD1 initially projects a rectangular box of 40 µm × 50 µm on the atoms when loading the BEC from the red dipole traps. A sequence of images is then displayed, interpolating between the initial box and a tube of 3 µm × 50 µm. This sequence contains 160 images, changed every 2 ms. We recall that the pixel size of DMD1 is approximately 0.20 µm in the atomic plane. Thus, subsequent images differ by about one line of pixels on opposite sides of the rectangle. Although the DMD1 images have a flat bottom, the finite resolution of our objective (∼ 1 µm) smooths them. We estimate a transverse confinement of $l_y \simeq 1.5$ µm, corresponding to $\omega_y \simeq 2\pi \times 50$ Hz. We emphasize that the in-plane potential is not harmonic. The associated frequency corresponds to the effective value of a harmonic potential that would produce similar trapping.

We would like to verify that such a confinement allows us to use the 1D GPE. Equivalently, we wish to assess to what extent $\hbar\omega_{y,z} \gg k_B T, |\mu|$. Using $\mu = g_{1D}n$, we estimate $|\mu| \simeq h \times 1$ kHz, and $k_b T \simeq h \times 200$ Hz. Thus, the cloud is well confined along the z-direction, but several excited states are populated along the y-direction. However, we are dealing with binary mixtures, which allow us to relax the constraints on the confinement. Indeed, the spin dynamics are governed by another energy scale: $\delta g\, n$. For our mixture, $\delta g \simeq 0.013\, g_{1D}$ and we verify that $\hbar\omega_y \gtrsim |\delta g|\, n$, corresponding to $\omega_y/(2\pi) \gtrsim 30$ Hz. Besides, we can introduce the spin healing length $\xi_s = \hbar/\sqrt{2mn|\delta g|}$ (see Sec. 2.3). We notice that $\xi_s \simeq l_y$, which confirms that the spin dynamics are confined to the axial direction of the tube.

4.1.3 Control of the magnetic fields

The two spin states of our mixture have $m_F = \pm 1$, and are therefore sensitive to magnetic fields through the linear Zeeman effect. The corresponding energy shift reads:

$$\Delta E_{|F,m_F\rangle} = \mu_B g_F m_F \|\mathbf{B}\|\,, \tag{4.7}$$

where $g_{F=1} = -1/2$ is the Landé factor, and $\mathbf{B}$ the magnetic field. Hence, $\|\mathbf{B}\|$ sets a potential landscape for the atoms. In particular, a magnetic field gradient will result in a force on the atoms. Since the states $|1\rangle$, $|2\rangle$ have an opposite sensitivity, a given gradient would produce opposite forces. It is crucial for the experiments described in this manuscript to keep gradients as low as possible. In practice, we limit $|\nabla\|\mathbf{B}\||| \lesssim 5 \times 10^{-2}$ G/m in the atomic plane.

Ramsey interferometry

Ramsey interferometry enables us to estimate the residual magnetic-field gradients in the atomic plane. The principle is as follows:

- Starting from $|1\rangle$, use a $\pi/2$ MW pulse to transfer half the atoms in a spin state with a different magnetic field sensitivity. In practice, we use $|F = 2, m_F = -2\rangle$ as the second spin state to maximize our signal (see Eq. (4.9)).
- Wait for a given time t. Each atom in the cloud will accumulate a spatially-dependent phase:

$$\frac{t}{\hbar}\mu_B g_F m_F \nabla \|\mathbf{B}\| \cdot \mathbf{r} \quad \text{with} \quad \mathbf{r} = (x, y)\,. \tag{4.8}$$

  We ignore the global phase created by $\|\mathbf{B}\|$ since it has no spatial dependence. We also assume that the gradient is sufficiently small for the atoms to remain stationary during t. This condition limits the maximal waiting time. In practice, $t \lesssim 20\,\text{ms}$.
- Perform a second $\pi/2$ MW pulse. If a gradient is present, a stripe pattern appears, due to the differential dephasing between the two spin states. Its period is given by:

$$\mathbf{R} = \frac{h}{t\mu_B \Delta(g_F m_F)\nabla\|\mathbf{B}\|}\,, \tag{4.9}$$

  where $\Delta(g_F m_F) = (g_F m_F)_{|1,-1\rangle} - (g_F m_F)_{|2,-2\rangle} = 3/2$. Conversely, measuring the period yields $\nabla\|\mathbf{B}\|$. Note that we cannot determine the sign of the period, and, consequently, the sign of the magnetic field gradient. Since our goal is to cancel the gradient, this is irrelevant to the present discussion.

Due to small fluctuations of $\|\mathbf{B}\|$, the overall phase of the stripe pattern is random from one image to the next. Thus, we analyze each absorption image individually. An example is provided in Fig. 4.1a. Then, we can identify the point at which we cancel the gradient using a set of measurements, as shown in Fig. 4.1b.

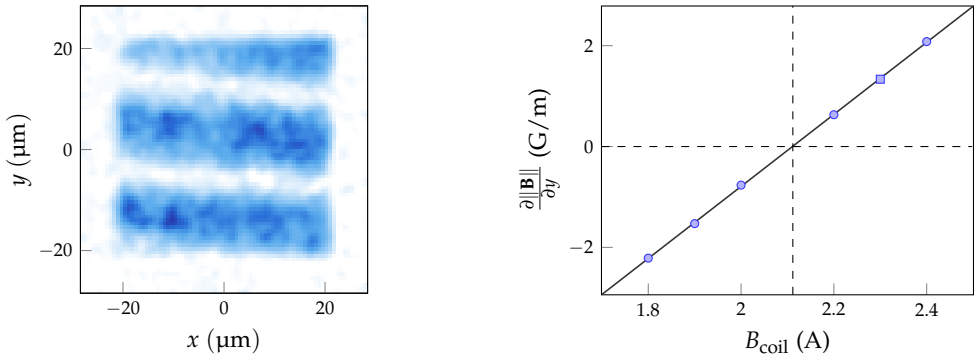

Figure 4.1: **(a)** Absorption image resulting from Ramsey interferometry. The initial cloud is in a box of size $42\,\mu\text{m} \times 42\,\mu\text{m}$. The waiting time was set to 20 ms. Since we cannot use partial MW repump, the density is quite high and not proportional to the OD. We are still able to extract the period of the modulation, hence $\nabla\|\mathbf{B}\|$. **(b)** Series of Ramsey interferometry measurements. We vary the current in one of the coil around the glass cell. Each point is the average of five images. The square corresponds to the average from which is taken the image shown in **(a)**. A linear fit (solid line) is performed, from which we extract the current at which the gradient cancels (shown with the dashed lines).

In practice, we use a set of orthogonal coils along x and y in order to cancel $\nabla\|\mathbf{B}\|$ in the atomic plane. We highlight one subtlety: since we cancel the gradient of the *norm* of the field, even coils in Helmholtz configuration can have an effect. Taking for instance a

field of the form:

$$\mathbf{B} = (B_\mathrm{x} + b_\mathrm{x} x)\mathbf{x} + (B_\mathrm{y} + b_\mathrm{y} y)\mathbf{y} + (B_\mathrm{z} - (b_\mathrm{x} + b_\mathrm{y})z)\mathbf{z}\,, \tag{4.10}$$

where B_i, b_i are the field and gradient along axis i respectively, possibly resulting from the combined effects of several coils. We take a quantization axis along y. Thus, B_y is greater than all other fields and we can make a development at first order of $\|\mathbf{B}\|$. Calculating the gradient of the norm, we obtain:

$$\frac{\partial\|\mathbf{B}\|}{\partial x} = \frac{B_\mathrm{x} b_\mathrm{x}}{B_\mathrm{y}} \quad \text{and} \quad \frac{\partial\|\mathbf{B}\|}{\partial y} = b_y\,, \tag{4.11}$$

Thus, canceling the *field* along x is sufficient to set $\partial_x\|\mathbf{B}\| = 0$.

Atomic dynamometer

We can independently confirm the Ramsey-interferometry results using a soliton. Indeed, solutions $u(x,t)$ of NLSE can also be expressed in a non-inertial reference frame with a uniform and constant force F. In a dimensionless form:

$$u(x,t) \longrightarrow u(x - Ft^2, t)\exp\left[-\mathrm{i}(xFt + F^2t^3/3)\right]. \tag{4.12}$$

Hence, when a wavepacket with zero initial velocity is imprinted at $x = 0$, its center follows $x_\mathrm{com}(t) = \frac{1}{2m}Ft^2$, where dimensional units are restored using Eq. (3.4). The displacement is the same as that of a free particle. In our case, the force is to be understood as a differential force between the two components of the mixture. We can give some order-of-magnitude estimates: with a gradient of 0.1 G/m, we have $x_\mathrm{com} \simeq 50\,\mu\mathrm{m}$ after $t = 400\,\mathrm{ms}$.

In practice, we sequentially use tubes oriented along orthogonal directions to confirm, and even fine-tune, the results obtained with Ramsey interferometry. For a given configuration of magnetic coils, we are limited by the discretization of the National Instruments analog cards that control the power supplies. Indeed, we use 12 bits analog cards, which means the output voltage varies in discrete steps of 5 mV. Using the slope of Fig. 4.1b and its equivalent along x, we estimate this corresponds to a precision of 36 mG/m along y and 15 mG/m along x.

This approach is valid in the low-depletion limit, when our system can be mapped to NLSE. Yet, a calculation involving both components yields at short times the same result, up to a renormalization of the force [see 86, Sec. 6.4.1]. We will discuss this point in more details in Sec. 5.1.4.

Curvature of the magnetic field

The procedure described above allows the cancellation of $\nabla\|\mathbf{B}\|$ in the atomic plane. However, we have so far neglected the effects of higher-order terms. Indeed, the coils surrounding the glass cell are not arranged in a Helmholtz configuration, and may produce a quadratic magnetic field norm. Modeling the fields, we realize that these coils may cause a harmonic potential with $\omega \simeq 2\pi \times 1\,\mathrm{Hz}$ acting on the minority component. Because the spin dynamics occur on the "slow" timescale τ_s, the effect of this potential can be seen on the atoms. This effect is particularly relevant for the experiment described in Chap. 6 for which the wavepacket is put into motion.

We mitigate this issue by changing the coils used to generate the quantization field. The coils closest to the glass cell are completely switched off, and we employ another pair of coils, placed at $\simeq 1\,\mathrm{m}$ from the atoms (see Chap. 1). With this configuration,

the residual quadratic potentials are below our detection threshold, and we will neglect them in the following.

4.1.4 Imprinting a waveform with the Raman beams

Our initial system consists of a 50 µm tube of atoms in $|1\rangle = |F = 1, m_F = -1\rangle$. Thanks to the flat-bottom potential imposed by the DMD1, the linear density is approximately uniform and we have $n_1 \simeq 570\,\mu\text{m}^{-1}$. An absorption image is shown in Fig. 4.3a, along with the linear atomic density. Then, we use another DMD with a pair of Raman beams shined on it to tailor the distribution of transferred atoms [105] (see Chap. 1 for details on the optical system).

However, it is not possible with our geometry to use Raman beams to populate the state $|2\rangle = |F = 1, m_F = +1\rangle$, starting from atoms in $|1\rangle$. Indeed, it would require $\Delta m_F = 2$, but this transition is suppressed by destructive interference [we can derive a similar calculation to the one done in 85, Appendix A]. Thus, we perform a two-step transfer through the intermediate state $|F = 2, m_F = 0\rangle$: first, the Raman beams illuminate the atoms with the desired spatial profile; subsequently, a global MW π-pulse is applied. This MW is resonant with the $|F = 2, m_F = 0\rangle \rightarrow |2\rangle$ transition, and the atoms in $|1\rangle$ are not affected. Each step lasts on the order of 10 µs, during which no atomic motion occurs. This process is illustrated in Fig. 4.2a. The resulting atomic densities are sketched in Fig. 4.2b. We give in Fig 4.3b an experimental image of the minority component, along with the integrated profile.

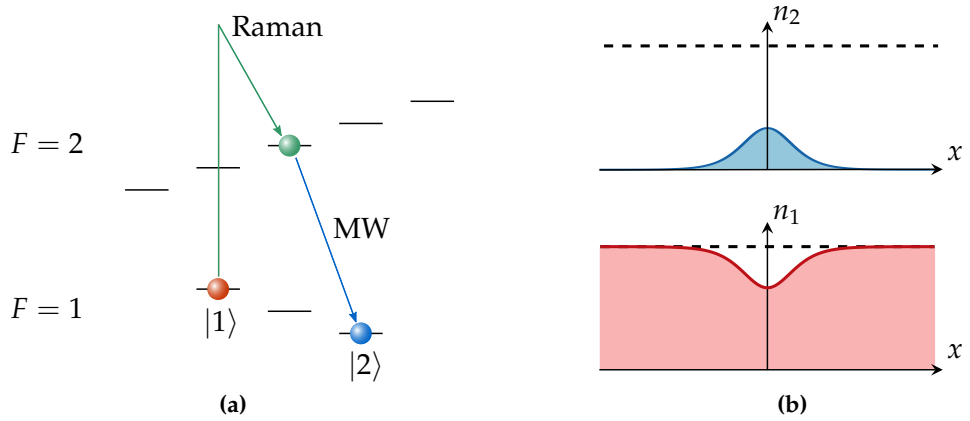

Figure 4.2: **(a)** Scheme of the electronic ground state $^5S_{1/2}$ of ^{87}Rb, with the hyperfine splitting between $F = 1$ and $F = 2$. The degeneracy of the different m_F states is lifted by a quantization field. The atoms are initially in $|1\rangle$. The Raman pulse is represented with the green arrow (two-photon transfer with polarizations π, σ_+), and it is followed by a MW pulse to drive the atoms to the state $|2\rangle$. **(b)** Sketch of the atomic densities in each spin state after the transfer shown in **(a)** is realized. The total density of atoms stays constant. The depletion is modulated through DMD dithering and/or varying the duration of the Raman pulse (see main text for details).

Controlling the depletion

We recall that the two Raman beams are co-propagating, and their intensity is given on the atomic plane by $I_1 s(x, y)$ and $I_2 s(x, y)$. The function s is dimensionless and describes both the Gaussian envelope of the beams and the modulation created by the

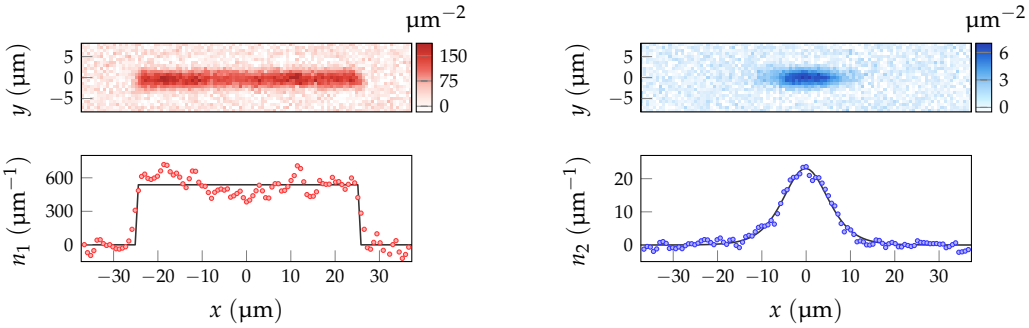

(a) Majority: $|1\rangle = |F = 1, m_F = -1\rangle$ atoms

(b) Minority: $|2\rangle = |F = 1, m_F = +1\rangle$ atoms

Figure 4.3: (a) Top: Absorption image of the initial atomic distribution, obtained from an average of 20 shots. All atoms are in $|1\rangle$. Bottom: Integrated density along the transverse direction, the density is approximately constant along the tube. The solid line is a rectangle that indicates the expected length of 50 μm, and the plateau is set to the average linear density of $\simeq 570\,\mu\text{m}^{-1}$. **(b)** Top: Absorption image of the atomic distribution of atoms in $|2\rangle$, obtained from an average of 15 shots. The wavepacket contains approximately 300 atoms. We displayed a profile $\propto 1/\sqrt{\cosh(\kappa x)}$ on the DMD. We selectively imaged the minority component only, but the bath of atoms in $|1\rangle$ is still present. Bottom: Integrated density along the transverse direction. The solid line is a fit to a bright soliton profile $\propto 1/\cosh^2(\kappa x)$. We obtain $1/\kappa \simeq 6.8\,\mu\text{m}$. Note that $n_2 \ll n_1$, we are well within the low-depletion regime.

DMD. Since the process is coherent, Rabi oscillations occur, and the fraction of transferred atoms after a pulse of duration t is:

$$f(x,y) = \sin^2\left(\Omega_R(x,y)\frac{t}{2}\right) \quad \text{with} \quad \Omega_R(x,y) \propto \sqrt{I_1 I_2}\, s(x,y)\,. \tag{4.13}$$

The Rabi frequency Ω_R is determined from the π-pulse calibration, giving t_π. This calibration is performed with a white image on the DMD, meaning that the maximum amount of light is reflected. We assume that the Gaussian shape of the beams is negligible over the extent of the wavepacket of atoms in $|2\rangle$, meaning t_π is uniform for our purposes. In practice, t_π is evaluated at the location where the wavepacket will be imprinted. Thus, we rewrite:

$$f(x,y) = \sin^2\left(\frac{\pi}{2}\frac{t}{t_\pi}\tilde{s}(x,y)\right)\,, \tag{4.14}$$

where $\tilde{s}$ is the modulation induced by the DMD only. Since the DMD is an amplitude and not an intensity modulator, it is natural to write $\tilde{s} = r^2$, where r is the pattern displayed on the DMD ($0 \leq r \leq 1$). We deduce that to obtain a target atomic distribution f, the DMD must project the pattern:

$$r(x,y) = \sqrt{\frac{t_\pi}{t}\frac{2}{\pi}\arcsin\left(\sqrt{f(x,y)}\right)} \quad \text{with} \quad 0 < t \leq t_\pi\,. \tag{4.15}$$

Naturally, t and f must be chosen to ensure $0 \leq r \leq 1$. Conversely, there are two ways to adjust the amplitude of f: the time of the pulse duration t and the DMD pattern r. These two parameters are used differently depending on the desired transfer fraction f:

- $f \ll 1$: we can linearize the arcsin function. Multiplying f by α then simply requires to change $t \to \sqrt{\alpha}t$ to keep r constant. Thus, we can vary the atomic profile

while maintaining the same DMD image. This was used for the experiments described in Sec. 4.2.

- $f \lesssim 1$: we set $t = t_\pi$ to be able to reach the highest depletion levels. Then, the pattern r is updated for each targeted f. This was used for the experiments described in Sec. 4.3, Chap. 5 and Chap. 6.

We could in principle use $t = t_\pi$ for all desired profiles. However, in the case $f \ll 1$, it would lead to $r \ll 1$, which is detrimental to the dithering used to smooth out the projected images.

4.2 The stationary soliton

4.2.1 Experimental realization

Given the tools discussed in the previous section, we now have all the ingredients necessary to create a bright soliton of the NLSE in our spin mixture. As discussed in Sec. 3.2.5, one could imprint a wavepacket with an arbitrary profile and atom number. If the number is high enough, the wavepacket will converge to a soliton, and additional atoms are radiated toward infinity. However, this approach is not well suited for experiments, since losses and other imperfections, such as finite size effects, may hinder this process. Thus, it is preferable to aim for the correct wavefunction to start with, meaning both the right shape and amplitude. We recall that the bright soliton, solution of GPE Eq. (4.6), is given by:

$$\psi(x,t) = \sqrt{\frac{\kappa N}{2}} \frac{1}{\cosh(\kappa x)} \exp\left(\mathrm{i}\frac{\hbar\kappa^2}{2m}t\right) \quad \text{with} \quad N = \frac{2\hbar^2\kappa}{m|g_{1D}|}, \tag{4.16}$$

where $1/\kappa$ is the width of the wavepacket, and N its atom number. The width is a free parameter, which generates a family of solutions. Since we canceled the potential $V(x)$ of Eq. (4.6) and the Raman beams do not imprint any phase, we focus on the bright soliton with no velocity. Given that we work with a mixture, and in the low-depletion limit, the interaction parameter is dressed by the bath (see Sec. 2.3.2) and can be written:

$$g_{1D} = g_{2,2} - \frac{g_{1,2}^2}{g_{1,1}} \simeq -0.026\, g\,, \tag{4.17}$$

where the second equality used the scattering lengths of Appendix B, and in particular $g_{1,1} = g_{2,2} \equiv g$. Due to the proximity of all interaction constants, we have $g_{1D} \simeq -2\,\delta g$. From the order of magnitude we have for the in-plane confinement, we can estimate for e.g. $1/\kappa = 6.5\,\mu\mathrm{m}$ an atom number $N \simeq 320$ atoms. However, since the potential created with the DMD is not harmonic, this value should be regarded as an order-of-magnitude estimate.

Experimentally, we fix κ by displaying a constant image on the DMD. Then, we varied the Raman pulse duration in order to transfer a different fraction of atoms from the state $|1\rangle$ to the state $|2\rangle$. Identifying the bright soliton amounts to checking which atom number yields a profile which is constant in time. Indeed, when the atom number is too small, the kinetic energy dominates over the interaction energy, causing the wavepacket to spread. Conversely, too many atoms result in the wavepacket contracting. We illustrate this process in Fig. 4.4a, where we highlight three of the curves to show the initial and final profiles.

This behavior can also be explained from the point of view of the IST. An initial profile with an amplitude which is too small (but still contains one eigenvalue λ_1) will

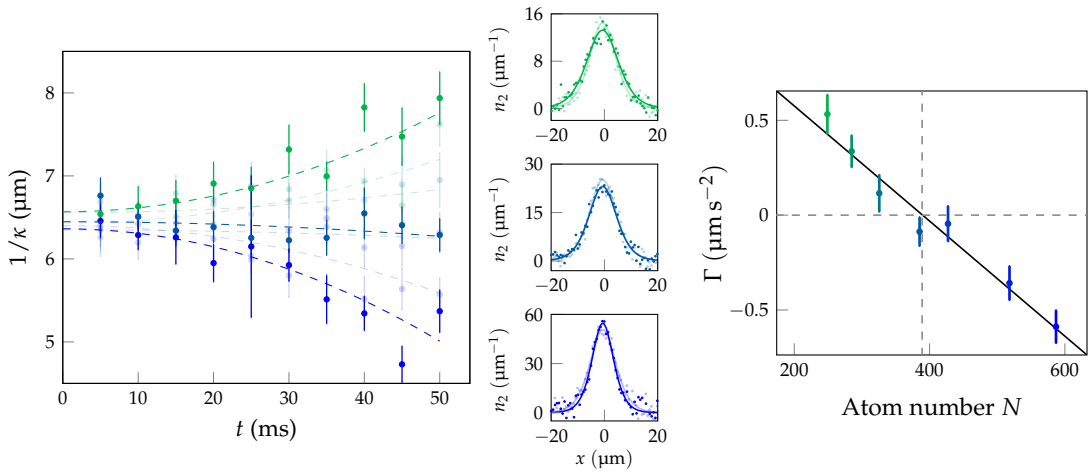

Figure 4.4: **(a)** The profile on the DMD is set to $1/\sqrt{\cosh(\kappa x)}$ with $1/\kappa = 6\,\mu\text{m}$. We observe a slight broadening at $t = 0$, likely due to the imprinting through the microscope objective. Varying the time of the Raman pulse leads to different amplitudes of the wavepacket. The color of the curves encodes the time of the Raman pulse, from lower (green) to higher (blue). We monitor the width of each wavepacket during the first 50 ms of the time evolution. The error bars are 1-σ errors from 12 repetitions of the experiment. The dashed lines are fits with parabolas $1/\kappa_0 + \Gamma t^2$, from which we extract the expansion or contraction rates. Three curves are shown with higher opacity, we highlight on the right their experimental profiles at the beginning (lesser opacity) and the end (higher opacity) of the time evolution. The solid lines correspond to fits with the function $A/\cosh^2(\kappa x)$, where A, κ are free parameters. Note that $n_1 \simeq 570\,\mu\text{m}^{-2}$ and the depletion remains below 0.1. **(b)** Summary of the extracted Γ, as a function of the atom number. The error bars are 1-σ fit errors of the parabolas. We verify that integrating the fitted profiles or the optical density gives compatible values for the atom number N. The solid line represents a linear regression of the points. From this, we determine the corresponding atom number of a bright soliton with initial width $1/\kappa = 6.45(19)\,\mu\text{m}$: we obtain $N = 389(10)$.

converge towards the solitonic profile associated with this eigenvalue. Since $\mathcal{I}(\lambda_1) < \mathcal{I}(\lambda_\kappa) = \kappa/2$, the resulting soliton has a larger width. The detailed study done by [73] shows that the width will oscillate, with some damping, and stabilize towards the solitonic value. The behavior we observe in Fig. 4.4a corresponds to the beginning of these oscillations. The expansion or contraction of each wavepacket is fitted with a parabola of the form $1/\kappa_0 + \Gamma t^2$, which is an approximation at short times of the evolution of the width of wavepackets. The results are summarized in Fig. 4.4b. We identify the atom number of the bright soliton by looking at the intercept of the solid line with zero, and obtain $N = 389(10)$. Thus, we manage to experimentally realize a bright soliton of NLSE, with our spin mixture.

4.2.2 Calibration of the interaction strength

The measurement of the atom number of a bright soliton, shown in Fig. 4.4, can also be interpreted as a calibration of g_{1D}. Indeed, according to Eq. (4.16), $|g_{1D}|$ scales inversely with N. We obtain:

$$g_{1D} = 2\hbar \left(a_{2,2} - \frac{a_{1,2}^2}{a_{1,1}} \right) \omega_\perp \quad \text{with} \quad \omega_\perp = 2\pi \times 334(27)\,\text{Hz}\,. \tag{4.18}$$

Thus, we have measured the interaction strength in our 1D sample, using the mapping of our mixture onto the NLSE. However, we should recall that this picture is only valid in the low-depletion regime. Although n_2/n_0 was kept below 0.1, we can still investigate possible corrections to our calibration. This point is developed in Chap. 5, where we show that the natural soliton of our mixture is the so-called *magnetic soliton*. Of course, it converges towards the bright soliton in the low-depletion limit. Using the results of Chap. 5, we illustrate in Fig. 4.5 the slight adjustment of our calibration of g_{1D}. We use the Root Mean Square (RMS) size of the wavepacket to be able to compare magnetic and bright solitons. We recall the definition:

$$\text{RMS}(f) = \sqrt{\int_{-\infty}^{\infty} x^2 f(x)\,\mathrm{d}x} \quad \text{with} \quad \int_{-\infty}^{\infty} f(x)\,\mathrm{d}x = 1\,, \tag{4.19}$$

which leads to $\text{RMS}\left(|\psi|^2_{\text{bright}}\right) = \pi/(\kappa\sqrt{12})$. We observe in Fig. 4.5 that the size of the wavepacket is modified when considering a magnetic soliton instead of a bright soliton in the low-depletion limit of our mixture. Conversely, using the calibration of Fig. 4.4 as a fixed point, we can adjust the interaction constant to have the curves intersect at this value (inset). We extract a corrected g_{1D}, with $\omega_\perp = 2\pi \times 347(28)$ Hz, to be compared to the result of Eq. (4.18). It corresponds to a 4% adjustment. Thus, the soliton of Fig. 4.4 allowed us to complete the calibration of our system.

4.2.3 "Excitation" of a soliton

The behavior observed in Fig. 4.4 is, in fact, the beginning of some oscillations. A natural question is whether these oscillations correspond to internal eigenmodes of a bright soliton. For certain equations, one can find long-lived oscillatory modes of the wavepacket [179, 244]. However, this behavior occurs only in non-integrable systems; bright solitons do not possess internal modes. This fact can be seen as a consequence of the IST that we described in Chap. 3: when only one eigenvalue is present in the spectrum, the wavepacket will evolve toward the corresponding soliton.

In this section, we detail a more straightforward approach using the Bogoliubov spectrum of a soliton to understand this phenomenon. We have already developed this

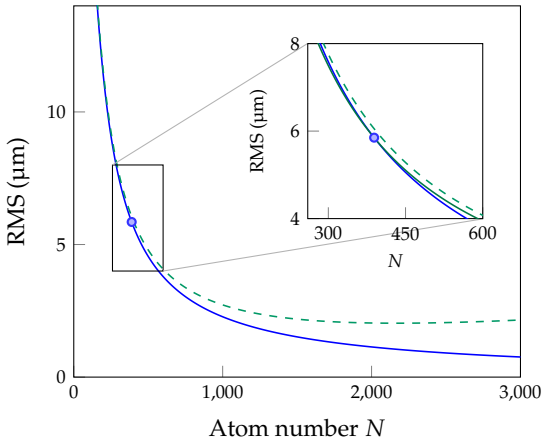

Figure 4.5: Size of the soliton for a given atom number, either the bright soliton (solid blue) or the magnetic soliton (dashed green) for a given g_{1D}. The blue point corresponds to our measure of the bright soliton (error bars have been omitted for clarity), it lies by construction on the solid blue line. The bright and magnetic soliton coincide at low atom number. The zoom highlights the slight discrepancy between the two around the soliton we realized. The additional solid green curve corresponds to the adjustment of a magnetic soliton to the experimental data, accounting for a minor correction to g_{1D}. It yields $\omega_\perp = 2\pi \times 347(28)$ Hz.

method in the case of modulational instability in Sec. 3.4. It consists of considering small perturbations around a known solution, the bright soliton, and linearizing the NLSE at first order in these perturbations. We take $u_0(x) = \kappa/\cosh(\kappa x)$ as the unperturbed bright-soliton wavefunction. We write the perturbed wavefunction:

$$u(x,t) = \left[u_0(x) + \epsilon\left(U(x)\mathrm{e}^{-\mathrm{i}\omega t} + V(x)\mathrm{e}^{\mathrm{i}\omega t}\right)\right]\mathrm{e}^{\mathrm{i}\kappa^2 t}, \tag{4.20}$$

with $\epsilon \ll 1$, and U, V are unknown functions, representing the spatial structure of the eigenmode of energy ω. Linearizing to first order in ϵ yields the following system:

$$\begin{cases} V(x)\left(\kappa^2+\omega\right) = \left(\partial_{xx} + 4|u_0|^2\right)V(x) \;\; + 2u_0^2 U^*(x)\,, \\ U^*(x)\left(\kappa^2-\omega\right) = \left(\partial_{xx} + 4|u_0|^2\right)U^*(x) + 2(u_0^*)^2 V(x)\,. \end{cases} \tag{4.21}$$

The resolution of this system is done in [245], and the results are more explicitly written in [246]. We focus on the energy dispersion, that one can obtain by solving the system in the limit $|x| \to \infty$, for which $u_0 \simeq 0$ [247]. The eigenmodes evolve as plane waves $\mathrm{e}^{\pm ikx}$ and we have:

$$\omega = k^2 + \kappa^2 \to \hbar\omega = \frac{\hbar^2}{2m}\left(k^2+\kappa^2\right) \quad \text{with} \quad k \in \mathbb{R}\,, \tag{4.22}$$

where we put back dimensions in the second expression. The constant term $\hbar^2\kappa^2/2m$ corresponds to $|\mu| = -\mu$, i.e. the chemical potential of the soliton [189]. Since this spectrum is bounded by $|\mu|$, any excitation comes at the cost of extracting one particle from the wavefunction. Moreover, since the eigenmodes behave like plane waves as $|x| \to \infty$, this particle is transported to infinity. Thus, there are no localized eigenmodes of a bright soliton [see 246, Appendix B, for a discussion about the Goldstone modes, which are not relevant in our context].

We illustrate this analysis with a concrete example, using the initial wavefunction:

$$u(x,0) = \underbrace{\frac{1}{\sqrt{1+\epsilon}}}_{A} \underbrace{\frac{1+\epsilon}{\cosh((1+\epsilon)x)}}_{\frac{\kappa_i}{\cosh(\kappa_i x)}} \quad \text{with} \quad \epsilon \ll 1\,. \tag{4.23}$$

We have that $\int |u|^2 \,\mathrm{d}x = 2$, the same mass as a bright soliton with $\kappa = 1$. What is the behavior of such a wavefunction? Some Bogoliubov modes become excited and carry particles from the initial wavefunction to infinity. The interference between these modes and the final wavefunction results in oscillations of the width of the wavepacket [see e.g. 246, Eq. (14-15)]. From Eq. (4.22), we deduce that the lowest frequency is given by $\hbar\kappa^2/2m$. This behavior is shown in Fig. 4.6a, where we simulate the evolution of the wavefunction of Eq. (4.23) with $\epsilon = 0.1$. This situation was experimentally realized in [248], and we highlight their results in Fig. 4.6b. A bright soliton was formed in a cigar-shaped trap. Then, they used a Feshbach resonance in order to quench the interaction parameter to a slightly different value. This amounts to a change of the width of the soliton, keeping constant the number of particles (see Eq. (3.4)).

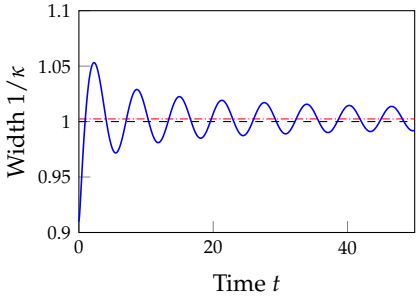

(a)

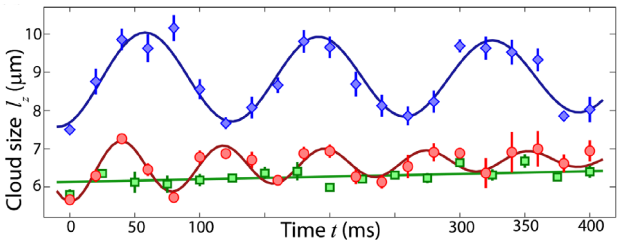

(b) Figure adapted from [248].

Figure 4.6: (a) Time evolution of the width of the wavefunction of Eq. (4.23) with $\epsilon = 0.1$, using a numerical simulation of GPE. The oscillations dampen towards the asymptotic limit $1/\kappa_f$ (see main text), shown with the red dashed-dotted line. The black dashed line is set to 1, and represents the width of a bright soliton with the mass of the initial wavepacket. **(b)** Experimental realization of the "excitation" of a bright soliton. The blue diamonds / curve result from a quench of the longitudinal frequency of the trap ω_z. The wavepacket oscillates at a frequency $\sqrt{3}\omega_z$ [249, 250]. When instead the interaction strength is quenched (red circles / curve) a different frequency is observed, following the interference with the Bogoliubov modes excitations. The green squares / curve are obtained when creating a bright soliton.

A more quantitative analysis can be performed using the IST. The eigenvalue of the wavefunction of Eq. (4.23) is $\lambda = \mathrm{i}\,(A - 1/2)\,\kappa_i$ [73]. The wavefunction will evolve towards the corresponding bright soliton of width $1/\kappa_f$, with $\mathrm{i}\kappa_f/2 = \lambda$ (see Sec. 3.2.5). We can deduce the amount of radiated particles N_r:

$$N_r = \underbrace{2}_{N_i} - \underbrace{2\kappa_f}_{N_f} = 2\left(1 - \sqrt{1+\epsilon}\right)^2 \sim \frac{\epsilon^2}{2}\,, \tag{4.24}$$

where we used the fact that the initial mass is equal to 2. We note that, owing to the quadratic dependence, N_r remains much smaller than the total atom number (see Sec. 4.3.2 for a discussion on experimental parameters and observing N_r). Eventually, the oscillations shown in Fig. 4.6a dampen, and the width reaches the limit $1/\kappa_f$. Thus,

the unperturbed bright soliton u_0 of Eq. (4.20) has a width $1/\kappa_f$ and the oscillation frequency is given by $\hbar\kappa_f^2/2m$, meaning the chemical potential of the final state.

4.3 Producing higher-order solitons

In the previous section, we explored the realization of a bright soliton and discussed perturbations to this solution. In Sec. 3.3.3 we discussed the possibility of obtaining multi-soliton solutions through the IST. In particular, [73] showed that using $u_n(x,0) = n\kappa/\cosh(\kappa x), n \in \mathbb{N}$, gives n eigenvalues, aligned along the imaginary axis. We have illustrated in Fig. 3.10 the cases $n = 2$ and $n = 3$. The experimental realization of such higher-order solitons is the focus of this section.

4.3.1 Study of the frequency

Since the n-soliton wavefunctions are real and positive at $t = 0$, we can use the Raman beams to imprint them directly onto the atoms. Moreover, they are proportional to the bright soliton by a factor n: creating a wavepacket with the same shape as a bright soliton but with an atom number scaled by n^2 realizes an n-soliton. We show in Fig. 4.7 experimental images for the case $n = 2$. We observe successive contractions and expansions of the wavepacket, with a periodic evolution. This breathing pattern was already observed by [75], using a single-component gas of ^{7}Li. Further insight can be gained

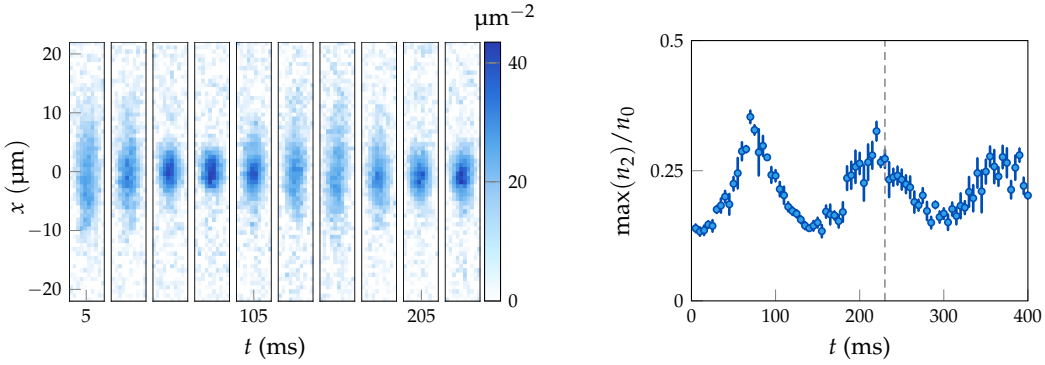

Figure 4.7: (a) Experimental images of the time evolution of a two-soliton of NLSE. The successive contractions and expansions of the wavepacket appear clearly. The initial width is set to $1/\kappa = 8\,\mu$m. The images are averaged from 15 repetitions of the experiment. **(b)** Maximum depletion of the minority component, obtained from a fit of the density profile with Eq. (4.28). The dashed gray line denotes the time of the last image of **(a)**. We obtain that $n_2/n_0 \lesssim 1/3$ at all times, compatible with a low-depletion regime. The error bars are 1-σ errors from 15 repetitions of the experiment.

from the results of the IST. Indeed, the eigenvalues of the two-soliton solution are:

$$\lambda_1 = \mathrm{i}\frac{\kappa}{2} \quad \text{and} \quad \lambda_2 = \mathrm{i}\frac{3\kappa}{2}\,. \tag{4.25}$$

Plugging these values in the kernel F, defined in Eq. (3.44b), of the Gelfand-Levitan-Marchenko integral equation, we obtain:

$$\begin{aligned} F(x,t) &= -\mathrm{i}\left(\tilde{c}_1(t)\mathrm{e}^{\mathrm{i}\lambda_1 x} + \tilde{c}_2(t)\mathrm{e}^{\mathrm{i}\lambda_2 x}\right)\,, \\ &= -\mathrm{i}\mathrm{e}^{-\mathrm{i}\kappa^2 t}\left(\tilde{c}_1(0)\mathrm{e}^{-\kappa x/2} + \tilde{c}_2(0)\mathrm{e}^{-8\mathrm{i}\kappa^2 t}\mathrm{e}^{-3\kappa x/2}\right)\,, \end{aligned} \tag{4.26}$$

where we used $b(\xi) = 0$ for the two-soliton wavefunction. We can gain some insight without performing the inversion of the scattering data. Since the overall phase factor of F is irrelevant, we deduce that F is periodic with frequency:

$$f = \frac{4}{\pi}\kappa^2 \rightarrow f = \frac{2}{\pi}\frac{\hbar\kappa^2}{m}, \tag{4.27}$$

where we reintroduced dimensions in the second expression. This periodicity is directly transferred to the function $u(x,t)$ through the linear Gelfand-Levitan-Marchenko Eq. (3.43). Remarkably, the frequency depends only on κ, and the interaction strength g_{1D} does not appear. This stems from the relation $1/t_0 = \hbar/(2mx_0^2)$ linking the quantities of Eq. (3.4). We verify this relation experimentally by extracting the breathing frequency of the wavepacket. We present the results in Fig. 4.8 for a wavepacket of width $1/\kappa = 8\,\mu$m, and we confirm that we manage to realize a two-soliton. We did not vary the wavepacket width, as significantly larger widths are not feasible in our finite-size system. Additionally, a smaller width implies a larger depletion, which is beyond the scope of the NLSE description. It will be the subject of Chap. 5, in which we provide a more general description of our mixture.

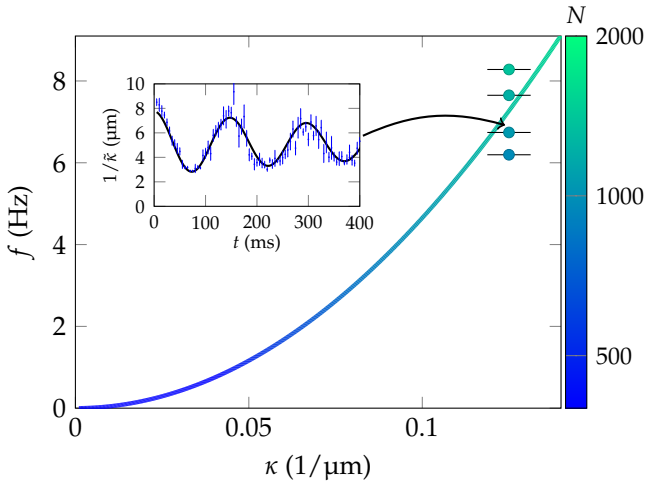

Figure 4.8: The solid line indicates the breathing frequency of the exact two-soliton solution $2\kappa/\cosh(\kappa x)$, given by Eq. (4.27). It is color-coded by the atom number on a logarithmic scale, calculated from the calibration performed on the bright soliton. The circles are experimental data, using an imprinted width of $1/\kappa = 8\,\mu$m. The atom number in the wavepacket was slightly varied between each point, due to our experimental uncertainty on the amplitude to imprint for the two-soliton. Thus, they are slightly spread out vertically. The fact that they surround the solid line indicates the consistency of our calibrations and the experiment. Inset: time evolution of the width of the wavepacket, for the set of images shown in Fig. 4.7a (i.e. one given atom number). The error bars are 1-σ errors from 15 repetitions of the experiment. The frequency is extracted by fitting with a damped sine (solid black line, discussed in Sec. 4.3.2).

The wavepacket width at time t is obtained by fitting the atomic density profile with the function:

$$v_t(x) = \frac{A}{\cosh^2(\tilde{\kappa}(x - x_0))}, \tag{4.28}$$

where $A, \tilde{\kappa}, x_0$ are fitting parameters. It corresponds to the analytic solution of the two-soliton at times $t_k = k/f, k \in \mathbb{N}$. For $t \neq t_k$, one could resort to the exact solution given by Eq. (3.71). We decided not to use this solution on experimental data for two reasons:

- The function v_t is more robust to fit (imperfect) atomic images which include shot noise, atom loss, etc.
- We slightly varied the imprinted amplitude of the atomic wavefunction, meaning we set n close to 2 only up to experimental uncertainties. Thus, Eq. (3.71) does not describe perfectly all data either.

We verified on a numerical example the overlap of the fitted functions $v_t(x)$ and the exact solution $w = |u(x,t)|^2$ by computing:

$$I(t) = \frac{\|\langle w|v_t\rangle\|^2}{\|\langle w|w\rangle\|\|\langle v_t|v\rangle\|} = \frac{\int |w(x,t)v_t(x)|\,\mathrm{d}x}{\sqrt{\int |w(x,t)|^2\,\mathrm{d}x \int |v_t(x)|^2\,\mathrm{d}x}}\,. \tag{4.29}$$

We have $I \leq 1$ from the Cauchy–Schwarz inequality, and $I(t_k) = 1$. We obtain that $\overline{I(t)} \simeq 0.97$, where $\bar{\cdot}$ indicates the time average over one period, and $\forall\, t, I(t) > 0.93$. Thus, the function v_t provides a reliable estimate of the atomic wavefunction's RMS width.

4.3.2 Damping and radiation

Damping of the oscillations

As shown in the inset of Fig. 4.8, the width oscillations exhibit significant damping. This observation goes beyond the description established in Chap. 3, since the two-soliton solution is exactly periodic. We used a damped sine function to calibrate this decay:

$$\frac{1}{\tilde{\kappa}(t)} = A\mathrm{e}^{-t/\tau}\cos(2\pi f t) + o\,, \tag{4.30}$$

where A, τ, f, o are fitting parameters. Once again, this function does not correspond to the exact two-soliton solution, but it captures the experimental behavior, as well as that of wavefunctions slightly deviating from Eq. (3.71). For the two-soliton, we have $\tau \to \infty$. One possible explanation for the observed damping is that the imprinted wavefunction amplitude was slightly offset:

$$u_{\text{target}}(x) = \frac{2\kappa}{\cosh(\kappa x)} \to u_{\text{imprinted}}(x) = \frac{2\alpha\kappa}{\cosh(\kappa x)}\,, \tag{4.31}$$

where $\alpha \simeq 1$. This would lead to the atom number being off by a factor α^2, and also affects the oscillation frequency, by a factor $(2\alpha - 1)$ [73]. In addition, this excitation induces Bogoliubov modes (i.e. $b(\tilde{\xi}) \neq 0$), which interfere with the two-soliton. This interference could manifest as damping on the first oscillations. We test this hypothesis by performing numerical simulations of the GPE. However, we observe two discrepancies with the experimental points:

- The order of magnitude is incorrect. For example, taking $\alpha = 0.95$ yields $f_{\text{GPE}} \simeq 6.5\,\text{Hz}$, close to the curve shown in Fig. 4.8, but $\tau_{\text{GPE}} \simeq 3.0\,\text{s}$ whereas we observe $\tau = 0.64(8)\,\text{s}$.
- When $\alpha > 1$ there is no damping, and the amplitude rather increases during the first oscillations. This is inconsistent with the experimental data, for which the damping is similar on all points.

Therefore, we must consider a second hypothesis. Finite-temperature effects may perturb the exact solution. However, they are difficult to characterize, and lie beyond the

scope of this manuscript. Instead, we examine the effect of a weak harmonic-oscillator potential. This amounts to breaking the integrability of NLSE (we will discuss more thoroughly perturbations of the IST in Chap. 6). This hypothesis is reasonable given the discussions of Sec. 4.1.3. Thus, we add a potential term $V(x) = \frac{1}{2}m(2\pi f_{\mathrm{HO}})^2x^2$ to the numerical simulations of the GPE and vary f_{HO}. The results are presented in Fig. 4.9, where we fitted the time evolution of the width using Eq. (4.30) to extract τ. We deduce

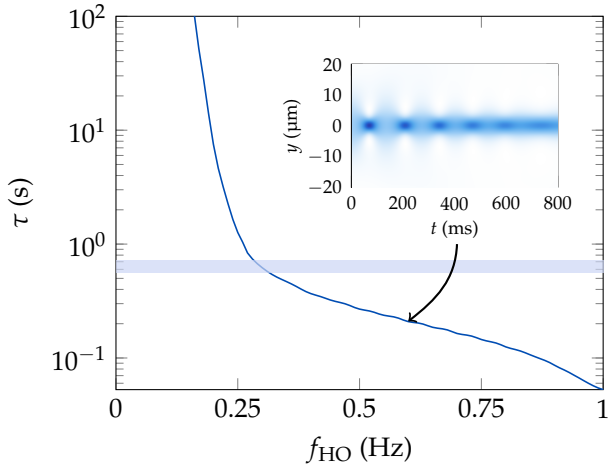

Figure 4.9: We simulate the time evolution of the initial wavefunction $2\kappa/\cosh(\kappa x)$, adding a harmonic potential of frequency f_{HO} in the NLSE. The damping τ diverges when $f_{\mathrm{HO}} \to 0$. The blue area indicates the value of τ corresponding to the inset in Fig. 4.8, with its width representing the 1-σ uncertainty. This damping is compatible with a frequency $f_{\mathrm{HO}} \simeq 0.3\,\mathrm{Hz}$. The inset illustrates the time evolution for $f_{\mathrm{HO}} = 0.6\,\mathrm{Hz}$, the decay of the oscillations is clearly visible. Note that a resurgence of the breathing pattern appears, beyond the experimental time frame [246].

that a frequency $f_{\mathrm{HO}} \lesssim 0.5\,\mathrm{Hz}$ is sufficient to explain the experimental observations. This value is compatible with our estimate of the quadratic field, and affects by less than 0.1 % the density of the bath. We also note that in [75] they used $f_{\mathrm{HO}} = 1.12\,\mathrm{Hz}$. In both cases, we verify $f/f_{\mathrm{HO}} \gg 1$; the breathing frequency is dominated by the two-soliton.

We mention two additional factors, which have negligible effects:

- Atom loss: the one-body lifetime of the cloud is approximately 2 s. Thus, more than 80% of the atoms remain after 400 ms. A significant atom loss leads to a chirp of the oscillation frequency [251], which is not observed on the experimental data.
- Averaging: due to the fluctuations in the imprinted atom number, each repetition of the experiment gives a slightly different frequency. This may lead to dephasing. However, we verify that this effect is negligible by measuring the fluctuations at $t = 0$. We have $\delta N_2/N_2 \lesssim 6\%$ for all datasets, corresponding at first order to $\delta f/f \lesssim 6\%$. Thus, the dephasing is negligible on the observed timescale.

Radiated atoms

A second criterion to identify a two-soliton, in addition to its breathing frequency, is the absence of excited Bogoliubov modes. Thus, it is (in theory) possible to measure the atom number radiated from the original wavepacket: the minimum would correspond to the realization of a two-soliton. To make this reasoning more quantitative, we can extrapolate the discussion of Sec. 4.2.3 in the case of a two-soliton. Taking an initial

perturbed wavefunction given by Eq. (4.31), we calculate the number of radiated atoms:

$$\frac{N_i - N_f}{N_i} = \frac{8\kappa(\alpha-1)^2}{8\kappa\alpha^2} = \left(1 - \frac{1}{\alpha}\right)^2, \tag{4.32}$$

where N_i, N_f are the initial and final atom number in the wavepacket respectively. In practice, $\alpha \simeq 1$. Taking for instance $\alpha = 0.95$, we expect radiated atoms to account for approximately 0.3% of the total atom number. In our experiment, this amounts to 3-4 atoms; this is not detectable in our system.

Conclusion

In this chapter, we have demonstrated the experimental realization of multi-solitons and established a quantitative connection with the predictions of the IST. By imprinting tailored wavefunctions onto a 1D BEC, we generated two-soliton states and observed their characteristic periodic breathing dynamics. The measured oscillation frequency was found to agree with the theoretical value derived from the IST eigenvalue spectrum, confirming the underlying integrable structure of the NLSE.
We will develop in Chap. 5 a more complete description of our spin mixture, allowing us to realize solitonic states with an arbitrary depletion. This description will provide new insights on the spin dynamics, and extend the IST description.

III The Landau-Lifschitz description and results beyond integrability

5 Landau-Lifschitz multi-solitons in a Bose mixture

Outline of the current chapter

Introduction

The easy-axis Landau-Lifshitz Equation (LLE) provides a classical field description of a one-dimensional ferromagnet with uniaxial anisotropy, supporting localized excitations known as magnetic solitons. In our experiment, this model becomes directly relevant through its mapping onto the dynamics of a two-component spin mixture (Sec. 5.1).

A remarkable feature of the easy-axis LLE is its gauge equivalence to the attractive NLSE (Sec. 5.2), an integrable equation whose soliton content and scattering properties were recalled in Chap. 3. This equivalence offers a powerful route to constructing and interpreting solutions of the LLE: any NLSE soliton or multi-soliton solution can be mapped to a corresponding magnetic configuration in the spin mixture (Sec. 5.3). Exploiting this correspondence experimentally, we engineer multi-soliton states of the LLE and observe their subsequent time evolution (Sec. 5.4).

5.1 The Landau-Lifschitz equation

We introduce in this section an alternative description of our spin mixture, based on a formal analogy with a 1D ferromagnetic spin chain. Such an object is generally characterized by its local magnetization $\mathbf{M}(x,t)$. From this classical point of view, the dynamics are obtained from the LLE, first established by [252]. In a setting with uniaxial anisotropy, the LLE reads:

$$\frac{\partial \mathbf{M}}{\partial t} = \mathbf{M} \times \left(\frac{\partial^2 \mathbf{M}}{\partial x^2} + \beta (\mathbf{M} \cdot \mathbf{e}_z) \mathbf{e}_z \right) , \tag{5.1}$$

where $\mathbf{e}_z$ is the unit vector along the z axis, and β characterizes the magnetic anisotropy. We will detail the physical origin and meaning of this equation before linking it to our spin mixture and introducing some fundamental solutions: the magnetic solitons.

5.1.1 The 1D ferromagnetic spin chain

We follow in this section the development of [77]. A magnetic material with localized spins $\hat{\mathbf{S}}_i$ can be described by the Heisenberg XYZ Hamiltonian:

$$\hat{H} = -\frac{1}{2} \sum_{\langle i,j \rangle} \left(J_x \hat{S}_i^{(x)} \hat{S}_j^{(x)} + J_y \hat{S}_i^{(y)} \hat{S}_j^{(y)} + J_z \hat{S}_i^{(z)} \hat{S}_j^{(z)} \right) , \tag{5.2}$$

where J_k are positive constants denoting the exchange interaction along axis k, and the sum on j runs only over the nearest neighbors. We can formally rewrite this Hamiltonian by introducing $\hat{\mathbf{B}}_{\text{eff},i}$, corresponding to the local magnetic field generated by adjacent spins:

$$\hat{H} = \gamma \sum_i \hat{\mathbf{S}}_i \cdot \hat{\mathbf{B}}_{\text{eff},i} \quad \text{with} \quad \hat{B}_{\text{eff},i}^{(k)} = -\frac{J_k}{2\gamma} \left(\hat{S}_{i+1}^{(k)} + \hat{S}_{i-1}^{(k)} \right) , \tag{5.3}$$

where γ has the dimension of a gyromagnetic ratio. Using the Heisenberg equation of motion, we obtain for each spin i:

$$\frac{\partial \hat{\mathbf{S}}_i}{\partial t} = -\gamma \hat{\mathbf{S}}_i \times \hat{\mathbf{B}}_{\text{eff},i} . \tag{5.4}$$

The LLE is recovered in the long-wavelength approximation, which assumes that the spin dynamics vary slowly over a lattice spacing and can therefore be described in the

continuum limit. We define the magnetization as $\mathbf{M}(x_i) \propto \langle \hat{\mathbf{S}}_i \rangle$ and assume that the exchange interaction constants J_k are close to each other. This leads to:

$$\frac{\partial \mathbf{M}}{\partial t} = \gamma \mathbf{M} \times \mathbf{B}_{\text{eff}} \quad \text{with} \quad \mathbf{B}_{\text{eff}} = \left(\alpha \frac{\partial^2 \mathbf{M}}{\partial x^2} + (J_x - J_y) M^{(x)} \mathbf{e}_x + (J_z - J_y) M^{(z)} \mathbf{e}_z \right) , \quad (5.5)$$

where $M^{(k)} = \mathbf{M} \cdot \mathbf{e}_k$, and α is a positive constant, related to the inner spacing between spins. This equation describes the general case of a biaxial ferromagnet, for which $J_x \neq J_y \neq J_z$. In the following, we focus on the uniaxial case $J_x = J_y$. Introducing $\beta = J_z - J_y$, we recover Eq. (5.1) after rescaling time and space into dimensionless units.

The physical interpretation of the different terms in $\mathbf{B}_{\text{eff}}$ is straightforward. The second derivative of the magnetization corresponds to the exchange energy, which favors the local alignment of neighboring spins. The anisotropic term accounts for the differences between the exchange coefficients J_k, thereby favoring alignment along specific directions. In particular, setting $\beta > 0$ leads to the so-called *easy-axis* anisotropy, where the magnetization aligns along the z axis in the ground state, whereas $\beta < 0$ corresponds to the *easy-plane* anisotropy, for which the magnetization lies in the x–y plane.

Angular variables description

The norm of the magnetization $\|\mathbf{M}\|$ is a conserved quantity of Eq. (5.1). Assuming that it is spatially uniform, we can parametrize the magnetization using spherical coordinates:

$$\mathbf{M} = \begin{pmatrix} \sin(\theta)\cos(\varphi) \\ \sin(\theta)\sin(\varphi) \\ \cos(\theta) \end{pmatrix} \quad (5.6)$$

where we have set $\|\mathbf{M}\| = 1$ without loss of generality. The LLE (5.1) can then be rewritten as a pair of coupled equations for θ and φ [77]:

$$\begin{cases} \dfrac{\partial}{\partial t}\left[\cos(\theta)\right] = -\dfrac{\partial}{\partial x}\left(\sin^2(\theta)\dfrac{\partial \varphi}{\partial x}\right) \\ \sin(\theta)\dfrac{\partial \varphi}{\partial t} = \dfrac{\partial^2 \theta}{\partial x^2} - \sin(\theta)\cos(\theta)\left(\beta + \left(\dfrac{\partial \varphi}{\partial x}\right)^2\right) . \end{cases} \quad (5.7)$$

This formulation will allow for a direct connection with our spin mixture.

5.1.2 Mapping to a spin mixture

The mean-field description of our system involves the two spin components ψ_1 and ψ_2, whose evolution follows the coupled GPE (2.39). Since these fields are complex, they can be expressed in terms of four real variables. In order to establish a link with Eq. (5.7), it is necessary to reduce the description to two independent variables.

We consider the experimentally relevant case where $g_{1,1} = g_{2,2} \equiv g$ and $\delta g = g_{1,2} - g \ll g$. In this limit, the total density can be approximated as constant,[1] so that $n_1 + n_2 = n_0$ [76, 253]. Introducing the angles θ and φ, and the global phase χ, we write:

$$\begin{pmatrix} \psi_1 \\ \psi_2 \end{pmatrix} = \sqrt{n_0}\, e^{i\chi/2} \begin{pmatrix} \cos(\theta/2) e^{-i\varphi/2} \\ \sin(\theta/2) e^{+i\varphi/2} \end{pmatrix} , \quad (5.8)$$

[1] The correction term is of order $\delta g / g \simeq 0.01$. Strictly speaking, this approximation is valid only when neither n_1 nor n_2 are too close to zero [253].

where the individual phases are $\phi_1 = (\chi - \varphi)/2$ and $\phi_2 = (\chi + \varphi)/2$. The total particle current is given by:

$$J(x,t) = \frac{\hbar}{m}\mathcal{I}\left(\psi_1^*\frac{\partial\psi_1}{\partial x} + \psi_2^*\frac{\partial\psi_2}{\partial x}\right) = \frac{\hbar n_0}{2m}\left(\frac{\partial\chi}{\partial x} - \cos(\theta)\frac{\partial\varphi}{\partial x}\right). \tag{5.9}$$

Thus, we can express the global phase χ as a function of θ, φ and J. Because the total density is assumed constant, we have $\partial_x J = 0$. Choosing the reference frame such that $J(x,t) = 0$, we find:

$$\frac{\partial\chi}{\partial x} = \cos(\theta)\frac{\partial\varphi}{\partial x}. \tag{5.10}$$

In fact, setting $J = 0$ is justified for a system with strict boundary conditions. The more general case is discussed in [106, Sec. 2.3.3]. Substituting Eq. (5.8) into the coupled GPE (2.39) and eliminating χ via Eq. (5.10), we obtain the following equations on θ and φ:

$$\begin{cases} \dfrac{\partial}{\partial t}\left[\cos(\theta)\right] = \dfrac{\partial}{\partial x}\left(\sin^2(\theta)\dfrac{\partial\varphi}{\partial x}\right) \\ \sin(\theta)\dfrac{\partial\varphi}{\partial t} = \dfrac{\partial^2\theta}{\partial x^2} - \sin(\theta)\cos(\theta)\left(\mathrm{sign}(\delta g) + \left(\dfrac{\partial\varphi}{\partial x}\right)^2\right). \end{cases} \tag{5.11}$$

We have used dimensionless variables defined through the spin healing length $\xi_s = \hbar/\sqrt{2mn_0|\delta g|}$ and characteristic time $\tau_s = \hbar/(n_0|\delta g|)$. The correspondence between Eq. (5.7) and (5.11) is then immediate: the spin mixture behaves as a ferromagnetic spin chain with anisotropy parameter $\beta = \mathrm{sign}(\delta g) = \pm 1$. This analogy is illustrated in Fig. 5.1, where we sketch a magnetic soliton (a localized excitation, see Sec. 5.1.3) for both a spin chain and a two-component spin mixture. Thus, an immiscible mixture ($\delta g > 0$)

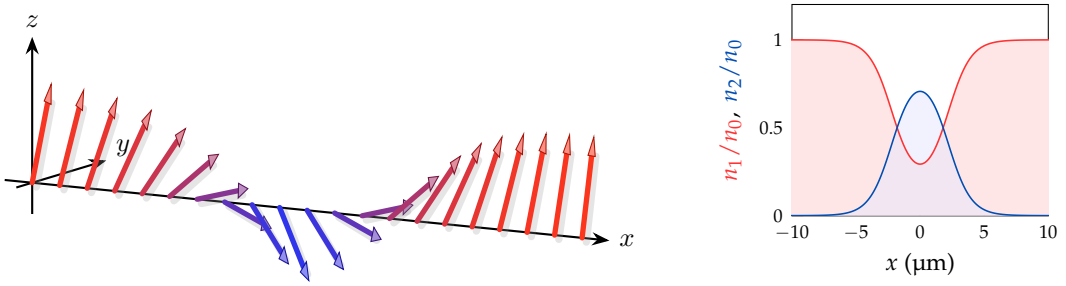

(a) Ferromagnetic spin chain **(b)** Two-component spin mixture

Figure 5.1: (a) 1D spin chain for an easy-axis ferromagnet. Each arrow represents the magnetization on a given site. The color indicates the angle θ with the z axis. This configuration illustrates a magnetic soliton at rest, for which $\varphi = 0$. **(b)** Immiscible spin mixture described by coupled GPE. We have a bath of atoms in $|1\rangle$, in which are immersed a packet of atoms in $|2\rangle$. The equilibrium state corresponds to a magnetic soliton.

is equivalent to an easy-axis ferromagnet: a spin pointing along z corresponds to a fully polarized state, with $n_1 = n_0$ or $n_2 = n_0$. We thereby recover the demixed configuration described in Sec. 2.3. Conversely, a miscible mixture ($\delta g < 0$) maps to an easy-plane ferromagnet, for which the spin lies predominantly in the transverse x–y plane.

Low-depletion limit

We have discussed in Sec. 2.3.2 the limit $n_2/n_0 \ll 1$, under which our spin mixture can be described by a single effective GPE. Using the spherical coordinates θ and φ, this

corresponds to the condition $\theta \ll 1$. Following [77], we introduce the complex field ψ as:

$$\psi = \sqrt{|\beta|}\,\frac{M^{(x)} + \mathrm{i}M^{(y)}}{2} \quad \text{and} \quad M^{(z)} = \sqrt{1 - \frac{4}{|\beta|}|\psi|^2} \simeq 1 - \frac{2}{|\beta|}|\psi|^2\,, \tag{5.12}$$

where the last approximation holds for $\theta \ll 1$. Eq. (5.1) can then be rewritten in the form:

$$\mathrm{i}\frac{\partial\psi}{\partial t} = -M^{(z)}\frac{\partial^2\psi}{\partial x^2} + \psi\frac{\partial^2 M^{(z)}}{\partial x^2} + \beta M^{(z)}\psi\,. \tag{5.13}$$

We substitute $M^{(z)}$ by its expansion to first order in $|\psi|^2$, retaining only the leading nonlinear term proportional to $|\psi|^2\psi$. We neglect higher-order nonlinearities, which involve spatial derivatives. Disregarding terms proportional to ψ, which can be removed through a gauge transformation, we obtain:

$$\mathrm{i}\frac{\partial\psi}{\partial t} + \frac{\partial^2\psi}{\partial x^2} + 2\,\mathrm{sign}(\beta)|\psi|^2\psi = 0\,, \tag{5.14}$$

which is the canonical dimensionless form of the GPE. The sign of β determines whether the interactions are attractive or repulsive, in agreement with the effective coupling constant derived in Eq. (2.46). Besides, we recover $\psi = \psi_2$ in the limit $\theta \to 0$, which was expected following the low-depletion limit established in Sec. 2.3.2.

5.1.3 The magnetic soliton

The ground state of Eq. (5.1) corresponds to a uniform chain of spins aligned along the z axis. We now investigate the solitary-wave excitations of the LLE [254], which are known as *magnetic solitons*. We summarize here some key results and refer the interested reader to [77] for a comprehensive review. Magnetic solitons were first experimentally realized in cold-atom systems with miscible spin mixtures, corresponding to the easy-plane ferromagnetic regime ($\delta g < 0$) [214, 255]. In the following, we focus on the easy-axis configuration, $\delta g > 0$.

We look for traveling-wave solutions of the form [77]:

$$\theta(x,t) = \theta(x - vt) \quad \text{and} \quad \varphi(x,t) = \phi(x - vt) + \Omega t\,, \tag{5.15}$$

where v denotes the soliton velocity and Ω is an internal precession frequency. Including the parameter Ω allows one to derive a more general family of solutions [whereas setting $\Omega = 0$, as in e.g. 256, restricts the class of accessible solutions]. Then, the system of Eq. (5.7) can be integrated to obtain [see 77, 86, for mathematical details]:

$$\begin{cases} \cos(\theta(\tilde{x})) = 1 - \dfrac{4\kappa^2}{2 + \Omega + \sqrt{\Omega^2 + v^2}\cosh(2\kappa\tilde{x})} \\ \phi(\tilde{x}) = \dfrac{1}{2}v\tilde{x} + \arctan\left[\dfrac{2\Omega - v^2 + 2\sqrt{\Omega^2 + v^2}}{2\kappa v}\tanh(\kappa\tilde{x})\right], \end{cases} \tag{5.16}$$

where $\kappa = \sqrt{1 + \Omega - v^2/4}$ and $\tilde{x} = x - vt$. Solutions exist only when the condition $\Omega - v^2/4 > -1$ is satisfied. The quantity $1/\kappa$ characterizes the width of the wavepacket. In the low-depletion limit, $1/\kappa$ tends to the width of a bright soliton, see e.g. Eq. (3.46).

Conserved quantities

The solutions described by Eq. (5.16) correspond to magnetic solitons. In light of the discussions in Chap. 3, the existence of a soliton basis suggests that the LLE is integrable via the IST. This point will be developed in Sec. 5.2. We simply highlight here the existence of several important conserved quantities [86, 257]:

- The magnetization N:
$$N = \frac{1}{2}\int_{-\infty}^{+\infty} [1-\cos(\theta)]\,\mathrm{d}x \tag{5.17}$$
which quantifies the spin deviation from the ground state. In the spin-mixture picture, it corresponds to the number of atoms N_2 in the minority component $|2\rangle$, given in dimensional units by $N_2 = n_0\xi_s N$. It can be expressed as a function of Ω and v:
$$\sinh(N) = \frac{2\kappa}{\sqrt{\Omega^2+v^2}}\,. \tag{5.18}$$

- The total momentum P:
$$P = \frac{1}{2}\int_{-\infty}^{+\infty} [1-\cos(\theta)]\,\frac{\partial\varphi}{\partial x}\,\mathrm{d}x\,. \tag{5.19}$$
Using Eq. (5.10), we can rewrite P as a function of the phase of the majority component $\phi_1 = (\chi-\phi)/2$. This leads to the expression:
$$P = \phi_1(-\infty) - \phi_1(+\infty) = \Delta\phi_1\,. \tag{5.20}$$

- The energy E:
$$E = \frac{1}{4}\int_{-\infty}^{+\infty}\left\{\left(\frac{\partial\theta}{\partial x}\right)^2 + \sin^2(\theta)\left[1+\left(\frac{\partial\varphi}{\partial x}\right)^2\right]\right\}\mathrm{d}x\,. \tag{5.21}$$
For a magnetic soliton, it can be expressed as:
$$E = 2\kappa = 2\tanh(N/2) + 4\frac{\sin^2(P/2)}{\sinh(N)}\,. \tag{5.22}$$
The energy is thus a periodic function of the momentum. This property suggests the existence of Bloch Oscillations (BOs) in this system [257, 258], which will be discussed in Sec. 5.1.4.

The number of atoms N does not uniquely define a magnetic soliton: a constant N corresponds to an ellipse in the Ω-v plane. This property is illustrated in Fig. 5.2. The point $(\Omega, v) = (0,0)$ corresponds to $N \to \infty$, where the minority component forms a domain extended over the whole space, thus fully replacing the majority component. Larger ellipses around this point correspond to solitons with a smaller number of atoms in the minority component.

The ensemble of solutions at a given N lead to different momenta and energies, as shown in Fig. 5.3. Only the solution for which $P = \Delta\phi_1 = 0$ minimizes the energy, whereas $P = \pm\pi$ maximizes it. This property follows immediately from Eq. (5.22).

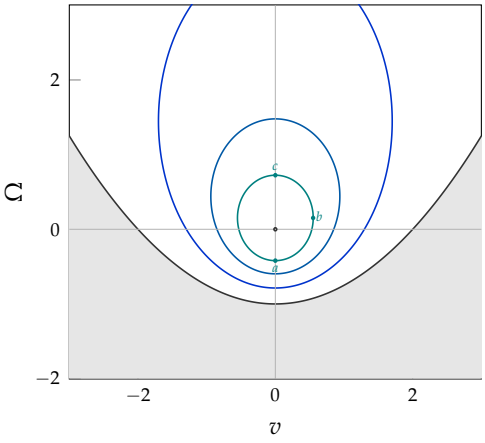

Figure 5.2: Schematic representation of the Ω-v plane characterizing the magnetic solitons. The gray area indicates the region where no magnetic soliton exists. The point $(\Omega, v) = (0, 0)$ is also excluded. The ellipses correspond to contours of constant N, with $N = 1, 1.5$, and 2 from blue to green. The magnetic solitons at the points a, b, and c are illustrated in Fig. 5.3.

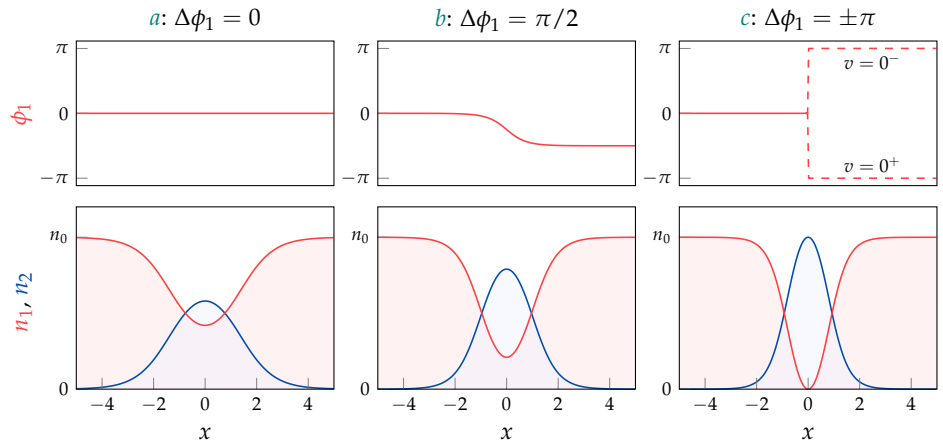

Figure 5.3: Magnetic solitons at different points of the Ω-v plane (see Fig. 5.2) for $N = 2$. The phase of the bath ϕ_1 is plotted in the top panels. It exhibits a phase jump of $\Delta\phi_1 = P$, the momentum of the soliton. The corresponding densities of the two components of the spin mixture are shown in the bottom panels. At the maximal value of Ω (point c), the majority is fully depleted, and we observe a discontinuity in its phase.

5.1.4 Bloch oscillations of a magnetic soliton

This section describes a work performed during my thesis, which resulted in a publication [215]. It is extensively described in previous PhD theses [86, 106], and we highlight here only the main results.

Bloch Oscillations are a remarkable phenomenon, first introduced to describe the periodic motion of a single particle in a lattice subjected to a constant force [259, 260]. In simple terms, they can be understood as Bragg reflections in the particle's momentum space, occurring when its associated wavelength matches the lattice period. BOs were first observed in cold-atom systems using optical lattices [261–263], and this property remains widely exploited, for instance in precision measurement experiments [264].

Extending BOs to systems of interacting particles is generally challenging due to damping effects [265]. Nevertheless, BOs with a halved period were observed by [266, 267] in systems of two strongly interacting particles. Perhaps more intriguing is the existence of BOs in the absence of any lattice. In particular, impurities in bulk systems have been shown to exhibit energy dispersions that are periodic with respect to momentum, a key ingredient for the realization of BOs [268]. Such oscillations were later experimentally demonstrated, despite the presence of strong dissipation, in [269].

Magnetic solitons constitute a system with a macroscopic number of particles and offer the possibility of observing BOs of the minority component wavepacket without any lattice [215, 258]. We now consider the addition of a small, uniform force to our system. In the LLE framework, the presence of a potential corresponds to the addition of a spatially varying external magnetic field. In our spin mixture, this situation maps to an external potential $V(x)$ applied to the minority component. We assume that the applied force is weak enough for the system to remain well described by a magnetic soliton, although the parameters Ω and v become time-dependent [86, 257]. This defines an adiabatic regime, valid when the work done by the force over the soliton's spatial extent is small compared to the interaction energy $\delta g\, n_0$. In this limit, the energy dispersion takes the form:

$$E = 2\tanh(N/2) + 4\frac{\sin^2(P(t)/2)}{\sinh(N)} - N\,F\,x(t) \quad \text{with} \quad P(t) = P(0) + N\,F\,t\,, \tag{5.23}$$

which shows that the momentum follows Newton's law applied to the magnetic soliton, experiencing a total force NF. The soliton's motion can then be deduced from the Hamilton–Jacobi equations, with its velocity given by $v(t) = \partial E/\partial P$. Restoring dimensional units, the period of the resulting oscillations reads:

$$T = \frac{n_0\, h}{N_2 f}\,, \tag{5.24}$$

where $f = F\hbar/(\tau_s \xi_s)$ is the dimensional force. Comparing this expression with the period of BOs in a lattice of spacing a, $T = h/(af)$, we find that the oscillation period is reduced by a factor equal to the number of particles in the minority wavepacket N_2, while the inverse density of the bath plays the role of the lattice period.

Experimentally, the magnetic soliton is created using the techniques described in Chap. 4: Raman beams locally flip the spin of a fraction of the atoms in a tube of uniform density. The resulting soliton initially possesses a flat phase profile, corresponding to $(\Omega(0), v(0)) = (-|\Omega_0|, 0)$, where Ω_0 is set by the number of atoms in the minority component. A magnetic field gradient, typically $b \simeq 1\,\mathrm{G/m}$, is then applied, inducing

an oscillatory motion of the soliton, as shown in Fig. 5.4. This motion corresponds to the wavepacket exploring the family of magnetic solitons represented by the ellipse in Fig. 5.2, in an anticlockwise manner. During this process, a phase difference gradually builds up across the soliton and reverses its sign each time $\Delta\phi_1$ reaches multiples of π.

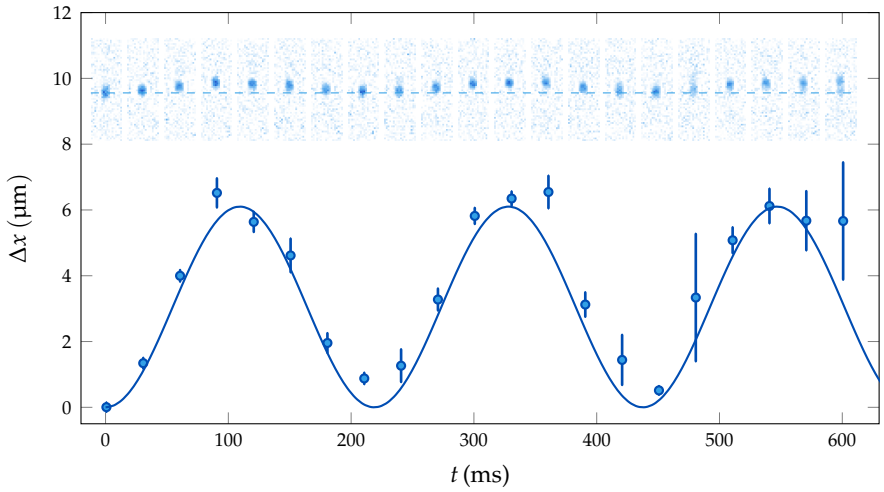

Figure 5.4: Bloch Oscillations of the wavepacket of the minority component. The absorption images are separated by 30 ms, with the dashed line indicating the initial center-of-mass position as a guide to the eye. The minority component contains $N_2 = 1300(100)$ atoms, within a bath of density $n_0 \simeq 370\,\mu\text{m}^{-1}$. The applied force is $f = 9.0(7) \times 10^{-28}\,\text{N}$, leading to a measured oscillation period of $T = 219(3)$ ms, in excellent agreement with the expected value $T = 210(16)$ ms.

The phase of the majority component is thus intrinsically coupled to the oscillations of the magnetic soliton. This phase can be probed by matter-wave interferometry, as illustrated in Fig. 5.5. A second tube of atoms, identical to the bath and containing no magnetic soliton, is used as a phase reference (see schematic in Fig. 5.5b). After a time-of-flight expansion, interference fringes appear, allowing one to extract the phase difference $\Delta\phi_1$ across the soliton position. In particular, measurements taken at $t = kT/2$, with $k \in \mathbb{N}$, yield alternating values of $\Delta\phi_1 = 0$ and π.

We have seen that BOs arise in our system as a consequence of the periodicity of the energy with respect to the momentum, as given by Eq. (5.22). This property is not specific to magnetic solitons: it can be shown to emerge more generally in one-dimensional systems in the thermodynamic limit [215, 270]. However, such a periodic energy–momentum dispersion is not, by itself, sufficient to ensure the observation of BOs. The adiabaticity criterion discussed above must also be satisfied. For instance, in the case of dark–bright solitons (see Chap. 3 for an introduction), the spatial extent of the soliton diverges at mid-period ($t = T/2$). In this regime, the work done by the external force over the soliton's size can no longer be neglected, and the adiabatic approximation breaks down [see 86, 106, for detailed discussions and numerical simulations].

5.2 A gauge transformation between NLSE and LLE

We have discussed in the previous section several solutions of the LLE in the easy-axis regime, in particular the magnetic solitons characterized by the parameters Ω and v (or equivalently κ and v). The existence of such a complete family of solitonic solutions already suggests that the LLE is integrable. Integrability in the isotropic case ($\beta = 0$) was established by [271], who constructed a Lax pair and carried out the IST. In parallel,

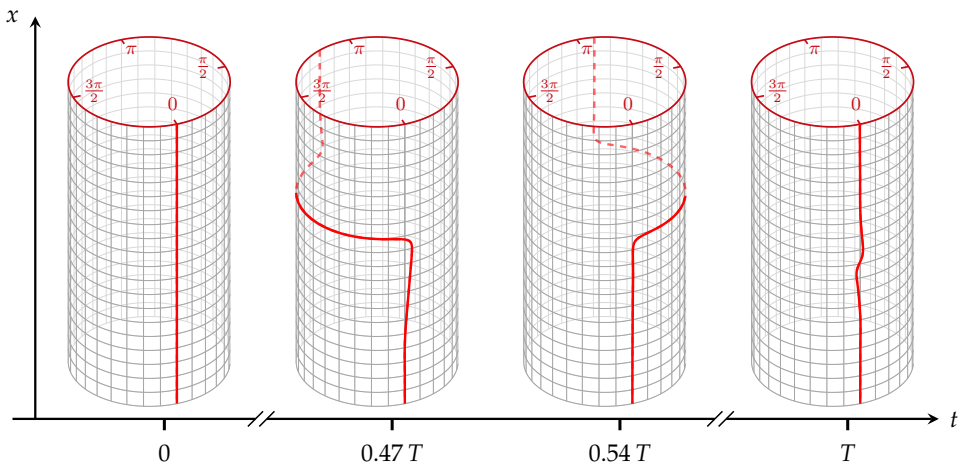

(a) Simulated phase evolution of the majority component.

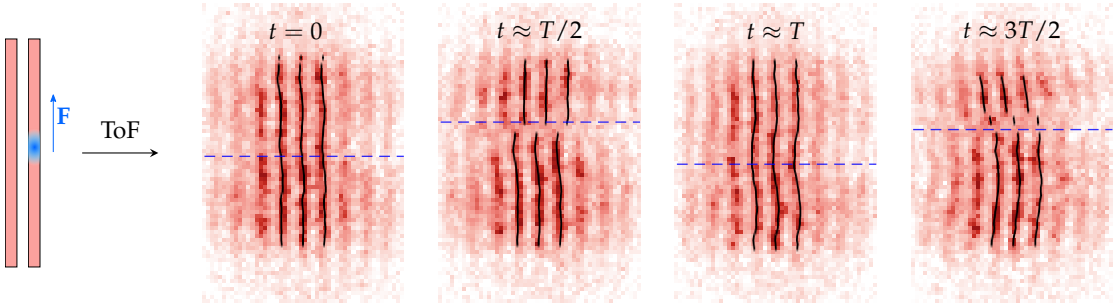

(b) Absorption images of matter-wave interferences.

Figure 5.5: (a) Simulated phase ϕ_1 of the majority component at different times during the BO. Each cylinder represents the atomic tube, with the red line indicating the spatial variation of the phase (dashed on the back surface). The phase jump reverses sign near $t = T/2$, corresponding to the turnaround of the minority wavepacket. **(b)** Left: Schematic of the two interfering tubes of atoms. The left tube contains no magnetic soliton and serves as a phase reference. Right: Matter-wave interference patterns obtained after time-of-flight. The OD is saturated to emphasize the fringe contrast, and not proportional to atomic density. The blue dashed line indicates the position of the minority component, extracted from an independent measurement. The black solid lines highlight the position of the interference fringes, showing that the phase jump $\Delta\phi_1$ alternates between $\simeq 0$ (at integer multiples of the period T) and $\simeq \pm\pi$ (at half-integer multiples $T/2, 3T/2, \ldots$).

Lakshmanan demonstrated that the isotropic LLE is algebraically equivalent to the NLSE [272, 273], directly linking the magnetization $\mathbf{M}$ and the wavefunction ψ. This result revealed a deep correspondence between the two equations. In this section, we present the IST for the easy-axis LLE and show how this equation is closely connected to the NLSE.

5.2.1 Lax Pair of the LLE

The LLE is known to be integrable in the general case of a biaxial ferromagnet ($J_x \neq J_y \neq J_z$) [274, 275]. In this framework, the Lax pair is expressed using elliptic functions of the spectral parameter λ, defined on a rectangle of the complex plane, and the scattering coefficients $a(\lambda)$ and $b(\lambda)$ satisfy specific periodicity relations. The inverse-scattering reconstruction then reduces to solving a Riemann–Hilbert problem on a torus [274, 275]. This more involved procedure lies beyond the scope of the present manuscript. Here, we restrict ourselves to the easy-axis case, which is the relevant regime for the mapping to our spin mixture.

We begin by expressing the magnetization vector in matrix form:

$$\hat{M} = M^{(x)}\hat{\sigma}_x + M^{(y)}\hat{\sigma}_y + M^{(z)}\hat{\sigma}_z = \begin{pmatrix} M^{(z)} & M^{(x)} - \mathrm{i}M^{(y)} \\ M^{(x)} + \mathrm{i}M^{(y)} & -M^{(z)} \end{pmatrix}, \tag{5.25}$$

where $\hat{\sigma}_i$ denote the Pauli matrices, and we write $\hat{\sigma} \equiv \hat{\sigma}_z$ in the following. We recall that integrability is encoded in the existence of a Lax pair $(\hat{L}, \hat{A})$ generating the associated auxiliary linear problem:

$$\partial_x \Phi = \hat{L}\Phi \tag{5.26a}$$

$$\partial_t \Phi = \hat{A}\Phi\,. \tag{5.26b}$$

Consistency of these equations requires the compatibility (or zero-curvature) condition:

$$\partial_x(\partial_t\Phi) = \partial_t(\partial_x\Phi) \quad \Longleftrightarrow \quad \hat{L}_t - \hat{A}_x + [\hat{L}, \hat{A}] = 0 \quad \forall\lambda\,, \tag{5.27}$$

which is satisfied if and only if $\mathbf{M}$ solves the LLE. A suitable Lax pair for the easy-axis LLE, following [78, 276, 277], is given by:

$$\begin{cases} \hat{L}(x,t;\lambda) = \dfrac{1}{4}\left[\hat{\sigma}, \hat{M}\right] + \mathrm{i}\lambda\hat{M}\,, \\ \hat{A}(x,t;\lambda) = -\dfrac{\mathrm{i}}{4}\left[\hat{\sigma}, \hat{M}\hat{M}_x\right] + \dfrac{\mathrm{i}}{2}M^{(z)}\hat{\sigma} + \lambda\left(\hat{M}\hat{M}_x + \dfrac{1}{2}\left[\hat{\sigma}, \hat{M}\right]\right) + 2\mathrm{i}\lambda^2\hat{M}\,, \end{cases} \tag{5.28}$$

where subscripts indicate partial derivatives and we have set $\beta = 1$ in Eq. (5.1). Both operators are polynomial in the spectral parameter $\lambda \in \mathbb{C}$. We denote by $\hat{L}^{(i)}$ (resp. $\hat{A}^{(i)}$) the coefficient multiplying λ^i in $\hat{L}$ (resp. $\hat{A}$).

5.2.2 Gauge equivalence

Lax pairs of different equations can be related by a so-called *gauge equivalence* [278]: if one can find a matrix $\hat{g}$ satisfying:

$$\begin{cases} \hat{L} = \hat{g}\hat{L}'\hat{g}^{-1} + \hat{g}_x\hat{g}^{-1}\,, \\ \hat{A} = \hat{g}\hat{A}'\hat{g}^{-1} + \hat{g}_t\hat{g}^{-1}\,, \end{cases} \tag{5.29}$$

where $(\hat{L}', \hat{A}')$ is the Lax pair of a second integrable equation. Then, the solutions of the two scattering problems are simply related:

$$\begin{cases} \partial_x \Phi = \hat{L}\Phi \\ \partial_t \Phi = \hat{A}\Phi \end{cases} \iff \begin{cases} \partial_x(\hat{g}^{-1}\Phi) = \hat{L}'(\hat{g}^{-1}\Phi)\,, \\ \partial_t(\hat{g}^{-1}\Phi) = \hat{A}'(\hat{g}^{-1}\Phi)\,. \end{cases} \tag{5.30}$$

Such a gauge equivalence linking the isotropic LLE and attractive NLSE was pointed out by [279]. A few years later, the easy-axis LLE was also shown to be equivalent to the attractive NLSE [80, 81]. Note that this relation does not extend straightforwardly to the easy-plane LLE (despite the claim of [276], which was later corrected by [80, 278]).

Our goal is to obtain an explicit expression for g, which would allow us to relate a solution $u(x,t)$ of the NLSE to a magnetization field $\mathbf{M}$ of the LLE through Eq. (5.29). We first recall a Lax pair for the attractive NLSE. Following the conventions of [279]:

$$\begin{cases} \hat{L}'(x,t;\lambda) = \begin{pmatrix} 0 & u^* \\ -u & 0 \end{pmatrix} + \mathrm{i}\lambda\hat{\sigma}\,, \\ \hat{A}'(x,t;\lambda) = \mathrm{i}\begin{pmatrix} |u|^2 & u_x^* \\ u_x & -|u|^2 \end{pmatrix} + 2\lambda\begin{pmatrix} 0 & u^* \\ -u & 0 \end{pmatrix} + 2\mathrm{i}\lambda^2\hat{\sigma}\,, \end{cases} \tag{5.31}$$

where, here and in the following, primes indicate quantities associated with the NLSE. Assuming the existence of g, we now derive the conditions that it must satisfy. Expanding Eq. (5.29) order by order in λ yields five equations:

$$\hat{L}^{(0)} = \hat{g}\hat{L}'^{(0)}\hat{g}^{-1} + \hat{g}_x\hat{g}^{-1}\,, \tag{5.32a}$$

$$\mathrm{i}\hat{M} = \mathrm{i}\hat{g}\hat{\sigma}\hat{g}^{-1}\,, \tag{5.32b}$$

$$\hat{A}^{(0)} = \hat{g}\hat{A}'^{(0)}\hat{g}^{-1} + \hat{g}_t\hat{g}^{-1}\,, \tag{5.32c}$$

$$\hat{M}\hat{M}_x + 2\hat{L}^{(0)} = 2\hat{g}\hat{L}'^{(0)}\hat{g}^{-1}\,, \tag{5.32d}$$

$$2\mathrm{i}\hat{M} = 2\mathrm{i}\hat{g}\hat{\sigma}\hat{g}^{-1}\,. \tag{5.32e}$$

We omit explicit spatial and temporal dependencies for compactness. Eq. (5.32b) and (5.32e) are identical, and express the condition: $\hat{M} = \hat{g}\hat{\sigma}\hat{g}^{-1}$. From Eq. (5.25) we deduce that $\hat{M}^\dagger = \hat{M}$, with $\cdot^\dagger$ denoting Hermitian transpose. Thus, $\hat{g}^{-1} = \hat{g}^\dagger$, and $\hat{g}$ is a unitary matrix. Combining Eq. (5.32a) and (5.32b), one finds:

$$\hat{M}\hat{M}_x = -2\hat{g}_x\hat{g}^{-1}\,, \tag{5.33}$$

using the identities $\hat{M}\hat{L}^{(0)}\hat{M} = -\hat{L}^{(0)}$ and $\hat{\sigma}\hat{L}'^{(0)}\hat{\sigma} = -\hat{L}'^{(0)}$. Then, Eq. (5.32d) follows automatically. Finally, Eq. (5.32c) determines the time evolution of $\hat{g}$, leading to a differential equation once an initial condition is specified.

Thus, we aim to construct $\hat{g}$ such that Eqs. (5.32a) and (5.32b) hold for an initial condition $u(x,0)$, which directly yields the corresponding magnetization $\mathbf{M}(x,0)$. These conditions can be combined into:

$$\hat{g}^{-1}\hat{g}_x = -\hat{L}'^{(0)} + \frac{1}{4}\left[\hat{g}^{-1}\hat{\sigma}\hat{g}, \hat{\sigma}\right]\,. \tag{5.34}$$

Since $\hat{g}$ is a unitary matrix, it can be parametrized by two functions g_1 and g_2 as:

$$\hat{g} = \begin{pmatrix} g_1 & -g_2^* \\ g_2 & g_1^* \end{pmatrix} \quad \text{and} \quad |g_1|^2 + |g_2|^2 = 1\,. \tag{5.35}$$

Substituting this form into Eq. (5.34) and extracting the lower-left entry gives:

$$u(x,0) = g_1 g_{2x} - g_2 g_{1x} + g_1 g_2 \,. \tag{5.36}$$

Next, we express g_1 and g_2 in terms of the polar angles of $\mathbf{M}$, using in particular the identity $\hat{M} = \hat{g}\hat{\sigma}\hat{g}^{-1}$ (details are given in Appendix C). This leads to the differential equation:

$$u(x,0) = \frac{1}{2}\left[\theta_x + \sin\theta\,(\mathrm{i}\varphi_x + 1)\right] \exp\left[\mathrm{i}\left(\varphi - 2\int_{-\infty}^{x} \sin^2\left(\frac{\theta}{2}\right)\varphi_y \,\mathrm{d}y\right)\right]. \tag{5.37}$$

We have taken $\hat{g} \in \mathrm{SU}(2)$; allowing instead $\det \hat{g} = e^{\mathrm{i}\gamma}$, $\gamma \in \mathbb{R}$ would merely multiply u by a global (and irrelevant) phase, which we omit in Eq. (5.37) for clarity. If the initial condition $u(x,0)$ is real, then:

$$u(x,0) = \frac{1}{2}\left(\theta_x + \sin\theta\right) \quad \text{and} \quad \varphi = 0\,. \tag{5.38}$$

These differential equations can be solved numerically (see Sec. 5.3.2), allowing us to construct solutions of the LLE starting from an initial solution of the NLSE.

5.2.3 The Kotlyarov method

In addition to the gauge equivalence discussed in the previous section, the equivalence between the easy-axis LLE and the attractive NLSE was also established by Kotlyarov [79]. His approach does not rely on comparing the Lax pairs of the two equations. Instead, he starts directly from the LLE and introduces an auxiliary matrix $\hat{\Theta}$, which can be identified with $\hat{L}'^{(0)}$, which satisfies a differential equation comparable to Eq. (5.34). The key point is that, under appropriate boundary conditions, the matrix elements of $\hat{\Theta}$ are shown to obey the attractive NLSE.

Because [79] is difficult to access, we reproduce and detail the main steps of this method in Appendix C. Following this procedure, one ultimately recovers the differential Eq. (5.37), which establishes the correspondence between the initial NLSE field $u(x,0)$ and the magnetization profile $\mathbf{M}(x,0)$.

5.3 Description of new LLE solutions

We have detailed in Sec. 5.1.3 the fundamental solutions of the easy-axis LLE, namely the magnetic solitons. However, given the integrability of this equation and its gauge equivalence with the attractive NLSE, one naturally expects a much richer solution set, including multi-soliton states. This topic has been extensively explored in the literature; for instance, [280–285] develop several techniques to construct multi-soliton solutions. These approaches, however, seldom yield simple closed-form expressions for the resulting configurations.

In this section, we provide a more accessible description of these multi-soliton solutions by exploiting the gauge equivalence established above and the well-known solitonic solutions of the NLSE reviewed in Chap. 3.

5.3.1 Conservation of the IST spectrum and time evolution

Following Eq. (5.30), the Jost solutions of the scattering problems for the LLE and the NLSE exhibit important common properties. In particular, the proportionality of the solutions Φ, Ψ associated with a given eigenvalue λ_k is identical for both equations.

Thus, the eigenvalues λ_k are conserved under the gauge equivalence. We recall that they characterize the presence of solitons in a given solution (see Chap. 3). Hence, we can construct multi-soliton solutions of the LLE using the simple procedure:

- Choose the scattering data λ_k, c_k (we set $b(\xi) = 0$, that is a solution with no radiative part).
- Express the NLSE solution $u(x)$ using Eq. (3.71).
- Solve the differential Eq. (5.37) to obtain $\mathbf{M}(x)$.

However, we do not a priori conserve the quantities c_k during the gauge transformation. This property was shown to hold for the isotropic LLE [279], but is not verified in the easy-axis case. Thus, this transformation from NLSE to LLE is injective, and we are not guaranteed to recover all multi-solitons of LLE. This point is discussed in further details in Sec. 5.3.3.

A key question concerns the time evolution of the magnetization $\mathbf{M}(x,t)$. We can address this on several levels. First, the solution of the differential Eq. (5.37) can be determined for any fixed time t. Consequently, the possible time periodicity of $u(x,t)$ is transferred to the magnetization $\mathbf{M}(x,t)$. Another approach consists in examining the scattering data. We have seen for the NLSE that λ_k is time independent, and that $c_k(t) = c_k(0)\,\mathrm{e}^{4\mathrm{i}\lambda_k^2 t}$. In the case of the LLE, only the second relation is slightly modified, and we obtain $c_k(t) = c_k(0)\,\mathrm{e}^{4\mathrm{i}(\lambda_k^2+\beta^2)t}$ [see e.g. 78, Eq. (22)]. However, this global phase $\mathrm{e}^{4\mathrm{i}\beta^2 t}$ is common to all eigenvalues and therefore does not affect the behavior of the reconstructed solution.

Following these arguments, the magnetization $\mathbf{M}(x,t)$ inherits the same temporal behavior as the corresponding NLSE solution $u(x,t)$. We illustrate this result through numerical simulations in Sec. 5.3.2, before describing the experimental realizations in Sec. 5.4.

5.3.2 LLE n-solitons

In this section, we describe several LLE multi-soliton configurations obtained through the gauge equivalence with the NLSE. For simplicity, we restrict ourselves to purely imaginary eigenvalues λ_k, which correspond to stationary (zero-velocity) solitons.

A paradigmatic and experimentally relevant class of NLSE multi-solitons arises from the initial condition $u(x) = n\kappa/\cosh(\kappa x)$ with $n \in \mathbb{N}^*$, which we studied in Sec. 4.3 for $n = 1$ and $n = 2$. As shown in [73], this profile generates discrete eigenvalues:

$$\lambda_k = \mathrm{i}\,(2k-1)\kappa/2, \qquad k = 1, \dots, n\,, \tag{5.39}$$

and no radiative component, i.e. $b(\xi) = 0$. Moreover, choosing $\kappa \ll 1$ ensures an immediate mapping between the NLSE and the LLE, owing to the low-depletion limit discussed in Sec. 5.1.2 and 2.3.2. The gauge equivalence then allows us to explore the corresponding LLE multi-solitons for arbitrary values of κ.

Setting $n = 1$ (a single bright soliton for $u(x)$) yields a magnetic soliton for $\mathbf{M}(x)$. This is consistent with the Ω–v plane characterization of magnetic solitons shown in Fig. 5.2: it can be recast as a κ–v plane using $\kappa = \sqrt{1+\Omega-v^2/4}$. In this representation, the domain of existence is simply $\kappa > 0$, and the κ–v plane may be viewed as the complex plane of the eigenvalue λ_k, as illustrated in Fig. 5.6a. We also note that the point $(\kappa, v) = (1, 0)$, meaning $\lambda_k = \mathrm{i}/2$, is singular, since the magnetization N diverges there.

Fig. 5.6 presents two examples of $n = 2$ multi-solitons for $\kappa = 0.31$ and $\kappa = 0.5$. Their qualitative behavior depends crucially on whether one of the eigenvalues fulfills $\mathcal{I}(\lambda_k) > 1/2$. Besides, we recover the low-depletion limit whenever all eigenvalues satisfy $\mathcal{I}(\lambda_k) \ll 1$.

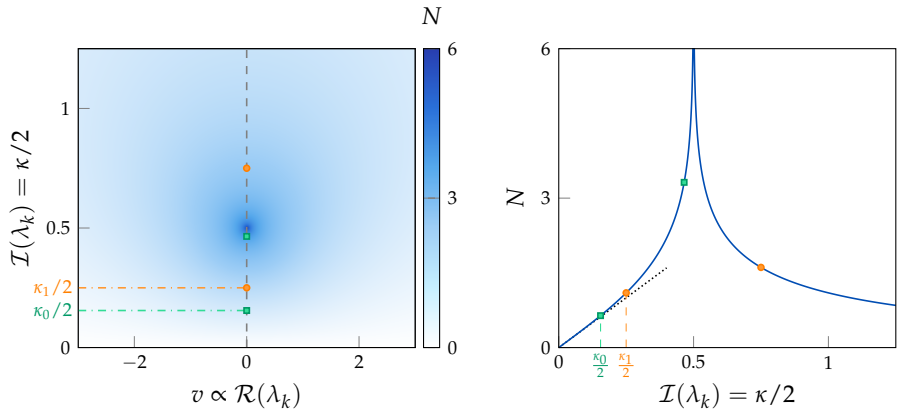

(a) Examples of scattering data for several multi-solitons.

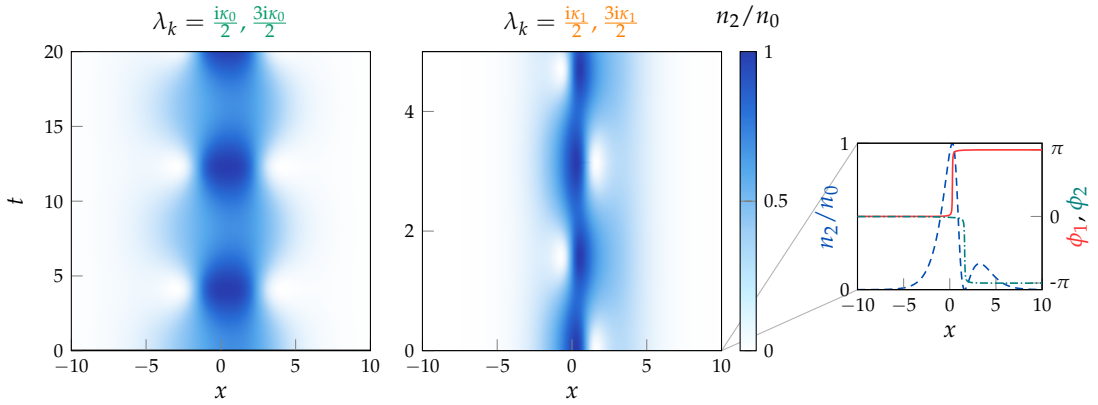

(b) Time evolution of selected multi-solitons.

Figure 5.6: (a,b) Numerical examples of two multi-solitons generated from the eigenvalues $\lambda_k = i\kappa/2,\ 3i\kappa/2$, corresponding to the NLSE multi-solitons of Sec. 4.3 [73]. **(a)** Left: Scattering data in the κ–v plane, with green squares for $\kappa_0 = 0.31$ and orange circles for $\kappa_1 = 0.5$. The blue colorbar indicates the magnetization N of the associated magnetic soliton, and highlights the divergence at $\lambda_k = i/2$. Right: Cut at $v = 0$ (dashed gray line of left panel). For $\kappa \ll 1$ the curve becomes a straight line, $N = 2\kappa$, as expected in the low-depletion regime. It is shown with the dotted black line. **(b)** Time evolution of the minority component for the two multi-solitons. Left: A breather-like dynamics similar to the 2-soliton solution of Sec. 4.3, featuring a flat initial phase. Right: A multi-soliton with phase discontinuities at $t = 0$ in both the majority (ϕ_1, solid red) and minority (ϕ_2, green dash-dotted) components, shown in the inset. These discontinuities arise when one eigenvalue lies above $\kappa = 1$, and we note that the magnetic soliton associated to this eigenvalue also exhibits such behavior (see Fig. 5.3, right panel). In the case when $\kappa > 1$ (not illustrated here), both eigenvalues are above the divergence, and an additional phase jump appears in φ.

More generally, arbitrary distributions of eigenvalues λ_k generate multi-soliton states of the LLE. However, retaining the initial condition $u(x) = n\kappa/\cosh(\kappa x)$ offers a concrete practical advantage: since $u(x) \in \mathbb{R}$, the initial magnetization is obtained solving Eq. (5.38), and it allows us to set the phase $\varphi = 0$. In this case, it is sufficient to ensure $\theta \in [0, \pi]$ in order to obtain a positive wavefunction at $t = 0$. Hence, one can imprint the corresponding multi-soliton experimentally on our spin mixture using the

Raman beams described in Chap. 4. This requirement is satisfied in the left panel of Fig. 5.6b, and we verify numerically that having $\mathcal{I}(\lambda_k) < 1/2$, $\forall k$ is a sufficient condition for multi-solitons of the form $u(x) = n\kappa/\cosh(\kappa x)$, with $n \in \mathbb{N}^*$. Following Eq. (5.39), this inequality sets more stringent requirements on κ as n increases. For instance, it leads to $\kappa < 1/3$ for $n = 2$, and $\kappa < 1/5$ for $n = 3$.

5.3.3 Symmetry breaking

A notable feature of LLE multi-solitons is the emergence, when the eigenvalues λ_k increase beyond the low-depletion limit, of an asymmetric density profile, illustrated for instance in the inset of Fig. 5.6b. This behavior may be unexpected given that both the LLE and the associated NLSE initial condition $u(x) = n\kappa/\cosh(\kappa x)$ are parity-symmetric. Although this asymmetry is most striking when one of the eigenvalues satisfies $\mathcal{I}(\lambda_k) > 1/2$, it is already visible in regimes where all eigenvalues remain below this threshold, as in the left panel of Fig. 5.6b. We highlight this point in Fig. 5.7 by considering the case of $n = 3$, and increasing values of κ, up to $\mathcal{I}(\lambda_k) \lesssim 1/2$.

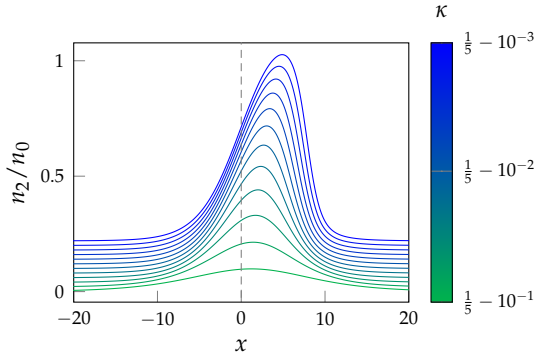

Figure 5.7: Multi-solitons of the LLE, obtained via the gauge equivalence with the NLSE, and using the input profile $u(x) = 3\kappa/\cosh(\kappa x)$. The largest eigenvalue is $\lambda_k = 5i\kappa/2$, imposing the constraint $\kappa < 1/5$ to remain below the divergence of the magnetization N. The dashed gray line marks the position $x = 0$. As κ increases, both a shift of the center-of-mass and a growing asymmetry of the density profile become apparent. Curves are slightly vertically offset for clarity.

Despite this apparent asymmetry, parity symmetry is preserved at the level of the LLE. Indeed, for any given magnetization profile $\mathbf{M}(x)$, a symmetric counterpart exists and is obtained through the parity transformation $x \leftrightarrow -x$. For clarity, considering a real function $u(x)$, the corresponding solutions may be obtained from either of the relations:

$$u(x) = \frac{1}{2}\left(\theta_x + \sin\theta\right) \tag{5.40a}$$

$$u(x) = \frac{1}{2}\left(\theta_x - \sin\theta\right) . \tag{5.40b}$$

The sign difference between Eq. (5.40a) and (5.40b) reflects the implementation of the parity transformation, noting that the global phase of u is physically irrelevant. More formally, this structure follows directly from the Kotlyarov construction discussed in Appendix C, or equivalently from choosing alternative but equivalent Lax pairs for the LLE. This highlights the non-uniqueness of the gauge transformation. Numerically, Eq. (5.40a) is stable when integrated from $x \to -\infty$, while Eq. (5.40b) is stable when integrated from $x \to +\infty$. Applying these constructions to the $n = 2$ NLSE multi-soliton yields the two distinct profiles shown in the left and center panels of Fig. 5.8.

A natural question then arises: does a given gauge transformation allow one to recover the full family of LLE multi-solitons? A closer inspection of Fig. 5.7 shows that the observed asymmetry is correlated with a shift of the center of mass of the wavepacket. This shift originates from a differential modification of the coefficients c_k associated with each soliton. For magnetic solitons, this relation between the coefficients c_k and the soliton position can be established analytically [see 78, Eq. (32)]. Owing to the linear structure of the IST, one therefore expects that appropriately shifting the relative positions of the constituent solitons allows one to generate all asymmetric LLE multi-soliton profiles. We verify this expectation numerically by constructing identical wavepackets either via the gauge transformation or directly from the IST multi-soliton solutions [78]. An example is shown in the right panel of Fig. 5.8, where a relative displacement of two NLSE solitons reproduces the desired LLE profile after the gauge transformation, meaning the multi-soliton of the center panel.

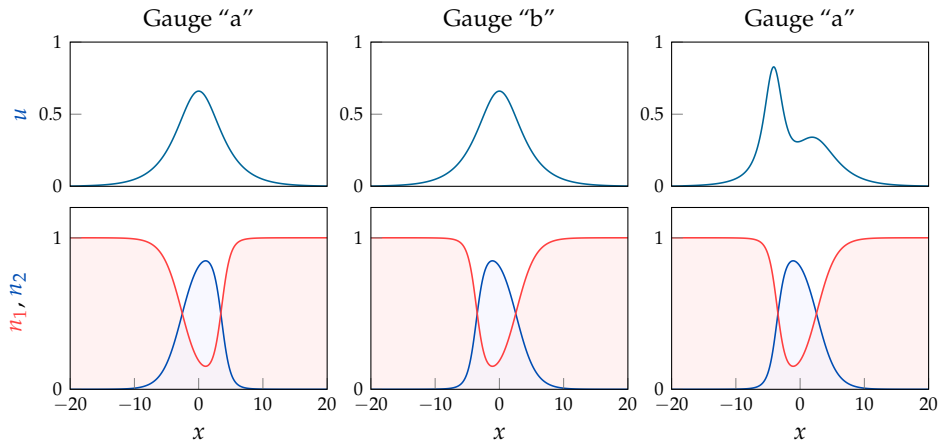

Figure 5.8: Examples of gauge transformed multi-solitons, with the NLSE profiles in the top panels and the corresponding LLE profiles below. The center-of-mass of all solutions has been set to zero. The left and right panels are generated using Eq. (5.40a), called Gauge “a”, and highlight that it is possible to have a given LLE profile and its $x \leftrightarrow -x$ symmetric by altering the relative positions of the solitons of the NLSE solution. The center panel uses a different gauge transformation, given by Eq. (5.40b) and called Gauge “b”, and shows that one can recover the symmetric of the solution of the left panel by another mean.

5.4 Experimentally increasing the depletion

In Chap. 4, we described the experimental realization of NLSE multi-solitons, taking advantage of the low-depletion limit of our spin mixture, which allowed it to be accurately described as a one-component attractive NLSE. This realization naturally fits within the more general mapping of a two-component spin mixture to a ferromagnetic spin chain. Exploiting this correspondence, we can experimentally realize LLE multi-solitons with arbitrary depletion, thereby extending the family of solutions explored in Chap. 4 beyond the low-depletion regime.

5.4.1 2-solitons from NLSE to LLE

Experimentally, we follow the procedure outlined in Chap. 4 to prepare a multi-soliton state. Starting from a bath of atoms at uniform density $n_0 \simeq 550\,\mu\text{m}^{-1}$, a controlled fraction of atoms is transferred to the other spin state using spatially selective

Raman beams. In this way, we realize LLE multi-solitons that are gauge-equivalent to the NLSE profile $u(x) = n\kappa/\cosh(\kappa x)$, with the corresponding imprinted wavefunction obtained by integrating Eq. (5.38).

The implementation of the $n = 2$ case is shown in Fig. 5.9. We choose $1/\kappa = 5\,\mu\text{m}$, corresponding in dimensionless units to $\kappa = 0.30(2)$. Representative absorption images are displayed in Fig. 5.9a and can be compared to numerical simulations in Fig. 5.6b: we observe the characteristic breathing associated with 2-solitons. As highlighted in Fig. 5.9b, the depletion reaches values close to unity, demonstrating that the system is far from the low-depletion limit and that the prepared states are genuine multi-solitons of the LLE.

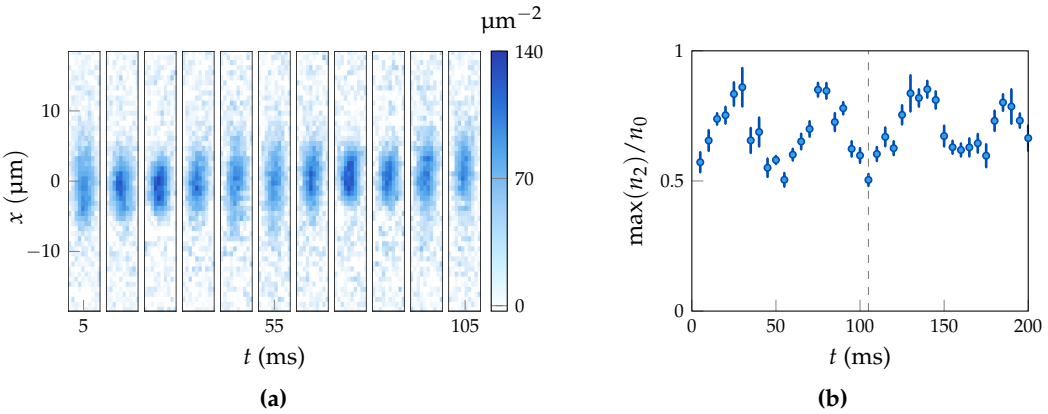

Figure 5.9: (a,b) Realization of a LLE multi-soliton, with $\kappa = 0.30(2)$ and eigenvalues $\lambda_k = \mathrm{i}\kappa/2, 3\mathrm{i}\kappa/2$. We present in **(a)** averaged absorption images of the minority component, spanning two periods of the temporal evolution. **(b)** Maximum depletion of the minority component, obtained from a fit of the density profile with Eq. (4.28). The dashed gray line denotes the time of the last image of **(a)**. The error bars are 1-σ errors from 15 repetitions of the experiment.

Following the discussion of Sec. 5.3.1, the temporal evolution of NLSE multi-solitons is preserved under the gauge transformation. As a result, $n = 2$ solitons of the LLE exhibit a breathing dynamics at a frequency, given by the same formula (see Chap. 4):

$$f = \frac{4}{\pi}\kappa^2 \rightarrow f = \frac{2}{\pi}\frac{\hbar\kappa^2}{m}, \tag{5.41}$$

where, in the second expression, we have reintroduced physical dimensions. Here, κ sets the width of the NLSE multi-soliton $u(x)$, which only corresponds to the width of the LLE multi-soliton in the low-depletion limit. We test this prediction in Fig. 5.10, comparing Eq. (5.41) with the measured temporal evolution of the atomic wavepacket over a broad range of widths $1/\kappa$, extending beyond the low-depletion limit explored in Fig. 4.8. We find excellent agreement across all experimentally realized parameters, with two additional widths compared to Fig. 4.8.

5.4.2 Exploring 3-solitons

Our experimental platform also enables the realization of multi-solitons with $n > 2$. In Fig. 5.11, we show an example of the time evolution of a 3-soliton state with $\kappa = 0.19(1)$. For this value of κ, the largest eigenvalue approaches $\mathrm{i}/2$, resulting in a depletion close to unity. Unlike the $n = 2$ case, where a single beating frequency produces a clean breathing motion with the frequency of Eq. (5.41), the presence of three discrete

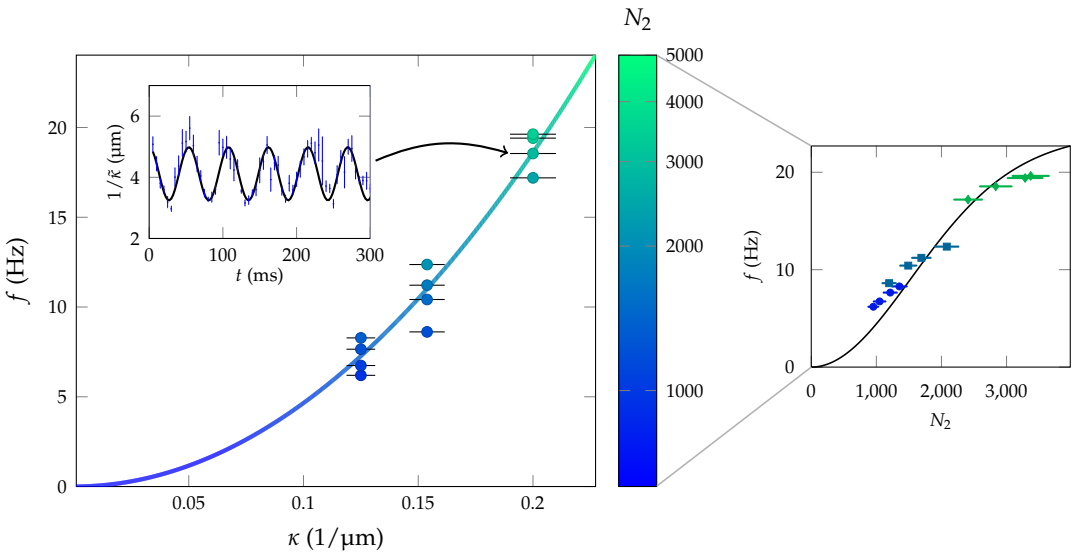

Figure 5.10: Left: The solid line shows the breathing frequency of the exact two-soliton solution, color-coded by atom number on a logarithmic scale, obtained from the calibration performed on the bright soliton (see Chap. 4). Circles are experimental data obtained for three different imprinted eigenvalues $1/\kappa$. The total atom number in the wavepacket varies slightly between data points, due to our experimental uncertainty on the amplitude to imprint for the two-soliton, producing a small vertical spread. Their distribution around the solid line demonstrates the consistency of our calibrations and measurements. Inset: temporal evolution of the wavepacket width $1/\tilde{\kappa}$ for the data set shown in Fig. 5.9a, fitted with the function of Eq. (4.28). Error bars represent 1-σ uncertainties from 15 repetitions. The resulting breathing frequency is extracted from a fit to a damped sinusoid (solid black line). Right: We present the same experimental data, but the breathing frequency is plotted as a function of the atom number (colorbar of the left panel). The three sets of widths are given from blue to green with the circles, squares and diamonds for increasing values of κ. The solid black line indicates the theoretical frequency. Its position results notably from our calibrations of the atom number and interaction strength, and may be altered by possible systematic errors.

eigenvalues introduces multiple beating terms. These generate several harmonics, giving rise to a more intricate breathing dynamics. This behavior is consistent with the numerical NLSE 3-soliton shown in Fig. 3.10b, which already exhibits the same multi-frequency structure.

Furthermore, the 3-soliton highlights the asymmetry discussed in Sec. 5.3.3. The initial magnetization profile corresponds to the one plotted in Fig. 5.7 for $\kappa = 0.19$, and we observe that this asymmetry persists throughout the subsequent evolution, as clearly visible in Fig. 5.11c.

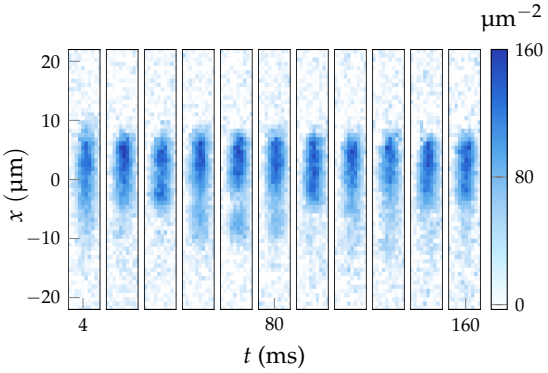

(a) Experimental absorption images.

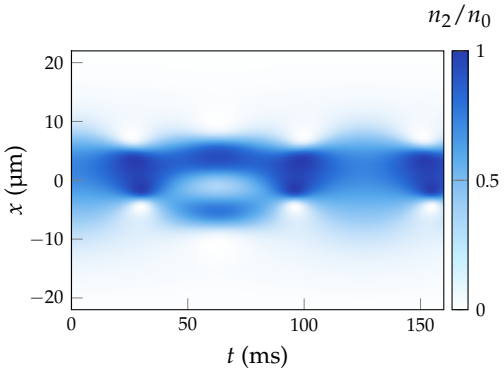

(b) Numerical simulation.

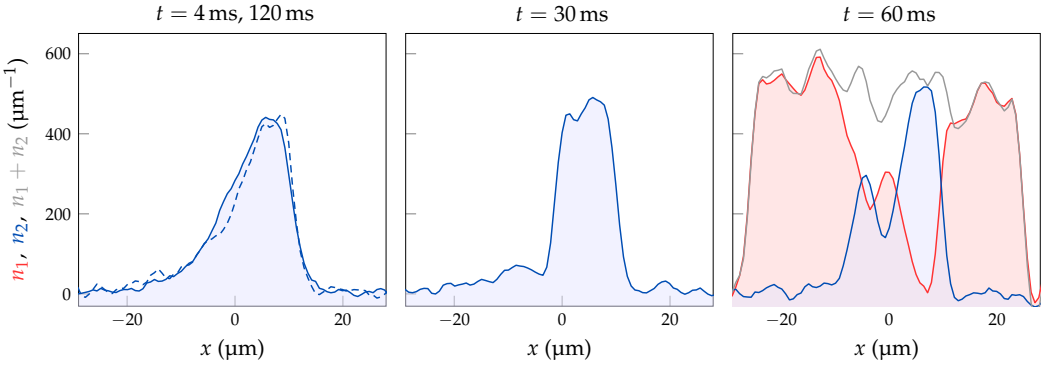

(c) Density profiles at selected times.

Figure 5.11: **(a)** Time evolution of a LLE multi-soliton with $n = 3$, engineered with $\kappa = 0.19(1)$. The largest eigenvalue lies close to $i/2$, corresponding to a depletion approaching unity. Compared to the $n = 2$ case, the dynamics are markedly more intricate, arising from the beating between the three discrete eigenvalues. A characteristic period $T \simeq 120\,\text{ms}$ can be identified. **(b)** Numerical simulation of the time evolution of a LLE 3-soliton, taking $\kappa = 0.195$. It is shown with the same space and time boundaries as the experimental images of **(a)**, using the experimental parameters of n_0 and δg to put dimensions on the axis. The same breathing behavior, with several harmonics, is observed, with an overall period of 125 ms. **(c)** Density profiles of the minority component at different times: $t = 4\,\text{ms}$, 30 ms, and $60\,\text{ms} \simeq T/2$, highlighting the pronounced spatial asymmetry discussed in Sec. 5.3.3. The profile at $t = 120\,\text{ms}$ is also plotted in the first panel in dashed lines, and illustrates the periodic behavior. The majority component is also shown in the right panel, indicating that the total density, plotted with the solid gray line, remains approximately uniform. This point is consistent with the assumption required for mapping the spin mixture onto the easy-axis LLE.

Conclusion

In this chapter, we established the mapping between the well-known easy-axis LLE and a two-component Bose mixture. We characterized its fundamental excitations, the magnetic solitons, and probed their dynamics through BOs [215].
We then detailed the gauge equivalence between the easy-axis LLE and the attractive NLSE, which provides a unifying framework in which magnetic excitations of a ferromagnet and nonlinear waves of the NLSE share the same integrable structure. Through the mapping to our spin mixture, this correspondence becomes experimentally accessible: the initial magnetization profile can be engineered directly from a chosen NLSE soliton or multi-soliton configuration, and its subsequent evolution reflects the underlying scattering data.
Up to this point, the dynamics were interpreted within the framework of a perfectly integrable equation. In Chap. 6, we investigate controlled perturbations to integrability. We show how weak integrability breaking provides a powerful experimental probe of the inverse-scattering structure: multi-solitons gradually decompose into their constituent solitons, making their encoded spectral information directly observable through soliton fission.

6 Integrability breaking: an inner view into the IST

Outline of the current chapter

Introduction

Integrable equations, such as the NLSE, LLE, or KdV equation, provide idealized models for a variety of physical systems. Real systems, however, inevitably exhibit features that fall outside these ideal models: particle losses, higher-order nonlinearities, external potentials, or other perturbations. These effects can often be incorporated by adding corrective terms to the equation, but doing so typically undermines integrability. Nevertheless, such deviations can still be addressed perturbatively by extending the IST framework to weakly non-integrable regimes.

In Sec. 6.1, we introduce the basic elements of perturbation theory for the NLSE within the IST formalism and summarize several key results established in optical fiber systems. In Sec. 6.2, we then explore how a weak external potential can induce a controlled breaking of integrability, in the sense that the solitonic content of a wavepacket remains well-defined and evolves in a predictable manner. Finally, Sec. 6.3 presents the corresponding experimental observations, in the contexts of both the NLSE and the LLE.

6.1 Correcting terms in the NLSE: one way into integrability breaking

Modifying the NLSE generally breaks its integrability. One possible route is to modulate the interaction strength in time [286]. When the modulation is strong, the dynamics become highly non-perturbative, and the resulting effective "eigenvalues" can even display fractal structures [287]. In contrast, remaining in the perturbative regime preserves much of the intuition provided by the IST: the soliton eigenvalues undergo only small shifts, and the overall solitonic content of a wavepacket remains unchanged [288]. In this section, we summarize several results and illustrative examples of this perturbative approach.

6.1.1 Perturbation theory

Perturbation theory within the IST provides a systematic way to track how weak non-integrable terms affect the scattering data of the NLSE. The general formalism, developed notably by [289, 290], shows that small perturbations induce slow, explicit evolution equations for both the discrete (solitonic) and continuous (radiative) components of the spectrum. These methods were applied by [291] to quantify the deformation of a single soliton under weak perturbations, and later extended to the case of two well-separated solitons, revealing how their parameters evolve independently at leading order [292]. It was also demonstrated how slowly varying external media, such as gradients, enter the IST evolution and modify soliton parameters adiabatically [293]. A comprehensive overview of these approaches and their implications for soliton dynamics is given in the review [82].

Let us consider a perturbation term R added to the NLSE:

$$\mathrm{i}u_t + u_{xx} + 2|u|^2 u = \mathrm{i}\epsilon R[u]\,. \tag{6.1}$$

Such a term may represent, for instance, particle losses, $\epsilon R[u] = \gamma u(x)$, or the action of an external potential, $\epsilon R[u] = -\mathrm{i}V_{\mathrm{ext}}(x)u(x)$. The compatibility condition of Eq. (6.1) with the Lax pair $(\hat{L}, \hat{A})$ of the unperturbed NLSE becomes:

$$\frac{\mathrm{d}\hat{L}}{\mathrm{d}t} + \left[\hat{L}, \hat{A}\right] = \mathrm{i}\epsilon\hat{R} \quad \text{with} \quad \hat{R} = \begin{pmatrix} 0 & R[u] \\ -R[u]^* & 0 \end{pmatrix}. \tag{6.2}$$

Following the developments of [291], we consider the eigenvalue equation $\hat{L}\Phi = \lambda\Phi$, with the Jost function $\Phi = \begin{pmatrix}\phi_a & \phi_b\end{pmatrix}^\mathsf{T}$, and compute its time derivative. Because of the perturbation, the eigenvalue λ may be time dependent. Writing:

$$\left(\hat{L} - \lambda\right) \underbrace{\left(\Phi_t - \hat{A}\Phi\right)}_{=0} = -\mathrm{i}\epsilon\hat{R}\Phi + \lambda_t\Phi\,, \tag{6.3}$$

and taking the scalar product on the left with $\tilde{\Phi}$, one finds:

$$\frac{\partial\lambda}{\partial t} = \mathrm{i}\epsilon\frac{\langle\tilde{\Phi}, \hat{R}\Phi\rangle}{\langle\tilde{\Phi}, \Phi\rangle} \quad \text{with} \quad \langle\psi, \phi\rangle = \int\sum\psi_i^*\phi_i\,\mathrm{d}x\,, \tag{6.4}$$

Writing $\tilde{\Phi} = (\phi_b^*, \phi_a^*)$ allows a simplification for the discrete spectrum, thanks to the identity given in [291, Eq. (2.25)]:

$$\frac{\partial\lambda_k}{\partial t} = \frac{c_k}{a'(\lambda_k)}\epsilon\int_{-\infty}^{+\infty} R[u]^*\phi_a^2 - R[u]\phi_b^2\,\mathrm{d}x\,. \tag{6.5}$$

where $c_k, a'(\lambda_k)$ are the scattering data associated with a discrete eigenvalue λ_k, introduced in Chap. 3. This formula gives the exact evolution of the discrete eigenvalues and does not, in itself, rely on ϵ being small. In the integrable limit $\epsilon = 0$, we recover that $\partial_t\lambda_k = 0$, as expected. To obtain the complete dynamics of the perturbed system, Eq. (6.5) must be complemented by the evolution equations for the remaining scattering data, as discussed in [82, 291]. The difficulty of this method lies in the fact that one must compute explicitly the Jost function associated to λ_k, contrary to the general IST method which only relies on the scattering data.

Adiabatic approximation

The formalism described above makes it possible to characterize solutions of perturbed integrable equations in terms of their scattering data, and thus in terms of solitons. However, analytical progress generally requires additional approximations, especially because explicit expressions of the Jost functions are available only for one- and two-soliton solutions. The two-soliton case is discussed in Sec. 6.1.2; here, we focus on the single bright soliton and mention some results obtained within the adiabatic approximation.

We consider an initial wavepacket of the form:

$$u(x,0) = \frac{\kappa\mathrm{e}^{\mathrm{i}kx}}{\cosh(\kappa x)}\,, \tag{6.6}$$

corresponding to the discrete eigenvalue $\lambda_1 = \mathrm{i}\kappa/2 - k/2$. The adiabatic approximation [291] assumes that a weak perturbation modifies the soliton only slightly: the waveform remains a bright soliton at all times, but its parameters evolve slowly with t. In particular, the soliton width and velocity are allowed to become time-dependent: $k \to k(t)$ and $\kappa \to \kappa(t)$. Under this assumption, the perturbed IST evolution equations for the scattering data reduce to a pair of ordinary differential equations for these two parameters.

For the specific case of particle losses, described by $R[u] = \gamma u(x)$ ($\gamma < 0$), [291] obtained the analytical solution:

$$\kappa = \kappa_0\exp(2\gamma t) \quad \text{and} \quad k = k_0\,, \tag{6.7}$$

where κ_0, k_0 are the initial values. This result shows that the soliton retains a constant velocity while its width $1/\kappa(t)$ increases exponentially. This behavior is quite natural, since the atom number of the NLSE soliton is proportional to κ. The prediction of Eq. (6.7) is compared in Fig. 6.1 with numerical simulations of the NLSE including losses, and we highlight in Fig. 6.1b the regime of validity of the adiabatic approximation.

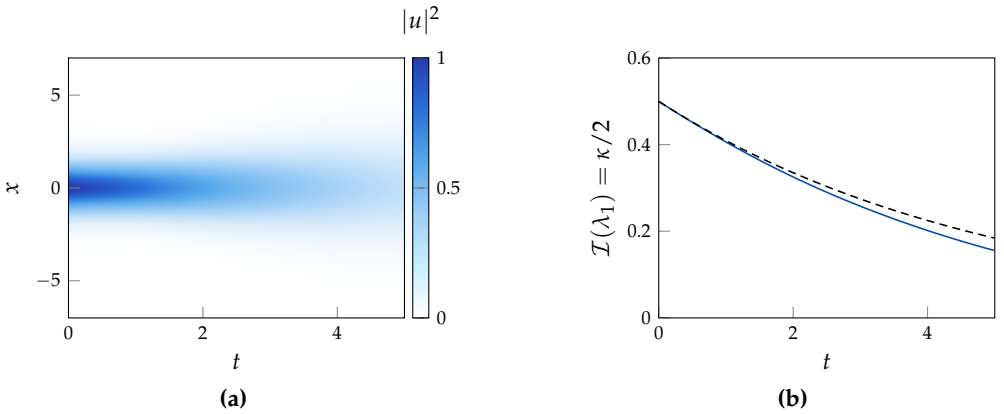

Figure 6.1: (a) Numerical simulation of the temporal evolution of a bright soliton, with the initial profile of Eq. (6.6), setting $k = 0$ and $\kappa = 1$. Losses are included, with $\gamma = -0.1$. **(b)** The solid blue line gives the time evolution of the eigenvalue λ_1 of the soliton shown in **(a)**, while the black dashed line is the result of the adiabatic approximation, given in Eq. (6.7). We only display the imaginary part of the eigenvalue, since the real part, corresponding to the velocity, uniformly cancels. The agreement is excellent at low times. Importantly, the smallness of γ alone is not sufficient; the actual requirement is $\gamma t_{\max} \ll 1$ as emphasized in [294]. Once this condition is violated, the cumulative effect of losses becomes too large for the soliton to remain well-described by slowly varying parameters.

6.1.2 n-soliton perturbations

The perturbation theory developed within the IST framework has provided a wealth of analytical results for bright solitons, particularly in the regime of weak perturbations where controlled approximations are available [82]. In contrast, extending these methods to multi-soliton states remains significantly more challenging. While the case of two well-separated solitons can be treated under suitable assumptions [292], a general and tractable perturbative theory for arbitrary n-soliton solutions is still lacking.

Multi-soliton waveforms possess an intricate internal structure: their constituent solitons interact nonlinearly through their phases, amplitudes, and collision dynamics. As a result, perturbations can trigger a wide variety of behaviours. For instance, in the presence of linear losses, [294] demonstrated that the discrete spectrum exhibits a remarkably complex time evolution driven by inter-soliton interactions. We illustrate this phenomenon in Fig. 6.2, using as initial condition the $n = 3$ multi-soliton. Under losses, we observe that two eigenvalues first coalesce, before separating into two branches of identical amplitude but opposite velocities. Such behaviour depends sensitively on the initial relative phases of the constituent solitons and highlights the highly nontrivial dynamics of perturbed multi-soliton states. Similarly, [251] showed that, under linear losses, the asymptotic broadening of an $n = 2$ multi-soliton depends sensitively on the loss coefficient γ. In particular, the pulse width exhibits an oscillatory dependence on γ, and, for certain values, the asymptotic broadening can even exceed that expected from linear Schrödinger dispersion.

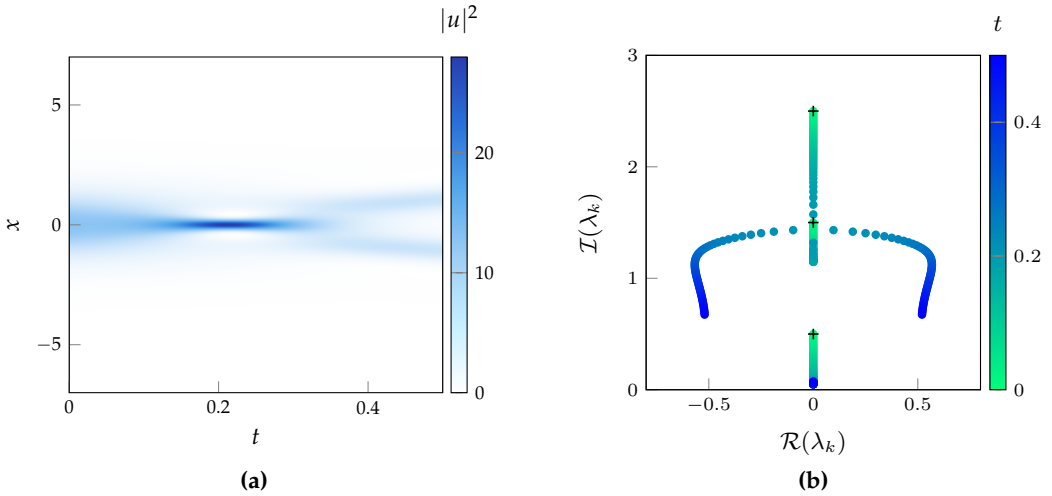

Figure 6.2: **(a)** Numerical simulation of the temporal evolution of the $n = 3$ multi-soliton, corresponding to the initial profile $u(x,0) = 3/\cosh(x)$. A perturbation in the form of linear losses with strength $\gamma = 1$ is included. After an initial contraction, the waveform splits into two components propagating with opposite velocities. **(b)** Time evolution of the discrete eigenvalues associated with the perturbed waveform in panel **(a)**. Black crosses mark the initial values. The two largest eigenvalues first collide on the imaginary axis at $t \simeq 0.2$, after which they split symmetrically by developing opposite real parts (corresponding to opposite velocities). This illustrates the nontrivial spectral dynamics induced by perturbations in multi-soliton states.

The case of wavepackets containing two solitons can be treated numerically thanks to the existence of closed-form analytical expressions for the corresponding Jost functions [294]. In this situation, one may integrate Eq. (6.5) directly, updating at each step the Jost functions $\phi_{a,b}$, the associated scattering data, and the field $u(x,t)$. This approach was developed by [295], who investigated a variety of perturbations relevant to optical fibers. It was further analyzed by [294], who benchmarked the IST-based perturbative evolution of the eigenvalues against direct numerical simulations of the perturbed NLSE in the presence of losses.

6.1.3 Perturbations in optical fibers

Optical fibers have provided a well-controlled platform to experimentally study the NLSE and its solitonic solutions [38, 74]. During the 1980s, the narrowing of optical pulses has allowed the characterization of higher-order nonlinear terms, thus realizing the breaking of the integrability of the NLSE.

Raman shift

In silica fibers the nonlinear response of the medium has a delayed component arising from molecular vibrations, associated with stimulated Raman scattering. For a localized pulse, this delayed response transfers energy from the high-frequency side of the spectrum toward the low-frequency side, producing a cumulative red-shift of the pulse's central frequency as it propagates, the Raman self-frequency shift. In the envelope equation, this effect appears as an additional perturbation term of the form $R[u] \propto u\,\partial_x|u|^2$ in the NLSE [296]. The phenomenon was first observed experimentally by [297], who reported the appearance of a satellite peak at a shifted frequency for optical pulses close to the bright-soliton regime.

The presence of this Raman term has important implications for multi-soliton states. Using numerical simulations, [298, 299] proposed that the Raman shift could be used to induce the fission of higher-order solitons of the form $u(x) = n/\cosh(x)$. This prediction was later confirmed experimentally by [300], who observed the breakup of an $n = 10$ pulse into several distinct constituents when sufficiently powerful pulses were used.

Beyond soliton fission, the Raman effect can also reveal the underlying solitonic content of a more general wavepacket. This principle was demonstrated by [301] for the case $n = 2$. They showed that, in an appropriate parameter regime, the weak breaking of integrability caused by the Raman term predominantly modifies the solitons' velocities, while leaving their amplitudes essentially unchanged. We reproduce in Fig. 6.3a numerical simulations based on their experimental parameters, illustrating the gradual separation of the two solitons. The imaginary parts of their associated eigenvalues remain nearly constant (Fig. 6.3b), indicating that their amplitudes are preserved. As a result, the system's late-time profile directly reveals the number and relative strengths of the solitons present initially. Due to the absence of femtosecond-resolved imaging at the time, [301] relied on autocorrelation measurements at the fiber output. The appearance of multiple lobes in the autocorrelation trace provided indirect but clear evidence for the presence and separation of the two solitons.

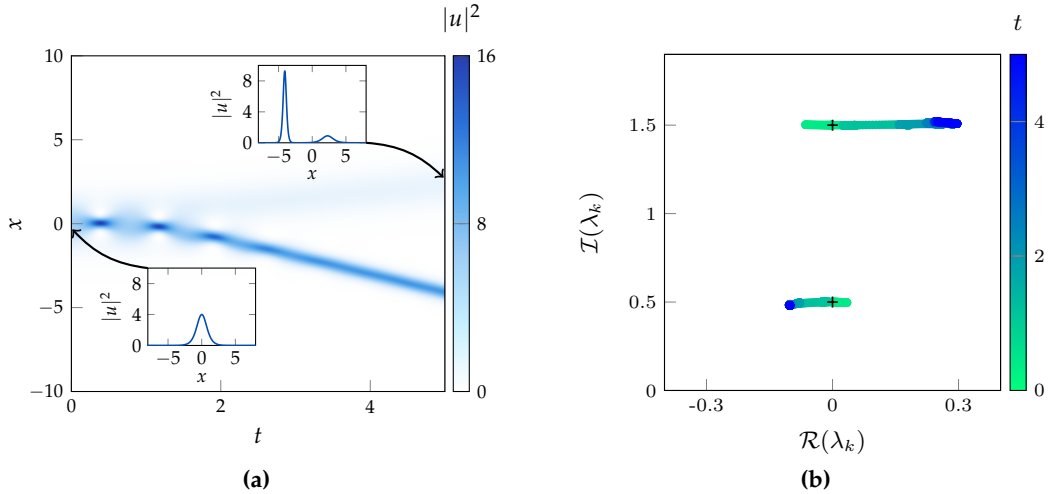

Figure 6.3: **(a)** Numerical simulation of the $n = 2$ multi-soliton including the Raman perturbation, with parameters chosen to reproduce the experiment of [301]. The insets show the initial and final wavepackets, highlighting the fission of the initial two-soliton into two bright solitons of different amplitudes. Since the imaginary parts of the eigenvalues satisfy $\mathcal{I}(\lambda_k) = \kappa_k/2$, and the peak intensity of each soliton is $\max(|u|^2) = \kappa_k^2$, the ratio of their heights is close to 9. **(b)** Time evolution of the eigenvalues λ_k corresponding to the perturbed waveform in **(a)**. The black crosses indicate the initial eigenvalues λ_k. The Raman shift acts mainly during the pulse compressions, producing a "staircase" evolution of the real parts of λ_k, i.e. the soliton velocities. Meanwhile the imaginary parts remain approximately constant, indicating that each soliton's amplitude is nearly preserved. Thus, the asymptotic state reveals the solitonic content of the initial multi-soliton wavepacket.

Dipersion management

Optical fibers offer the possibility to vary the effective nonlinear coefficient or the group-velocity dispersion along the propagation direction, for instance through controlled modulation of the core diameter. It is important to note that, compared to BECs

described by the GPE, the roles of space and time in the NLSE for optical fibers are interchanged. This leads to the framework of dispersion-managed fibers, described by an NLSE with a periodically varying dispersion coefficient [302]. Such longitudinal variations act as a controlled breaking of integrability and enable a broad range of soliton-manipulation strategies [66]. In particular, [288] showed numerically that a weak modulation at the intrinsic breathing frequency of a n-soliton induces a resonant response that eventually separates its constituent solitons. At higher modulation strengths, [303] demonstrated experimentally that a multi-soliton undergoes a pronounced fission into several bright solitons. However, the magnitude of the perturbation prevented the resulting amplitudes from faithfully reflecting the initial solitonic content.

6.2 Integrability breaking with a potential

In the previous sections, we discussed several mechanisms through which the integrability of the NLSE can be broken by the addition of perturbative terms. Such modifications generally induce nontrivial dynamics, while the IST framework may still be employed to interpret the resulting evolution in terms of solitonic degrees of freedom. The main distinction with the fully integrable case presented in Chap. 3 lies in the fact that the discrete eigenvalues λ_k become time-dependent.

Nevertheless, when the perturbation remains sufficiently weak, the evolution of the scattering data can be controlled. In particular, certain perturbations predominantly affect the real part of the discrete eigenvalues, corresponding to the soliton velocities, while leaving their imaginary parts, and thus their amplitudes, nearly unchanged. This situation arises, for instance, in the presence of the Raman self-frequency shift in optical fibers [302], illustrated in Fig. 6.3, or when spatially modulating the refractive index in planar Kerr waveguides [see for instance the numerical studies of 304, 305]. In such cases, one effectively realizes an "experimental IST": the number and amplitudes of the solitons are preserved, and the long-time dynamics reveals the individual solitons that were encoded in the initial wavepacket. This approach is particularly valuable for probing bound states of multiple solitons, where several constituents co-propagate at the same velocity.

6.2.1 Adding a small potential

Among the various routes to integrability breaking in the NLSE, a natural possibility consists in introducing an external potential. Examples include step-like potentials [306, 307] or localized defects approaching a Dirac delta function [308]. We recall that the NLSE remains integrable in the presence of a constant uniform force, highlighting that not all external potentials remove integrability.

This method is particularly well-suited to ultracold-atom platforms, where external potentials can be shaped with high precision using additional laser beams. In our experiment, such control is achieved using the DMD2, which allows for the programmable creation of tailored potential landscapes. We consider a Gaussian perturbation of the NLSE, implemented by choosing in Eq. (6.1) the perturbation term:

$$\mathrm{i}\epsilon R[u] = V_{\mathrm{ext}}(x)\, u(x) = \epsilon \exp\left[-\frac{(x-x_0)^2}{\sigma^2}\right] u(x)\,, \tag{6.8}$$

where x_0 and σ denote the position and the spatial width of the potential, respectively. We show in Fig. 6.4 an example of a time evolution of a 2-soliton, as well as the eigenvalues of the wavepacket in Fig. 6.4b. We observe that each soliton acquires a small

velocity, while their amplitude is conserved: the solitonic content is revealed at the end of the time evolution.

Besides, once the spatial overlap between the external potential V_{ext} and the wavefunction u becomes negligible, the perturbation term $R[u]$ effectively vanishes. In practice, when the solitons acquire a sufficiently large velocity, they rapidly leave the region where the potential is significant. Beyond this time, the system can again be regarded as effectively integrable: the discrete spectrum becomes time independent and the conservation properties associated with solitons are restored.

6.2.2 Which depth for the potential?

In the limit $\epsilon \to 0$, the perturbation vanishes and the dynamics reduce to those of the integrable NLSE. Conversely, for $\epsilon \gg 1$, the perturbation becomes strongly non-perturbative and leads to a substantial distortion of the wavepacket, largely modifying both the discrete and continuous scattering data, independently of the initial solitonic content. This raises the practical question of choosing an appropriate value of ϵ that maximizes the velocity imparted to the solitons, so as to induce a rapid spatial separation, while preserving their amplitudes.

Restricting ourselves to the case of a two-soliton bound state, we investigate in Fig. 6.5 the effect of varying the depth of the potential, considering both positive and negative values of ϵ. In this regime, we find that the perturbation of the solitons' amplitude remain below the percent level, while the induced velocities are sufficient to separate the constituent solitons after only a few breathing periods.

We further observe numerically that choosing $\epsilon < 0$ results in a slower separation of the solitons. In this case, the larger-amplitude soliton undergoes oscillatory motion in the vicinity of the perturbation, as illustrated in the inset of Fig. 6.5. This behavior makes negative values of ϵ less favorable for experimental implementations, and motivates restricting to $\epsilon > 0$, that is a repulsive potential, in the following.

6.2.3 Application to a two-component mixture

The results discussed above were derived for the one-component attractive NLSE. We now turn to their applicability to our experimental platform, which consists of a two-component (spin) mixture. Some numerical results were developed for spin mixtures by [309], in the case of attractive interactions.

Low-depletion limit

In the limit $n_2/n_0 \ll 1$, where the density of the minority component is much smaller than that of the bath, we showed in Sec. 2.3.2 that the coupled GPEs can be mapped onto an effective one-component attractive GPE. In this mapping, the interaction strength is dressed by the bath, and an effective external potential arises, see Eq. (2.47), which is given by:

$$V_{\text{ext}}(x) = \left(1 - \frac{g_{1,2}}{g}\right) \tilde{V}_{\text{ext}}(x) = -0.013 \tilde{V}_{\text{ext}}(x)\,, \tag{6.9}$$

where $\tilde{V}_{\text{ext}}$ denotes a potential applied equally to both components, and the numerical value in the second equality corresponds to the interaction parameters of our mixture. In particular, the condition $\epsilon > 0$ discussed above implies that $\tilde{V}_{\text{ext}}$ must be attractive, i.e. $\tilde{V}_{\text{ext}} < 0$.

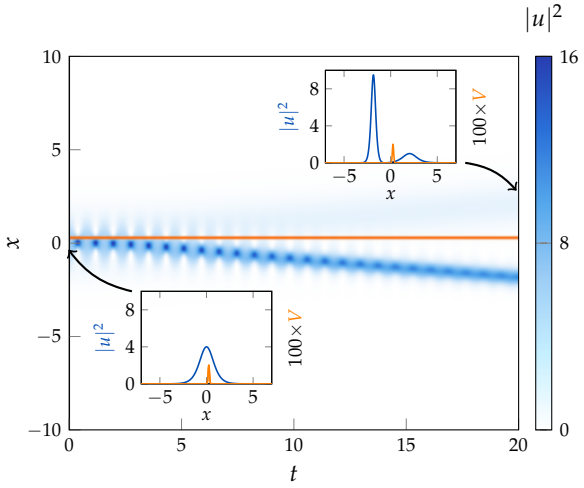

(a) Time evolution of the perturbed 2-soliton.

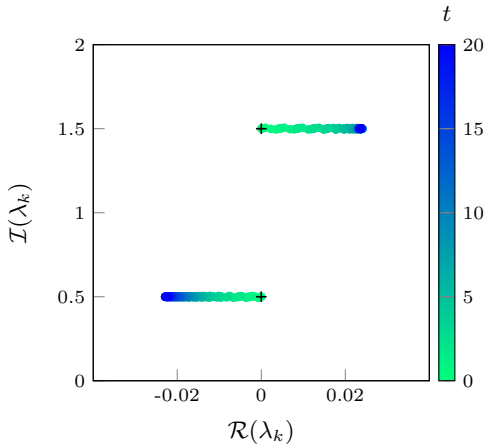

(b) Evolution of the eigenvalues of the 2-soliton.

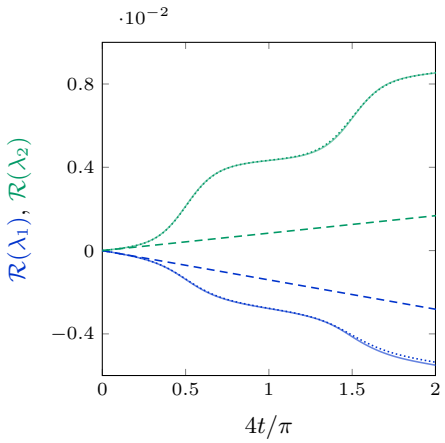

(c) Initial perturbation of the eigenvalues.

Figure 6.4: Numerical simulation of the time evolution of a two-soliton state of NLSE with initial wavepacket $u(x) = 2/\cosh(x)$, in the presence of the localized perturbation defined in Eq. (6.8). The parameters are $\sigma = 0.1$, $\epsilon = 0.02$, and $x_0 = 0.25$. The initial discrete eigenvalues are $\lambda_1 = \mathrm{i}/2$ and $\lambda_2 = 3\mathrm{i}/2$. **(a)** Spatiotemporal evolution of the wavepacket. Insets highlight the initial and final states, showing that the two constituent solitons acquire different velocities due to the perturbation. The wavepacket is shown in blue, while the external potential is shown in orange and magnified in the insets for clarity. **(b)** Time evolution of the discrete eigenvalues associated with the wavepacket in **(a)**. The imaginary parts remain approximately constant, with less than 2% deviations, while the real parts evolve during the time interval when $R[u]$ is significant, in agreement with the observed real-space dynamics. Black crosses indicate the initial eigenvalues. **(c)** Close-up of the early-time evolution of the real parts of the two eigenvalues. Time is rescaled in units of the two-soliton breathing period. Solid lines correspond to the numerical evolution, while dashed lines show the prediction of first-order perturbation theory, given by Eq. (6.5) evaluated at $t = 0$. Excellent agreement is observed at times small compared to the first contraction of the multi-soliton, occurring at $t = \pi/8$. The dotted curves correspond to numerical integration of the Eq. (6.5), calculating the Jost solutions as well as u at each time step. We followed the method described in [294, 295].

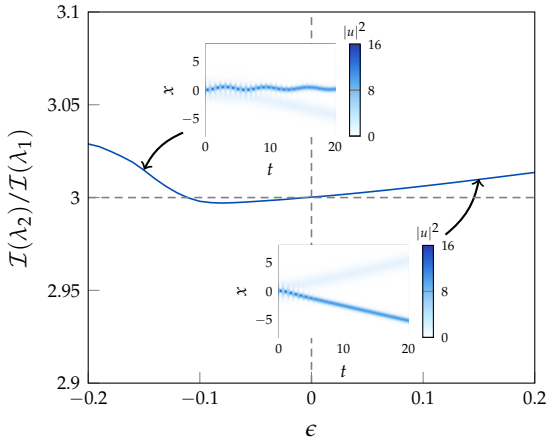

Figure 6.5: Starting from a two-soliton wavepacket ($n = 2$), we introduce at $t = 0$ the localized perturbation defined in Eq. (6.8), with $\sigma = 0.1$, $x_0 = 0.25$, and a variable depth ϵ. After the solitons have separated, the discrete spectrum of the wavefunction is computed. We plot the ratio of the soliton amplitudes, given by the ratio of the imaginary parts of the discrete eigenvalues. Only small deviations from the integrable value of 3 are observed, as indicated by the dashed gray lines. The sum of the imaginary parts of the eigenvalues is conserved to good accuracy (deviations below 0.4 %, and below 0.05 % for $\epsilon > 0$), indicating that the reflection coefficient remains negligible ($b(\xi) \simeq 0$) and that no significant radiation is produced. Insets show the spatiotemporal evolution of the wavepacket for $\epsilon = -0.15$ and $\epsilon = 0.15$.

Perturbations of the LLE

For arbitrary depletion of the minority component, the dynamics must be described within the LLE framework. Since the addition of an external potential breaks integrability, the results obtained for the NLSE cannot be directly transferred via the gauge transformation established in Chap. 3. Nevertheless, the general structure of perturbation theory, and in particular Eq. (6.5), remains valid. However, analytical treatments of perturbed multi-solitons are still out of reach in this more general setting.

We therefore resort to numerical simulations of the coupled GPEs to assess the effect of the localized potential introduced in Eq. (6.8). The position of the perturbation is chosen relative to the center of mass of the multi-soliton, whose intrinsic asymmetry leads to a shift of the density maximum. Overall, we obtain results qualitatively similar to those found for the one-component NLSE in Sec. 6.2.2, with the following notable differences:

- If $|x_0|$ is chosen too small (with a threshold that depends on κ and is of order unity), the solitons do not separate within the simulated time window. Instead, both solitons acquire nearly identical velocities.
- The dressing of the interactions by the bath allows for larger values of the perturbation strength ϵ. As in the low-depletion limit, achieving a splitting of the solitons with opposite velocities requires an attractive external potential, following the minus sign of Eq. (6.9).

6.3 Experimentally separating 2-solitons

We now turn to the experimental separation of multi-solitons. In the context of the NLSE, the dissociation of multi-solitons has been investigated in optical waveguides [310, 311], albeit using strong perturbations that significantly modify the initial discrete

spectrum. In the context of optical fibers, we have already discussed the pioneering work of [301], in which a Raman self-frequency shift induced the splitting of a 2-soliton. We also mention the recent work of [312], where several solitons separate as a result of a careful engineering of the initial conditions, while the system remains integrable.

6.3.1 Calibration of the potential

Following the discussion of the previous section, our goal is to realize a localized attractive potential, due to the minus sign of Eq. (6.9). In the experiment, however, the optical potentials generated with the DMDs rely on repulsive light at 532 nm. To circumvent this constraint, we project on DMD2 a spatially uniform background intensity, onto which a localized dark feature is imprinted at the desired position of the potential. This approach effectively creates an attractive potential relative to the surrounding background.

Prior to imprinting the local perturbation, we compensate for the Gaussian envelope of the beam and for residual optical imperfections by implementing a feedback loop on the DMD image, yielding a flat-top intensity profile at the position of the atoms. This calibration procedure has been described in detail in previous works [see, e.g., Sec. 5.1.3 of 106]. Once the beam is flattened, we superimpose the desired optical potential, which in the present case corresponds to a Gaussian profile with negative amplitude.

The shape of the potential is calibrated using a LDA applied to a homogeneous two-dimensional gas at $T = 0$. Within this framework, the external potential satisfies $V(\mathbf{r}) = -gn(\mathbf{r})$ up to a constant term accounting for the chemical potential. Accurate measurements of the atomic density therefore provide direct access to the local potential landscape. This calibration procedure is illustrated in Fig. 6.6, from which we extract both the amplitude and the width of the potential. These measurements demonstrate that we can reliably generate an attractive potential with well-controlled position and strength.

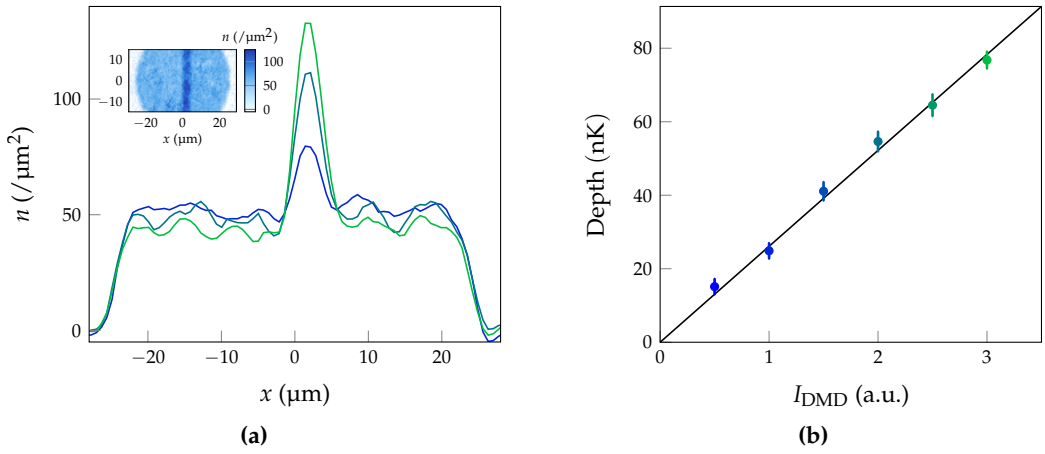

Figure 6.6: (a) One-dimensional cuts of the atomic density in the presence of a localized attractive potential, for several values of the potential amplitude. Each density profile is fitted with a Gaussian function, allowing us to extract the width of the potential, $\sigma = 2.1(1)\,\mu$m, as well as its depth. The inset shows an averaged absorption image; the excess atomic density is localized at the position of the potential. Away from this region, the density remains flat, confirming that the constant background offset does not affect the atoms. **(b)** Summary of the calibration of the potential depth as a function of the light intensity projected by the DMD. The color code corresponds to the density profiles shown in **(a)**.

6.3.2 Splitting of a 2-soliton

We first prepare a multi-soliton with $n = 2$, following the procedure described in Chap. 4. A localized potential is then ramped linearly over 100 ms up to its final amplitude and positioned slightly off-center with respect to the multi-soliton. Absorption images of the minority component are subsequently recorded, with a representative example shown in Fig. 6.7a. In order to have a longer accessible length for the solitons to propagate, we change the bath geometry from a 50 µm long tube to a 20 µm radius ring, as shown in Fig. 1.5. The images are subsequently unwrapped to simplify their analysis. The transverse confinement is also recalibrated, with the protocol given in Chap. 4, in order to account for the change of the DMD profile.

Because the two solitons are expected to have markedly different amplitudes, by a factor of 9 in density in the NLSE limit, we acquire two successive images within the same experimental sequence, using different MW pulses to obtain an OD optimized for each soliton.

The results for a low-depletion multi-soliton are shown in Fig. 6.7. The wavepacket initially undergoes a contraction, as expected from the intrinsic breathing dynamics of a 2-soliton, before separating into two distinct wavepackets at around 150 ms. Each component then propagates independently, conserving both its atom number and spatial width, hallmarks of solitonic behavior. A quantitative analysis of the two wavepackets is presented in Fig. 6.7b, confirming their solitonic nature. The measured ratio of atom numbers is $N_2/N_1 = 3.2 \pm 0.1$, in good agreement with the NLSE prediction of 3.

This experiment can be interpreted within the perspective of an "experimental IST". By applying a controlled, localized perturbation that primarily affects the solitons' velocities while preserving their amplitudes, the system effectively transitions back to an integrable regime after the interaction with the external potential. The final state thus provides direct access to the discrete scattering data of the initial wavepacket, allowing the solitonic content of the multi-soliton to be revealed experimentally.

6.3.3 Splitting from NLSE to LLE

For the NLSE, the atom number carried by a soliton is proportional to its amplitude parameter κ, so that $N_k \propto \mathcal{I}(\lambda_k)$. As a result, the ratio of atom numbers in a split 2-soliton directly reflects the ratio of the imaginary parts of the corresponding eigenvalues. This simple relation, however, does not extend to magnetic solitons described within the LLE framework.

Indeed, as shown in Chap. 5, magnetic solitons with a fixed atom number populate an ellipse in the eigenvalue plane, following Eq. (5.18). Restricting to zero-velocity solitons, such as those shown in the right panel of Fig. 5.6a, the atom-number ratio for a 2-soliton can be written as:

$$\frac{N_2}{N_1} = \frac{\tanh^{-1}(3\kappa)}{\tanh^{-1}(\kappa)}, \tag{6.10}$$

where we have used the identity $\tanh(N/2) = (2 + \Omega - \sqrt{\Omega^2 + v^2})/2\kappa$ in the case $v = 0$ (we recall that $\Omega = \kappa^2 - 1 < 0$ in our situation). In the limit $\kappa \to 0$, corresponding to a weak depletion of the bath, one has $\tanh^{-1}(x) \simeq x$, and the NLSE result $N_2/N_1 = 3$ is recovered. Eq. (6.10) is plotted in Fig. 6.8 over the range $\kappa \in [0, 1/3]$, which corresponds to 2-solitons prepared with a flat phase at $t = 0$, as discussed in Chap. 5.

By preparing multi-solitons with different values of κ, and thus varying the depletion of the mixture, we apply the same splitting protocol as in the low-depletion regime. The resulting wavepackets can again be identified with the constituent solitons of the initial bound state. The measured ratio of atom numbers, shown in Fig. 6.8, therefore provides

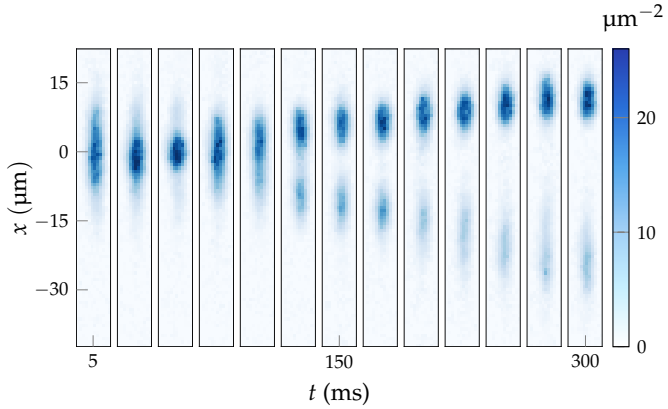

(a) Absorption images with highest MW repump pulse.

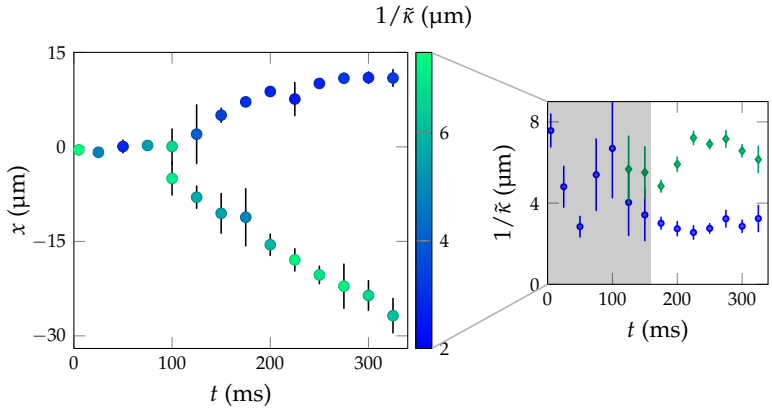

(b)

Figure 6.7: Experimental splitting of a 2-soliton of initial width $1/\kappa = 8\,\mu\text{m}$, thanks to a localized potential. It is raised during the first 100 ms up to an amplitude of $-9(1)$ nK. It corresponds to $\epsilon \simeq -0.013 \times -8 \simeq 0.1$ in dimensionless units ($9\,\text{nK} \times k_B \simeq 8\, n_0 |\delta g|$). **(a)** Mean absorption images showing the initial breathing of the multi-soliton, before it separates into two wavepackets, each of them evidencing characteristic behaviors of solitons. The potential is placed at $x_0 \lesssim 0$. The precise position is manually adjusted in order to maximize the splitting distance between the two solitons at a given time. It is therefore not well-calibrated, and we estimate it is situated around $x_0 \simeq -1/(2\kappa) \simeq -4\,\mu\text{m}$. **(b)** Analysis of the positions and widths of the wavepackets shown in **(a)**. The widths remain approximately constant after the separation, and their ratio is close to 3, as expected from the NLSE limit. The widths are detailed in the right panel. The grey area indicates the time during which the two solitons are not properly split, during which we notably observe the first breathing period of the wavepacket. After their separation, the widths remain approximately constant.

a direct experimental signature of the nature of the multi-soliton: it interpolates between the NLSE limit at weak depletion and the more general LLE behavior, which exhibits a pronounced divergence as κ increases.

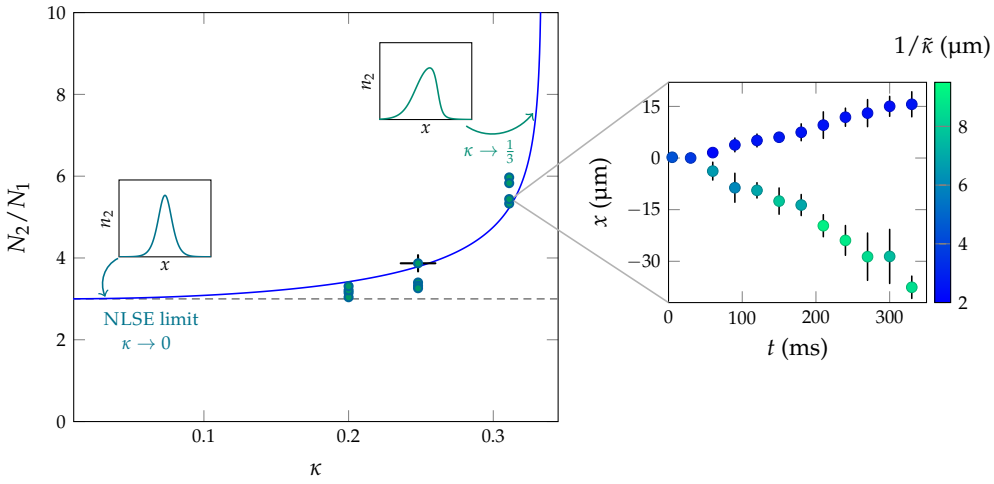

Figure 6.8: Ratio of atom numbers N_2/N_1 of the two solitons obtained after splitting a 2-soliton, as a function of the soliton parameter κ. The solid line corresponds to the theoretical prediction of Eq. (6.10), derived within the LLE framework for zero-velocity magnetic solitons. The dashed horizontal line indicates the NLSE limit $N_2/N_1 = 3$, recovered for $\kappa \to 0$ (low-depletion regime). Experimental data points are obtained by preparing multi-solitons with varying depletion and applying the same splitting protocol. The small vertical dispersion in the points for each value of κ corresponds to slight variations of the initial atom number, similarly to the experiments of Chap. 5. The error bars are only represented for one of the points, and are similar for all experimental values. The deviation from the NLSE value highlights the crossover from the weakly depleted regime to the more general LLE description. The right panel illustrates the splitting of a 2-soliton in the LLE regime, similarly to that of Fig. 6.7b for the NLSE. We clearly observe the formation of two wavepackets, each forming a magnetic soliton.

Conclusion

In this chapter, we investigated how weak perturbations of integrable models can be used to probe and control the solitonic content of nonlinear wavepackets. Within the Inverse Scattering Transform framework, such perturbations induce a slow evolution of the scattering data, allowing solitons to remain well-defined while their eigenvalues evolve in time.

We reviewed perturbation theory for the NLSE, from the adiabatic description of single solitons to the more intricate dynamics of multi-soliton states, where interactions lead to nontrivial eigenvalue evolution. Although a general analytical theory for perturbed multi-solitons is still lacking, numerical approaches provide valuable insight into these dynamics.

Focusing on localized external potentials, we showed that integrability can be broken in a controlled manner, predominantly affecting soliton velocities while preserving their amplitudes. This regime effectively realizes an "experimental IST", in which the final state reveals the discrete spectrum of the initial wavepacket.

Applying this approach to a two-component ultracold Bose gas, we demonstrated the controlled splitting of 2-solitons, from the NLSE limit to the more general LLE description. These results illustrate how controlled integrability breaking enables the identification and manipulation of multi-soliton states in complex experimental systems.

SUMMARY AND OUTLOOK

This thesis has explored the physics of solitons and integrability in nonlinear wave equations, using ultracold atomic gases as a controllable experimental platform. By combining experimental realizations, theoretical mappings, and perturbative approaches within the Inverse Scattering Transform framework, it provides a coherent investigation of how solitonic structures emerge, persist, and can be revealed when integrability is weakly broken.

Chapter 1 introduced the experimental apparatus and the tools developed to study nonlinear dynamics in ultracold atomic gases. We described the production of quasi-two-dimensional Bose-Einstein Condensates of ^{87}Rb and the preparation of two-component spin mixtures with precise control over internal and external degrees of freedom. Particular emphasis was placed on optical and microwave techniques enabling state preparation, coherent spin manipulation, and high-resolution imaging. The use of Digital Micro-mirror Devices was detailed, highlighting their role in engineering tailored optical potentials with spatial and temporal control. Together, these tools establish a versatile platform capable of realizing effective one-dimensional dynamics and implementing controlled perturbations, which are essential for probing integrability and soliton physics experimentally.

In Chapter 2, we developed the theoretical framework describing our system at the mean-field level. Starting from the many-body Hamiltonian, we justified the use of coupled Gross-Pitaevskii Equations in the weakly interacting and low-temperature regime. We discussed superfluidity in inhomogeneous systems, emphasizing its connection to phase coherence and its quantitative characterization through the superfluid fraction. The properties of spin mixtures were then introduced, with a focus on interaction parameters and collective modes. Finally, we identified a relevant regime in which the dynamics of the minority component can be mapped onto an effective single component attractive Nonlinear Schrödinger Equation, laying the groundwork for the emergence of bright solitons in an otherwise repulsive atomic gas.

Chapter 3 was devoted to the concept of integrability and the IST, with a particular focus on the attractive NLSE. We presented the IST as a nonlinear analogue of the Fourier Transform, providing a formal solution of the equation in terms of scattering data. The physical interpretation of this formalism was emphasized, notably the correspondence between discrete eigenvalues and solitons. We discussed single- and multi-soliton solutions, including bound states with equal velocities, and highlighted how their dynamics encode conserved quantities of the integrable system. This chapter established the conceptual link between soliton dynamics and the hidden integrable structure that underpins the subsequent experimental and perturbative studies.

In Chapter 4, we presented the experimental realization of multi-soliton wavepackets in a two-component ultracold Bose gas. By exploiting deterministic wavefunction imprinting in a spin mixture, we demonstrated the controlled generation of states corresponding to multi-soliton solutions of the NLSE. We characterized their temporal evolution, observing hallmark features such as breathing dynamics and robust shape preservation. Particular attention was given to equal-velocity multi-solitons, whose dynamics reflect their underlying scattering data.

Chapter 5 introduced an alternative description of the spin mixture based on an analogy with ferromagnetic spin chains governed by the Landau-Lifshitz Equation. We established a formal mapping between this equation and the NLSE through a gauge transformation, allowing solitonic solutions to be translated between the two frameworks. This mapping enabled the realization and characterization of magnetic solitons and multi-soliton states, evidencing the similarities and differences from their NLSE counterparts. The chapter highlighted how the same experimental platform can access different integrable models, enriching the physical interpretation of observed solitonic dynamics.

Finally, Chapter 6 addressed the effects of integrability breaking and the use of perturbation theory within the IST framework. We reviewed key results of perturbative IST for the NLSE and illustrated how weak perturbations induce a controlled time evolution of the scattering data. We demonstrated experimentally and numerically that suitably chosen perturbations, such as localized potentials, can predominantly affect soliton velocities while preserving their amplitudes. This allowed the experimental separation of bound multi-soliton states, effectively revealing their solitonic content at long times. Extending these ideas to spin mixtures, we showed how the same perturbative approach can be applied beyond the NLSE limit. By varying the depletion of the minority component, we explored a continuous crossover from the effective attractive NLSE to the more general LLE description. In both regimes, the controlled splitting of bound multi-soliton states provides direct experimental access to their solitonic content. This approach thus offers a practical means to probe how integrable structures are modified across different effective descriptions of the system.

The level of control achieved in this work over multi-soliton states and over controlled departures from integrability opens natural perspectives toward the experimental study of integrable turbulence. In such regimes, nonlinear wavefields are no longer described by isolated coherent structures, but rather by dense ensembles of interacting solitons, whose collective behavior is nevertheless constrained by the integrable structure of the underlying equations. The ability demonstrated here to access the solitonic content of a wavepacket through weak, well-calibrated perturbations provides a powerful tool to probe these dynamics beyond the single- or few-soliton level, and to experimentally connect microscopic scattering data to macroscopic observables.

Complementary to optical fiber platforms, ultracold atomic gases provide a set of experimental capabilities that are particularly well matched to the study of soliton gases and long-time nonlinear dynamics. While optical fibers excel at accessing propagation-based phenomena over long effective distances, cold-atom systems naturally allow the implementation of closed or periodic geometries, enabling the observation of temporal evolution without continuous energy injection or loss. In addition, integrability-breaking terms, such as external potentials or time-dependent magnetic-field gradients, can be introduced in a controlled and reversible manner, making it possible to finely tune the departure from integrable dynamics and to dynamically shape the system's evolution within a single experimental sequence.

Moreover, the high degree of control over state preparation in atomic systems enables the deterministic imprinting of tailored initial waveforms, as well as the reproducible generation of disordered or many-soliton configurations. This flexibility offers a natural route toward controlled studies of modulational instability. Techniques such as phase imprinting further provide access to controlled soliton velocities and relative phases could also be impleted in our system. The would allow the systematic exploration of the soliton phase space relevant to soliton gases and integrable turbulence.

From a theoretical perspective, soliton gases have recently emerged as effective models for the late-time dynamics of modulationally unstable systems, where an initially coherent wavepacket evolves into an ensemble of interacting solitons with well-defined statistical properties. Such descriptions naturally connect to the framework of generalized hydrodynamics, which provides a coarse-grained description of integrable many-body systems in terms of conserved quasiparticle densities. The experimental platform developed here appears particularly well suited to testing these ideas, and to exploring how soliton-gas descriptions extend to multicomponent systems and to regimes interpolating between the NLSE and LLE limits.

APPENDICES

A List of publications

During this thesis, the projects I was involved in led to the following publications:

- *Superfluid fraction in an interacting spatially modulated Bose-Einstein condensate*, G. Chauveau, C. Maury, F. Rabec, C. Heintze, G. Brochier, S. Nascimbene, J. Dalibard and J. Beugnon, Physical Review Letters 130, 226003 (2023).
- *Bloch oscillations of a soliton in a one-dimensional quantum fluid*, F. Rabec, G. Chauveau, G. Brochier, S. Nascimbene, J. Dalibard, and J. Beugnon, Nature Physics 21, 1541–1547 (2025).
- *Superfluid Fraction of a 2D Bose-Einstein Condensate in a Triangular Lattice*, F. Rabec, G. Brochier, S. Wattellier, G. Chauveau, Y. Li, S. Nascimbene, J. Dalibard, and J. Beugnon, arXiv:2511.04575 (2025), submitted to Physical Review Letters.

The experimental work detailed in Chap. 4-6 is also the subject of an article in preparation.

B Magnetic Dipole-Dipole Interactions

B.1 Interactions in a two-component Bose gas

We consider a mixture of two states labelled 1 and 2. The interaction potential between two atoms A, B, at positions $\mathbf{r}_A, \mathbf{r}_B$, is given by:

$$V_{\alpha,\beta,\gamma,\delta}(\mathbf{r}_A - \mathbf{r}_B) = \langle A : \mathbf{r}_A, \gamma \,;\, B : \mathbf{r}_B, \delta | \, \hat{V} \, | A : \mathbf{r}_A, \alpha \,;\, B : \mathbf{r}_B, \beta \rangle \,, \tag{B.1}$$

where all greek indices are either 1 or 2. The interaction Hamiltonian resulting from this potential reads:

$$\hat{H}_{\text{int}} = \frac{1}{2} \sum_{\alpha,\beta,\gamma,\delta} \iint V_{\alpha,\beta,\gamma,\delta}(\mathbf{r} - \mathbf{r}') \; \hat{\Psi}^\dagger_\gamma(\mathbf{r}) \, \hat{\Psi}^\dagger_\delta(\mathbf{r}') \, \hat{\Psi}_\beta(\mathbf{r}') \, \hat{\Psi}_\alpha(\mathbf{r}) \; \mathrm{d}^3 r \, \mathrm{d}^3 r' \,, \tag{B.2}$$

We notice that it contains both elastic and inelastic terms. In the following, we restrict ourselves to elastic processes. For contact interactions, the interaction Hamiltonian is recast in the following form:

$$\begin{aligned} \hat{H}_{\text{contact}} = & \frac{2\pi\hbar^2 a_{1,1}}{m} \int \hat{\Psi}^\dagger_1(\mathbf{r}) \, \hat{\Psi}^\dagger_1(\mathbf{r}) \, \hat{\Psi}_1(\mathbf{r}) \, \hat{\Psi}_1(\mathbf{r}) \; \mathrm{d}^3 r \\ & + \frac{2\pi\hbar^2 a_{2,2}}{m} \int \hat{\Psi}^\dagger_2(\mathbf{r}) \, \hat{\Psi}^\dagger_2(\mathbf{r}) \, \hat{\Psi}_2(\mathbf{r}) \, \hat{\Psi}_2(\mathbf{r}) \; \mathrm{d}^3 r \\ & + \frac{4\pi\hbar^2 a_{1,2}}{m} \int \hat{\Psi}^\dagger_1(\mathbf{r}) \, \hat{\Psi}^\dagger_2(\mathbf{r}) \, \hat{\Psi}_2(\mathbf{r}) \, \hat{\Psi}_1(\mathbf{r}) \; \mathrm{d}^3 r \,, \end{aligned} \tag{B.3}$$

where a_{ij} correspond to the scattering lengths between atoms of components i and j. Magnetic Dipole-Dipole Interactions lead us to consider the following interaction potential between atoms A and B:

$$\hat{V}_{\text{mag}} = \frac{\mu_0 \mu_B^2}{\pi r^3} \left[\hat{\mathbf{s}}_A \cdot \hat{\mathbf{s}}_B - 3(\hat{\mathbf{s}}_A \cdot \mathbf{u})(\hat{\mathbf{s}}_B \cdot \mathbf{u}) \right] \,, \tag{B.4}$$

where $\hat{\mathbf{s}}_{A,B}$ denotes the spin of the outer electron of atom A, B respectively, r is the distance between the atoms, and $\mathbf{u}$ the unit vector linking A and B. Our goal is to evaluate the contribution of this potential in the interaction Hamiltonian of Eq. (B.2).

B.2 The $|1,-1\rangle$, $|1,+1\rangle$ mixture

In the following we will note $|1\rangle = |F = 1, m_F = -1\rangle$ and $|2\rangle = |F = 1, m_F = +1\rangle$. We will calculate the matrix elements of V for this mixture. Since Eq. (B.4) involves only the electron spin, we express $|1\rangle$ and $|2\rangle$ in the basis of the electron and nuclear spins.

Thus, we decompose these states in the basis $|s_z, i_z\rangle$:

$$|1\rangle = -\sqrt{\frac{3}{4}}\left|\frac{1}{2};-\frac{3}{2}\right\rangle + \frac{1}{2}\left|-\frac{1}{2};-\frac{1}{2}\right\rangle, \tag{B.5}$$

$$|2\rangle = \sqrt{\frac{3}{4}}\left|-\frac{1}{2};\frac{3}{2}\right\rangle - \frac{1}{2}\left|\frac{1}{2};\frac{1}{2}\right\rangle. \tag{B.6}$$

It is necessary to evaluate $\hat{s}_i|1,2\rangle$, with $i = x,y,z$. Since $\hat{s}_x = \frac{1}{2}(\hat{s}_+ + \hat{s}_-)$ and $\hat{s}_y = \frac{1}{2}(\hat{s}_+ - \hat{s}_-)$, their action would change the electronic spin, resulting in $m_F = 0$ states. Thus, these operators cancel in the $|1\rangle, |2\rangle$ basis. All we need to do is evaluate the matrix elements of the operator $\hat{s}_z$. We write:

$$\hat{s}_z|1\rangle = \frac{1}{2}\left(-\sqrt{\frac{3}{4}}\left|\frac{1}{2};-\frac{3}{2}\right\rangle - \frac{1}{2}\left|-\frac{1}{2};-\frac{1}{2}\right\rangle\right), \tag{B.7}$$

$$\hat{s}_z|2\rangle = \frac{1}{2}\left(\sqrt{\frac{3}{4}}\left|-\frac{1}{2};\frac{3}{2}\right\rangle + \frac{1}{2}\left|\frac{1}{2};\frac{1}{2}\right\rangle\right). \tag{B.8}$$

Because the matrix elements of the operators $\hat{s}_x, \hat{s}_y$ are null, we only need to calculate the contributions of the following operator:

$$\hat{V}'_{\text{mag}} = \frac{\mu_0\mu_B^2}{\pi r^3}\,(1-3\cos^2\theta)\,\hat{s}_{zA}\hat{s}_{zB}\,, \tag{B.9}$$

where θ is the angle between u and the quantization axis. We evaluate successively the terms in Eq. (B.2):

$$\begin{aligned} V_{1111} &= \frac{\mu_0\mu_B^2}{16\pi r^3}\,(1-3\cos^2\theta)\,,\\ V_{2222} &= \frac{\mu_0\mu_B^2}{16\pi r^3}\,(1-3\cos^2\theta)\,,\\ V_{1212} &= V_{2121} = -\frac{\mu_0\mu_B^2}{16\pi r^3}\,(1-3\cos^2\theta)\,,\\ V_{1221} &= V_{2121} = 0. \end{aligned} \tag{B.10}$$

B.3 Shift in scattering lengths

It remains to evaluate the integral:

$$\hat{H}_{\text{mag}} = \frac{\mu_0\mu_B^2}{16\pi}\iint \frac{1-3\cos^2\theta}{r^3}\,\hat{\Psi}_2^\dagger(\mathbf{r}_A)\,\hat{\Psi}_1^\dagger(\mathbf{r}_B)\,\hat{\Psi}_2(\mathbf{r}_B)\,\hat{\Psi}_1(\mathbf{r}_A)\;\mathrm{d}^3r_A\,\mathrm{d}^3r_B\,. \tag{B.11}$$

We first note that its average value cancels in the case of a uniform 3D gas. We consider the case of the quantization axis lying in the atomic plane, which is relevant for this manuscript. The general case is discussed in [115, 241]. Using a uniform density with a gaussian distribution along z, we compute $\langle\hat{H}_{\text{mag}}\rangle$ by using first a small exclusion radius r_0 around the origin (and $r_0 \to 0$ at the end of the calculation). Comparing with the results of Eq. (B.3) allows us to express the results as a shift in scattering lengths. We obtain:

- $a_{1,1} = a_{1,1}^{(0)} - \frac{\mu_0}{16\pi}\frac{m\mu_B^2}{3\hbar^2} = a_{1,1}^{(0)} - 0.18\,a_B$
- $a_{2,2} = a_{2,2}^{(0)} - \frac{\mu_0}{16\pi}\frac{m\mu_B^2}{3\hbar^2} = a_{2,2}^{(0)} - 0.18\,a_B$

- $a_{1,2} = a_{1,2}^{(0)} + \frac{\mu_0}{16\pi}\frac{m\mu_B^2}{3\hbar^2} = a_{1,2}^{(0)} + 0.18\, a_B$

where $a_{i,j}^{(0)}$ are the scattering lengths given in Eq. (4.1).

C Equivalence of the NLSE and easy-axis LLE

We have explained in Chap. 5 that the NLSE and easy-axis LLE are equivalent in some sense. More specifically, we have shown that we can link their Lax pairs by a gauge transformation. Besides, it was shown by [79] that one can obtain an explicit formula to link solutions of these two equations, using only some algebraic properties. However, this article is only available in Russian (and in printed form). The goal of this Appendix is to reproduce, detail and comment the calculations performed in this article. We are helped in this task by [313], which is somewhat close in the sense that it treats the case of the easy-plane LLE (which is not equivalent to NLSE).

C.1 Parametrization

We first write the LLE in the easy-axis settings:

$$\mathbf{M}_t = \mathbf{M} \times \left[\mathbf{M}_{xx} + \beta \left(\mathbf{M} \cdot \mathbf{e}^{(z)}\right) \mathbf{e}^{(z)}\right] \quad \text{with} \quad \beta > 0\,, \tag{C.1}$$

where $\mathbf{M} = \left(M^{(x)}, M^{(y)}, M^{(z)}\right)$ is the magnetization vector, and $\mathbf{e}^{(z)}$ the unit vector in the direction z. The subscripts denote partial differentiation with respect to the given variable. Using the Pauli matrices, we can rather rewrite this equation in the following form:

$$i\hat{M}_t = \frac{1}{2}[\hat{M}, \hat{M}_{xx}] + \frac{\beta}{4}\left\{\hat{M}, \hat{\sigma}\right\}\left[\hat{M}, \hat{\sigma}\right]\,, \tag{C.2}$$

where:

$$\hat{M} = \begin{pmatrix} M^{(z)} & M^{(x)} - \mathrm{i}M^{(y)} \\ M^{(x)} + \mathrm{i}M^{(y)} & -M^{(z)} \end{pmatrix}\,, \quad \hat{\sigma} = \begin{pmatrix} 1 & 0 \\ 0 & -1 \end{pmatrix}\,, \tag{C.3}$$

and $[\cdot,\cdot]$, $\{\cdot,\cdot\}$ are the commutator and anticommutator respectively. Due to our parametrization: $\hat{M}^2 = \mathbb{1}_2$, $\hat{M}^\dagger = \hat{M}$ and $\mathrm{Tr}\,\hat{M} = 0$, with $\cdot^\dagger$ denoting the Hermitian transpose. Anticipating some calculations of Sec. C.3, there exists a matrix $\hat{g} \in \mathrm{SU}(2)$ such that:

$$\hat{M} = \hat{g}\hat{\sigma}\hat{g}^\dagger \quad \text{and} \quad \left\{\hat{g}^\dagger\hat{g}_x, \hat{\sigma}\right\} = 0\,. \tag{C.4}$$

We recall that $\hat{g}^{-1} = \hat{g}^\dagger$ and $\det(\hat{g}) = 1$ due to $\hat{g}$ belonging to the special unitary group. We can use these relations to rewrite Eq. (C.2). Multiplying it by $-\hat{g}^\dagger$ on the left and $\hat{g}$ on the right, we obtain:

$$\mathrm{i}\left[\hat{\sigma}, \hat{g}^\dagger\hat{g}_t\right] = 2\left(\hat{g}^\dagger\hat{g}_x\right)_x - \frac{\beta}{4}\left[\hat{\sigma}, \hat{R}\hat{\sigma}\hat{R}\right] \quad \text{with} \quad \hat{R} = \hat{g}^\dagger\hat{\sigma}\hat{g}\,, \tag{C.5}$$

where we used the fact that $(\hat{g}\hat{g}^\dagger)_x = 0 = (\hat{g}^\dagger\hat{g})_x$ to simplify the equation. We note the useful identities: $\hat{R}^\dagger = \hat{R}$ and $\hat{R}^2 = \mathbb{1}_2$.

C.2 Link with NLSE

We introduce the matrices:

$$\hat{\Theta} = \hat{g}^\dagger\hat{g}_x + \epsilon\frac{\sqrt{\beta}}{4}\left[\hat{\sigma}, \hat{R}\right] , \tag{C.6a}$$

$$\hat{D} = \hat{g}^\dagger\hat{g}_t + \epsilon\frac{\mathrm{i}\sqrt{\beta}}{4}\left[\hat{\Theta}, \hat{R}\right] , \tag{C.6b}$$

where $\epsilon = \pm 1$, and the consequences of the choice of sign are explained in Sec. C.4. It allows us to rewrite Eq. (C.5) under the following form:

$$\mathrm{i}\left[\hat{\sigma}, \hat{D}\right] = 2\hat{\Theta}_x . \tag{C.7}$$

General solutions of equations of the form $\mathrm{i}\left[\hat{\sigma}, \hat{D}\right] = \hat{X}$ can be written: $\hat{D} = \hat{X}_0 + \hat{X}_1$ where $\hat{X}_0$ is a solution of the homogeneous equation, meaning $[\hat{\sigma}, \hat{X}_0] = 0$, and $\hat{X}_1$ is a particular solution. Thus, we introduce the scalar function $b(x,t)$:

$$\hat{D} = b\hat{\sigma} - \frac{\mathrm{i}}{2}\left[\hat{\sigma}, \hat{\Theta}_x\right] . \tag{C.8}$$

One can check that the second part of the right-hand-side verifies Eq. (C.7), using the fact that $\left\{\hat{\sigma}, \hat{\Theta}_x\right\} = 0$.

We now write the identity:

$$\left(\hat{g}^\dagger\hat{g}_x\right)_t - \left(\hat{g}^\dagger\hat{g}_t\right)_x + \left[\hat{g}^\dagger\hat{g}_t, \hat{g}^\dagger\hat{g}_x\right] = 0 . \tag{C.9}$$

We can replace in this equation the expressions of $\hat{\Theta}$ and $\hat{D}$ to obtain:

$$\hat{\Theta}_t - \hat{D}_x + \left[\hat{D}, \hat{\Theta}\right] + \hat{\mathcal{T}} = 0 , \tag{C.10}$$

with $\hat{\mathcal{T}}$ grouping the terms depending directly on β:

$$\begin{aligned}\hat{\mathcal{T}} &= -\epsilon\frac{\sqrt{\beta}}{4}\left([\hat{\sigma}, \hat{R}]_t - \mathrm{i}[\hat{\Theta}, \hat{R}]_x + [\hat{D}, [\hat{\sigma}, \hat{R}]] + \mathrm{i}[[\hat{\Theta}, \hat{R}], \hat{\Theta}]\right) + \frac{\mathrm{i}\beta}{16}[[\hat{\Theta}, \hat{R}], [\hat{\sigma}, \hat{R}]] , \\ &= -\mathrm{i}\frac{\beta}{2}[\hat{\sigma}, \hat{\Theta}] ,\end{aligned} \tag{C.11}$$

where we notably used $\hat{R}_t = [\hat{R}, \hat{g}^\dagger\hat{g}_t]$ and $\hat{R}_x = [\hat{R}, \hat{g}^\dagger\hat{g}_x]$ to go from the first to the second line. Since $\hat{\Theta}$ is anti-Hermitian and $\left\{\hat{\sigma}, \hat{\Theta}\right\} = 0$, we can parametrize it as:

$$\hat{\Theta} = \begin{pmatrix} 0 & -\psi^* \\ \psi & 0 \end{pmatrix} . \tag{C.12}$$

Thus, we can naturally seperate Eq. (C.10) into its diagonal and off-diagonal parts. The diagonal part leads to:

$$b_x\mathbb{1}_2 = -\mathrm{i}\left\{\hat{\Theta}_x, \hat{\Theta}\right\} , \tag{C.13}$$

where we used Eq. (C.7) and the derivative of Eq. (C.8). It can be readily integrated to give:

$$b\mathbb{1}_2 = -\mathrm{i}(\hat{\Theta}^2 + \alpha(t)\mathbb{1}_2)\,. \tag{C.14}$$

Then, the off-diagonal part of Eq. (C.10) reads:

$$\mathrm{i}\hat{\Theta}_t - \frac{1}{2}\left[\hat{\sigma}, \hat{\Theta}_{xx}\right] + \left(\hat{\Theta}^2 + \alpha(t)\mathbb{1}_2 + \frac{\beta}{2}\mathbb{1}_2\right)\left[\hat{\sigma}, \hat{\Theta}\right] = 0 \tag{C.15}$$

Taking the lower-left coefficient of the matrix leads to:

$$\mathrm{i}\psi_t + \psi_{xx} + 2|\psi|^2\psi - (2\alpha(t) + \beta)\psi = 0\,. \tag{C.16}$$

We can set $\alpha(t)$ thanks to the boundary conditions on M. We take the natural boundary conditions for an easy-axis ferromagnet:

$$\lim_{|x|\to\infty} \hat{M}(x,t) = \hat{\sigma} \quad \text{and} \quad \lim_{|x|\to\infty} \hat{M}_x(x,t) = 0\,, \tag{C.17}$$

which translates in terms of the matrix $\hat{g}$:

$$\lim_{|x|\to\infty} \hat{g}(x,t) = \mathbb{1}_2 \quad \text{and} \quad \lim_{|x|\to\infty} \hat{g}_x(x,t) = 0\,. \tag{C.18}$$

Thus, we obtain $\alpha(t) = 0$. Taking $\tilde{\psi} = \psi \mathrm{e}^{-\mathrm{i}\beta t}$ eventually leads to the usual form of the NLSE:

$$\mathrm{i}\tilde{\psi}_t + \tilde{\psi}_{xx} + 2|\tilde{\psi}|^2\tilde{\psi} = 0\,. \tag{C.19}$$

We have shown the equivalence between the easy-axis LLE and NLSE. It remains to derive an explicit formula $\psi = f(M)$. Remarkably, we have an equivalence whatever the sign of ϵ.

C.3 Expliciting the matrix $\hat{g}$

We can parametrize $\mathbf{M}$ with polar coordinates on the unit sphere, which leads to:

$$\hat{M} = \begin{pmatrix} \cos\theta & \sin\theta\,\mathrm{e}^{-\mathrm{i}\varphi} \\ \sin\theta\,\mathrm{e}^{+\mathrm{i}\varphi} & -\cos\theta \end{pmatrix}, \tag{C.20}$$

where θ and φ are functions of x, t. We want to show the existence of a matrix g satisfying Eq. (C.4). We will prove this by constructing the matrix explicitly. We take a matrix $\hat{g}$ of the following form:

$$\hat{g}(x,t) = \begin{pmatrix} g_1 & -g_2^* \\ g_2 & g_1^* \end{pmatrix} \tag{C.21}$$

and write $g_1 = \cos\alpha\,\mathrm{e}^{\mathrm{i}\delta}$, $g_2 = \sin\alpha\,\mathrm{e}^{\mathrm{i}\gamma}$. We have $\hat{g} \in \mathrm{SU}(2)$. Then, calculating $\hat{g}\hat{\sigma}\hat{g}^\dagger$ shows that this expression equals M if and only if we set: $\alpha = \theta/2$ and $\gamma - \delta = \varphi$. Looking at the anticommutator of Eq. (C.4), we establish the equivalence:

$$\left\{\hat{g}^\dagger\hat{g}_x, \hat{\sigma}\right\} = 0 \iff \delta_x = -\varphi_x \sin^2\left(\frac{\theta}{2}\right). \tag{C.22}$$

Thus, the following matrix $\hat{g}$ satisfies Eq. (C.4):

$$\hat{g}(x,t) = \begin{pmatrix} \cos\frac{\theta}{2}\,\mathrm{e}^{\mathrm{i}\delta} & -\sin\frac{\theta}{2}\,\mathrm{e}^{-\mathrm{i}(\delta+\varphi)} \\ \sin\frac{\theta}{2}\,\mathrm{e}^{\mathrm{i}(\delta+\varphi)} & \cos\frac{\theta}{2}\,\mathrm{e}^{-\mathrm{i}\delta} \end{pmatrix} \quad \text{with} \quad \delta(x,t) = -\int_{-\infty}^{x} \sin^2\left(\frac{\theta}{2}\right)\varphi_y \,\mathrm{d}y \,. \tag{C.23}$$

We note that $\hat{g}$ is not uniquely defined since one can add a phase $\xi(t)$ to $\delta(x,t)$. However, using the boundary conditions of Eq. (C.17) leads to $\xi(t) = 0$.

C.4 Expression of ψ

We plug the expression of Eq. (C.23) in the definition of Θ:

$$\begin{aligned} \psi &= g_1 g_{2x} - g_{1x} g_2 + \epsilon\sqrt{\beta} g_1 g_2 \,, \\ &= \frac{1}{2}\left[\theta_x + \sin\theta\left(\mathrm{i}\varphi_x + \epsilon\sqrt{\beta}\right)\right] \exp\left[\mathrm{i}\left(\varphi - 2\int_{-\infty}^{x} \sin^2\left(\frac{\theta}{2}\right)\varphi_y \,\mathrm{d}y\right)\right] . \end{aligned} \tag{C.24}$$

In the final expression of [79] and in the review [77, Eq. (6.38)] the choice of $\epsilon = -1$ was made. Since the overall phase of ψ is irrelevant for NLSE, we realize that flipping the sign of ϵ corresponds to the change of variable $x \to -x$. Thus, by interpreting Eq. (C.24) as a differential equation and solving for θ, φ given a particular ψ, it yields a priori two solutions that are symmetric with respect to one another. Numerically, $\epsilon = +1$ gives a stable solution when integrating from a boundary condition $x \to -\infty$, and likewise for $\epsilon = -1$ and $x \to +\infty$ (changing the definition of $\delta(x,t)$ accordingly).

Eventually, we have seen that $\tilde{\psi} = \psi \mathrm{e}^{-\mathrm{i}\beta t}$ is a solution of the NLSE:

$$\mathrm{i}\tilde{\psi}_t + \tilde{\psi}_{xx} + 2|\tilde{\psi}|^2\tilde{\psi} = 0 \,. \tag{C.25}$$

Thus, we have an explicit expression linking solutions of NLSE and LLE in the easy-axis case. This result cannot be extended to the easy-plane case. Indeed, changing the sign in front of β in Eq. (C.2) leads to the substitution $\epsilon \to \mathrm{i}\epsilon$, and the matrix $\hat{\Theta}$ would not be anti-Hermitian anymore. The implications of this result are discussed in [313].

BIBLIOGRAPHY

[1] M. Planck. "Ueber das Gesetz der Energieverteilung im Normalspectrum". In: *Annalen der Physik* 309.3 (1901), pp. 553–563 (cit. on p. 1).

[2] M. Schlosshauer, J. Kofler, and A. Zeilinger. "A snapshot of foundational attitudes toward quantum mechanics". In: *Studies in History and Philosophy of Science Part B: Studies in History and Philosophy of Modern Physics* 44.3 (2013), pp. 222–230 (cit. on p. 1).

[3] A. Einstein, B. Podolsky, and N. Rosen. "Can Quantum-Mechanical Description of Physical Reality Be Considered Complete?" In: *Physical Review* 47.10 (1935), pp. 777–780 (cit. on p. 1).

[4] A. Aspect, J. Dalibard, and G. Roger. "Experimental Test of Bell's Inequalities Using Time-Varying Analyzers". In: *Physical Review Letters* 49.25 (1982), pp. 1804–1807 (cit. on p. 1).

[5] S. Bose. "Plancks Gesetz und Lichtquantenhypothese". In: *Zeitschrift für Physik* 26.1 (1924), pp. 178–181 (cit. on p. 1).

[6] A. Einstein. "Quantentheorie des einatomigen idealen Gases". In: *Sitzungsberichte der Preussischen Akademie der Wissenschaften* (1924), pp. 261–267 (cit. on p. 1).

[7] M. H. Anderson, J. R. Ensher, M. R. Matthews, C. E. Wieman, and E. A. Cornell. "Observation of Bose-Einstein Condensation in a Dilute Atomic Vapor". In: *Science* 269.5221 (1995), pp. 198–201 (cit. on pp. 1, 8).

[8] K. B. Davis, M. -O. Mewes, M. R. Andrews, N. J. van Druten, D. S. Durfee, D. M. Kurn, and W. Ketterle. "Bose-Einstein Condensation in a Gas of Sodium Atoms". In: *Physical Review Letters* 75.22 (1995), pp. 3969–3973 (cit. on pp. 1, 8).

[9] C. C. Bradley, C. A. Sackett, J. J. Tollett, and R. G. Hulet. "Evidence of Bose-Einstein Condensation in an Atomic Gas with Attractive Interactions". In: *Physical Review Letters* 75.9 (1995), pp. 1687–1690 (cit. on p. 1).

[10] M. R. Andrews, C. G. Townsend, H.-J. Miesner, D. S. Durfee, D. M. Kurn, and W. Ketterle. "Observation of Interference Between Two Bose Condensates". In: *Science* 275.5300 (1997), pp. 637–641 (cit. on p. 1).

[11] I. Bloch, T. W. Hänsch, and T. Esslinger. "Measurement of the spatial coherence of a trapped Bose gas at the phase transition". In: *Nature* 403.6766 (2000), pp. 166–170 (cit. on p. 1).

[12] B. Keimer, S. A. Kivelson, M. R. Norman, S. Uchida, and J. Zaanen. "From quantum matter to high-temperature superconductivity in copper oxides". In: *Nature* 518.7538 (2015), pp. 179–186 (cit. on p. 1).

[13] E. P. Gross. "Structure of a quantized vortex in boson systems". In: *Il Nuovo Cimento (1955-1965)* 20.3 (1961), pp. 454–477 (cit. on pp. 1, 22).

[14] L. P. Pitaevskii. "Vortex lines in an imperfect Bose gas". In: *Soviet Physics Journal of Experimental and Theoretical Physics* 13.2 (1961), pp. 451–454 (cit. on pp. 1, 22).

[15] M.-O. Mewes, M. R. Andrews, N. J. van Druten, D. M. Kurn, D. S. Durfee, C. G. Townsend, and W. Ketterle. "Collective Excitations of a Bose-Einstein Condensate in a Magnetic Trap". In: *Physical Review Letters* 77.6 (1996), pp. 988–991 (cit. on p. 1).

[16] K. W. Madison, F. Chevy, W. Wohlleben, and J. Dalibard. "Vortex Formation in a Stirred Bose-Einstein Condensate". In: *Physical Review Letters* 84.5 (2000), pp. 806–809 (cit. on p. 1).

[17] R. Onofrio, C. Raman, J. M. Vogels, J. R. Abo-Shaeer, A. P. Chikkatur, and W. Ketterle. "Observation of Superfluid Flow in a Bose-Einstein Condensed Gas". In: *Physical Review Letters* 85.11 (2000), pp. 2228–2231 (cit. on pp. 1, 25).

[18] C.-L. Navier. "Sur les lois du mouvement des fluides, en ayant égard à l'adhésion des molécules". In: *Mémoires de l'Académie Royale des Sciences de l'Institut de France* 6 (1822), pp. 389–440 (cit. on p. 1).

[19] G. G. Stokes. "On the Theories of the Internal Friction of Fluids in Motion, and of the Equilibrium and Motion of Elastic Solids". In: *Transactions of the Cambridge Philosophical Society* 8 (1845), pp. 287–318 (cit. on p. 1).

[20] D. J. Korteweg and G. de Vries. "XLI. On the change of form of long waves advancing in a rectangular canal, and on a new type of long stationary waves". In: *The London, Edinburgh, and Dublin Philosophical Magazine and Journal of Science* 39.240 (1895), pp. 422–443 (cit. on pp. 1, 40).

[21] G. B. Whitham. "A general approach to linear and non-linear dispersive waves using a Lagrangian". In: *Journal of Fluid Mechanics* 22.2 (1965), pp. 273–283 (cit. on p. 1).

[22] V. E. Zakharov. "Stability of periodic waves of finite amplitude on the surface of a deep fluid". In: *Journal of Applied Mechanics and Technical Physics* 9.2 (1968), pp. 190–194 (cit. on pp. 2, 42).

[23] Q. Fontaine, T. Bienaimé, S. Pigeon, E. Giacobino, A. Bramati, and Q. Glorieux. "Observation of the Bogoliubov Dispersion in a Fluid of Light". In: *Physical Review Letters* 121.18 (2018), p. 183604 (cit. on p. 2).

[24] R. W. Boyd. *Nonlinear Optics*. 3rd. San Diego: Academic Press, 2008 (cit. on p. 2).

[25] G. P. Agrawal. *Nonlinear Fiber Optics*. 6th. New York: Academic Press, 2019 (cit. on p. 2).

[26] S. H. Strogatz. *Nonlinear dynamics and chaos: with applications to physics, biology, chemistry, and engineering*. Second edition. Boulder: Westview Press, 2015 (cit. on p. 2).

[27] E. N. Lorenz. "Deterministic Nonperiodic Flow". In: *Journal of the Atmospheric Sciences* 20.2 (1963), pp. 130–141 (cit. on p. 2).

[28] M. T. Landahl and E. Mollo-Christensen. *Turbulence and Random Processes in Fluid Mechanics*. Cambridge: Cambridge University Press, 1992 (cit. on p. 2).

[29] A. N. Kolmogorov. "The local structure of turbulence in incompressible viscous fluid for very large Reynolds numbers". In: *Proceedings of the Royal Society of London. Series A: Mathematical and Physical Sciences* 434.1890 (1991), pp. 9–13 (cit. on p. 2).

[30] N. Navon, A. L. Gaunt, R. P. Smith, and Z. Hadzibabic. "Emergence of a turbulent cascade in a quantum gas". In: *Nature* 539.7627 (2016), pp. 72–75 (cit. on p. 2).

[31] N. Akhmediev, B. Kibler, F. Baronio, M. Belić, W.-P. Zhong, Y. Zhang, W. Chang, J. M. Soto-Crespo, P. Vouzas, P. Grelu, C. Lecaplain, K. Hammani, S. Rica, A. Picozzi, M. Tlidi, K. Panajotov, A. Mussot, A. Bendahmane, P. Szriftgiser, G. Genty, J. Dudley, A. Kudlinski, A. Demircan, U. Morgner, S. Amiraranashvili, C. Bree, G. Steinmeyer, C. Masoller, N. G. R. Broderick, A. F. J. Runge, M. Erkintalo, S. Residori, U. Bortolozzo, F. T. Arecchi, S. Wabnitz, C. G. Tiofack, S. Coulibaly, and M. Taki. "Roadmap on optical rogue waves and extreme events". In: *Journal of Optics* 18.6 (2016), p. 063001 (cit. on p. 2).

[32] N. Akhmediev, J. M. Soto-Crespo, and N. Devine. "Breather turbulence versus soliton turbulence: Rogue waves, probability density functions, and spectral features". In: *Physical Review E* 94.2 (2016), p. 022212 (cit. on p. 2).

[33] D. R. Solli, C. Ropers, P. Koonath, and B. Jalali. "Optical rogue waves". In: *Nature* 450.7172 (2007), pp. 1054–1057 (cit. on p. 2).

[34] A. Chabchoub, N. P. Hoffmann, and N. Akhmediev. "Rogue Wave Observation in a Water Wave Tank". In: *Physical Review Letters* 106.20 (2011), p. 204502 (cit. on p. 2).

[35] B. Kibler, K. Hammani, C. Michel, C. Finot, and A. Picozzi. "Rogue waves, rational solitons and wave turbulence theory". In: *Physics Letters A* 375.35 (2011), pp. 3149–3155 (cit. on p. 2).

[36] J. S. Russell. *Report on Waves*. British Association for the Advancement of Science, 1845 (cit. on pp. 2, 40).

[37] N. J. Zabusky and M. D. Kruskal. "Interaction of "Solitons" in a Collisionless Plasma and the Recurrence of Initial States". In: *Physical Review Letters* 15.6 (1965), pp. 240–243 (cit. on pp. 2, 41).

[38] L. F. Mollenauer, R. H. Stolen, and J. P. Gordon. "Experimental Observation of Picosecond Pulse Narrowing and Solitons in Optical Fibers". In: *Physical Review Letters* 45.13 (1980), pp. 1095–1098 (cit. on pp. 2, 42, 60, 113).

[39] T. Dauxois and M. Peyrard. *Physique des solitons*. EDP Sciences, 2004 (cit. on pp. 2, 40, 42).

[40] E. Fermi, J. Pasta, S. Ulam, and M. Tsingou. *Studies of Nonlinear Problems*. Tech. rep. LA-1940. Los Alamos, NM: Los Alamos Scientific Laboratory, 1955 (cit. on p. 2).

[41] A. Mussot, C. Naveau, M. Conforti, A. Kudlinski, F. Copie, P. Szriftgiser, and S. Trillo. "Fibre multi-wave mixing combs reveal the broken symmetry of Fermi–Pasta–Ulam recurrence". In: *Nature Photonics* 12.5 (2018), pp. 303–308 (cit. on p. 2).

[42] G. Vanderhaegen, P. Szriftgiser, A. Kudlinski, M. Conforti, S. Trillo, M. Droques, and A. Mussot. "Observation of four Fermi-Pasta-Ulam-Tsingou recurrences in an ultra-low-loss optical fiber". In: *Optics Express* 28.12 (2020), p. 17773 (cit. on p. 2).

[43] C. S. Gardner, J. M. Greene, M. D. Kruskal, and R. M. Miura. "Method for Solving the Korteweg de Vries Equation". In: *Physical Review Letters* 19.19 (1967), pp. 1095–1097 (cit. on pp. 2, 41, 46).

[44] V. Zakharov and A. Shabat. "Exact Theory of Two-dimensional Self-focusing and One-dimensional Self-modulation of Waves in Nonlinear Media". In: *Soviet Journal of Experimental and Theoretical Physics* 34.1 (1972), pp. 62–69 (cit. on pp. 2, 46, 48, 53, 54).

[45] M. J. Ablowitz, D. J. Kaup, A. C. Newell, and H. Segur. "The Inverse Scattering Transform-Fourier Analysis for Nonlinear Problems". In: *Studies in Applied Mathematics* 53.4 (1974), pp. 249–315 (cit. on pp. 2, 46, 51, 52, 58, 62).

[46] P. D. Lax. "Integrals of nonlinear equations of evolution and solitary waves". In: *Communications on Pure and Applied Mathematics* 21.5 (1968), pp. 467–490 (cit. on pp. 2, 46, 47).

[47] V. E. Zakharov and S. V. Manakov. "On the complete integrability of a nonlinear Schrödinger equation". In: *Theoretical and Mathematical Physics* 19.3 (1974), pp. 551–559 (cit. on p. 2).

[48] I. Bloch, J. Dalibard, and W. Zwerger. "Many-body physics with ultracold gases". In: *Reviews of Modern Physics* 80.3 (2008), pp. 885–964 (cit. on p. 3).

[49] D. M. Stamper-Kurn and M. Ueda. "Spinor Bose gases: Symmetries, magnetism, and quantum dynamics". In: *Reviews of Modern Physics* 85.3 (2013), pp. 1191–1244 (cit. on p. 3).

[50] P. Courteille, R. S. Freeland, D. J. Heinzen, F. A. van Abeelen, and B. J. Verhaar. "Observation of a Feshbach Resonance in Cold Atom Scattering". In: *Physical Review Letters* 81.1 (1998), pp. 69–72 (cit. on p. 3).

[51] C. Chin, R. Grimm, P. Julienne, and E. Tiesinga. "Feshbach resonances in ultracold gases". In: *Reviews of Modern Physics* 82.2 (2010), pp. 1225–1286 (cit. on pp. 3, 21).

[52] I. Bloch. "Ultracold quantum gases in optical lattices". In: *Nature Physics* 1.1 (2005), pp. 23–30 (cit. on p. 3).

[53] K. Henderson, C. Ryu, C. MacCormick, and M. G. Boshier. "Experimental demonstration of painting arbitrary and dynamic potentials for Bose–Einstein condensates". In: *New Journal of Physics* 11.4 (2009), p. 043030 (cit. on p. 3).

[54] M. Greiner, O. Mandel, T. Esslinger, T.W. Hänsch, and I. Bloch. "Quantum phase transition from a superfluid to a Mott insulator in a gas of ultracold atoms". In: *Nature* 415.6867 (2002), pp. 39–44 (cit. on pp. 3, 26).

[55] T. Bourdel, L. Khaykovich, J. Cubizolles, J. Zhang, F. Chevy, M. Teichmann, L. Tarruell, S. J. J. M. F. Kokkelmans, and C. Salomon. "Experimental Study of the BEC-BCS Crossover Region in Lithium 6". In: *Physical Review Letters* 93.5 (2004), p. 050401 (cit. on p. 3).

[56] A. D. Ludlow, M. M. Boyd, J. Ye, E. Peik, and P. O. Schmidt. "Optical atomic clocks". In: *Reviews of Modern Physics* 87.2 (2015), pp. 637–701 (cit. on p. 3).

[57] A. Browaeys and T. Lahaye. "Many-body physics with individually controlled Rydberg atoms". In: *Nature Physics* 16.2 (2020), pp. 132–142 (cit. on p. 3).

[58] W. S. Bakr, J. I. Gillen, A. Peng, S. Fölling, and M. Greiner. "A quantum gas microscope for detecting single atoms in a Hubbard-regime optical lattice". In: *Nature* 462.7269 (2009), pp. 74–77 (cit. on p. 3).

[59] J. F. Sherson, C. Weitenberg, M. Endres, M. Cheneau, I. Bloch, and S. Kuhr. "Single-atom-resolved fluorescence imaging of an atomic Mott insulator". In: *Nature* 467.7311 (2010), pp. 68–72 (cit. on p. 3).

[60] U. Schneider, L. Hackermüller, J. P. Ronzheimer, S. Will, S. Braun, T. Best, I. Bloch, E. Demler, S. Mandt, D. Rasch, and A. Rosch. "Fermionic transport and out-of-equilibrium dynamics in a homogeneous Hubbard model with ultracold atoms". In: *Nature Physics* 8.3 (2012), pp. 213–218 (cit. on p. 3).

[61] A. Mazurenko, C. S. Chiu, G. Ji, M. F. Parsons, M. Kanász-Nagy, R. Schmidt, F. Grusdt, E. Demler, D. Greif, and M. Greiner. "A cold-atom Fermi–Hubbard antiferromagnet". In: *Nature* 545.7655 (2017), pp. 462–466 (cit. on p. 3).

[62] L. Khaykovich, F. Schreck, G. Ferrari, T. Bourdel, J. Cubizolles, L. D. Carr, Y. Castin, and C. Salomon. "Formation of a Matter-Wave Bright Soliton". In: *Science* 296.5571 (2002), pp. 1290–1293 (cit. on pp. 3, 42, 43).

[63] S. Burger, K. Bongs, S. Dettmer, W. Ertmer, K. Sengstock, A. Sanpera, G. V. Shlyapnikov, and M. Lewenstein. "Dark Solitons in Bose-Einstein Condensates". In: *Physical Review Letters* 83.25 (1999), pp. 5198–5201 (cit. on pp. 3, 42, 43).

[64] J. H. V. Nguyen, P. Dyke, D. Luo, B. A. Malomed, and R. G. Hulet. "Collisions of matter-wave solitons". In: *Nature Physics* 10.12 (2014), pp. 918–922 (cit. on pp. 3, 42).

[65] B. Eiermann, T. Anker, M. Albiez, M. Taglieber, P. Treutlein, K.-P. Marzlin, and M. K. Oberthaler. "Bright Bose-Einstein Gap Solitons of Atoms with Repulsive Interaction". In: *Physical Review Letters* 92.23 (2004), p. 230401 (cit. on p. 3).

[66] B. A. Malomed. *Soliton Management in Periodic Systems*. Boston: Kluwer Academic Publishers, 2006 (cit. on pp. 3, 115).

[67] M. Mitchell, A. Di Carli, G. S. Leon, A. L. Rooij, S. Kuhr, and E. Haller. "Floquet solitons and dynamics of periodically driven matter waves with negative effective mass". In: *Physical Review Letters* 127.24 (2021), p. 243603 (cit. on p. 3).

[68] R. Cruickshank, F. Lorenzi, A. L. Rooij, E. Kerr, T. Hilker, S. Kuhr, L. Salasnich, and E. Haller. "Experimental Observation of Single- and Multisite Matter-Wave Solitons in an Optical Accordion Lattice". In: *Phys. Rev. Lett.* 135 (26 2025), p. 263404 (cit. on p. 3).

[69] C.-A. Chen and C.-L. Hung. "Observation of Universal Quench Dynamics and Townes Soliton Formation from Modulational Instability in Two-Dimensional Bose Gases". In: *Physical Review Letters* 125.25 (2020), p. 250401 (cit. on pp. 3, 44).

[70] B. Bakkali-Hassani, C. Maury, Y.-Q. Zou, É. Le Cerf, R. Saint-Jalm, P. C. M. Castilho, S. Nascimbene, J. Dalibard, and J. Beugnon. "Realization of a Townes Soliton in a Two-Component Planar Bose Gas". In: *Physical Review Letters* 127.2 (2021), p. 023603 (cit. on pp. 3, 13, 21, 44).

[71] C. Becker, S. Stellmer, P. Soltan-Panahi, S. Dörscher, M. Baumert, E. Richter, J. Kronjäger, K. Bongs, and K. Sengstock. "Oscillations and interactions of dark and dark–bright solitons in Bose–Einstein condensates". In: *Nature Physics* 4.6 (2008), pp. 496–501 (cit. on pp. 3, 45).

[72] C. Hamner, J. J. Chang, P. Engels, and M. A. Hoefer. "Generation of Dark-Bright Soliton Trains in Superfluid-Superfluid Counterflow". In: *Physical Review Letters* 106.6 (2011), p. 065302 (cit. on pp. 3, 45).

[73] J. Satsuma and N. Yajima. "B. Initial Value Problems of One-Dimensional Self-Modulation of Nonlinear Waves in Dispersive Media". In: *Progress of Theoretical Physics Supplement* 55 (1974), pp. 284–306 (cit. on pp. 3, 54, 55, 60–62, 77, 79, 80, 82, 100, 101).

[74] R. H. Stolen, W. J. Tomlinson, and L. F. Mollenauer. "Observation of pulse restoration at the soliton period in optical fibers". In: *Optics Letters* 8.3 (1983), p. 186 (cit. on pp. 3, 60, 113).

[75] D. Luo, Y. Jin, J. H. V. Nguyen, B. A. Malomed, O. V. Marchukov, V. A. Yurovsky, V. Dunjko, M. Olshanii, and R. G. Hulet. "Creation and Characterization of Matter-Wave Breathers". In: *Physical Review Letters* 125.18 (2020), p. 183902 (cit. on pp. 3, 60, 80, 83).

[76] C. Qu, L. P. Pitaevskii, and S. Stringari. "Magnetic Solitons in a Binary Bose-Einstein Condensate". In: *Physical Review Letters* 116.16 (2016), p. 160402 (cit. on pp. 3, 45, 89).

[77] A. M. Kosevich, B. A. Ivanov, and A. S. Kovalev. "Magnetic Solitons". In: *Physics Reports* 194.3 (1990), pp. 117–238 (cit. on pp. 3, 45, 88, 89, 91, 140).

[78] A. E. Borovik, S. Klama, and S. I. Kulinich. "Integration of the Landau-Lifshitz equation with preferred-axis anisotropy by the method of the inverse scattering problem". In: *Physica D: Nonlinear Phenomena* 32.1 (1988), pp. 107–134 (cit. on pp. 4, 97, 100, 103).

[79] V. P. Kotlyarov. "Equivalence of the Landau-Lifshitz equation and nonlinear Schrödinger equation". In: *Doklady Akad. Nauk Ukr. Ser. A* 10 (1981), pp. 9–13 (cit. on pp. 4, 99, 137, 140).

[80] A. Kundu and O. Pshaev. "Comments on the gauge equivalence between Heisenberg spin chains with single-site anisotropy and nonlinear Schrodinger equations". In: *Journal of Physics C: Solid State Physics* 16.17 (1983), p. L585 (cit. on pp. 4, 98).

[81] G. R. W. Quispel and H. W. Capel. "The nonlinear Schrödinger equation and the anisotropic Heisenberg spin chain". In: *Physics Letters A* 88.7 (1982), pp. 371–374 (cit. on pp. 4, 98).

[82] Y. S. Kivshar and B. A. Malomed. "Dynamics of solitons in nearly integrable systems". In: *Reviews of Modern Physics* 61.4 (1989), pp. 763–915 (cit. on pp. 4, 110–112).

[83] L. Corman. "The two-dimensional Bose Gas in box potentials". PhD thesis. Université Paris sciences et lettres, 2016 (cit. on p. 8).

[84] J. L. Ville. "Quantum gases in box potentials : sound and light in bosonic Flatland". PhD thesis. Université Paris sciences et lettres, 2018 (cit. on pp. 8, 15).

[85] R. Saint-Jalm. "Exploring two-dimensional physics with Bose gases in box potentials: phase ordering and dynamical symmetry". PhD thesis. Université Paris Sciences et Lettres, 2019 (cit. on pp. 8, 11, 14, 17, 73).

[86] G. Chauveau. "Exploring the dynamics of zero-temperature Bose gases : measurement of the superfluid fraction and observation of Bloch-like oscillations of a magnetic soliton". PhD thesis. Sorbonne Université, 2024 (cit. on pp. 8, 25, 32, 72, 91, 92, 94, 95).

[87] M.-S. Chang, C. D. Hamley, M. D. Barrett, J. A. Sauer, K. M. Fortier, W. Zhang, L. You, and M. S. Chapman. "Observation of Spinor Dynamics in Optically Trapped Rb 87 Bose-Einstein Condensates". In: *Physical Review Letters* 92.14 (2004), p. 140403 (cit. on p. 8).

[88] L. E. Sadler, J. M. Higbie, S. R. Leslie, M. Vengalattore, and D. M. Stamper-Kurn. "Spontaneous symmetry breaking in a quenched ferromagnetic spinor Bose–Einstein condensate". In: *Nature* 443.7109 (2006), pp. 312–315 (cit. on p. 8).

[89] D. Linnemann, H. Strobel, W. Muessel, J. Schulz, R. J. Lewis-Swan, K. V. Kheruntsyan, and M. K. Oberthaler. "Quantum-Enhanced Sensing Based on Time Reversal of Nonlinear Dynamics". In: *Physical Review Letters* 117.1 (2016), p. 013001 (cit. on p. 8).

[90] J. L. Basdevant and J. Dalibard. *Mécanique quantique*. Éditions de l'École Polytechnique. 2002 (cit. on p. 8).

[91] D.A. Steck. *Rubidium 87 D Line Data*. 2003 (cit. on pp. 9, 16).

[92] A. Keshet and W. Ketterle. "A distributed, graphical user interface based, computer control system for atomic physics experiments". In: *Review of Scientific Instruments* 84.1 (2013), p. 015105 (cit. on p. 9).

[93] M.-S. Chang, Q. Qin, W. Zhang, L. You, and M. S. Chapman. "Coherent spinor dynamics in a spin-1 Bose condensate". In: *Nature Physics* 1.2 (2005), pp. 111–116 (cit. on pp. 9, 35, 68).

[94] R. Grimm, M. Weidemüller, and Y. B. Ovchinnikov. "Optical Dipole Traps for Neutral Atoms". In: *Advances In Atomic, Molecular, and Optical Physics* 42 (2000), pp. 95–170 (cit. on p. 10).

[95] N. D. Mermin and H. Wagner. "Absence of Ferromagnetism or Antiferromagnetism in One- or Two-Dimensional Isotropic Heisenberg Models". In: *Physical Review Letters* 17.22 (1966), pp. 1133–1136 (cit. on pp. 11, 24).

[96] P. C. Hohenberg. "Existence of Long-Range Order in One and Two Dimensions". In: *Physical Review* 158.2 (1967), pp. 383–386 (cit. on pp. 11, 24).

[97] Z. Hadzibabic and J. Dalibard. "Two-dimensional Bose fluids: An atomic physics perspective". In: *La Rivista del Nuovo Cimento* 34.6 (2011), pp. 389–434 (cit. on pp. 11, 21, 24, 25).

[98] T. C. Li, H. Kelkar, D. Medellin, and M. G. Raizen. "Real-time control of the periodicity of a standing wave: an optical accordion". In: *Optics Express* 16.8 (2008), pp. 5465–5470 (cit. on p. 11).

[99] J. L. Ville, T. Bienaimé, R. Saint-Jalm, L. Corman, M. Aidelsburger, L. Chomaz, K. Kleinlein, D. Perconte, S. Nascimbène, J. Dalibard, and J. Beugnon. "Loading and compression of a single two-dimensional Bose gas in an optical accordion". In: *Physical Review A* 95.1 (2017), p. 013632 (cit. on p. 11).

[100] M. E. Gehm, K. M. O'Hara, T. A. Savard, and J. E. Thomas. "Dynamics of noise-induced heating in atom traps". In: *Physical Review A* 58.5 (1998), pp. 3914–3921 (cit. on p. 11).

[101] Sébastien M. Popoff, Louis Malosse, Rodrigo Gutiérrez-Cuevas, Yaron Bromberg, Jean Commre, Marie Glanc, Raphaël Galicher, and Maxime W. Matthès. "A practical guide to Digital Micro-mirror Devices (DMDs) for wavefront shaping". In: *arXiv:2311.17496* (2025) (cit. on p. 12).

[102] P. Zupancic, P. M. Preiss, R. Ma, A. Lukin, M. E. Tai, M. Rispoli, R. Islam, and M. Greiner. "Ultra-precise holographic beam shaping for microscopic quantum control". In: *Optics Express* 24.13 (2016), pp. 13881–13893 (cit. on p. 12).

[103] R. W. Floyd and L. Steinberg. "An adaptive algorithm for spatial gray scale". In: *Proceedings of the Society for Information Display* 17 (1975) (cit. on p. 13).

[104] C. Dorrer and J. D. Zuegel. "Design and analysis of binary beam shapers using error diffusion". In: *Journal of the Optical Society of America B* 24.6 (2007), pp. 1268–1275 (cit. on p. 14).

[105] Y.-Q. Zou, É. Le Cerf, B. Bakkali-Hassani, C. Maury, G. Chauveau, P. C. M. Castilho, R. Saint-Jalm, S. Nascimbene, J. Dalibard, and J. Beugnon. "Optical control of the density and spin spatial profiles of a planar Bose gas". In: *Journal of Physics B: Atomic, Molecular and Optical Physics* 54.8 (2021), 08LT01 (cit. on pp. 13, 73).

[106] F. Rabec. "Inducing Periodic Effects in Bose-Einstein Condensates : Bloch Oscillations of Solitons and Superfluid Fraction". These de doctorat. Sorbonne université, 2025 (cit. on pp. 13, 17, 25, 26, 28, 29, 31, 32, 90, 94, 95, 119).

[107] I. I. Rabi, J. R. Zacharias, S. Millman, and P. Kusch. "A New Method of Measuring Nuclear Magnetic Moment". In: *Physical Review* 53.4 (1938), pp. 318–318 (cit. on p. 14).

[108] I. Dotsenko, W. Alt, S. Kuhr, D. Schrader, M. Müller, Y. Miroshnychenko, V. Gomer, A. Rauschenbeutel, and D. Meschede. "Application of electro-optically generated light fields for Raman spectroscopy of trapped cesium atoms". In: *Applied Physics B* 78.6 (2004), pp. 711–717 (cit. on p. 14).

[109] L. Chomaz, L. Corman, T. Yefsah, R. Desbuquois, and J. Dalibard. "Absorption imaging of a quasi-two-dimensional gas: a multiple scattering analysis". In: *New Journal of Physics* 14.5 (2012), p. 055001 (cit. on p. 16).

[110] L. Corman, J. L. Ville, R. Saint-Jalm, M. Aidelsburger, T. Bienaimé, S. Nascimbène, J. Dalibard, and J. Beugnon. "Transmission of near-resonant light through a dense slab of cold atoms". In: *Physical Review A* 96.5 (2017), p. 053629 (cit. on p. 16).

[111] R. Saint-Jalm, M. Aidelsburger, J. L. Ville, L. Corman, Z. Hadzibabic, D. Delande, S. Nascimbene, N. Cherroret, J. Dalibard, and J. Beugnon. "Resonant-light diffusion in a disordered atomic layer". In: *Physical Review A* 97.6 (2018), p. 061801 (cit. on p. 16).

[112] L. Chomaz. "Coherence and superfluidity of Bose gases in reduced dimensions : from harmonic traps to uniform fluids". PhD thesis. Ecole normale supérieure - ENS Paris, 2014 (cit. on p. 17).

[113] G. Reinaudi, T. Lahaye, Z. Wang, and D. Guéry-Odelin. "Strong saturation absorption imaging of dense clouds of ultracold atoms". In: *Optics Letters* 32.21 (2007), pp. 3143–3145 (cit. on p. 17).

[114] Y.-Q. Zou, B. Bakkali-Hassani, C. Maury, É Le Cerf, S. Nascimbene, J. Dalibard, and J. Beugnon. "Tan's two-body contact across the superfluid transition of a planar Bose gas". In: *Nature Communications* 12.1 (2021), p. 760 (cit. on p. 17).

[115] B. Bakkali-Hassani. "Testing scale invariance in a two-dimensional Bose gas: preparation and characterization of solitary waves". PhD thesis. Sorbonne Université, 2021 (cit. on pp. 17, 68, 134).

[116] P. A. Altin, G. McDonald, D. Döring, J. E. Debs, T. H. Barter, J. D. Close, N. P. Robins, S. A. Haine, T. M. Hanna, and R. P. Anderson. "Optically trapped atom interferometry using the clock transition of large 87Rb Bose–Einstein condensates". In: *New Journal of Physics* 13.6 (2011), p. 065020 (cit. on p. 17).

[117] L. Pitaevskii and S. Stringari. *Bose-Einstein Condensation and Superfluidity*. Oxford University Press, 2016 (cit. on pp. 20–22, 24, 27, 30).

[118] J. Dalibard. "From van der Waals universality to Fano–Feshbach resonances". In: *Cours du Collège de France* (2021) (cit. on pp. 20, 21).

[119] M. Olshanii and L. Pricoupenko. "Rigorous Approach to the Problem of Ultraviolet Divergencies in Dilute Bose Gases". In: *Physical Review Letters* 88.1 (2001), p. 010402 (cit. on p. 20).

[120] A. Marte, T. Volz, J. Schuster, S. Dürr, G. Rempe, E. G. M. van Kempen, and B. J. Verhaar. "Feshbach Resonances in Rubidium 87: Precision Measurement and Analysis". In: *Physical Review Letters* 89.28 (2002), p. 283202 (cit. on p. 21).

[121] S. K. Adhikari. "Quantum scattering in two dimensions". In: *American Journal of Physics* 54.4 (1986), pp. 362–367 (cit. on p. 21).

[122] D. S. Petrov, M. Holzmann, and G. V. Shlyapnikov. "Bose-Einstein Condensation in Quasi-2D Trapped Gases". In: *Physical Review Letters* 84.12 (2000), pp. 2551–2555 (cit. on pp. 21, 69).

[123] D. S. Petrov and G. V. Shlyapnikov. "Interatomic collisions in a tightly confined Bose gas". In: *Physical Review A* 64.1 (2001), p. 012706 (cit. on p. 21).

[124] D. S. Petrov, D. M. Gangardt, and G. V. Shlyapnikov. "Low-dimensional trapped gases". In: *Journal de Physique IV (Proceedings)* 116 (2004), pp. 5–44 (cit. on pp. 21, 22).

[125] R. Saint-Jalm, P. C. M. Castilho, É. Le Cerf, B. Bakkali-Hassani, J.-L. Ville, S. Nascimbene, J. Beugnon, and J. Dalibard. "Dynamical Symmetry and Breathers in a Two-Dimensional Bose Gas". In: *Physical Review X* 9.2 (2019), p. 021035 (cit. on p. 21).

[126] T. D. Lee, K. Huang, and C. N. Yang. "Eigenvalues and Eigenfunctions of a Bose System of Hard Spheres and Its Low-Temperature Properties". In: *Physical Review* 106.6 (1957), pp. 1135–1145 (cit. on p. 22).

[127] J. Dalibard. "From the two-body problem to the macroscopic case". In: *Cours du Collège de France* (2022) (cit. on p. 22).

[128] N. Bogolubov. "On the theory of superfluidity". In: *Soviet Physics Journal of Experimental and Theoretical Physics* 11.1 (1947) (cit. on p. 23).

[129] J. L. Ville, R. Saint-Jalm, É. Le Cerf, M. Aidelsburger, S. Nascimbène, J. Dalibard, and J. Beugnon. "Sound Propagation in a Uniform Superfluid Two-Dimensional Bose Gas". In: *Physical Review Letters* 121.14 (2018), p. 145301 (cit. on pp. 23, 31).

[130] C. Mora and Y. Castin. "Extension of Bogoliubov theory to quasicondensates". In: *Physical Review A* 67.5 (2003), p. 053615 (cit. on p. 23).

[131] V. L. Berezinskii. "Destruction of long-range in one-dimensional and two-dimensional systems possessing a continuous symmetry group. II. Quantum systems". In: *Soviet Physics Journal of Experimental and Theoretical Physics* 34.3 (1972), pp. 610–616 (cit. on p. 24).

[132] J. M. Kosterlitz and D. J. Thouless. "Ordering, metastability and phase transitions in two-dimensional systems". In: *Journal of Physics C: Solid State Physics* 6.7 (1973), p. 1181 (cit. on p. 24).

[133] N. Prokof'ev, O. Ruebenacker, and B. Svistunov. "Critical Point of a Weakly Interacting Two-Dimensional Bose Gas". In: *Physical Review Letters* 87.27 (2001), p. 270402 (cit. on p. 24).

[134] D. J. Bishop and J. D. Reppy. "Study of the Superfluid Transition in Two-Dimensional $^{4}\mathrm{He}$ Films". In: *Physical Review Letters* 40.26 (1978), pp. 1727–1730 (cit. on p. 25).

[135] Z. Hadzibabic, P. Krüger, M. Cheneau, B. Battelier, and J. Dalibard. "Berezinskii–Kosterlitz–Thouless crossover in a trapped atomic gas". In: *Nature* 441.7097 (2006), pp. 1118–1121 (cit. on p. 25).

[136] Oliver Penrose and Lars Onsager. "Bose-Einstein Condensation and Liquid Helium". In: *Physical Review* 104.3 (1956), pp. 576–584 (cit. on p. 25).

[137] G. Chauveau, C. Maury, F. Rabec, C. Heintze, G. Brochier, S. Nascimbene, J. Dalibard, J. Beugnon, S. M. Roccuzzo, and S. Stringari. "Superfluid Fraction in an Interacting Spatially Modulated Bose-Einstein Condensate". In: *Physical Review Letters* 130.22 (2023), p. 226003 (cit. on pp. 25, 29).

[138] F. Rabec, G. Brochier, S. Wattellier, G. Chauveau, Y. Li, S. Nascimbene, J. Dalibard, and J. Beugnon. "Superfluid Fraction of a 2D Bose-Einstein Condensate in a Triangular Lattice". In: *arXiv:2511.04575* (2025) (cit. on pp. 25, 29, 31, 32).

[139] C. Maury. "Probing few and many-body physics in a planar Bose gas". PhD thesis. Sorbonne Université, 2023 (cit. on p. 25).

[140] P. Kapitza. "Viscosity of Liquid Helium below the λ-Point". In: *Nature* 141.3558 (1938), pp. 74–74 (cit. on p. 25).

[141] J. F. Allen and A. D. Misener. "Flow of Liquid Helium II". In: *Nature* 141.3558 (1938), pp. 75–75 (cit. on p. 25).

[142] C. Raman, M. Köhl, R. Onofrio, D. S. Durfee, C. E. Kuklewicz, Z. Hadzibabic, and W. Ketterle. "Evidence for a Critical Velocity in a Bose-Einstein Condensed Gas". In: *Physical Review Letters* 83.13 (1999), pp. 2502–2505 (cit. on p. 25).

[143] D. E. Miller, J. K. Chin, C. A. Stan, Y. Liu, W. Setiawan, C. Sanner, and W. Ketterle. "Critical Velocity for Superfluid Flow across the BEC-BCS Crossover". In: *Physical Review Letters* 99.7 (2007), p. 070402 (cit. on p. 25).

[144] A. Amo, J. Lefrère, S. Pigeon, CL Adrados, C. Ciuti, I. Carusotto, R. Houdré, E. Giacobino, and A. Bramati. "Superfluidity of polaritons in semiconductor microcavities". In: *Nature Physics* 5.11 (2009), pp. 805–810 (cit. on p. 25).

[145] C. Michel, O. Boughdad, M. Albert, P.-É. Larré, and M. Bellec. "Superfluid motion and drag-force cancellation in a fluid of light". In: *Nature Communications* 9.1 (2018), p. 2108 (cit. on p. 25).

[146] R. Desbuquois, L. Chomaz, T. Yefsah, J. Léonard, J. Beugnon, C. Weitenberg, and J. Dalibard. "Superfluid behaviour of a two-dimensional Bose gas". In: *Nature Physics* 8.9 (2012), pp. 645–648 (cit. on p. 25).

[147] W. H. Keesom and G. E. Macwood. "The viscosity of liquid helium". In: *Physica* 5.8 (1938), pp. 737–744 (cit. on p. 26).

[148] A. J. Leggett. "Can a Solid Be "Superfluid"?" In: *Physical Review Letters* 25.22 (1970), pp. 1543–1546 (cit. on pp. 26–29).

[149] J. Dalibard. "Coherence and superfluidity in atomic gases". In: *Cours du Collège de France* (2016) (cit. on pp. 26, 27).

[150] L. Tisza. "Transport Phenomena in Helium II". In: *Nature* 141.3577 (1938), pp. 913–913 (cit. on p. 26).

[151] L. Landau. "Theory of the Superfluidity of Helium II". In: *Physical Review* 60.4 (1941), pp. 356–358 (cit. on p. 26).

[152] G. B. Hess and W. M. Fairbank. "Measurements of Angular Momentum in Superfluid Helium". In: *Physical Review Letters* 19.5 (1967), pp. 216–218 (cit. on p. 26).

[153] P. Christodoulou, M. Gałka, N. Dogra, R. Lopes, J. Schmitt, and Z. Hadzibabic. "Observation of first and second sound in a BKT superfluid". In: *Nature* 594.7862 (2021), pp. 191–194 (cit. on p. 26).

[154] L. A. Sidorenkov, M. K. Tey, R. Grimm, Y.-H. Hou, L. Pitaevskii, and S. Stringari. "Second sound and the superfluid fraction in a Fermi gas with resonant interactions". In: *Nature* 498.7452 (2013), pp. 78–81 (cit. on p. 26).

[155] Timon A. Hilker, Lena H. Dogra, Christoph Eigen, Jake A. P. Glidden, Robert P. Smith, and Zoran Hadzibabic. "First and Second Sound in a Compressible 3D Bose Fluid". In: *Physical Review Letters* 128.22 (2022), p. 223601 (cit. on p. 26).

[156] A. J. Leggett. "On the Superfluid Fraction of an Arbitrary Many-Body System at T=0". In: *Journal of Statistical Physics* 93.3 (1998), pp. 927–941 (cit. on pp. 26, 29).

[157] M. P. A. Fisher, P. B. Weichman, G. Grinstein, and D. S. Fisher. "Boson localization and the superfluid-insulator transition". In: *Physical Review B* 40.1 (1989), pp. 546–570 (cit. on p. 26).

[158] C. Menotti, M. Krämer, L. Pitaevskii, and S. Stringari. "Dynamic structure factor of a Bose-Einstein condensate in a one-dimensional optical lattice". In: *Physical Review A* 67.5 (2003), p. 053609 (cit. on p. 26).

[159] G. Watanabe, G. Orso, F. Dalfovo, L. P. Pitaevskii, and S. Stringari. "Equation of state and effective mass of the unitary Fermi gas in a one-dimensional periodic potential". In: *Physical Review A* 78.6 (2008), p. 063619 (cit. on p. 26).

[160] G. Orso and S. Stringari. "Superfluid fraction and Leggett bound in a density-modulated strongly interacting Fermi gas at zero temperature". In: *Physical Review A* 109.2 (2024), p. 023301 (cit. on p. 26).

[161] S. Giorgini, L. Pitaevskii, and S. Stringari. "Effects of disorder in a dilute Bose gas". In: *Physical Review B* 49.18 (1994), pp. 12938–12944 (cit. on p. 26).

[162] K. T. Geier, J. Maki, A. Biella, F. Dalfovo, S. Giorgini, and S. Stringari. "Superfluidity and sound propagation in disordered Bose gases". In: *Physical Review Research* 7.1 (2025), p. 013187 (cit. on p. 26).

[163] P. B. Blakie, L. Chomaz, D. Baillie, and F. Ferlaino. "Compressibility and speeds of sound across the superfluid-to-supersolid phase transition of an elongated dipolar gas". In: *Physical Review Research* 5.3 (2023), p. 033161 (cit. on p. 26).

[164] G. Biagioni, N. Antolini, B. Donelli, L. Pezzè, A. Smerzi, M. Fattori, A. Fioretti, C. Gabbanini, M. Inguscio, L. Tanzi, and G. Modugno. "Measurement of the superfluid fraction of a supersolid by Josephson effect". In: *Nature* 629.8013 (2024), pp. 773–777 (cit. on p. 26).

[165] P. B. Blakie. "Superfluid fraction tensor of a two-dimensional supersolid". In: *Journal of Physics B: Atomic, Molecular and Optical Physics* 57.11 (2024), p. 115301 (cit. on pp. 27, 28, 31).

[166] W. M. Saslow. "Superfluidity of Periodic Solids". In: *Physical Review Letters* 36.19 (1976), pp. 1151–1154 (cit. on pp. 28, 29).

[167] W. M. Saslow. "On the Superfluid Fraction and the Hydrodynamics of Supersolids". In: *Journal of Low Temperature Physics* 169.3 (2012), pp. 248–263 (cit. on p. 28).

[168] J. Tao, M. Zhao, and I. B. Spielman. "Observation of Anisotropic Superfluid Density in an Artificial Crystal". In: *Physical Review Letters* 131.16 (2023), p. 163401 (cit. on p. 29).

[169] E. Busley, L. E. Miranda, A. Redmann, C. Kurtscheid, Kirankumar K. Umesh, F. Vewinger, M. Weitz, and J. Schmitt. "Compressibility and the equation of state of an optical quantum gas in a box". In: *Science* 375.6587 (2022), pp. 1403–1406 (cit. on p. 32).

[170] E. Timmermans. "Phase Separation of Bose-Einstein Condensates". In: *Physical Review Letters* 81.26 (1998), pp. 5718–5721 (cit. on pp. 33, 34).

[171] D. S. Hall, M. R. Matthews, J. R. Ensher, C. E. Wieman, and E. A. Cornell. "Dynamics of Component Separation in a Binary Mixture of Bose-Einstein Condensates". In: *Physical Review Letters* 81.20 (1998), pp. 4531–4531 (cit. on p. 33).

[172] S. Tojo, Y. Taguchi, Y. Masuyama, T. Hayashi, H. Saito, and T. Hirano. "Controlling phase separation of binary Bose-Einstein condensates via mixed-spin-channel Feshbach resonance". In: *Physical Review A* 82.3 (2010), p. 033609 (cit. on p. 33).

[173] S. De, D. L. Campbell, R. M. Price, A. Putra, Brandon M. Anderson, and I. B. Spielman. "Quenched binary Bose-Einstein condensates: Spin-domain formation and coarsening". In: *Physical Review A* 89.3 (2014), p. 033631 (cit. on pp. 33, 68).

[174] P. Ao and S. T. Chui. "Binary Bose-Einstein condensate mixtures in weakly and strongly segregated phases". In: *Physical Review A* 58.6 (1998), pp. 4836–4840 (cit. on p. 34).

[175] R. A. Barankov. "Boundary of two mixed Bose-Einstein condensates". In: *Physical Review A* 66.1 (2002), p. 013612 (cit. on p. 34).

[176] J. Stenger, S. Inouye, D. M. Stamper-Kurn, H.-J. Miesner, A. P. Chikkatur, and W. Ketterle. "Spin domains in ground-state Bose–Einstein condensates". In: *Nature* 396.6709 (1998), pp. 345–348 (cit. on p. 35).

[177] B. P. Anderson, P. C. Haljan, C. A. Regal, D. L. Feder, L. A. Collins, C. W. Clark, and E. A. Cornell. "Watching Dark Solitons Decay into Vortex Rings in a Bose-Einstein Condensate". In: *Physical Review Letters* 86.14 (2001), pp. 2926–2929 (cit. on pp. 35, 45).

[178] Z. Dutton and C. Clark. "Effective one-component description of two-component Bose-Einstein condensate dynamics". In: *Physical Review A* 71.6 (2005), p. 063618 (cit. on p. 35).

[179] B. Bakkali-Hassani, C. Maury, S. Stringari, S. Nascimbene, J. Dalibard, and J. Beugnon. "The cross-over from Townes solitons to droplets in a 2D Bose mixture". In: *New Journal of Physics* 25.1 (2023), p. 013007 (cit. on pp. 35, 77).

[180] J. Boussinesq. *Essai sur la théorie des eaux courantes*. 1877 (cit. on p. 40).

[181] K. B. Dysthe and H. L. Pécseli. "Non-linear Langmuir wave modulation in collisionless plasmas". In: *Plasma Physics* 19.10 (1977), p. 931 (cit. on p. 42).

[182] A. Hasegawa and F. Tappert. "Transmission of stationary nonlinear optical pulses in dispersive dielectric fibers. I. Anomalous dispersion". In: *Applied Physics Letters* 23.3 (1973), pp. 142–144 (cit. on p. 42).

[183] P. L. Kelley. "Self-Focusing of Optical Beams". In: *Physical Review Letters* 15.26 (1965), pp. 1005–1008 (cit. on p. 42).

[184] A. L. Marchant, T. P. Billam, T. P. Wiles, M. M. H. Yu, S. A. Gardiner, and S. L. Cornish. "Controlled formation and reflection of a bright solitary matter-wave". In: *Nature Communications* 4.1 (2013), p. 1865 (cit. on p. 42).

[185] P. Medley, M. A. Minar, N. C. Cizek, D. Berryrieser, and M. A. Kasevich. "Evaporative Production of Bright Atomic Solitons". In: *Physical Review Letters* 112.6 (2014), p. 060401 (cit. on p. 42).

[186] O. J. Wales, A. Rakonjac, T. P. Billam, J. L. Helm, S. A. Gardiner, and S. L. Cornish. "Splitting and recombination of bright-solitary-matter waves". In: *Communications Physics* 3.1 (2020), p. 51 (cit. on p. 42).

[187] J. Denschlag, J. E. Simsarian, D. L. Feder, Charles W. Clark, L. A. Collins, J. Cubizolles, L. Deng, E. W. Hagley, K. Helmerson, W. P. Reinhardt, S. L. Rolston, B. I. Schneider, and W. D. Phillips. "Generating Solitons by Phase Engineering of a Bose-Einstein Condensate". In: *Science* 287.5450 (2000), pp. 97–101 (cit. on p. 42).

[188] A. R. Fritsch, M. Lu, G. H. Reid, A. M. Piñeiro, and I. B. Spielman. "Creating solitons with controllable and near-zero velocity in Bose-Einstein condensates". In: *Physical Review A* 101.5 (2020), p. 053629 (cit. on p. 42).

[189] J. Dalibard. "Solitons and matter waves". In: *Cours du Collège de France* (2025) (cit. on pp. 43, 47, 54, 58, 78).

[190] D. M. Greenberger. "Some remarks on the extended Galilean transformation". In: *American Journal of Physics* 47.1 (1979), pp. 35–38 (cit. on p. 42).

[191] F. Copie, P. Suret, and S. Randoux. "Space–time observation of the dynamics of soliton collisions in a recirculating optical fiber loop". In: *Optics Communications* 545 (2023), p. 129647 (cit. on p. 42).

[192] C. A. Sackett, J. M. Gerton, M. Welling, and R. G. Hulet. "Measurements of Collective Collapse in a Bose-Einstein Condensate with Attractive Interactions". In: *Physical Review Letters* 82.5 (1999), pp. 876–879 (cit. on p. 43).

[193] L. D. Carr and Y. Castin. "Dynamics of a matter-wave bright soliton in an expulsive potential". In: *Physical Review A* 66.6 (2002), p. 063602 (cit. on p. 43).

[194] N. G. Parker, S. L. Cornish, C. S. Adams, and A. M. Martin. "Bright solitary waves and trapped solutions in Bose–Einstein condensates with attractive interactions". In: *Journal of Physics B: Atomic, Molecular and Optical Physics* 40.15 (2007), p. 3127 (cit. on p. 43).

[195] Y. Castin and C. Herzog. "Bose–Einstein condensates in symmetry breaking states". In: *Comptes Rendus de l'Académie des Sciences - Series IV - Physics* 2.3 (2001), pp. 419–443 (cit. on p. 43).

[196] I. Masakatsu and T. Hajime. "Solitons in a One-Dimensional Bose System with the Repulsive Delta-Function Interaction". In: *Journal of the Physical Society of Japan* (1980) (cit. on p. 43).

[197] E. Kaminishi, T. Mori, and S. Miyashita. "Construction of quantum dark soliton in one-dimensional Bose gas". In: *Journal of Physics B: Atomic, Molecular and Optical Physics* 53.9 (2020), p. 095302 (cit. on p. 43).

[198] N. Meyer, H. Proud, M. Perea-Ortiz, C. O'Neale, M. Baumert, M. Holynski, J. Kronjäger, G. Barontini, and K. Bongs. "Observation of Two-Dimensional Localized Jones-Roberts Solitons in Bose-Einstein Condensates". In: *Physical Review Letters* 119.15 (2017), p. 150403 (cit. on p. 44).

[199] E. A. Kuznetsov. "Solitons in a parametrically unstable plasma". In: *Doklady Akademii Nauk SSSR* 236 (1977), pp. 575–577 (cit. on p. 44).

[200] Y. C. Ma. "The Perturbed Plane-Wave Solutions of the Cubic Schrödinger Equation". In: *Studies in Applied Mathematics* 60.1 (1979), pp. 43–58 (cit. on pp. 44, 64).

[201] N. N. Akhmediev and V. I. Korneev. "Modulation instability and periodic solutions of the nonlinear Schrödinger equations". In: *Theoretical and Mathematical Physics* 69 (1986), pp. 1089–1093 (cit. on pp. 44, 64).

[202] D. H. Peregrine. "Water waves, nonlinear Schrödinger equations and their solutions". In: *The Journal of the Australian Mathematical Society Series B* 25.1 (1983), pp. 16–43 (cit. on p. 44).

[203] V. E. Zakharov and L. A. Ostrovsky. "Modulation instability: The beginning". In: *Physica D: Nonlinear Phenomena* 238.5 (2009), pp. 540–548 (cit. on p. 44).

[204] J. M. Dudley, G. Genty, A. Mussot, A. Chabchoub, and F. Dias. "Rogue waves and analogies in optics and oceanography". In: *Nature Reviews Physics* 1.11 (2019), pp. 675–689 (cit. on p. 44).

[205] B. Kibler, J. Fatome, C. Finot, G. Millot, F. Dias, G. Genty, N. Akhmediev, and J. M. Dudley. "The Peregrine soliton in nonlinear fibre optics". In: *Nature Physics* 6.10 (2010), pp. 790–795 (cit. on p. 45).

[206] B. Kibler, J. Fatome, C. Finot, G. Millot, G. Genty, B. Wetzel, N. Akhmediev, F. Dias, and J. M. Dudley. "Observation of Kuznetsov-Ma soliton dynamics in optical fibre". In: *Scientific Reports* 2.1 (2012), p. 463 (cit. on p. 45).

[207] B. Frisquet, B. Kibler, and G. Millot. "Collision of Akhmediev Breathers in Nonlinear Fiber Optics". In: *Physical Review X* 3.4 (2013), p. 041032 (cit. on p. 45).

[208] A. Romero-Ros, G. C. Katsimiga, S. I. Mistakidis, S. Mossman, G. Biondini, P. Schmelcher, P. Engels, and P. G. Kevrekidis. "Experimental Realization of the Peregrine Soliton in Repulsive Two-Component Bose-Einstein Condensates". In: *Physical Review Letters* 132.3 (2024), p. 033402 (cit. on p. 45).

[209] S. V. Manakov. "On the theory of two-dimensional stationary self-focusing of electromagnetic wave". In: *Soviet Journal of Experimental and Theoretical Physics* 38.2 (1974), pp. 248–253 (cit. on pp. 45, 63).

[210] D. N. Christodoulides. "Black and white vector solitons in weakly birefringent optical fibers". In: *Physics Letters A* 132.8-9 (1988), pp. 451–452 (cit. on p. 45).

[211] S. Trillo, E. M. Wright, G. I. Stegeman, and S. Wabnitz. "Optical solitary waves induced by cross-phase modulation". In: *Optics Letters* 13.10 (1988), p. 871 (cit. on p. 45).

[212] T. Busch and J. R. Anglin. "Dark-Bright Solitons in Inhomogeneous Bose-Einstein Condensates". In: *Physical Review Letters* 87.1 (2001), p. 010401 (cit. on p. 45).

[213] Q. H. Park and H. Shin. "Systematic construction of multicomponent optical solitons". In: *Physical Review E* 61.3 (2000), pp. 3093–3106 (cit. on p. 45).

[214] A. Farolfi, D. Trypogeorgos, C. Mordini, G. Lamporesi, and G. Ferrari. "Observation of Magnetic Solitons in Two-Component Bose-Einstein Condensates". In: *Physical Review Letters* 125.3 (2020), p. 030401 (cit. on pp. 45, 91).

[215] F. Rabec, G. Chauveau, G. Brochier, S. Nascimbene, J. Dalibard, and J. Beugnon. "Bloch oscillations of a soliton in a one-dimensional quantum fluid". In: *Nature Physics* 21 (2025), pp. 1541–1547 (cit. on pp. 45, 68, 94, 95, 107).

[216] M. J. Ablowitz and H. Segur. *Solitons and the Inverse Scattering Transform*. Studies in Applied and Numerical Mathematics. Society for Industrial and Applied Mathematics, 1981 (cit. on pp. 46, 48–50, 52, 53).

[217] J. Yang. *Nonlinear Waves in Integrable and Nonintegrable Systems*. Mathematical Modeling and Computation. Society for Industrial and Applied Mathematics, 2010 (cit. on pp. 55, 57–59, 63).

[218] M. I. Yousefi and F. R. Kschischang. "Information Transmission Using the Nonlinear Fourier Transform, Part II: Numerical Methods". In: *IEEE Transactions on Information Theory* 60.7 (2014), pp. 4329–4345 (cit. on p. 55).

[219] S. K. Turitsyn, J. E. Prilepsky, L L. Frumin, and M. Kamalian. "Nonlinear Fourier transform for optical data processing and transmission: advances and perspectives". In: *Optica* 4.3 (2017), pp. 307–322 (cit. on pp. 55, 56).

[220] G. Boffetta and A.R Osborne. "Computation of the direct scattering transform for the nonlinear Schroedinger equation". In: *Journal of Computational Physics* 102.2 (1992), pp. 252–264 (cit. on pp. 56, 57).

[221] L. D. Faddeev and L. A. Takhtajan. *Hamiltonian Methods in the Theory of Solitons*. Berlin, Heidelberg: Springer Berlin Heidelberg, 1987 (cit. on p. 57).

[222] V. E. Zakharov and A. B. Shabat. "Integration of nonlinear equations of mathematical physics by the method of inverse scattering. II". In: *Functional Analysis and Its Applications* 13.3 (1979), pp. 166–174 (cit. on p. 59).

[223] R. Radhakrishnan, D. P. Tchofo, and G. Millot. "Efficient control of the energy exchange due to the Manakov vector-soliton collision". In: *Physical Review E* 69.4 (2004), p. 046607 (cit. on p. 63).

[224] V. E. Zakharov and A. B. Shabat. "Interaction between solitons in a stable medium". In: *Soviet Journal of Experimental and Theoretical Physics* 64.5 (1973), pp. 1627–1639 (cit. on pp. 63, 64).

[225] K. E. Strecker, G. B. Partridge, A. G. Truscott, and R. G. Hulet. "Formation and propagation of matter-wave soliton trains". In: *Nature* 417.6885 (2002), pp. 150–153 (cit. on p. 64).

[226] P. J. Everitt, M. A. Sooriyabandara, M. Guasoni, P. B. Wigley, C. H. Wei, G. D. McDonald, K. S. Hardman, P. Manju, J. D. Close, C. C. N. Kuhn, S. S. Szigeti, Y. S. Kivshar, and N. P. Robins. "Observation of a modulational instability in Bose-Einstein condensates". In: *Physical Review A* 96.4 (2017), p. 041601 (cit. on p. 64).

[227] J. H. V. Nguyen, D. Luo, and R. G. Hulet. "Formation of matter-wave soliton trains by modulational instability". In: *Science* 356.6336 (2017), pp. 422–426 (cit. on p. 64).

[228] E. R. Tracy and H. H. Chen. "Nonlinear self-modulation: An exactly solvable model". In: *Physical Review A* 37.3 (1988), pp. 815–839 (cit. on pp. 64, 65).

[229] Y. C. Ma and M. J. Ablowitz. "The Periodic Cubic Schrõdinger Equation". In: *Studies in Applied Mathematics* 65.2 (1981), pp. 113–158 (cit. on p. 65).

[230] E. R. Tracy, H. H. Chen, and Y. C. Lee. "Study of Quasiperiodic Solutions of the Nonlinear Schrödinger Equation and the Nonlinear Modulational Instability". In: *Physical Review Letters* 53.3 (1984), pp. 218–221 (cit. on p. 65).

[231] A. R. Its, A. V. Rybin, and M. A. Sall'. "Exact integration of nonlinear Schrödinger equation". In: *Theoretical and Mathematical Physics* 74.1 (1988), pp. 20–32 (cit. on p. 65).

[232] A. R. Osborne. *Nonlinear Ocean Waves and the Inverse Scattering Transform*. Vol. 97. International Geophysics. Elsevier, 2010 (cit. on p. 65).

[233] A. L. Islas and C. M. Schober. "Predicting rogue waves in random oceanic sea states". In: *Physics of Fluids* 17.3 (2005), p. 031701 (cit. on p. 65).

[234] C. Rogers and W. F. Shadwick. *Bäcklund transformations and their applications*. Mathematics in science and engineering v. 161. New York: Academic Press, 1982 (cit. on p. 66).

[235] R. Hirota. "Exact envelope-soliton solutions of a nonlinear wave equation". In: *Journal of Mathematical Physics* 14.7 (1973), pp. 805–809 (cit. on p. 66).

[236] J. Hietarinta. *Introduction to the Hirota bilinear method*. Integrability of Nonlinear Systems. Springer Berlin Heidelberg, 1997 (cit. on p. 66).

[237] G. Roberti, G. El, A. Tovbis, F. Copie, P. Suret, and S. Randoux. "Numerical spectral synthesis of breather gas for the focusing nonlinear Schrödinger equation". In: *Physical Review E* 103.4 (2021), p. 042205 (cit. on p. 66).

[238] H. Schmaljohann, M. Erhard, J. Kronjäger, M. Kottke, S. van Staa, L. Cacciapuoti, J. J. Arlt, K. Bongs, and K. Sengstock. "Dynamics of F = 2 Spinor Bose-Einstein Condensates". In: *Physical Review Letters* 92.4 (2004), p. 040402 (cit. on p. 68).

[239] A. Widera, F. Gerbier, S. Fölling, T. Gericke, O. Mandel, and I. Bloch. "Precision measurement of spin-dependent interaction strengths for spin-1 and spin-2 ^{87}Rb atoms". In: *New Journal of Physics* 8.8 (2006), p. 152 (cit. on p. 68).

[240] E. G. M. van Kempen, S. J. J. M. F. Kokkelmans, D. J. Heinzen, and B. J. Verhaar. "Interisotope Determination of Ultracold Rubidium Interactions from Three High-Precision Experiments". In: *Physical Review Letters* 88.9 (2002), p. 093201 (cit. on p. 68).

[241] Y.-Q. Zou, B. Bakkali-Hassani, C. Maury, É. Le Cerf, S. Nascimbene, J. Dalibard, and J. Beugnon. "Magnetic Dipolar Interaction between Hyperfine Clock States in a Planar Alkali Bose Gas". In: *Physical Review Letters* 125.23 (2020), p. 233604 (cit. on pp. 69, 134).

[242] T. Lahaye, C. Menotti, L. Santos, M. Lewenstein, and T. Pfau. "The physics of dipolar bosonic quantum gases". In: *Reports on Progress in Physics* 72.12 (2009), p. 126401 (cit. on p. 69).

[243] I. Bouchoule and J. Dubail. "Generalized hydrodynamics in the one-dimensional Bose gas: theory and experiments". In: *Journal of Statistical Mechanics: Theory and Experiment* 2022.1 (2022), p. 014003 (cit. on p. 70).

[244] Y. S. Kivshar, D. E. Pelinovsky, T. Cretegny, and M. Peyrard. "Internal Modes of Solitary Waves". In: *Physical Review Letters* 80.23 (1998), pp. 5032–5035 (cit. on p. 77).

[245] D. J. Kaup. "Perturbation theory for solitons in optical fibers". In: *Physical Review A* 42.9 (1990), pp. 5689–5694 (cit. on p. 78).

[246] W. Sroyngoen and J. R. Anglin. "Soliton resuscitations: asymmetric revivals of the breathing mode of an atomic bright soliton in a harmonic trap". In: *arXiv: 2502.09016* (2025) (cit. on pp. 78, 79, 83).

[247] Y. Castin and C. Herzog. "Bose–Einstein condensates in symmetry breaking states". In: *Comptes Rendus de l'Académie des Sciences - Series IV - Physics* 2.3 (2001), pp. 419–443 (cit. on p. 78).

[248] A. Di Carli, C. D. Colquhoun, G. Henderson, S. Flannigan, G. Oppo, A. J. Daley, S. Kuhr, and E. Haller. "Excitation Modes of Bright Matter-Wave Solitons". In: *Physical Review Letters* 123.12 (2019), p. 123602 (cit. on p. 79).

[249] S. Stringari. "Dynamics of Bose-Einstein condensed gases in highly deformed traps". In: *Physical Review A* 58.3 (1998), pp. 2385–2388 (cit. on p. 79).

[250] C. Menotti and S. Stringari. "Collective oscillations of a one-dimensional trapped Bose-Einstein gas". In: *Physical Review A* 66.4 (2002), p. 043610 (cit. on p. 79).

[251] K.J. Blow and N.J. Doran. "The asymptotic dispersion of soliton pulses in lossy fibres". In: *Optics Communications* 52.5 (1985), pp. 367–370 (cit. on pp. 83, 112).

[252] L. D. Landau and E. Lifshitz. "On the theory of the dispersion of magnetic permeability in ferromagnetic bodies". In: *Physikalische Zeitschrift der Sowjetunion* 8 (1935), pp. 153–159 (cit. on p. 88).

[253] T. Congy, A. Kamchatnov, and N. Pavloff. "Dispersive hydrodynamics of nonlinear polarization waves in two-component Bose-Einstein condensates". In: *SciPost Physics* 1.1 (2016), p. 006 (cit. on p. 89).

[254] K. A. Long and A. R. Bishop. "Nonlinear excitations in classical ferromagnetic chains". In: *Journal of Physics A: Mathematical and General* 12.8 (1979), pp. 1325–1339 (cit. on p. 91).

[255] X. Chai, D. Lao, K. Fujimoto, R. Hamazaki, M. Ueda, and C. Raman. "Magnetic Solitons in a Spin-1 Bose-Einstein Condensate". In: *Physical Review Letters* 125.3 (2020), p. 030402 (cit. on p. 91).

[256] X. Chai, L. You, and C. Raman. "Magnetic solitons in an immiscible two-component Bose-Einstein condensate". In: *Physical Review A* 105.1 (2022), p. 013313 (cit. on p. 91).

[257] A. M. Kosevich, V. V. Gann, A. I. Zhukov, and V. P. Voronov. "Magnetic soliton motion in a nonuniform magnetic field". In: *Journal of Experimental and Theoretical Physics* 87.2 (1998), pp. 401–407 (cit. on pp. 92, 94).

[258] S. Bresolin, A. Roy, G. Ferrari, A. Recati, and N. Pavloff. "Oscillating Solitons and ac Josephson Effect in Ferromagnetic Bose-Bose Mixtures". In: *Physical Review Letters* 130.22 (2023), p. 220403 (cit. on pp. 92, 94).

[259] F. Bloch. "Über die Quantenmechanik der Elektronen in Kristallgittern". In: *Zeitschrift für Physik* 52.7 (1929), pp. 555–600 (cit. on p. 94).

[260] C. Zener. "A Theory of the Electrical Breakdown of Solid Dielectrics". In: *Proceedings of the Royal Society of London. Series A* 145.855 (1934), pp. 523–529 (cit. on p. 94).

[261] M. Ben Dahan, E. Peik, J. Reichel, Y. Castin, and C. Salomon. "Bloch Oscillations of Atoms in an Optical Potential". In: *Physical Review Letters* 76.24 (1996), pp. 4508–4511 (cit. on p. 94).

[262] S. R. Wilkinson, C. F. Bharucha, K. W. Madison, Qian Niu, and M. G. Raizen. "Observation of Atomic Wannier-Stark Ladders in an Accelerating Optical Potential". In: *Physical Review Letters* 76.24 (1996), pp. 4512–4515 (cit. on p. 94).

[263] Z. A. Geiger, K. M. Fujiwara, K. Singh, R. Senaratne, S. V. Rajagopal, M. Lipatov, T. Shimasaki, R. Driben, V. V. Konotop, T. Meier, and D. M. Weld. "Observation and Uses of Position-Space Bloch Oscillations in an Ultracold Gas". In: *Physical Review Letters* 120.21 (2018), p. 213201 (cit. on p. 94).

[264] L. Morel, Z. Yao, P. Cladé, and S. Guellati-Khélifa. "Determination of the fine-structure constant with an accuracy of 81 parts per trillion". In: *Nature* 588.7836 (2020), pp. 61–65 (cit. on p. 94).

[265] M. Gustavsson, E. Haller, M. J. Mark, J. G. Danzl, G. Rojas-Kopeinig, and H.-C. Nägerl. "Control of Interaction-Induced Dephasing of Bloch Oscillations". In: *Physical Review Letters* 100.8 (2008), p. 080404 (cit. on p. 94).

[266] P. M. Preiss, R. Ma, M. E. Tai, A. Lukin, M. Rispoli, P. Zupancic, Y. Lahini, R. Islam, and M. Greiner. "Strongly correlated quantum walks in optical lattices". In: *Science* 347.6227 (2015), pp. 1229–1233 (cit. on p. 94).

[267] G. Corrielli, A. Crespi, G. Della Valle, S. Longhi, and R. Osellame. "Fractional Bloch oscillations in photonic lattices". In: *Nature Communications* 4.1 (2013), p. 1555 (cit. on p. 94).

[268] D. M. Gangardt and A. Kamenev. "Bloch Oscillations in a One-Dimensional Spinor Gas". In: *Physical Review Letters* 102.7 (2009), p. 070402 (cit. on p. 94).

[269] F. Meinert, M. Knap, E. Kirilov, K. Jag-Lauber, M. B. Zvonarev, E. Demler, and H. Nägerl. "Bloch oscillations in the absence of a lattice". In: *Science* 356.6341 (2017), pp. 945–948 (cit. on p. 94).

[270] F. Bloch. "Superfluidity in a Ring". In: *Physical Review A* 7.6 (1973), pp. 2187–2191 (cit. on p. 95).

[271] L. A. Takhtajan. "Integration of the continuous Heisenberg spin chain through the inverse scattering method". In: *Physics Letters A* 64.2 (1977), pp. 235–237 (cit. on p. 95).

[272] M. Lakshmanan, T. W. Ruijgrok, and C. J. Thompson. "On the dynamics of a continuum spin system". In: *Physica A: Statistical Mechanics and its Applications* 84.3 (1976), pp. 577–590 (cit. on p. 97).

[273] M. Lakshmanan. "Continuum spin system as an exactly solvable dynamical system". In: *Physics Letters A* 61.1 (1977), pp. 53–54 (cit. on p. 97).

[274] A. V. Mikhailov. "The Landau-Lifschitz equation and the Riemann boundary problem on a torus". In: *Physics Letters A* 92.2 (1982), pp. 51–55 (cit. on p. 97).

[275] Y. L. Rodin. "The Riemann boundary problem on Riemann surfaces and the inverse scattering problem for the Landau-Lifschitz equation". In: *Physica D: Nonlinear Phenomena* 11.1 (1984), pp. 90–108 (cit. on p. 97).

[276] K. Nakamura and T. Sasada. "Gauge equivalence between one-dimensional Heisenberg ferromagnets with single-site anisotropy and nonlinear Schrödinger equations". In: *Journal of Physics C: Solid State Physics* 15.26 (1982), p. L915 (cit. on pp. 97, 98).

[277] A. E. Borovik and S. I. Kulinich. "Integration of the nonlinear dynamics of a uniaxial ferromagnet by the method of the inverse scattering problem". In: *Soviet Physics Journal of Experimental of Theoretical Physics* 39.7 (1984), pp. 320–324 (cit. on p. 97).

[278] A. Kundu. "Landau–Lifshitz and higher-order nonlinear systems gauge generated from nonlinear Schrödinger-type equations". In: *Journal of Mathematical Physics* 25.12 (1984), pp. 3433–3438 (cit. on pp. 97, 98).

[279] V. E. Zakharov and L. A. Takhtadzhyan. "Equivalence of the nonlinear Schrödinger equation and the equation of a Heisenberg ferromagnet". In: *Theoretical and Mathematical Physics* 38.1 (1979), pp. 17–23 (cit. on pp. 98, 100).

[280] R. F. Bikbaev, A. I. Bobenko, and A. R. Its. "Landau-Lifshitz equation, uniaxial anisotropy case: Theory of exact solutions". In: *Theoretical and Mathematical Physics* 178.2 (2014), pp. 143–193 (cit. on p. 99).

[281] A. E. Borovik. "N-soliton solutions of the nonlinear Landau-Lifshitz equation". In: *Soviet Physics Journal of Experimental of Theoretical Physics* 28.10 (1978), pp. 629–632 (cit. on p. 99).

[282] D. Bian, B. Guo, and L. Ling. "High-Order Soliton Solution of Landau–Lifshitz Equation". In: *Studies in Applied Mathematics* 134.2 (2015), pp. 181–214 (cit. on p. 99).

[283] E. Date, M. Jimbo, M. Kashiwara, and T. Miwa. "Landau-Lifshitz equation: solitons, quasi-periodic solutions and infinite-dimensional Lie algebras". In: *Journal of Physics A: Mathematical and General* 16.2 (1983), pp. 221–236 (cit. on p. 99).

[284] Z. Chen, N. Huang, and Z. Liu. "An inverse scattering transform for the Landau-Lifschitz equation for a spin chain with an easy axis". In: *Journal of Physics: Condensed Matter* 7.23 (1995), p. 4533 (cit. on p. 99).

[285] R. Li, X. Geng, and B. Xue. "A generalization of the Landau-Lifschitz equation: breathers and rogue waves:" in: *Journal of Nonlinear Mathematical Physics* 27.2 (2020), p. 279 (cit. on p. 99).

[286] A. I. Konyukhov, E. V. Shchurkin, L. A. Mel'nikov, A. A. Sysolyatin, and K. S. Gochelashvili. "On the All-Fiber Optical Methods of the Generation and Recognition of Soliton States". In: *Journal of Experimental and Theoretical Physics* 128.3 (2019), pp. 384–395 (cit. on p. 110).

[287] A. I. Konyukhov. "Management of the discrete eigenvalues of the nonlinear Schrödinger equation using periodic dispersion perturbation". In: *Chaos, Solitons & Fractals* 178 (2024), p. 114391 (cit. on p. 110).

[288] H. Sakaguchi and B. A. Malomed. "Resonant nonlinearity management for nonlinear Schrödinger solitons". In: *Physical Review E* 70.6 (2004), p. 066613 (cit. on pp. 110, 115).

[289] D. J. Kaup. "A Perturbation Expansion for the Zakharov–Shabat Inverse Scattering Transform". In: *SIAM Journal on Applied Mathematics* 31.1 (1976), pp. 121–133 (cit. on p. 110).

[290] J. P. Keener and D. W. McLaughlin. "Solitons under perturbations". In: *Physical Review A* 16.2 (1977), pp. 777–790 (cit. on p. 110).

[291] V. I. Karpman and E. M. Maslov. "Perturbation theory for solitons". In: *Soviet Journal of Experimental and Theoretical Physics* 46.2 (1977), pp. 281–291 (cit. on pp. 110, 111).

[292] V. I. Karpman and V. V. Solov'ev. "A perturbational approach to the two-soliton systems". In: *Physica D: Nonlinear Phenomena* 3.3 (1981), pp. 487–502 (cit. on pp. 110, 112).

[293] D. J. Kaup and A. C. Newell. "Solitons as particles, oscillators, and in slowly changing media: a singular perturbation theory". In: *Proceedings of the Royal Society of London. A. Mathematical and Physical Sciences* 361.1707 (1978), pp. 413–446 (cit. on p. 110).

[294] J. E. Prilepsky and S. A. Derevyanko. "Breakup of a multisoliton state of the linearly damped nonlinear Schrödinger equation". In: *Physical Review E* 75.3 (2007), p. 036616 (cit. on pp. 112, 113, 117).

[295] T. Okamawari, A. Hasegawa, and Y. Kodama. "Analyses of soliton interactions by means of a perturbed inverse-scattering transform". In: *Physical Review A* 51.4 (1995), pp. 3203–3220 (cit. on pp. 113, 117).

[296] Y. Kodama and A. Hasegawa. "Nonlinear pulse propagation in a monomode dielectric guide". In: *IEEE Journal of Quantum Electronics* 23.5 (1987), pp. 510–524 (cit. on p. 113).

[297] F. M. Mitschke and L. F. Mollenauer. "Discovery of the soliton self-frequency shift". In: *Optics Letters* 11.10 (1986), p. 659 (cit. on p. 113).

[298] E. A. Golovchenko, E. M. Dianov, A. M. Prokhorov, and V. N. Serkin. "Decay of optical solitons". In: *Soviet Physics Journal of Experimental and Theoretical Physics* 42.2 (1985), pp. 74–77 (cit. on p. 114).

[299] P. K. A. Wai, C. Menyuk, Y. Lee, and H. Chen. "Nonlinear pulse propagation in the neighborhood of the zero-dispersion wavelength of monomode optical fibers". In: *Optics Letters* 11 (1986), pp. 464–466 (cit. on p. 114).

[300] P. Beaud, W. Hodel, B. Zysset, and H. Weber. "Ultrashort pulse propagation, pulse breakup, and fundamental soliton formation in a single-mode optical fiber". In: *IEEE Journal of Quantum Electronics* 23.11 (1987), pp. 1938–1946 (cit. on p. 114).

[301] K. Tai, N. Bekki, and A. Hasegawa. "Fission of optical solitons induced by stimulated Raman effect". In: *Optics Letters* 13.5 (1988), p. 392 (cit. on pp. 114, 119).

[302] A. Hasegawa and Y. Kodama. *Solitons in Optical Communications*. Oxford: Oxford University Press, 1995 (cit. on p. 115).

[303] A. A. Sysoliatin, A. K. Senatorov, A. I. Konyukhov, A. A. Melnikov, and V. A. Stasyuk. "Soliton fission management by dispersion oscillating fiber". In: *Optics Express* 15.25 (2007), p. 16302 (cit. on p. 115).

[304] A. Suryanto and E. van Groesen. "Self-splitting of multisoliton bound states in planar Kerr waveguides". In: *Optics Communications* 258.2 (2006), pp. 264–274 (cit. on p. 115).

[305] K. Zhou, Z. Guo, and S. Liu. "Position dependent splitting of bound states in periodic photonic lattices". In: *Journal of the Optical Society of America B* 27.5 (2010), p. 1099 (cit. on p. 115).

[306] B. A. Malomed, N. N. Rosanov, and S. V. Fedorov. "Dynamics of nonlinear Schrödinger breathers in a potential trap". In: *Physical Review E* 97.5 (2018), p. 052204 (cit. on p. 115).

[307] V. Dunjko and M. Olshanii. "Resilience of constituent solitons in multisoliton scattering off barriers". In: *arXiv:1501.00075* (2020) (cit. on p. 115).

[308] O. V. Marchukov, B. A. Malomed, V. A. Yurovsky, M. Olshanii, V. Dunjko, and R. G. Hulet. "Splitting of nonlinear-Schrödinger-equation breathers by linear and nonlinear localized potentials". In: *Physical Review A* 99.6 (2019), p. 063623 (cit. on p. 115).

[309] C. L. Grimshaw, S. A. Gardiner, and B. A. Malomed. "Splitting of two-component solitary waves from collisions with narrow potential barriers". In: *Physical Review A* 101.4 (2020), p. 043623 (cit. on p. 116).

[310] O. Katz, Y. Lahini, and Y. Silberberg. "Multiple breakup of high-order spatial solitons". In: *Optics Letters* 33.23 (2008), p. 2830 (cit. on p. 118).

[311] C. Ciret, S.-P. Gorza, C. Husko, G. Roelkens, B. Kuyken, and F. Leo. "Physical origin of higher-order soliton fission in nanophotonic semiconductor waveguides". In: *Scientific Reports* 8.1 (2018), p. 17177 (cit. on p. 118).

[312] A. Mucci, P. Suret, F. Copie, S. Randoux, R. Mullyadzhanov, and A. Gelash. "Manipulation of Strongly Interacting Solitons in Optical Fiber Experiments". In: *Physical Review Letters* 134.19 (2025), p. 193804 (cit. on p. 119).

[313] V. P. Kotlyarov. "On the gauge equivalence of the equation of dynamics for uniaxial ferromagnets". In: *Journal of Physics C: Solid State Physics* 17.5 (1984), pp. L139–L143 (cit. on pp. 137, 140).